

**INVESTIGATIONS OF THE ZINC-CERIUM
HYBRID FLOW BATTERY**

by

Georgios Nikiforidis

A thesis presented in fulfilment of the requirements for the degree of

Doctor of Philosophy

2012

ACKNOWLEDGMENTS

I would like to thank my supervisor Dr. Leonard Berlouis for giving me the chance to work on this exciting project and also for his continued help, support and guidance throughout the course of my PhD and beyond.

I also would like to express my gratitude to David Hodgson, David Hall and Scott Lilley of Plurion Ltd. and also Jim Morrow and Neil Hodgson of the University of Strathclyde for their help and assistance on various aspects of this project.

Many thanks also to Scottish Funding Council's SPIRIT studentship and Plurion Ltd. for funding this project.

In addition I would like to thank members of the Skabara, Mills and Liggat groups as well as Evelyn Caldwell of the Berlouis group for making this experience rather enjoyable.

Finally, I would like to thank my family for their continued support and advice over the many years of my education.

ABSTRACT

Electrochemical energy storage devices such as batteries, including redox flow batteries (RFB's) are among the leading electricity energy storage technologies for the future because of their lower operating cost, scale-ability and versatility. This study was concerned with the evaluation of the zinc-cerium hybrid redox flow battery system and obtaining its optimum operating parameters. The clear advantage that the zinc-cerium flow cell has over other current flow battery systems such as the all-vanadium RFB is that the cell voltage is ~ 2.5 V (*c.f.* 1.3 V for the VRFB) and therefore greater power can be delivered from a single unit.

During this project, the half-cell reactions were studied on a variety of electrode substrates, using different electrolyte compositions and temperature. The efficiency of the zinc-half cell reaction was examined on several carbon-based substrates and on three of these (the PVE, HDPE and PVDF composites), coulombic efficiencies of *c.a.* 95% were obtained. Nucleation studies indicated that a high density of nuclei ($\sim 10^6$) was formed on these carbon substrates from solutions containing 1.5 mol dm^{-3} zinc ions in 2.7 mol dm^{-3} methane sulfonic acid. This led to the formation of more uniform deposits and minimised dendritic growth. The surfaces of the substrates following numerous zinc deposition-dissolution cycles were characterised using SEM and optical microscopy. Although some deterioration of the electrode surface was found in most of the substrates examined, the PVE, HDPE and PVDF were not severely affected and good cycling performance could be maintained over 200 cycles. During these cycles, hydrogen evolution was not a serious issue because of the inhibition of this reaction on the electrodeposited zinc substrate.

The study on the positive half-cell reaction, that of the Ce(IV)/Ce(III) was carried out using a range of Pt and Pt-Ir based coatings on a titanium base. The high positive potential (~ 1.4 V) of this reaction eliminated the use of carbon-based substrates due to oxidation issues. Higher temperatures (60°C) were found to favour this reaction (*viz.* higher i_o and D values) but the solubility of the cerium species in the methanesulfonic acid was found to be dependent on both temperature and on the acid concentration/water content. The charge discharge current densities that could be applied on these substrates were not greater than $\pm 25 \text{ mA cm}^{-2}$ due to the OER. The η_V values recorded were *ca.* 85%.

The temperature range between 45°C and 55°C was found to be best for operating the redox flow cell while it was found that the coulombic efficiency increased with zinc concentration ($\eta_C \sim 95\%$ at $2 \text{ mol dm}^{-3} \text{ Zn}^{2+}$). The η_V did not exceed 70% in the flow cell but in the case of the undivided system (*i.e.* with no membrane separator), the values found were *ca.* 77%. The η_ε values obtained for the flow cell were *ca.* 55% for the PVE and PVDF carbon composite electrodes at current densities of $\pm 10 \text{ mA cm}^{-2}$.

Contents

Chapter 1	8
1.1 Introduction.....	8
1.2 Objectives	11
1.3. Thesis outline	11
Chapter 2.....	13
2.1 Flow batteries.....	13
2.2 Types of Flow Batteries	15
2.2.1 History of Redox Flow Batteries	15
2.2.2 RFB Operation	16
2.2.3 Electrochemical reactions of various RFB systems.....	19
2.2.4 Undivided RFB	21
2.2.5 Summary of existing RFB	23
2.3 Hybrid Flow batteries	25
2.4 Zinc-Cerium RFB	28
2.4.1 Zinc deposition reaction.....	30
2.4.2 Ce(IV)/Ce(III) reaction	32
2.5 Conclusions.....	34
Chapter 3.....	43
3.1 Steady state and non steady state techniques	43
3.2 Three electrode cell.....	44
3.3 Simple electron transfer reactions.....	46
3.3.1 Nernst equation	46
3.3.2 Butler-Volmer equation	48
3.3.3 Nernst diffusion layer	52
3.3.4 Cyclic voltammetry.....	54
3.3.5 Randles-Sevcik equation.....	56
3.4 Potential step techniques	57
3.4.1 Instantaneous and progressive nucleation.....	58
3.4.2 Electric Double layer	62
3.4.3 A.C. Impedance	64
3.5 Rotating disk electrode	67
3.5.1 Levich equation.....	69
3.5.2 Kouteky-Levich equation.....	70
3.6 Galvanic Cycles - General remarks and methodology	72
3.7 Hydrogen evolution reaction.....	74
3.8 Oxygen evolution reaction.....	76

3.9 Scanning electrode microscope.....	77
3.10 Thermogravimetric analysis.....	78
3.11 ICP-MS	79
Chapter 4.....	82
4.1 Chemical reagents.....	82
4.2 Zinc and cerium electrolytes.....	86
4.2.1 Sodium methanesulfonate solutions	87
4.3 Carbon composite materials for the zinc-cerium RFB	88
4.3.1 Correlation of electrode rotation rate with Re for the electrodes used on the negative half cell reaction of the zinc cerium flow cell.....	91
4.4 Pt based substrates for the positive side of the zinc cerium RFB	92
4.4.1 Determining the specific electrochemical area of the Pt and Pt/Ir electrodes	94
4.4.2 Correlation of electrode rotation rate with Re for the electrodes on the positive half cell reaction of the zinc cerium cell	95
4.5 Batch Cell.....	96
4.6 Flow cell.....	97
4.6.1 Cell velocity of the zinc cerium flow cell.....	99
4.7 Undivided zinc-cerium redox cell.....	101
Chapter 5.....	104
5.1 Cyclic Voltammetry.....	104
5.1.1 Effect of mass transport	106
5.1.2 Effect of temperature	108
5.1.3 Effect of carbon composite materials	110
5.1.4 Effect of zinc (II) ion concentration.....	111
5.1.5 Effect of methanesulfonic acid concentration.....	112
5.1.6 Effect of additives on zinc electrodeposition.....	113
5.2 Kinetic parameters on the negative side of the zinc - cerium RFB	115
5.2.1 Introduction.....	115
5.2.2 Tafel extrapolation	116
5.2.3 Polarisation resistance.....	117
5.2.4 Exchange current density of zinc in methanesulfonic acid.....	118
5.3 Zinc deposition from a sodium methanesulfonate solution containing 10×10^{-3} mol dm^{-3} Zn(II).....	119
5.3.1 RDE study.....	119
5.3.2 Scan rate dependence in 1×10^{-2} mol dm^{-3} Zn(II) and 2.5×10^{-1} mol dm^{-3} Na(CH ₃ SO ₃).....	124
5.3.3 Note - comparison of D values from sections 5.3.1 and 5.3.2.....	126
5.4 Nucleation studies on the formation of zinc nuclei during zinc deposition.....	127

5.4.1 Nucleation studies in a solution consisting of various concentrations of Zn(II) in 5.7 mol dm ⁻³ CH ₃ SO ₃ H	127
5.4.2 Nucleation studies in a solution consisting of various concentrations of Zn(II) in sodium methanesulfonate solutions	130
5.5 Galvanic Cycles	134
5.5.1 Effect of rotation rate	134
5.5.1.1 Calculation of limiting current density (<i>i_L</i>) for the zinc deposition reaction containing 1.5 mol dm ⁻³ Zn(II) ions.	136
5.5.2 Effect of temperature	137
5.5.3 Different carbon composite materials	139
5.5.4 Effect of charging time on η_C and η_V	143
5.5.5 Effect of discharge current density	145
5.5.6 Effect of zinc methanesulfonate concentration	147
5.5.7 Effect of methanesulfonic acid concentration	149
5.5.8 Effect of operating conditions on zinc deposit morphologies	150
5.5.9 Effect of additives on galvanic cycles	154
5.6 Conclusion	156
Chapter 6	160
6.1 Introduction	160
6.2 Determination of the Pt surface area for the electrodes for the positive half cell electrolyte	161
6.3 Cyclic Voltammetry in 8 × 10 ⁻¹ mol dm ⁻³ Ce(III) and 6.9 mol dm ⁻³ CH ₃ SO ₃ H	165
6.3.1 Different electrode materials	165
6.3.2 Effect of rotation speed	168
6.3.3 Effect of temperature	170
6.3.4 Scan rate dependence on the reduction of Ce(IV)	172
6.4 Cyclic Voltammetry in various Ce(IV) solutions in 6.9 mol dm ⁻³ CH ₃ SO ₃ H	173
6.4.1 Pt electrode in 5.9 × 10 ⁻¹ mol dm ⁻³ Ce(IV) / 7 × 10 ⁻² mol dm ⁻³ Ce(III), 7 × 10 ⁻¹ mol dm ⁻³ Zn(II) and 6.9 mol dm ⁻³ CH ₃ SO ₃ H	173
6.4.2 Pt electrode in 5 × 10 ⁻³ mol dm ⁻³ Ce(IV) in 6.9 mol dm ⁻³ CH ₃ SO ₃ H	176
6.4.3 Platinised-titanium mesh in 8 × 10 ⁻² mol dm ⁻³ Ce(IV) / 7.2 × 10 ⁻¹ mol dm ⁻³ Ce(III) and 6.9 mol dm ⁻³ CH ₃ SO ₃ H - effect of temperature	179
6.4.4 Pt Ir substrates in 2 × 10 ⁻¹ mol dm ⁻³ Ce(IV) and 6.9 mol dm ⁻³ CH ₃ SO ₃ H	181
6.4.5 Pt substrates in 2 × 10 ⁻¹ mol dm ⁻³ Ce(IV) and 6.9 mol dm ⁻³ CH ₃ SO ₃ H	182
6.5 Kinetics of the Ce(III)/Ce(IV) reaction onto different substrates	184
6.5.1 Introduction	184
6.5.2 Polarisation resistance	184
6.5.3 Tafel extrapolation	187

6.5.4 Electrochemical Impedance Spectroscopy	191
6.6 Galvanic cycles	196
6.6.1 Introduction.....	196
6.6.2 Effect of rotation rate	197
6.6.3 Effect of temperature	200
6.6.4 Effect of charge and discharge current density.....	202
6.6.5 Effect of prolonged cycling on the Pt and Pt-It substrates.....	204
6.7 Conclusion	206
Chapter 7.....	209
7.1 Introduction.....	209
7.2 Batch cell	210
7.2.1 Electrolytes	210
7.2.1 Solutions 1 and 2.....	211
7.2.2 Solution 3.....	212
7.2.3 Solution 4.....	213
7.2.4 Solution 5.....	213
7.2.5 Solution 6.....	215
7.2.6 Conclusions.....	215
7.3 Zinc Cerium flow cell.....	216
7.3.1 Electrolytes	216
7.3.2 Electrolyte 1	219
7.3.3 Electrolytes 2 and 3.....	220
7.3.4 Electrolyte 4.....	222
7.3.5 Electrolyte 5	226
7.3.6 Electrolyte 6.....	228
7.3.7 Electrolyte 7.....	230
7.3.8 Electrolyte 8.....	231
7.3.9 Conclusions.....	235
7.4 Undivided cell.....	236
7.4.1 Electrolytes	236
7.4.2 Electrolyte 1	237
7.4.2 Electrolyte 2.....	238
7.4.3 Summary of Electrolytes 3-6	240
7.4.5 Conclusions.....	240
Chapter 8.....	242
8.1. Conclusions.....	242
8.2. Future work.....	244

Chapter 1

1.1 Introduction

Energy storage is the most dominant factor in economic development with the widespread use of chemical fuels like gasoline and natural gas as well as the introduction of electricity in the late 19th century. Chemical fuels such as coal, gasoline, diesel fuel, natural gas, propane, biodiesel and ethanol became dominant in energy storage and are prevailing in both electrical generation and energy transportation via the usage of heat engines that convert the mechanical to the electrical energy. Energy storage systems can be categorised as mechanical (hydraulic/compressed/flywheel energy storage), electrical (capacitor, supercapacitor), chemical (hydrogen, biofuel, hydrogen peroxide, liquid nitrogen), electrochemical (batteries), biological (starch, glycogen) and thermal (ice storage, molten salt, cryogenic liquid air or nitrogen). The resources of energy storage are traditionally less cost-effective than power generation resources.

For large scale energy storage, grid energy storage allows the producers of energy to send excess electricity over the electricity transmission grid to electricity storage sites which become producers in periods of high electricity demand. This is done in order to increase the efficiency, minimize the cost of energy production while also to facilitate the use of intermittent energy sources such as photovoltaics and wind turbines. Intermittent energy sources are unpredictable though and hence difficult to rely on. Still, the use of these energy sources is of crucial importance as in an electrical power grid without energy storage the energy sources that rely on energy stored within fuel such as gas or oil must be scaled up and down to match the rise and fall of energy production from intermittent energy sources. A further advancement on the electrical grid was made in the United States in 2009 with the integration of smart electrical grids [1]. These digitally enabled electrical grids gather, distribute and act on information based on the behaviour of the supplier and consumers aiming to improve the efficiency, robustness and economics of the electricity services.

In the majority of the developed countries, such as the United States, the capacity factor of power generating sources (*i.e* the ratio of the actual output of these power generating resources over a period of time and the potential output if they had operated at full capacity) is as low as 40% [2]. Therefore, an average 40% of the installed capacity is utilized leading to excess power generation and transmission being underused every year. Insufficient energy storage could lead to problems like reduced reliability raised volatility, and threatened

security [3]. Currently for large energy storage applications, only pumped hydro and compressed gas are cost effective. Pumped hydro consists of two reservoirs with a height differential and a pipe connecting them while compressed gas involves air passed through a compressor during discharge with the air expanding as it is being mixed with fuels such as oil. Pumped storage hydroelectricity is the largest capacity form of grid energy storage available with more than 99% of bulk storage capacity worldwide, *viz.* 127.000 MW [4]. However, these technologies are limited by geography and are not flexible (*i.e* geology is important) [5].

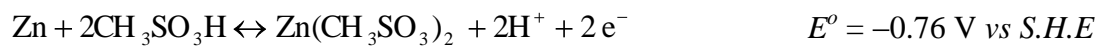
One possible technology for large-scale storage is large-scale flow batteries. The electrochemical energy storage devices such as batteries, fuel cells and flow batteries are among the leading electricity energy storage (EES) technologies for the future because of their lower operating cost, flexibility, scale-ability and versatility. These relatively new technologies able to store large quantities of energy have the potential to increase the flexibility of power systems and improve the response to a rising demand of energy as well as minimizing environmental damage. Rechargeable flow batteries can be used as a rapid response storage medium and hence facilitate load levelling *i.e* to store excess electrical power during low demand period and for release as demand rises, which is the main application of an energy storage system. It reduces the large fluctuations that occur in electricity demand by storing excess energy during off-peak hours for use during periods of high demand. Load levelling provides some advantages over electric power transmission systems such as a more effective use of existing plant investment, flexibility of operation and better response to price changes. It is also crucial for remote power systems. Stored electricity can be made readily available to meet immediate changes in demand allowing effective operation of base load units at high levels of power. This technique can be also applied for use with other renewable energy sources, such as solar (photovoltaic cells) and wind (wind turbine). With the use of flow batteries, electricity transmission companies would be able to increase the load factor of their transmission lines while distribution companies can use energy storage to replace or defer investment in generating on their electrical network.

Conventional batteries such as the lead-acid battery and the lithium-ion store their active material on the electrodes or in the electrolyte between the electrodes. However, fuel cells are different from batteries in that they require a constant source of fuel (*i.e* hydrogen) and oxygen to run. Flow batteries allow storage of the active materials external to the battery and these reactants are circulated through the cell stack as required. Various classes of flow batteries exist including the redox flow battery, in which all electroactive species are

dissolved in the electrolyte. The energy of the RFB can be determined independently of the battery power because it is related to the electrolyte volume whereas the power is related to the reactor size.

The first RFB systems were developed during the 70's [6]. These batteries do not require any special terrain and compared to the conventional batteries (lead-acid) they are easier and less costly to maintain. The modular nature of RFB enhances its transportability and makes its construction and maintenance costs the lowest among other energy storage systems. The discharge time of a RFB at full power can be varied, as required, from several minutes to many days. They can be discharged completely without damaging the cells, which leads to more robust charge-discharge cycles. The production of energy on site could reduce burdens on electricity distribution systems and promote the widespread use of renewable and cleaner energy. Numerous redox flow battery technologies are currently under development such as the all vanadium battery, the polysulfide bromide battery, the uranium redox flow battery as well as the zinc/bromine (Zn/Br) and zinc/cerium(Zn/Ce) flow cells [7][8].

The zinc/cerium cell is a relatively new redox flow technology, which has been developed by Plurion Ltd. [9] [10]. This cell in its basic form consists of a single cell with a cation exchange membrane separating the anode and the cathode. Both cerium and zinc half-cell reactions have high standard electrode potentials, which results in high cell potentials and power output. At the negative electrode during charging, the metal ions move from the solution and deposit on the solid cathode (*e.g.* carbon electrode). The reduction reaction which occurs is:



Eq.1.1

During discharge, the reverse reaction occurs where the deposited metal moves from the metal lattice and strips back into the solution, releasing electrons that can do external work. At the positive electrode during charging, oxidation of the Ce(III) to Ce(IV) occurs [11]. The positive standard electrode potential lies between 1.28 V and 1.72 V vs. Ag|AgCl [11].



Eq.1.2

The overall zinc-cerium cell reaction is thus:



Eq.1.3

The current density applied to this system is as high as 40 mA cm^{-2} to 50 mA cm^{-2} , while the open circuit cell voltage is at least 2.2 V , which is nearly double of any other flow cells currently in use. Hence, the ratio of power to weight is extremely high, and hence this characteristic enhances the performance and mobility of the zinc-cerium battery. In addition, all chemicals used in this system have low impact in both human being and the environment. Methanesulfonic acid is used as a solvent for both zinc and cerium species. The reason why methanesulfonic acid is used in the zinc-cerium battery is that it can dissolve and thus store a very high cerium concentration [12] while a concentration of 2.16 mol dm^{-3} is sufficient for the zinc species [13]. The conductivity of the above acid (k) is similar to that of hydrochloric acid and is less corrosive than most common acids, such as hydrochloric acid and sulfuric acid [14].

1.2 Objectives

The main objective of this work was to develop and evaluate the performance of the zinc-cerium redox flow battery. However, the initial stages of this research project focused on the fundamental chemistry of the zinc and cerium half cell reactions. Factors such as electrode materials, kinetics of the reactions, temperature, chemical side reactions and concentration of electroactive materials were investigated in order to define the operating parameters. Once the information from the half-cell studies had been analysed, a pilot redox flow battery was set up and the parameters for optimum performance of the redox flow battery system were determined.

1.3. Thesis outline

This thesis comprises of eight chapters. The first chapter introduces the zinc-cerium redox flow battery and discusses the objectives of this project. Chapter 2 provides a comprehensive description of the background and recent development on the flow battery field. Chapter 3 discusses the theory that underpins the methodology of the experimental techniques used in this project. Chapter 4 describes the experimental set-up used in this study. Chapters 5 and 6 investigate the electrochemical behaviour of the zinc and the cerium half cell reactions, respectively. Chapter 7 examines the experimental work on the zinc-cerium flow cell system. Finally, Chapter 8 presents general conclusive remarks on this study and sets out proposals for future work on the zinc-cerium flow battery system.

[1]

http://energy.gov/sites/prod/files/oeprod/DocumentsandMedia/DOE_SG_Book_Single_Pages%281%29.pdf accessed: Nov. 2011

[2] *The Electricity Advisory Committee,*

http://www.oe.energy.gov/DocumentsandMedia/final-energy-storage_12-16-08.pdf accessed: Nov. 2011

[3] J. Makansi, J. Abboud, *Energy Storage Council White Paper*, (2002).

[4] Energy storage-packing some power. *The Economist*. 03-03-2011.

[5] T. Nguyen, R.F. Savinell, *The electrochemical Society Interface.*, (2010).

[6] M. Bartolozzi, *J. Power Sources.*, **27**, 219-234, (1989).

[7] C. Ponce de León, A. Frías-Ferrer, J. González-García, D.A. Szánto, F.C. Walsh, *J. Power Sources.*, **160**, 716-732, (2006).

[8] M. Skyllas-Kazacos, M.H. Chakrabarti, S.A. Hajimolana, F.S. Mjalli, M. Saleem, *J. Electrochem. Soc.*, **158**, (8), 55-79, (2011).

[9] R.L. Clarke, B.J. Dougherty, S. Harrison, J.P. Millington, S. Mohanta, US 2006/0063065 A1, Battery with bifunctional electrolyte (2005).

[10] R. L. Clarke, B. J. Dougherty, S. Harrison, P. J. Millington, S. Mohanta, US 2004/0202925 A1, Cerium Batteries (2004).

[11] J. Bard, L.R. Faulkner, *Electrochemical Methods - Fundamentals and Applications*, 2nd Edition, Wiley, (2001).

[12] R.M. Spotnitz, R.P. Kreh, J.T. Lundquist, P.J. Press, *J. Applied Electrochem.*, **20**, 209-215, (1990).

[13] M.D. Gernon, M. Wu, T. Buszta, P. Janney, *Green Chem.*, **1**, 127-140, (1999).

[14] <http://www.arkema-inc.com/index.cfm?pag=127> accessed: Nov. 2011

Chapter 2

2.1 Flow batteries

A flow battery is a form of rechargeable battery in which the electrolyte containing one or more dissolved electroactive species flows through an electrochemical cell that converts the chemical electroactive species to electrical energy. The electrolytes containing the electroactive species act as liquid energy carriers and are pumped simultaneously through the two half cells separated by an ion exchange membrane. Flow batteries can be rapidly recharged or charged by simply replacing the liquid electrolyte, which of course is not feasible in the case of the primary batteries [1]. The first such battery to be developed was a zinc/chlorine system in which the chlorine was stored in a separate cylinder [2]. It was first used in 1884 by Charles Renard to power his airship which contained its own on board chlorine generator.

During charging, the electrical energy supplied in the flow battery system causes a chemical reduction reaction in one electrolyte and an oxidation reaction in the other. The thin ion exchange membrane between the half-cells prevents the electrolytes from mixing but allows selected ions to pass through in order to complete the electrical circuit. During discharge, the chemical energy contained in the electrolyte is released in the reverse electrochemical reactions and electrical energy can be drawn from the cell. When in use, the electrolytes are continuously pumped in a closed loop between reactor and storage tanks.

The energy capacity requirement of a flow battery is addressed by the size of the external storage components while the power rating of the system is determined by the size and number of electrodes in the cell stacks. High power batteries are constructed using a multiple stack of cells in a bipolar arrangement [3] [4]. One face of the bipolar electrode acts as the anode surface and the opposite face as the cathode surface. The great advantage of this system is that it provides almost unlimited electrical storage capacity the limitation imposed only by the capacity of the electrolyte storage reservoirs. The desirables in the design of a flow battery system are moderate costs, convenience and reliability in operation as well as appropriate reaction engineering and versatility. As with all battery systems, the performance of the flow battery depends on cell geometry, electrode reactions and their kinetics as well as design and composition of the electrode components.

Different types of flow batteries exist and the most common are those in which all the electroactive materials remain soluble in the liquid electrolyte. In such a redox flow battery,

the power conversion component is independent of the chemical energy capacity of the device whereas in the hybrid flow battery this becomes limited by the amount of solid material that can be deposited and accommodated within the reactor. The hybrid flow battery is thus one in which one or more electroactive components are deposited as a solid layer at the anode and cathode [2]. Fuel cells [5] can be also considered as a type of flow battery as the energy of the system is determined independently of the battery power as the fuel cell is externally stored to the cell. However, fuel cells are distinguishable from redox flow batteries by the fact that although there is a flow of reactants to the electrodes in both cases, the chemical reaction in the fuel cell is often irreversible within the electrochemical fuel cell (*i.e* the hydrogen fuel cell [6]). However, fuel cells with reversible reaction have been reported such as the regenerative fuel cell and the reversible solid oxide fuel cell [7].

Electrochemical device	Site of reactants/products	Electrolyte conditions	Separator
Static battery	Active electrode material	Static and held within cell	Microporous polymer separator
Redox flow cell	Aqueous electrolytes in reservoirs	Electrolyte recycles through the cell	Ion exchange membrane (cationic or anionic)
Hybrid flow cell	Aqueous electrolytes in reservoirs (metal deposition in at least one side of the electrode)	Electrolyte recycles through the cell	Ion exchange membrane (cationic or anionic)
Fuel cell	Gaseous or liquid fuel plus air	Solid polymer or ceramic acts as solid electrolyte within cell	Ion exchange membrane polymer or ceramic

Table 2.1: Comparisons between conventional static battery, redox flow cell and fuel cell [8].

2.2 Types of Flow Batteries

2.2.1 History of Redox Flow Batteries

Early research on the redox flow battery (RFB) was carried out in the 1970's by the National Aeronautics and Space Administration (NASA) [9], the Energy Development Associates (EDA) [10], the Exxon Corporation and several Japanese research institutes [11] on the Ir/Cr, Ir/Ti [12] [13] and Ru(bpy)₃/(BF₄)²⁻ [14] systems. The first redox flow battery was the iron-chromium system developed by L.H. Thaller in 1974 [15]. Further development in this system was conducted by Lopez *et al.* [16]. During the 1980's the all-vanadium redox system was successfully developed by Maria Skyllas-Kazacos *et al.* [17] [18] and currently more than 30 large-scale plants have been installed globally [19] [20] [21] [22] due to its high energy efficiency *viz.* >80%. The great success of the all vanadium RFB has also led to the development of the vanadium-cerium [23], the vanadium-polyhalide [24] [25], the vanadium-bromine [25], the vanadium-magnesium [26], the vanadium-acetylacetonate [27] and the vanadium-crystone dioxide [28] systems as they can provide higher cell potentials and energy densities (Wh L⁻¹).

During the last decade, other RFB's have been developed, such as the soluble lead-acid [29] [30], the zinc-cerium [31], the zinc-nickel [32], the cadmium-chloranil [33] and the copper-lead dioxide [34] systems. These batteries categorised as undivided flow batteries utilize a single electrolyte and therefore the use of ion-exchange membranes is not required. Actinide RFB systems such as the uranium RFB [35] and the neptunium RFB [35] have also been developed. Uranium and neptunium acetylacetonate complexes were chosen due to their large solubility in aprotic solvents. The bromine-polysulfide flow battery (*i.e. Regenesys*[®] cell) was first patented in 1983 and has been studied since by various groups [36] [37].

Reviews of RFBs have been given by Bartolozzi *et al.* [2] in 1989 and then by Ponce de León *et al.* [8] in 2006. The latter focused on the characteristics of the flow batteries such as open-circuit potential, power density, energy efficiency and charge-discharge behaviour. Since then, a number of further reviews regarding the progress on flow battery research and development have come out [38] [39] [40], indicating the rapid expansion of interest in this field of energy storage.

2.2.2 RFB Operation

The concept of the RFB is simple and poses low environmental impacts compared to the more conventional systems, such as the stationary lead acid battery [41]. Redox energy storage systems normally employ two soluble redox couples as electroactive species that are oxidised or reduced to store or to deliver energy. The electrode reactions taking place must be reversible and the oxidised and reduced species involved must ideally be soluble in their respective electrolytes. These batteries are rechargeable, usually without any change on the chemistry and morphology of the electrode materials. Fig.2.1 shows the basic aspects of a redox flow cell.

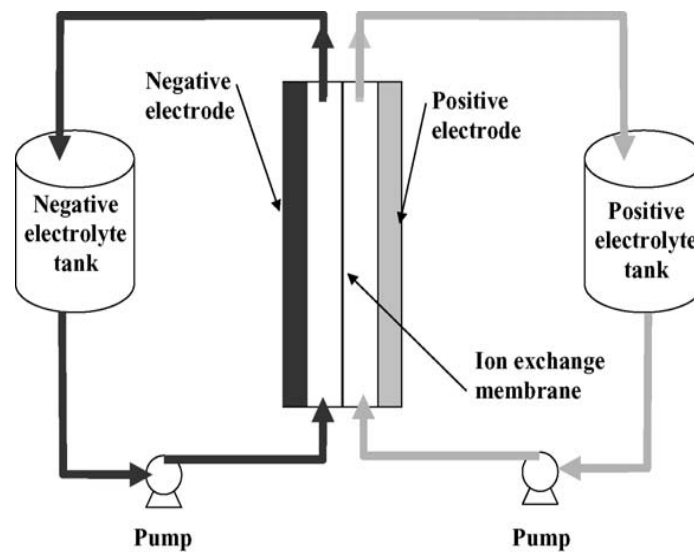


Fig.2.1: Unit redox flow cell for energy storage [8].

The electrodes are separated by an ion exchange membrane while the reactants contained in separate storage tanks, are recirculated through the half cells where the electrochemical reactions take place. The ion-exchange membrane is a thin sheet of polymer designed to allow the transport of either ions or cations but not both. Transport of ions should occur via migration. The polymers have fixed ionic groups (sulfonate or carboxylate for cation-permeable membranes or tetraalkylammonium groups for anion-permeable membranes) that are designed to prevent the passage of ions of the same charge and allow the transport of ions of the opposite charge. The fixed ionic groups are bound to a polymer background designed to allow the appropriate level of hydration as the latter is essential for obtaining an acceptable conductivity. Other features of the ion exchange membrane involve permeability to the charge balancing ions of the supporting electrolyte such as protons and good thermal stability in order to ensure the battery's cycle life [42]. Modern membranes give good selectivity with $t_+ = 0.95-0.99$ but they are never totally selective for cation vs

anions. The disadvantages of the membrane involve finite lifetime, complication of the cell design, construction and maintenance, increase of the power costs and finally volumetric transfer of water [33]. A vast range of ion exchange membranes is used for these systems, especially for the vanadium based redox flow cells *viz.* ion/cation exchange membrane [43] and Nafion[®] [44] [45]. Nafion[®] membranes are based on a perfluorohydrocarbon backbone with sulfonate or carboxylate fixed ionic groups. The perfluorohydrocarbon provides rigidity and resistance to chemical attack by the acid while the ionic groups introduce the selectivity in ion migration. The latest membranes used for vanadium based systems are based on sulfonated polyfluorenyl ether ketone (SPEEK) [46] and behave similarly to the Nafion[®] membranes [47] in terms of water uptake, swelling, ion exchange capacity and ion conductivity.

In practice, the electrochemical cell of the RFB unit is multiplied and forms a stack, consisting of a number of cells containing bipolar electrodes [4] as illustrated in Fig.2.2. Scale-up is achieved by increasing the size of the electrodes, adding more electrodes in each stack and also connecting the stacks in either parallel or series configuration. The power in this system is determined by the number of cells in the stack and the size of the electrodes (*viz.* $P = V \times I$), whereas the energy storage capacity is determined by the concentration and volume of the electrolyte (*i.e.* the number of moles of the electroactive species).

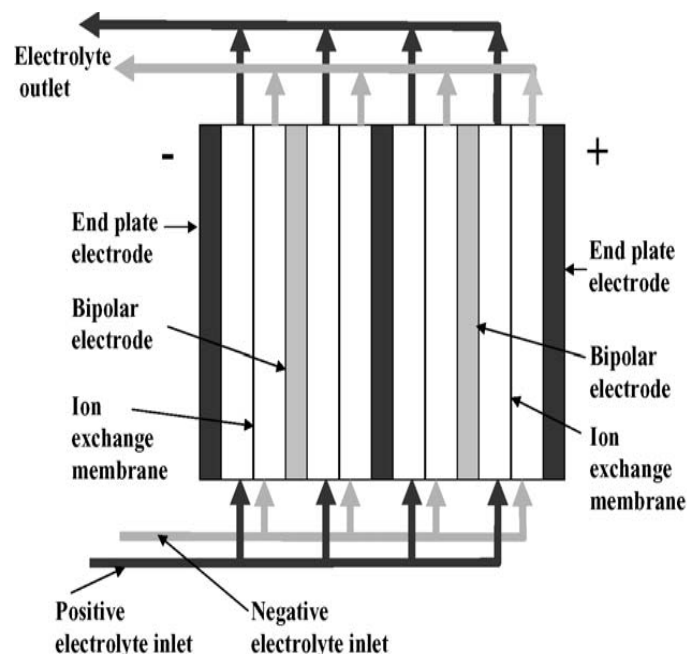


Fig.2.2: Stack consisted of four redox flow cells with electrodes [8].

Overall, the RFBs have the advantages of high power output, long energy storage time as well as cycle life, fast recharge by replacing the spent electrolyte, quick response times and no harmful emissions. On the other hand though, flow batteries are rather complicated systems that require the usage of pumps, sensors and flow and power management. The energy densities (Wh L^{-1}) in general are low when compared to other types of batteries such as portable batteries (Li-ion).

2.2.3 Electrochemical reactions of various RFB systems

Table 2.2 summarises the electrochemical reactions, the cell voltage and energy density of the current RFB systems. The negative electrode is the anode and the positive electrode is the cathode during the discharge of the battery. During charge the reactions are reversed.

Redox systems	Reactions (Charge - Discharge)	$E_{\text{cell}} / \text{V}$	Background Electrolyte -ve / +ve	Energy density (Wh L^{-1})*	Ref
All vanadium	-ve: $\text{V}^{3+} + \text{e}^{-} \leftrightarrow \text{V}^{2+}$ +ve: $\text{VO}^{2+} + \text{H}_2\text{O} \leftrightarrow \text{VO}_2^{+} + 2\text{H}^{+} + \text{e}^{-}$	1.40 V	1.5 mol dm^{-3} H_2SO_4	25-35	[17] [48]
V-Polyhalide	-ve: $\text{VCl}_3 + \text{e}^{-} \leftrightarrow \text{VCl}_2 + \text{Cl}^{-}$ +ve: $\text{Br}^{-} \leftrightarrow \text{Br}_2 + 2 \text{e}^{-}$	1.30 V	1.5 mol dm^{-3} HCl	50	[49]
V-Ce	-ve: $\text{V}^{3+} + \text{e}^{-} \leftrightarrow \text{V}^{2+}$ +ve: $2 \text{Ce}^{3+} \leftrightarrow 2\text{Ce}^{4+} + \text{e}^{-}$	1.87 V	1 mol dm^{-3} H_2SO_4	20-35	[50]
V-Br	-ve: $\text{ClBr}_2 + 2\text{e}^{-} \leftrightarrow 2\text{Br}^{-} + \text{Cl}^{-}$ +ve: $2\text{VBr}_2 + 2\text{Br}^{-} \leftrightarrow 2\text{VBr}_3 + 2\text{e}^{-}$	1.30 V	$1.5 - 2 \text{ mol dm}^{-3}$ HCl	20-35	[51] [52]
V-Mn	-ve: $\text{V}^{3+} + \text{e}^{-} \leftrightarrow \text{V}^{2+}$ +ve: $\text{Mn}^{2+} \leftrightarrow \text{Mn}^{3+} + \text{e}^{-}$	1.66 V	$1 - 5 \text{ mol dm}^{-3}$ H_2SO_4	20-35	[53]
Br- Polysulfide	-ve: $\text{S}_4^{2-} + 2\text{e}^{-} \leftrightarrow 2\text{S}_2^{2-}$ +ve: $2\text{Br}^{-} \leftrightarrow \text{Br}_2 + 2\text{e}^{-}$	1.50 V	5 mol dm^{-3} NaBr 1.2 mol dm^{-3} Na ₂ S	20-35	[54] [55]
Zn-Ce	-ve: $\text{Zn}^{2+} + 2\text{e}^{-} \leftrightarrow \text{Zn}_{(\text{s})}$ +ve: $2\text{Ce}^{3+} \leftrightarrow 2\text{Ce}^{4+} + \text{e}^{-}$	2.40 V	1 mol dm^{-3} $\text{CH}_3\text{SO}_3\text{H}$	25-40	[31] [56]
Fe-Cr	-ve: $\text{Fe}^{2+} \leftrightarrow \text{Fe}^{3+} + \text{e}^{-}$ +ve: $\text{Cr}^{3+} \leftrightarrow \text{Cr}^{2+} + \text{e}^{-}$	1.20 V	2 mol dm^{-3} HCl	20-35	[57] [58]
Fe-Ti	-ve: $\text{Fe}^{2+} \leftrightarrow \text{Fe}^{3+} + \text{e}^{-}$ +ve: $\text{Ti}^{4+} \leftrightarrow \text{Ti}^{3+} + \text{e}^{-}$	1.19 V	$3 - 3.5 \text{ mol dm}^{-3}$ HCl	14	[13] [59]
All Uranium	-ve: $\text{U}^{4+} \leftrightarrow \text{U}^{3+} + \text{e}^{-}$ +ve: $\text{UO}_2^{2+} \leftrightarrow \text{UO}_2^{+} + \text{e}^{-}$	0.70 V	acetylacetonone Aprotic solvents	**	[60]
All Neptunium	-ve: $\text{Np}^{4+} \leftrightarrow \text{Np}^{3+} + \text{e}^{-}$ +ve: $\text{NpO}_2^{2+} \leftrightarrow \text{NpO}_2^{+} + \text{e}^{-}$	0.70 V	1 mol dm^{-3} HNO ₃	**	[61] [62]
All Ruthenium	-ve: $[\text{Ru}(\text{acac})_3] \leftrightarrow [\text{Ru}(\text{acac})_3]^{+} + \text{e}^{-}$ +ve: $[\text{Ru}(\text{acac})_3]^{-} \leftrightarrow \text{Ru}(\text{acac})_3^{-} + \text{e}^{-}$ <i>acac</i> : acetylacetonate	1.75 V	Ru(acac) ₃ dissolved and TEABF ₄ in dry acetonitrile. TEABF ₄ : Tetraethyl ammonium tetrafluoroborate	**	[63]

Table 2.2: Electrochemical reactions of RFB.

*: For RFBs energy density is based on electrolyte volume only.

** : Not known.

The electrochemical reactions that occur in a flow cell have to be reversible. In order to obtain the high cell voltage, the redox potentials of the two electrochemical reactions have to be as far as possible. Fig.2.3 illustrates the half cell potential of various redox electrodes. For the zinc-cerium system the redox potentials are 2.2 V apart vs *S.H.E* (standard hydrogen electrode, 1 mol dm⁻³, 25°C and 1 × 10⁵ Pa).

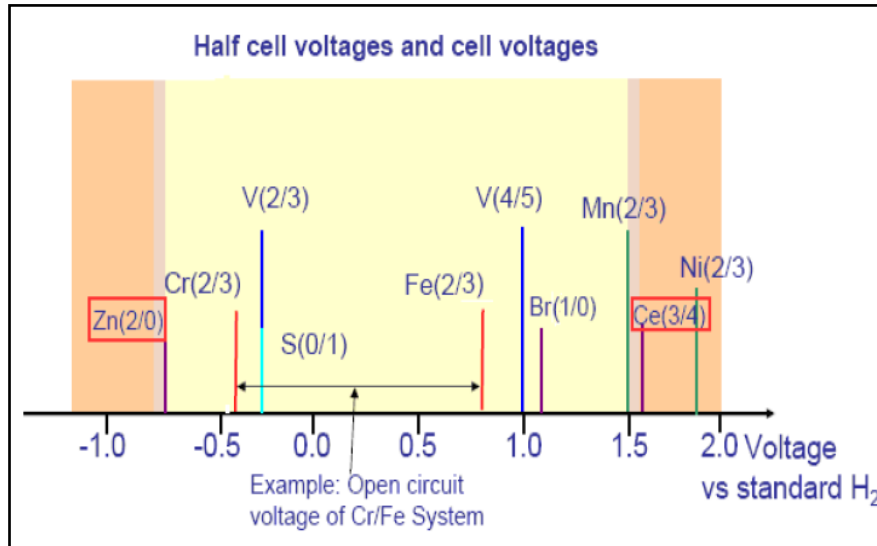


Fig.2.3: Half cell potentials for various redox couples [64].

2.2.4 Undivided RFB

This system differs from the conventional RFB systems due to the fact that it uses a single electrolyte and involves the formation of a solid product to at least one of the electrodes during charging (Fig.2.4). As mentioned previously, no membrane is required for these systems. Table 2.3 summarises the electrochemical reactions and the cell voltage of several such RFB systems.

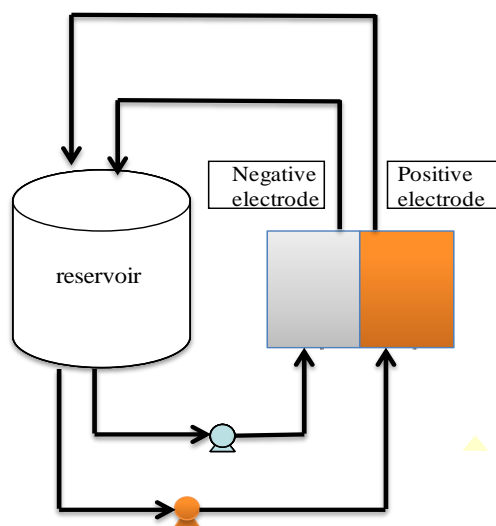


Fig.2.4: Schematic of an undivided RFB [65].

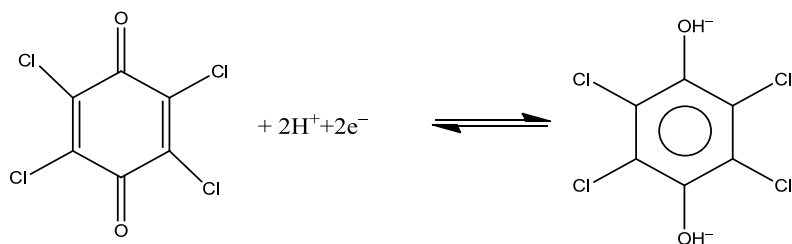
Undivided Redox systems	Reactions (Charge - Discharge)	$E_{\text{cell}} / \text{V}$	Background Electrolyte -ve /+ve	Energy density (Wh L^{-1})*	Ref
Pb - PbO_2	-ve: $\text{Pb}^{2+} + 2\text{e}^- \leftrightarrow \text{Pb}_{(\text{s})}$ +ve: $\text{Pb}^{2+} + 2\text{H}_2\text{O} \leftrightarrow \text{PbO}_{2(\text{s})} + 2\text{H}^+ + 4\text{e}^-$	1.62 V	1.5 mol dm^{-3} $\text{Pb}(\text{CH}_3\text{SO}_3)_2$	20-35	[66]
Cu - PbO_2	-ve: $\text{Cu}^{2+} + 2\text{e}^- \leftrightarrow \text{Cu}_{(\text{s})}$ +ve: $\text{Pb}^{2+} + 2\text{H}_2\text{O} \leftrightarrow \text{PbO}_{2(\text{s})} + 2\text{H}^+ + 4\text{e}^-$	1.30 V	0.5 mol dm^{-3} $\text{Cu}(\text{CH}_3\text{SO}_3)_2$ $\text{Pb}(\text{CH}_3\text{SO}_3)_2$	**	[67]
Zn-Ce	-ve : $\text{Zn}^{2+} + 2\text{e}^- \leftrightarrow \text{Zn}_{(\text{s})}$ +ve: $2\text{Ce}^{3+} \leftrightarrow 2\text{Ce}^{4+} + \text{e}^-$	2.40 V	0.5 mol dm^{-3} $\text{CH}_3\text{SO}_3\text{H}$	25-40	[68] [31]
Zn-Ni	-ve: $\text{Zn}(\text{OH})_4^{2-} + 2\text{e}^- \leftrightarrow \text{Zn} + 4\text{OH}^-$ +ve: $2 \text{Ni}(\text{OH})_2 + 2\text{OH}^- \leftrightarrow 2\text{NiOOH} + 2\text{H}_2\text{O} + 2\text{e}^-$	1.73 V	10 mol dm^{-3} KOH	**	[69]
Cd- Chloranil***	-ve: $\text{Cd}^{2+} + 2\text{e}^- \leftrightarrow \text{Cd}_{(\text{s})}$ +ve: $\text{QH}_2\text{Cl}_4 \leftrightarrow \text{QCl}_4 + 2\text{H}^+ + 2\text{e}^-$	1.12 V	Mixture of H_2SO_4 & $(\text{NH}_4)_2\text{SO}_4$ & CdSO_4	**	[33]

Table 2.3: Electrochemical reactions of undivided RFB.

*: For RFBs energy density is based on electrolyte volume only.

** : Not known.

*** Q: Chloranil is a quinone with a molecular formula $C_6Cl_4O_2$:



Both the undivided zinc-cerium and soluble lead flow batteries have been investigated by the University of Southampton [31] [70]. The average energy efficiency for the zinc cerium system was *ca.* 75% at 20 mA cm^{-2} while the discharge cell voltage was 2.1 V. The soluble lead-acid battery developed by Hazza *et al.* [71] contains sodium ligninsulfonate in the electrolyte in order to suppress the dendritic growth during lead electrodeposition under the application of 50 mA cm^{-2} . He reported that the nucleation overpotential for Pb deposition increased considerably by 100 mV. The use of hexadecyltrimethylammonium cation ($5 \times 10^{-3} \text{ mol dm}^{-3}$) has also been used in the soluble lead-acid battery [72] [73]. Rotating disk electrode investigations showed that this cation inhibits the Pb deposition as it adsorbs in the electrode surface shifting the Pb deposition potential by -110 mV . High voltage (80%) and coulombic efficiencies (90%) were reported under the application of constant current densities between 10 mA cm^{-2} and 160 mA cm^{-2} [74]. The copper-lead dioxide battery has a higher energy efficiency *viz.* $>83\%$ while its durability was reported to be up to 450 cycles [34]. Cheng *et al.* [75] [76] investigated the zinc-nickel single flow cell and reported high coulombic and energy efficiencies *viz.* 96% and 86% respectively over 1000 cycles. Finally, results obtained on a small scale cadmium-chloranil battery showed an energy efficiency of *ca.* 82% ($\eta_C = 99\%$) over 100 cycles at a current density of 10 mA cm^{-2} [33].

2.2.5 Summary of existing RFB

In the early days of the RFB, the systems of interest were mainly the Fe/Ti and the Fe/Cr couples. For the Fe/Ti couple, the passivation of TiO₂ was a major issue while for the Fe/Cr system the problems were located on the chromium side where apart from the competing hydrogen evolution reaction, the kinetics of the chromium reduction reaction were very slow [34] [30]. The energy efficiency of this system varied between 44% and 50% while the energy density of the system was *ca.* 12.25 Wh L⁻¹ [77].

In the all vanadium battery developed by Skyllas-Kazakos [37] the parallel hydrogen and oxygen evolution reactions are not that significant while the cross mixing of the electrolytes across the membrane does not lead to any contamination. The high energy efficiencies recorded for this system (>85%) are mainly the reason why has been studied extensively the last two decades [8] [78]. The charge and discharge current densities vary from 1 mA cm⁻² to 130 mA cm⁻² [8]. However, the relatively low specific energy (25 to 35 Wh kg⁻¹) of the system limits its applications [79]. Many research groups have investigated ways to increase the specific energy in particular, the voltage efficiency of the all vanadium flow cell by increasing the kinetics of the V(IV)/V(V) and V(III)/V(II) reactions [80], by introducing new electrode materials like carbon paper and carbon felt [81] and also by using sulfate-chloride mixed electrolytes [82]. Other vanadium based systems have been proposed such as the vanadium/polyhalide [24]. These have higher energy densities, double that of the all vanadium battery [83] *viz.* 50 Wh L⁻¹. Furthermore, it has been reported that the use of Mn(II)/Mn(III) [23] and Ce(IV)/Ce(III) [24] as positive electroactive species in the vanadium flow batteries does increase the standard rate constant (k^0) leading to lower overpotentials and higher voltage efficiencies *viz.* >80%. Furthermore, the use of mixed electrolytes would further increase the solubility of the active materials in the solution but at the same time add to the cost of the system since twice the amount of active material is required [8]. The cell potential for the vanadium-cerium flow battery is *ca.* 1.87 V while the coulombic efficiency recorded for this system is also high (87%) at a current density of 22 mA cm⁻² [50]. The optimum operating temperature for the vanadium-cerium electrolytes is reported to be 40°C by Pavlenova *et al.* [84] while Wang *et al.* [85] found that in the presence of chloride supporting electrolytes the all vanadium RFB remained stable at temperatures between 0°C and 50°C. Furthermore, Fang *et al.* [23] found that at relatively low sulfuric acid concentrations *viz.* 1 mol dm⁻³ and elevated temperatures (40°C) the kinetics of the cerium reaction are electrochemically favourable. According to Kreh *et al.* [86], cerium is highly

soluble in methanesulfonic acid, which led to further investigation of the cerium methanesulfonate electrolyte as the positive electroactive species for other RFBs [87].

As well as the vanadium RFB, the *Regenesys*[®] cell is another system with a nominal open circuit potential of 1.5 V and energy efficiencies in the range of 60% to 65% at charge/discharge current densities of 40 mA cm⁻² [88]. Due to its low cost and high energy density, large-scaled *Regenesys*[®] systems have already been reported [89] [90]. Regarding the actinide based RFBs, two systems have been proposed as a means of using excess depleted actinides for energy storage. A large amount of these elements are depleted from nuclear power industry and are stored without effective utilization [91]. The neptunium flow battery involves the Np(IV)/Np(III) and NpO₂²⁺/NpO₂⁺ couples in aqueous solution while the uranium flow battery uses the U(IV)/U(III) and UO₂²⁺/UO₂⁺ couples in organic solvents [92] [93]. The energy efficiency of the neptunium flow battery was found to be *ca.* 99% at a current density of 70 mA cm⁻² [94] while for the uranium flow battery was *ca.* 98% for the same current density. Still, the use of radioactive redox species is a major drawback on the further development of the actinide based RFB's.

2.3 Hybrid Flow batteries

This type of batteries differs from the common RFB in that at least one redox couple species is not fully soluble and can this be either a metal or a gas. The energy storage and power of the battery are not fully decoupled as the energy storage depends on the thickness, nature and morphology of the metallic layer formed. The majority of the hybrid flow batteries are zinc based due to the extensive use of zinc in the battery industry. The zinc-halogen batteries have advantages in energy density, cell potential and also have low cost. Hybrid flow batteries include the zinc-bromine [95], zinc-cerium [96], zinc-nickel [97], zinc-chlorine [98] and zinc-air [99] batteries.

As mentioned previously, the zinc-chlorine battery [98] was the first flow battery to be designed [2]. The zinc-bromine system is, however, the more well-known hybrid redox battery in terms of research and attention. It was firstly developed in the 1980's in Japan, and nowadays a few systems have been installed [100] [101]. The zinc-bromine RFB was developed during the same period as a competitor for the conventional lead-acid battery for vehicles [102] [103]. The zinc-cerium RFB has been under development since the early 1990's by the Electrochemical Design Associates Inc. [68]. Further investigation of this system was conducted by Plurion Systems Ltd. [64], the University of Southampton [104] and the University of Strathclyde [105]. Unlike the chemistry used in the zinc-chlorine and zinc-bromine flow batteries no condensation device is needed for this system to dissolve the halogen gases. The zinc-cerium system though is more expensive than those of zinc-halogen, due to the expense of the current platinised titanium positive electrode used and also its cerium electroactive species [106]. The zinc-air battery was firstly investigated during the 19th century (*Leclanche* batteries [107]). Later on G.W. Heise and E.A. Schumacher built the first commercial zinc-air battery [108]. These batteries are powered by oxidizing zinc with oxygen from air. Table 2.4 summarises the electrochemical reactions and the cell voltage of several hybrid flow systems.

Hybrid Systems	Reactions (Charge - Discharge)	$E_{\text{cell}} / \text{V}$	Background Electrolyte -ve /+ve	Energy density (Wh L ⁻¹)*	Ref
Zn-air	-ve: $\text{Zn}^{2+} + 2\text{e}^- \leftrightarrow \text{Zn}_{(\text{s})}$ During <i>Discharge</i> : $\text{O}_{2(\text{g})} + 2\text{H}_2\text{O} + 4\text{e}^- \leftrightarrow 4\text{OH}^-$ Chemical reactions (<i>Nickel electrode</i>): $\text{CH}_3\text{CH}_2\text{CH}_2\text{OH} + 4\text{NiOOH} + \text{H}_2\text{O} \rightarrow$ $\text{CH}_3\text{CH}_2\text{COOH} + 4\text{Ni}(\text{OH})_2$ $\text{CH}_3\text{CH}_2\text{COOH} + \text{KOH} \rightarrow \text{CH}_3\text{CH}_2\text{COOK} + \text{H}_2\text{O}$	1.70 V	6 mol dm ⁻³ KOH	1480-2000	[109] [110]
Zn-Ce	-ve: $\text{Zn}^{2+} + 2\text{e}^- \leftrightarrow \text{Zn}_{(\text{s})}$ +ve: $2\text{Ce}^{3+} \leftrightarrow 2\text{Ce}^{4+} + \text{e}^-$	2.34 V	CH ₃ SO ₃ H	25-40	[68] [87]
Zn-Br	-ve: $\text{Zn}^{2+} + 2\text{e}^- \leftrightarrow \text{Zn}_{(\text{s})}$ +ve: $2\text{Br}_3 \leftrightarrow 2\text{Br}_3^- + 2\text{e}^-$	1.60 V	ZnBr ₂ with excess of Br ₂	20-35	[111] [112]
Zn-Cl	-ve: $\text{Zn}^{2+} + 2\text{e}^- \leftrightarrow \text{Zn}_{(\text{s})}$ +ve: $2\text{Cl}^- \leftrightarrow \text{Cl}_{2(\text{g})} + 2\text{e}^-$	1.83 V	4 mol dm ⁻³ KCl	**	[111]
Zn-Ni	-ve: $\text{Zn}(\text{OH})_4^{2-} + 2\text{e}^- \leftrightarrow \text{Zn} + 4\text{OH}^-$ +ve: $2\text{Ni}(\text{OH})_2 + 2\text{OH}^- \leftrightarrow 2\text{NiOOH} + 2\text{H}_2\text{O} + 2\text{e}^-$	1.73 V	10 mol dm ⁻³ KOH	**	[68]

Table 2.4: Electrochemical reaction of hybrid flow systems.

*: For RFBs energy density is based on electrolyte volume only.

**: Not known.

Redflow Ltd. successfully installed a zinc-bromine battery up to 1 MW size with an energy efficiency of 74% over 1500 cycles [113] by improving the η_c (>90%) and η_v (>85%) while also decreasing the power loss in the pumps for the flowing electrolytes [114]. The specific energy density reported was *ca.* 65-75 Wh kg⁻¹ [96]. However, the slow kinetics of the bromine/bromide couple and the dendrite formation during zinc deposition are still major issues that have not been resolved, along with the toxicity of bromine. For the zinc-nickel battery, Cheng *et al.* [115] reported an energy efficiency of 88% at 10 mA cm⁻², which is as high as the all-vanadium battery energy efficiency. The nature of zinc deposition has been optimized for this system and the addition of 4×10^{-1} mol dm⁻³ ZnO to the electrolyte improves the stability of the nickel oxide electrode over 1000 cycles [116]. It is worthwhile noting that both zinc and nickel are commonly occurring elements in nature and can be fully recycled unlike other electrode materials such as cadmium and mercury.

The zinc-cerium battery uses methanesulfonic acid, the simplest of the alkylsulfonic acids, as a solvent. It is less corrosive than the sulfuric acid as well as more environmentally friendly [117]. In addition, methanesulfonic acid can dissolve and thus store a relatively high

cerium concentration (*viz.* $8 \times 10^{-1} \text{ mol dm}^{-3}$) [118]. The energy efficiency of the system has been reported to be 63% with coulombic efficiencies around 98% and voltage efficiencies of the order of 68% [119] at 50 mA cm^{-2} . For comparison, the reported η_e of the rechargeable zinc-air cells is around 60% at 20 mA cm^{-2} on a nickel electrode. In the latter case however, the charging voltage is considerably higher than the discharge leading to low voltage efficiencies [99]. The major drawback of the zinc-air system is design-related as zinc precipitation from the water-based electrolyte has to be closely monitored during the anodic dissolution of zinc. Zinc precipitation can cause pore blockage leading to poor coulombic efficiencies. Other issues regarding this system include dendrite formation, non-uniform zinc deposition and limited solubility of the electrolytes. Another zinc hybrid system, the zinc-chlorine battery, has a reported energy efficiency of 66% at an operating temperature of 25°C and current density of 25 mA cm^{-2} [98].

2.4 Zinc-Cerium RFB

The zinc/cerium cell is a new redox flow technology that has been developed in the last decade. Its great advantage is the very high power to weight ratio and its high open circuit cell voltage ($E_{cell}^{\circ} = -2.2 \text{ V vs S.H.E}$). The increase in the cell potential has a direct impact on the amount of power that can be delivered for a specified current density. The energy density of the system is reported to be between 20 Wh L^{-1} and 37.5 Wh L^{-1} [87] ($8 \times 10^{-1} \text{ mol dm}^{-3}$ Ce(III) carbonate assuming a potential of 2.0 V will give $96485 \times 2/3600 = 42.4 \text{ Wh L}^{-1} \times 0.8$ (*i.e* 80% discharge) = 34 Wh L^{-1}).

Methanesulfonic acid is used as the supporting electrolyte, as it allows both zinc and cerium electroactive species to dissolve at concentration larger than $8 \times 10^{-1} \text{ mol dm}^{-3}$. Methanesulfonic acid has been reported to minimize the decomposition of water into hydrogen and oxygen while also helping with the zinc deposition process [40]. The solubility of cerium (III) carbonate in methanesulfonic acid is about 10 times greater than in the sulfuric acid [120] [117]. Indeed, the solubility limits of both Ce(IV)/Ce(III) species can be as high as $8 \times 10^{-1} \text{ mol dm}^{-3}$ in methanesulfonic acid. Spotnitz *et al.* [121] reported that the solubility of Ce(IV) increases at high methanesulfonic acid concentrations while for the Ce(III) species the solubility decreases.

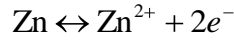
Furthermore, the use of this organic acid as the background electrolyte is sustainable as it is less harmful to the environment than other acids used in flow batteries such as sulfuric acid due to its low vapour pressure, absence of volatile organic compounds, low oxygen demand for degradation and low toxicological risk potential *viz.* $LD_{50} = 1000 \text{ mg kg}^{-1}$ [122] [123] [124]. It is odourless, chemically stable and free of nitrogen, phosphorous and halogens [117]. Methanesulfonic acid is favoured in this particular application, as zinc dendrites can be suppressed and so avoid short circuit during zinc electrodeposition [87]. It has also been found to be the electrolyte of choice for electrochemical processes involving tin, copper and lead [125]. This is because methanesulfonic acid is more controllable and gives high quality coatings of these metals.

The flow cell in its basic form consists of a single cell with a cation exchange membrane separating the anode and the cathode. The negative zinc electrolyte and the positive cerium electrolyte are stored externally in reservoirs and are circulated during the operation of the battery as illustrated in Fig.2.5. The overall reaction of the zinc-cerium redox flow cell during discharge is given below:

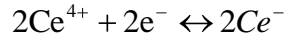


R.2.1

or in terms of the redox reactions:



R.2.2



R.2.3

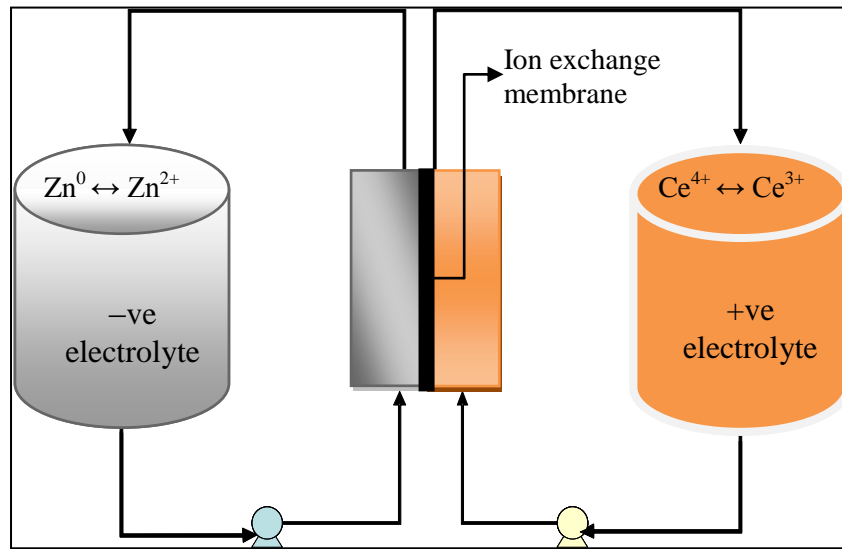


Fig.2.5: A single zinc-cerium cell with a cation exchange membrane.

In general, the actual cell voltage of a redox flow system can be expressed as:

$$E_{\text{cell}} = E_{\text{ocp}} - \sum |\eta| - \sum |IR| = E_{\text{eq,C}} - E_{\text{eq,A}} - |\eta_{\text{C}}| - |\eta_{\text{A}}| - IR_{\text{cell}} - IR_{\text{circuit}}$$

Eq.2.1

The cell potential, (E_{cell}) departs from its open circuit value due to kinetic, mass transport and ohmic effects. E_{ocp} is the open circuit potential calculated by using the Nernst equation [126]. The overpotential term (η) reflects the anode and cathode overpotentials at the electrodes calculated from the Butler-Volmer and Tafel equations [126], while the ohmic effect arises from resistances ($V = \sum IR$). The overpotentials arise from the kinetics of the electron transfer process. IR is the ohmic potential drop calculated from Ohm's law (*i.e* input of energy required to drive electrons through the cell). IR_{circuit} is caused by potential losses in electrodes, busbars and connectors while IR_{cell} is caused by potential losses in the electrolyte and the membrane separator. IR_{circuit} can be minimized through the use of good conductors with large cross-sectional areas while the IR_{cell} can be tackled by introducing highly conductive electrolytes, narrow inter-electrode spacing and well designed separators.

2.4.1 Zinc deposition reaction

In general, zinc-based systems suffer from a high rate of self-discharge because of the highly reducing zinc species. Main problems with all zinc systems include the high solubility of the zinc electrodeposit in the electrolyte, *i.e.* corrosion and also dendritic growth, leading to internal short circuits and premature failures as has been found in the zinc-halogen redox flow battery [127] [128]. As a result, extensive work has been carried out in order to optimize the design of electrolyte channels to minimize dendrite formation [8].

In the zinc-halogen batteries, zinc is deposited on an inert collector. Dendrite formation takes place on random cycling at shallow depths of discharge. Some of the factors that affect the zinc deposition here are the electrode substrate, the charging method, the cell geometry, the electrolyte hydrodynamics, the electrolyte composition and the zinc electrode morphology [129]. The investigation of aqueous zinc in sulfuric acid was carried out by Guillame *et al.* [130] who reported that HER (hydrogen evolution reaction) on stainless steel is inhibited by deposition of zinc while the deposit morphology was not influenced by the current density (*i.e.* 45 mA cm^{-2}). The same study also reported that increasing the concentration of the zinc species ($>2 \times 10^{-1} \text{ mol dm}^{-3}$) will yield higher deposition current efficiencies, *viz.* 80%.

The zinc-bromine battery problems involve the HER, which leads to lower coulombic efficiencies and also the non-uniform deposition of zinc on random cycling [131]. Van Parys *et al.* [129] investigated the zinc deposition mechanism with simultaneous hydrogen evolution in an acidic sulfate solution ($5 \times 10^{-2} \text{ mol dm}^{-3} \text{ ZnSO}_4$ and $1 \text{ mol dm}^{-3} \text{ Na}_2\text{SO}_4$). He found that if gas bubbles are formed in the mass transport controlled region the induced micro stirring effect increases the current density (due to the H^+ consumption the pH rises in the immediate vicinity of the electrode surface) while if the current is charge transport controlled, the current density decreased due to the increased resistance of the electrolyte. The zinc-nickel cell shows zinc dendrite penetration of the separator and redistribution of the zinc electrode active material on cycling as well as densification of the zinc electrode [131]. Ito *et al.* reported that high electrolyte flow rates *viz.* $>15 \text{ cm s}^{-1}$ improved the cycle life of the battery at 100% depth of discharge [132].

In the electrodeposition of metals, additives are widely used to control the form and nature of the electrodeposit (*viz.* deposit brightness, grain size, dendrites and nodules). Another objective of the additives is to reduce the HER during the charging of the battery *i.e.* zinc deposition. Glue and arabic gum are the most commonly used additives in the industry

for the zinc electrowinning process. Glue has been reported to decrease the grain size of the zinc deposit [133] while arabic gum changes the deposits orientation (*i.e* basal to intermediate plane) [134]. Nonetheless, research for better organic additives is ongoing. Diggle *et al.* [135] reported that TBABr (tetrabutyl ammonium bromide) can act as a suppressor of the dendritic growth whilst also increasing the compactness of zinc deposits in alkaline zincate electrolytes. Increasing additive concentration can also lead to the blockage of the active nucleation sites on the cathode surface by adsorption of the additive, thereby decreasing the overall energy efficiency. The use of gelatin (solid content: 80 mL g⁻¹) to chlorine based electrolytes (pH=4) decreased the adsorption of H⁺ ions on active zinc sites and thereby increasing the energy efficiency at 40°C [136].

Other organic additives reported to be superior to glue and arabic gum were nonylphenoxylethylene [137] and 2-butyne-1, 4-diol. The latter has been reported to improve the zinc current efficiency in the presence of Ni impurities in an acidic sulfate solution [138]. Furfuraldehydethiosemicarbazone (FrTSCN) and salcylaldehyde thiosemicarbazone (SaTSCN) have also been reported to achieve current efficiencies as high as 99% and 97% respectively, for the zinc deposition process in both alkaline and acidic solutions [139]. Ichino *et al.* [140] found that Pb(II) ions can be absorbed in the electrode surface and therefore strongly inhibit the HER reaction during the zinc deposition process in the presence of acidic sulfate electrolytes. Thiourea and urea are known to improve the crystallographic orientation (112 to 110) of the zinc deposition in a solution with pH=0.5 [141]. In addition, it has been reported that decreasing the pH from 5.4 to 1 of a zinc electrolyte containing chromium in $6 \times 10^{-1} \text{ mol dm}^{-3} \text{ ZnSO}_4 \cdot 7\text{H}_2\text{O}$ allows zinc deposition to occur before the HER process [142]. The minimization of the pH resulted in the minimisation of the formation of hydroxo-products of chromium in the electrolyte. According to Clarke *et al.* [68], compounds like indium can effectively increase the hydrogen overpotential [143]. The same effect has been reported also for the polyethylene glycols (PEGs) [144].

2.4.2 Ce(IV)/Ce(III) reaction

The Ce(IV)/Ce(III) couple has been primarily studied in sulfuric acid medium. According to Pavlenova *et al.* [84] the most favourable concentration of sulfuric acid medium is between 1 mol dm^{-3} and 2 mol dm^{-3} while the optimum temperature is 40°C . Another study conducted in sulfuric acid medium [50] reported that the existence of platinum dioxide on platinised titanium surfaces inhibits the oxidation of Ce(III) especially at high sweep rates. The reversibility of Ce(IV)/Ce(III) couple improves with the increase of sulfuric acid concentration. This was also confirmed by the study of Fang *et al.* [23] where constant current electrolysis showed that an increase in the concentration of the sulfuric acid, from $1 \times 10^{-1} \text{ mol dm}^{-3}$ to 2 mol dm^{-3} resulted in the reduction of the redox peak current due to the decrease in the diffusion coefficient for the cerium species ($10^{-2} \text{ mol dm}^{-3}$) in 1 mol dm^{-3} sulfuric acid on a glassy carbon electrode. Increased temperatures (40°C) accelerated the oxidation of Ce(III) as well as the reduction process of Ce(IV).

Recently, it was found that the Ce(IV)/Ce(III) couple is highly soluble in methanesulfonate acid ($>2 \text{ mol dm}^{-3}$), which makes this acid very attractive for its use in RFB application [87]. Raju *et al.* [145] reported a 97% current efficiency at a charge current density of 5 mA cm^{-2} in a solution containing $8 \times 10^{-1} \text{ mol dm}^{-3}$ Ce(III) methanesulfonate in 2 mol dm^{-3} acid medium at 50°C . Leung *et al.* [118] reported that the kinetics for the oxidation of Ce(III) and the reduction of Ce(IV) in methanesulfonic acid are slow (quasi-reversible) on a Pt disc electrode. He also found that the oxygen evolution reaction (OER) is less pronounced at higher temperatures. The OER in acidic medium has been extensively studied in a variety of substrates including IrO_2 [146] [147], RuO_2 [148], PbO_2 [149], and Ta_2O_5 [150]. The Ce(IV)/Ce(III) electroactive species were found to have higher reaction rate constants in the presence of ethylenediaminetetra-acetate (EDTA) ligands [151] in a solution containing $1 \times 10^{-1} \text{ mol dm}^{-3}$ $\text{Ce}(\text{SO}_4)_2$ in 1 mol dm^{-3} H_2SO_4 . The rate constant was *ca.* $3.1 \times 10^{-4} \text{ cm s}^{-1}$ while the diffusion coefficient was $2.4 \times 10^{-6} \text{ cm}^2 \text{ s}^{-1}$. The EDTA as well as the DTPA ligands could potentially enhance the prospect of new redox couple combinations for flow batteries, such as the all chromium, the vanadium-cerium and the iron-bromine systems.

Regarding the electrode materials for this reaction, Klekens *et al.* [152] reported that cerium reduction is independent of electrode material. For the cerium oxidation though, carbon based composites as well as glassy carbon have higher reversibility than platinum. Zhipeng *et al.* [153] reported that the kinetics of the cerium salts are faster in mixed acid media ($5 \times 10^{-1} \text{ mol dm}^{-3}$ H_2SO_4 and 2 mol dm^{-3} $\text{CH}_3\text{SO}_3\text{H}$) than in single acid at a graphite

electrode. Yet, at temperatures higher than 40°C and sulfuric acid concentrations greater than 2 mol dm⁻³, the carbon electrode will eventually degrade [84]. Maeda *et al.* [154] found that boron doped diamond electrodes in sulfuric acid solutions containing 3 × 10⁻³ mol dm⁻³ Ce₂(SO₄)₃ show a good performance for the cerium oxidation reaction due to the fact that they have a very high overpotential for OER as the adsorption of intermediate species is very difficult on this surface.

Bishop *et al.* [155] found that the Ce(IV)/Ce(III) reaction rate sequence for different electrodes in perchloric acid (from 1 mol dm⁻³ to 3 mol dm⁻³) was carbon>platinum>gold while in sulfuric acid (from 5 × 10⁻¹ mol dm⁻³ to 1.5 mol dm⁻³) it was carbon>gold>platinum. It was claimed that in the presence of sulfuric acid, gold increases its reaction rate due to its higher roughness factor, (*viz.* the state of the surface) [156]. However, gold is corroded by cerium (IV) solutions. Dimensionally stable anodes (DSA) have been reported for use in acidic solutions [157] [158]. In the chlor-alkali industry, DSA have replaced the graphite electrodes due to their longer service life and lower anodic overpotential [159] for Cl₂ evolution and high OER overpotential.

The introduction of mixed acid media (5 × 10⁻¹ mol dm⁻³ H₂SO₄ and 2 mol dm⁻³ CH₃SO₃H) for the Ce(III)/Ce(IV) redox couple has been proposed by Zhipeng *et al.* [153] as the Ce(III)/Ce(IV) reaction appears to follow reversible kinetics in this medium. In addition, the solubility of the cerium salts increased in the presence of the mixed-acid media. The saturation ionic point (*i.e.* the point of maximum concentration), K_{sp} defined as $K_{sp} = [\text{Ce}^{3+}]^2([\text{SO}_4^{2-}] + \text{HSO}_4^-)^3$ increased from 0.86 to 5.97. Furthermore, the reported energy efficiency was *ca.*74%, comparable to that of the all vanadium RFB. The acid strength has to be high enough in order to maintain the solubility of cerium(IV) species but at the same time not too high as the solubility of cerium(III) will decrease (1 mol dm⁻³ total cerium in 2 mol dm⁻³ methanesulfonic acid and 5 × 10⁻¹ mol dm⁻³ H₂SO₄).

From the literature, the preferable total cerium concentration is at 7 × 10⁻¹ mol dm⁻³, while the methanesulfonic acid concentration should be between 2.5 mol dm⁻³ and 3.5 mol dm⁻³ [87] [145] [160].

2.5 Conclusions

The rapidly growing demand of energy generated by renewable energy sources has given rise to massive market opportunities for RFBs. These systems possess features such as flexible design, long life, simplicity, safety and high reliability with acceptable operation and maintenance costs which is really important in the competitive electricity market. The production of energy on site could reduce burdens on electricity distribution systems and promote the widespread use of renewable and cleaner energy.

Since the 1970's several RFB systems have been investigated and developed. Recent advances include the all-neptunium battery, the high cell potential zinc-cerium hybrid battery while also various low cost, high-performance undivided cell systems such as the soluble lead flow battery. Along with the development of these energy storage systems, tremendous improvements on membranes, electrode materials and electrolyte compositions have been made. Further developments on the redox flow systems involve low cost, efficient and durable electrodes as well as highly selective and durable membranes. Improvements on the electrode structure and cell design can be made in order to minimise transport losses and deposit morphologies. The design should also aim to minimize pumping and shunt current losses.

The zinc cerium hybrid battery is a relatively new redox flow system with high power to weight ratio. In addition, due to the high standard electrode potential of both cerium and zinc redox reaction is aqueous media the open circuit potential is as high as 2.4 V. For the negative side of the flow battery, the corrosion of zinc is a major issue as in all zinc based batteries while the acidic environment promotes the hydrogen evolution reaction during the zinc deposition. The introduction of the appropriate surfactants or additives could decrease the corrosion rate and inhibit the HER. Regarding the positive side of the zinc-cerium flow battery, mixed acid media improved the reversibility of the Ce(IV)/Ce(III) couple as did elevated temperatures (40°C). Carbon based electrodes have shown a more reversible behaviour for Ce(IV)/Ce(III) reaction than the platinum electrode, however they degraded in the presence of the acid.

-
- [1] J.T. Kummer, D.G. Oei, *J. Appl. Electrochem.*, **12**, 87-100, (1982).
- [2] M. Bartolozzi, *J. Power Sources.*, **27**, 219-234, (1989).
- [3] R.K. Anand, D.R. Laws, K.F. Chow, B.Y. Chang, J.A. Crooks, R.M. Crooks, *Anal. Chem.*, **82**, 21, 8766-8774, (2010).
- [4] D. Pletcher, *A First Course in Electrode Process.* RSC publishing, 2nd Edition, pp 239-240, (2009).
- [5] L.H. Cutler, US Patent 3607420 (1969),
- [6] B. Sorensen. *Hydrogen and fuel cells, Emerging technologies and applications*, Elsevier Academic Press, pp.77, 113-151, (2005).
- [7] A. Hauch, S.H. Jensen, S.Ramousse, M. Mogensen, *J. Electrochem. Soc.*, **153**, (9), 741-747, (2006).
- [8] C. Ponce de Leon, A. Frias-Ferrer, J. Gonzalez-Garcia, D.A. Szanto, F.C. Walsh, *J. Power Sources.*, **160**, 716-732, (2006).
- [9] *U.S. Dept. of Energy, National Aeronautics and Space Administration.*, NASA TM-79067, 1-53, (1979).
- [10] P.C. Butler, D.W. Miller, A.E. Verardo, *17th Intersoc. Energy Conversion Eng. Conf., Los Angeles*, (1982).
- [11] <http://www.nedo.go.jp/english/index.html> last accessed: Dec. 2010
- [12] C. Liu, R. Galasco, R. Savinell, *J. Electrochem. Soc.*, **128**, 1755, (1981).
- [13] R. Savinell, C. Liu, R. Galasco, S. Chiang, J. Coetzee, *J. Electrochem. Soc.*, **126**, 357, (1979).
- [14] Y. Matsuda, K. Tanaka, M. Okada, Y. Takasu, M. Morita, M. Matsumura-Inoue, *J. Appl. Electrochem.*, **18**, 909, (1988).
- [15] L.H. Thaller, US Patent 3996064, **1976**.
- [16] M. Lopez-Atalaya, G. Codina, J.R. Perez, J.L. Vazquez, A. Aldaz, *J. Power Sources.*, **39**, 147, (1991).
- [17] M. Skyllas-Kazacos, M. Rychcik, P.G. Robins, A.G. Fane, M.A. Green, *J. Electrochem. Soc.*, **133**, 1057, (1986).
- [18] M. Skyllas-Kazacos, F. Grossmith, *J. Electrochem. Soc.*, **134**, (12), 2950-2953, (1987).
- [19] <http://www.aph.gov.au/House/committee/Isr/renewables/submissions/sub21.pdf>. assessed Nov. (2011).
- [20] W. Steeley, Electric Power Research Institute (EPRI) Report 1008434, Technical Update, Utah (2005).

-
- [21] P. Zhao, H. Zhang, H. Zhou, J. Chen, S. Gao, B. Yi, *J. Power Sources.*, **162**, 1416, (2006).
- [22] H. Zhang, Proceedings of 5th International Renewable Energy Storage Conference, Berlin, November, (2010).
- [23] B. Fang, S. Iwasa, Y. Wei, T. Arai, M. Kumagai, *Electrochim. Acta.*, **47**, (24), 3971-3976, (2002).
- [24] F.Q. Xue, Y.L. Wang, W.H. Wang, X.D. Wang, *Electrochim. Acta.*, **53**, 6636-6642, (2008).
- [25] M. Skyllas-Kazacos, *J. Power Sources.*, **124**, 299, (2003).
- [26] F. Xue, Y. Wang, W. Wang, X. Wang, *Electrochim. Acta.*, **53**, 6636 (2008).
- [27] Q. Liu, A. Sleightholme, A. Shinkle, Y. Li, L. Thompson, *Electrochem. Commun.*, **11**, 2312, (2009).
- [28] Y. Wen, J. Cheng, Y. Xun, P. Ma, Y.S. Yang, *Electrochim. Acta.*, **53**, 6018, (2008).
- [29] A. Hazza, D. Pletcher, R. Wills, *J. Power Sources.*, **149**, 103, (2005).
- [30] D. Pletcher, R. Wills. *J. Power Sources.*, **149**, 96-102, (2005).
- [31] P.K. Leung, C. Ponce de León, F.C. Walsh, *Electrochem. Commun.*, **13**, (8), 770-773, (2011).
- [32] Y. Xu, Y.H. Wen, J. Cheng, G.P. Cao, Y.S. Yang, *Electrochem. Commun.*, **11**, (9), 2639-2642, (2007).
- [33] Y. Xu, Y.H. Wen, J. Cheng, G.P. Cao, Y.S. Yang, *Electrochem. Commun.* **11**, 1422-1424, (2009).
- [34] J.Q. Pan, Y.Z. Sun, J. Cheng, Y. H. Wen, Y S. Yang, P.Y. Wan, *Electrochem. Comm.*, **10**, (9), 1226-1229, (2008).
- [35] Y. Shiokawa, H. Yamana, H. Moriyama, *J. Nucl. Sci. Tech.*, **37**, 253-256, (2000).
- [36] D. Scamman, G. Reade, E. Roberts, *J. Power Sources.*, **189**, 1220, (2009).
- [37] S. Licht, J. Davis, *J. Phys. Chem.*, **101**, 2540, (1997).
- [38] M.H. Chakrabarti, R.A.W. Dryfe, E.P.L. Roberts, *Electrochim. Acta.*, **52**, 2189-2195, (2007).
- [39] M. Skyllas-Kazacos, M.H. Chakrabarti, S.A. Hajimolana, F.S. Mjalli, M. Saleem, *J. Electrochem. Soc.*, **158**, (8), 55-79, (2011).
- [40] A.Z. Weber, T. Gostick, Q. Liu, *J. Appl. Electrochem.*, **41**, 1165-1166, (2011).
- [41] D. Pletcher, F.C. Walsh, R.G.A. Wills, *Encyclopedia of Electrochemical Power Sources*, 745-749, (2009).

-
- [42] X. Li, H. Zhang, Z. Mai, H. Zhanga, I. Vankelecom, *Energy Environ. Sci.*, **4**, 1147, (2011).
- [43] T. Sata, *Pure and App. Chem.*, **58**, 12, 1613-1626, (1986).
- [44] J. Xi, Z. Wu, X. Qiu, L. Chen, *J. Power Sources.*, **166**, 531, (2007).
- [45] http://www2.dupont.com/FuelCells/en_US/products/nafiction.html assessed Sept. (2011).
- [46] D. Chen, S. Wang, M. Xiao, Y. Meng, *J. Power Sources.*, **195**, 2089, (2010).
- [47] X. Teng, Y. Zhao, J. Xi, Z. Wu, X. Qiu, Chen L, *J. Power Sources.*, **189**, 1240, (2009).
- [48] E. Sum, M. Skyllas-Kazacos, *J. Power Sources.*, **15**, 179, (1985).
- [49] M. Skyllas-Kazacos, F. Grossmith, *J. Electrochem. Soc.*, **134**, (12), 2950-2953, (1987).
- [50] Y. Liu, X. Xia, H. Liu., *J. Power Sources.*, **130**, 299-305, (2004).
- [51] M. Skyllas-Kazacos, *J. Power Sources.*, **124**, (1), 299-302, (2003).
- [52] M. Skyllas-Kazacos, Y. Limantari, *J. Appl. Electrochem.*, **34**, 681, (2004).
- [53] F. Xue, Y. Wang, W. Wang, X. Wang, *Electrochim. Acta.*, **53**, 6636, (2008).
- [54] P. Morrissey, *Int. J. Ambient Energy.*, **21**, (4), 213, (2000).
- [55] F.C. Walsh, *Pure Appl. Chem.*, **73**, (12), 1819, (2001).
- [56] R.L. Clarke, B.J. Dougherty, S. Harrison, J.P. Millington, S. Mohanta, US 2006/0063065 A1, Battery with bifunctional electrolyte (2005).
- [57] P. Garces, M.A. Climent, A. Aldaz, *An. Quim.*, **83**, 9, (1987).
- [58] R.F. Gahn, N.H. Hagedorn, J.A. Johnson, "Cycling performance of the iron chromium redox energy storage system", NASA TM-87034, NASA, Dept. of Energy, US, (1985).
- [59] Y. Wang, Y. Lin, C. Wan, *J. Power Sources.*, **13**, 65, (1984).
- [60] Y. Shiokawa, T. Yamamura, K. Shirasaki, *J. Phys. Soc. Jpn.*, **75**, 137-142, (2006).
- [61] T. Yamamura, N. Watanabe, T. Yano, Y. Shiokawa, *J. Electrochem. Soc.*, **152**, 830, (2005).
- [62] T. Yamamura, N. Watanabe, Y. Shiokawa, *J. Alloys Compd.*, **139**, 408-412, 1260-1266, (2006).
- [63] M.H. Chakrabarti, E.P.L. Roberts, C. Bae, M. Saleem, *Energy Conversion and Management.*, **52**, 7, 2501-2508, (2011).
- [64] <http://www.plurionsystems.com/> assessed Nov. (2010).
- [65] C.H. Bae, E.P.L. Roberts, M.H. Chakrabarti, M. Saleem, *Int. J. Green Energy.*, **8**, 248, (2011).
- [66] A. Hazza, D. Pletcher, R. Wills, *J. Power Sources.*, **149**, 103, (2005).

-
- [67] D. Pletcher, H. Zhou, G. Kear, C.T.J. Low, F.C. Walsh, R.G.A Wills, *J. Power Sources.*, **180**, 621, (2008).
- [68] R.L. Clarke, B.J. Dougherty, S. Harrison, J.P. Millington, S. Mohanta, US 2004/0202925 A1, Cerium Batteries, (2004)
- [69] F. Xue, Y. Wang, W. Wang, X. Wang, *Electrochim. Acta.*, **53**, 6636, (2008).
- [70] J. Collins, X. Li, D. Pletcher, R. Tangirala, D. Stratton-Campbell, F. Walsh, C. Zhang, *J. Power Sources.*, **195**, 2975, (2010).
- [71] A. Hazza, D. Pletcher, R. Wills, *J. Phys. Chem.*, **6**, 1773-1778, (2004).
- [72] D. Pletcher, H. Zhou, G. Kear, C. Low, F. Walsh, R. Wills, *J. Power Sources.*, **180**, 630, (2008).
- [73] D.R.P. Egan, C.T.J. Low, F.C. Walsh, *J. Power Sources.*, **196**, 5725-5730, (2011).
- [74] R.G.A. Wills, J. Collins, D. Stratton-Campbell, C.T.J. Low, D. Pletcher, F.C. Walsh, *J Appl Electrochem.*, **40**, 955-965, (2010).
- [75] L. Zhang, J. Cheng, Y.S. Yang, Y.H. Wen, X.D. Wang, G.P. Cao, *J. Power Sources.*, **179**, (1), 381-387, (2008).
- [76] Y.Ito, M. Nyce, R. Plivelich, M. Klein, D. Steingart, S. Banerjee, *J. Power Sources.*, **196**, (4), 2340-2345, (2011).
- [77] C. Liu, R. Galasco, R. Savinell, *J. Electrochem. Soc.*, **129**, 2502, (1982).
- [78] T. Wu, K.H.S. Liu, S. Zhuang, D.Fang, S.Li, D. Lu, A. Su, *J. Solid State Electrochem.*, **16**, 579-585, (2012).
- [79] M. Skyllas-Kazacos, C. Peng, M. Cheng, *Electrochem. Solid State Lett.*, **2**, 121, (1999).
- [80] X. W. Wu, T. Yamamura, S. Ohta, Q.X. Zhang, F.Cong, C.M. Liu, K. Shirasaki, I. Satoh, T. Shikama, D. Lu, S.Q. Liu, *J. Appl. Electrochem.*, **41**, 1183-1190, (2011).
- [81] D.S. Aarona, Q. Liub, Z. Tanga, G.M. Grimb, A.B. Papandrewa, A. Turhanb, T.A. Zawodzinskia, M.M. Menchb, *J. Power Sources.*, **206**, 450-453, (2012).
- [82] L. Li, S. Kim, W. Wang, M. Vijayakumar, Z. Nie, B. Chen, J. Zhang, G. Xia, J. Hu, G. Graff, J. Liu, Z. Yang, *Adv. Energy Mater.*, **1**, 394-400, (2011).
- [83] H. Vafiadis, M. Skyllas-Kazacos, *J. Membr. Sci.*, **279**, 394, (2006).
- [84] A. Pavlenova, S. Creager, J. Navratil, Y. Wei, *J. Power Sources.*, **109**, 431, (2002).
- [85] S. Kim, M. Vijayakumar, W. Wang, J. Zhang, B. Chen, Z. Nie, F. Chen, J. Hu, L. Li, Z. Yang, *Phys. Chem. Chem. Phys.*, **13**, 18186-18193, (2011).
- [86] R.P. Kreh, R.M. Spotnitz, J.T. Lundquist, *J. Org. Chem.*, **54**, (7), 1526-1531 (1989).

-
- [87] R. Clarke, B. Dougherty, S. Mohanta, S. Harrison, Abstract 520, Joint International Meeting: 206th Meeting of the Electrochemical Society/2004 Fall Meeting of the Electrochemical Society of Japan, Honolulu, Hawaii, October 3-8, (2004).
- [88] D. Scamman, G. Reade, E. Roberts, *J. Power Sources.*, **189**, 1231, (2009).
- [89] F.C. Walsh, *Pure Appl. Chem.*, **73**, (12), 1819-1837, (2001).
- [90] News Release: US Department of Energy Smart Grid Program Award for Demonstration of V-Fuel Vanadium Battery Technology in the USA, 8th July 2010, <http://www.energy.gov/news2009/8305.htm>, last accessed: Dec. 2010.
- [91] K. Hasegawa, A. Kimura, T. Yamamura, Y. Shiokawa, *J. Phys. Chem. Solids*, **66**, 593, (2005).
- [92] K. Shirasaki, T. Yamamura, Y. Shiokawa, *J. Alloys Compd.*, **408**, 1296, (2006).
- [93] T. Yamamura, K. Shirasaki, D. Li, Y. Shiokawa, *J. Alloys Compd.*, **418**, 139, (2006).
- [94] T. Yamamura, N. Watanabe, Y. Shiokawa, *J. Alloys Compd.*, **408**, 1260, (2006).
- [95] H. Lim, A. Lackner, J. Knechtli, *J. Electrochem. Soc.*, **124**, 1154, (1977).
- [96] D. Linden, *Handbook of Batteries and Fuel Cells*, McGraw-Hill, New York, 2nd Edition, pp. 37, (1995).
- [97] L. Zhang, J. Cheng, Y. Yang, Y. Wen, X. Wang, G. Cao, *J. Power Sources.*, **179**, 381, (2008).
- [98] J. Jorné, J.T. Kim, D. Kralik, *J. Appl. Electrochem.*, **9**, 573-579, (1979).
- [99] Y. Wen, J. Cheng, S. Ning, Y. Yang, *J. Power Sources.*, **188**, 301, (2009).
- [100] <http://www.premiumpower.com>, last accessed: Jan. 2011.
- [101] [http://www.redflow.com.au/Files/PowerBOSZB600%20-Limited Warranty.pdf](http://www.redflow.com.au/Files/PowerBOSZB600%20-Limited+Warranty.pdf), last accessed: Jan. 2011.
- [102] T.R. Crompton, *Battery Reference Book*, Elsevier Science & Technology Books, Boston, 3rd edition, Chapter 14, (2000).
- [103] Factory Mutual Research Corporation, Norwood, MA 02062 (U.S.A.) *J. Power Sources.*, **5**, (4), (398-399), (1980).
- [104] P.K. Leung, C. Ponce-de-Leon, C. Lo, A.A. Shah, F.C. Walsh, *J. Power Sources.*, **11**, 5174-5185, (2011).
- [105] G. Nikiforidis, L. Berlouis, D. Hall, D. Hodgson, *J. Power Sources.*, **206**, 497- 503, (2012).
- [106] R.L. Clarke, B.J. Dougherty, S. Harrison, P.J. Millington, S. Mohanta, US 2004/0202925 A1, Cerium Batteries (2004).

-
- [107] Mertens, Joost, *The Theoretical Batteries of Georges Leclanche*, *Archives Internationales d'Histoire des Sciences.*, **49**, 142, 75-102, (1999).
- [108] G.W. Heise, E.A. Schumacher, *Transactions of the Electrochemical Society.*, **62**, 363, (1932).
- [109] Y. Wen, J. Cheng, S. Ning, Y. Yang, *J. Power Sources.*, **188**, 301, (2009).
- [110] J.S. Lee, S.T. Kim, R. Cao, N.S. Choi, M. Liu, K.T. Lee, J. Cho, *Adv. Energy Mater.*, **1**, 34-50, (2011).
- [111] H.S. Lim, A.M. Lackner, R.C. Knechtli, *J. Electrochem. Soc.*, **124**, 8, 1154-1157, (1977).
- [112] E. Manla, A. Nasiri, C.H. Rentel, M. Hughes, *Transactions on Industrial Electronics.*, **57**, 2, (2010).
- [113] R. Ltd. (2011) URL: <http://www.redflow.com.au/>. Accessed May (2011).
- [114] P. Singh, B. Jonshagen. *J. Power Sources.*, **35**, (4), 405-410, (1991).
- [115] L. Zhang, J. Cheng, Y. Yang, Y. Wen, X. Wang, G. Cao, *J. Power Sources.*, **179**, 381, (2008).
- [116] J. Cheng, Y. Wen, G. Cao, Y. Yang, *J. Power Sources.*, **196**, 1589, (2011).
- [117] Lutropur, Lutropur® MSA brochure, "Lutropur MSA 100 Methanesulfonic Acid: New applications involving methanesulfonic acid". http://www.performancechemicals.basf.com/ev-wcms-in/internet/en_GB/function/conversions:/publish/upload/EV/EV5/products/metal_surface_treatment_products/lutropur_msa/Lutropur_New_Applications_EVD0101_e.pdf (2009) last accessed: Nov. 2010.
- [118] P.K. Leung, C. Ponce de León, C.T.J. Low, F.C. Walsh, *Electrochim. Acta.*, **56** 6536-6546, (2011).
- [119] P.K. Leung, C. Ponce de Leon, C. Lo, A.A. Shah, F.C. Walsh, *J. Power Sources.*, **11**, 5174 -5185, (2011).
- [120] T. Raju, C. A. Basha, *Portugaliae Electroch. Acta*, **23**, 367-378, (2005).
- [121] M. Spotnitz, R.P. Kreh, J.T. Lundquist, P.J. Press, *J. Appl. Electrochemistry.*, **20**, 209-215, (1990).
- [122] <http://www.arkema-inc.com/index.cfm?pag=127> Accessed May (2011).
- [123] D.B. Roitman, J.J. McAlister, F.L. Oaks, *J. Chem. Eng. Data*, **39**, 56-60, (1994).
- [124] M.D. Gernon, M. Wu, T. Buszta, P. Janney, *Green Chem.*, **1**, 127-140, (1999).
- [125] C.T.J. Low, F.C. Walsh, *Surface & Coatings Technology.*, **202**, 1339-1349, (2008).

-
- [126] Southampton Electrochemistry Group, *Instrumental Methods in Electrochemistry*. Ellis Horwood Series in Physical Chemistry, 2nd Edition, (1990), pp 23, 33, 121-126.
- [127] G. Brodt, J. Haas, W. Hesse, H.U. Jaqer, *Method for electrolytic galvanizing using electrolytes containing alkane sulfonic acid*, US Patent 2003/0141195 A1 (31/07/2003).
- [128] A.J. Bard, L.R. Faulkner, *Electrochemical Methods: Fundamentals and Applications*. New York: John Wiley & Sons, pp. 291-298, 539-540, (1980).
- [129] H. Van Parys, G. Telias, V. Nedashkivskiy, B. Mollay, I. Vandendael, S. Van Damme, J. Deconinck, A. Hubin, *Electrochim. Acta.*, **55**, 20, 5709-5718, (2010).
- [130] P. Guillaume, N. Leclerc, C. Boulanger, J. Lecuire, F. Lapique, *J. Appl. Electrochem.*, **37**, (11), 1237-1243, (2007).
- [131] J. McBreen, *J. Electroanal. Chem.*, **168**, (1-2), 415-432, (1984).
- [132] Y. Ito, M. Nyce, R. Plivelich, M. Klein, D. Steingart, S. Banerjee, *J. Power Sources.*, **196**, 2340, (2011).
- [133] D.J. MacKinnon, R.M. Morrison, J.E. Moulard P.E. Warren, *J. Appl. Electrochem.*, **20**, 728, (1990).
- [134] C. Tripathy, I.N. Bhattacharya, P. Gopalakrishna, S.C. Das, *Trans. Indian. Inst. Met.*, **51**, 303, (1998).
- [135] B.C. Tripathy, S.C. Das, P. Singh, G.T. Hefter, *J. Applied Electrochemistry.*, **29**, 1229-1235, (1999).
- [136] D.S Baik. D.J Fray. *J. Applied Electrochemistry.*, **31**, (10), 1141-1147, (2001).
- [137] A.Y. Hosny. *Hydrometallurgy.*, **32**, 361, (1993).
- [138] D.L. Piron, D. Mathieu, M.D. Amboise. *Can. J. Chem. Eng.*, **65**, 685, (1981).
- [139] B. Kavitha, P. Santhosh, M. Renukadevi, A. Kalpana, P. Shakkthivel, T. Vasudevan, *Surface & Coatings Technology.*, **201**, 3438-3442, (2006).
- [140] R. Ichino, C. Cachet, R. Wiart, *Electrochim. Acta.*, **41**, (7/8), 1031-1039, (1996).
- [141] M. Mouanga, L. Ricq, J. Douglade P. Berg, *J. Appl. Electrochemistry.*, **37**, 283-289, (2007).
- [142] T. Boladjieva, M. Monev, A. Tomandi, H. Kronberger, G. Faflek. *J. Solid State Electrochem.*, **13**, 671-677, (2009).
- [143] C. Cachet, R. Wiart, *Electrochim. Acta.*, **44**, 4743-4751, (1999).
- [144] J.W. Kim, H.T. Kim, S.M. Park, *J. Electrochem. Soc.*, **151**, 103, (2004).
- [145] T. Raju, C.A. Basha, *Ind. Eng. Chem. Res.*, **47**, 8947-8952, (2008).

-
- [146] M. Musiani, F. Furlanetto, R. Bertoncello, *J. Electroanal. Chem.*, **465**, 160-167, (1999).
- [147] J.M. Hu, J.Q Zhang, C.N. Cao, *Int. J. Hydrogen Energy.*, **29**, 791-797, (2004).
- [148] S. Trasatti, *Electrochim. Acta.*, **45**, 2377, (2000).
- [149] M. Musiani, P. Guerriero, *Electrochim. Acta.*, **44**, 1499, (1998).
- [150] R. Mraz, J. Krysa, *J. Appl. Electrochem.*, **24**, 1262-1266, (1994).
- [151] P. Modiba, A.M. Crouch, *J. Appl. Electrochem.*, **38**, (9), 1293-1299, (2008).
- [152] P. Klekens, L. Steen, H. Ponche, *Electrochim. Acta.*, **26**, 841, (1981).
- [153] X. Zhipeng, X. Fengjiao, Z. Debi, *Energy fuels.*, **25**, 2399-2404, (2011).
- [154] Y. Maedaa, K. Satoa, R. Ramarajb, T.N. Raob, D.A. Trykb, A. Fujishima, *Electrochim. Acta.*, **44**, 3441-3449, (1999).
- [155] E. Bishop, P. Cofre, *Analyst.*, **106**, 316-322, (1981).
- [156] D. Devilliers, B. Devos, H. Groult, *J. New Materials for Electrochemical Systems.*, **10**, 187-193, (2007).
- [157] D. Devilliers, M.T. Dinh, E. Mahé, D. Krulic, N. Larabi, N. Fatouros, *J. New Materials for Electrochemical Systems.*, **9**, 221-232, (2006).
- [158] V. Devadoss, C.A. Basha, K. Jayaraman, *Ind. Eng. Chem. Res.*, **47**, 4607-4616, (2008).
- [159] D. Devilliers, E. Mahé, *Electrochim. Acta* (2010), doi:10.1016/j.electacta.2010.01.098 assessed Nov. (2011).
- [160] P.K. Leung, C. Ponce de Leon, C.T.J. Low, F.C. Walsh, *Electrochim. Acta.*, **56**, 2145-2153, (2011).

Chapter 3

3.1 Steady state and non steady state techniques

Both steady state and non-steady state techniques have been used for the determination of the kinetics of the zinc-cerium system independently. Steady state techniques such as rotating disk electrode techniques (RDE) are not conducted always in equilibrium but the response of the applied perturbation is measured after it has become independent of time. These techniques are mainly used for cells with well defined convective stirring so as to control the mass transport. Equilibrium techniques are techniques in which the measurements are made with the electrode reaction at equilibrium by the application of a small A.C. signal.

The majority of the non-steady techniques are carried out under conditions of semi-infinite linear diffusion to a plane electrode. These experiments are carried out on a timescale so as natural convection (*viz.* density and temperature difference in the bulk solution) is negligible. The timescale results are based on the assumption that the diffusion layer is still developing during experimentation, *i.e* the concentrations of the reactants, intermediates and products are a function of time and distance from the electrode surface. Migration effects are also negligible as there is an excess amount of inert electrolyte. Therefore, diffusion is the only mode of mass transport.

For the characterization of electrochemical process it is always preferable to normalize the value of the current by the surface area of the electrode and use the current density (i) with units of $mA\ cm^{-2}$.

3.2 Three electrode cell

A three electrode cell (Fig.3.1) is normally employed in the experiments. This system comprises of a working electrode, a reference electrode and a counter electrode.

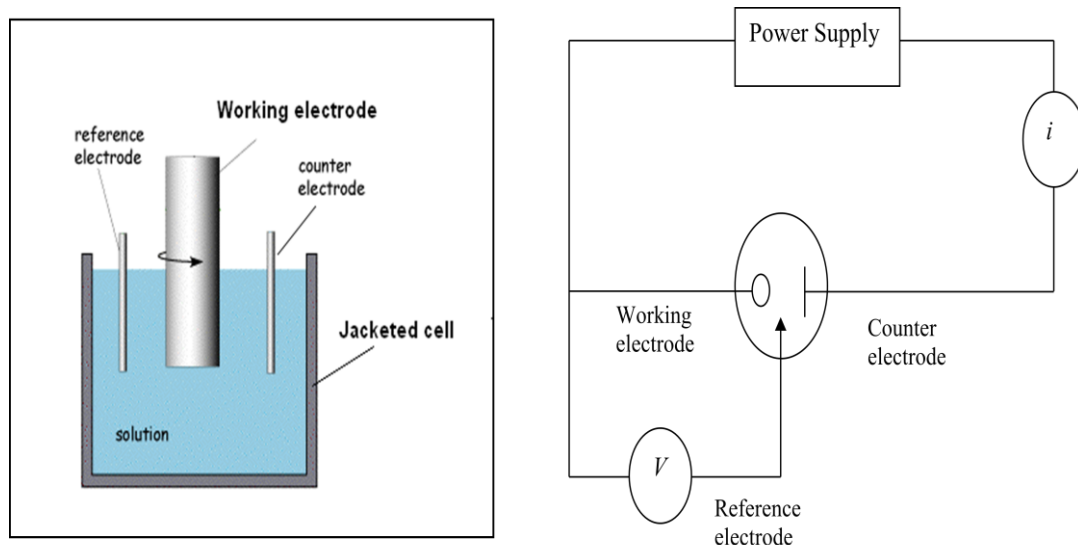


Fig.3.1: Three electrode cell and notation for the different electrodes [1].

The experiment must be designed so that the experimental data are totally determined by the chemistry at the working electrode. An essential feature of the working electrode is that it should not react with the solvent or the solution components. Regarding the counter electrode, the job of this electrode is to provide a current of equal magnitude but opposite sign to that at the working electrode. The two key requirements for the counter electrode are an electron-transfer reaction that occurs readily and whose chemistry does not interfere with the response of the working electrode. The normally large surface area of the counter electrode satisfies these two requirements. The counter electrode is chosen in such a way so that it should not produce substances during electrolysis that will reach and interfere with the working electrode reactions. The reference electrode is there to measure and control the interfacial potential between the working electrode and the solution. It draws no current from the cell *i.e* it is inert. Normally it comprises of a metal (e.g Hg, Ag) in contact with a sparingly soluble metal salt such as AgCl, Hg₂Cl₂ or Hg₂SO₄ and a solution containing the anion of the salt (e.g KCl, K₂SO₄) (Fig.3.2). Some common reference electrodes in aqueous solution and their potentials are given below vs standard hydrogen electrode (*S.H.E*). By convention the potential of the *S.H.E* is zero. This electrode consist of a high area Pt electrode in a solution containing 1 mol dm⁻³ proton and saturated with hydrogen, usually by passing H₂ through the solution [1].

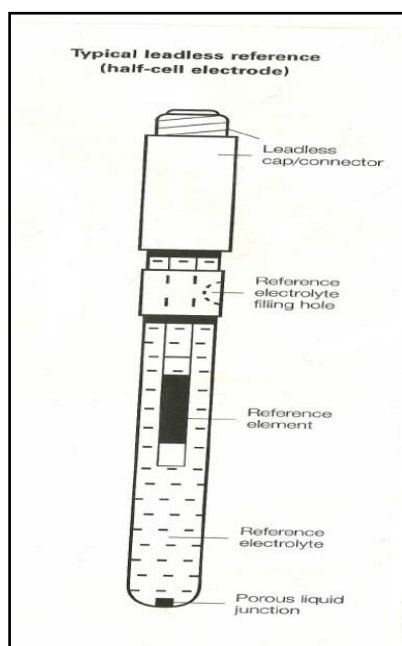
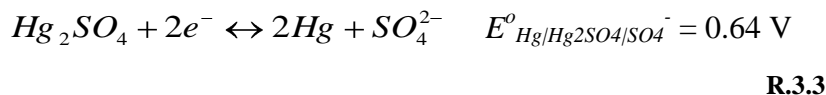


Fig.3.2: Apparatus of a reference electrode [2].

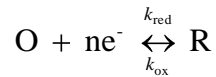
The potential of the reference electrode is dependent only on concentration of the anion in the reference compartment. However, if the bulky reference electrode was placed very close to the working electrode, it would cause shielding effects. Shielding denotes the blockage of part of the current path through the solution at the working electrode surface, which causes non uniform current distribution to arise at the electrode surface [1].

In solutions with high resistivity, the distance between the reference and working electrode can have a significant effect on the voltage required to drive a particular reaction. Because reference electrodes can be quite bulky in size they are usually introduced into the cell via a luggin capillary (*i.e* porous liquid junction) which is thin glass tube going from the reference electrode compartment to the working electrode surface. The distance between the luggin capillary and the working electrode is minimized for the majority of the measurements in order to limit the effect of the solution resistance.

3.3 Simple electron transfer reactions

3.3.1 Nernst equation

As with any chemical process, it is crucial to consider both the thermodynamics and the kinetics of the studied electron transfer process. Considering the electrode reaction where species [O] is capable of being reduced to [R]:



Eq.3.1

For an electrode reaction at equilibrium, the Nernst equation describes the fundamental relationship between the potential of an electrode and the concentration of the electroactive species at the electrode surface. Thus, if an electrode is at equilibrium with the solution in which it is immersed, the electrode will have a potential, invariant of time that will be thermodynamically related to the composition of the solution [1].

$$E = E^{\circ} + \frac{RT}{nF} \ln \left(\frac{C_{\text{O}}}{C_{\text{R}}} \right)$$

Eq.3.2

The equilibrium potential (E) is related to the standard potential (E°) of the oxidised and reduced couple as well as the surface concentrations of O and R *viz.* C_{O} and C_{R} respectively. When the surface concentrations of the oxidized and reduced species are equal, then the standard potential is equal to the particular equilibrium potential. The fact that there is no net current flowing through the cell indicates that there is no overall chemical change in it. However, a dynamic equilibrium exists at the surface of the working electrode and the exchange current density (i_o) expresses the amount of oxidation and reduction currents flowing at the equilibrium potential (*i.e.* the kinetics of the electrode reaction). The exchange current density is a convenient way of representing the rates of oxidation and reduction of a given single electrode at equilibrium, when no net loss or gain is experienced by the electrode material. i_o varies with the concentration of both O and R at the surface according to the following equation.

$$i_o = nFk^{\circ} C_{\text{O}}^{\alpha_A} C_{\text{R}}^{\alpha_C}$$

Eq.3.3

Where α_A and α_C are the transfer coefficients and k° is the standard rate constant at equilibrium [1]. The charge transfer coefficients can be determined by the relationship between the change in potential and the change in activation energy (*viz.* energy curve). Regarding the rate constant, following classical kinetics, it is to be expected that the rates of

oxidation and reduction will be a product of the rate constant and the concentration of a reactant at the site of the electron transfer, *i.e* the electrode surface ($x=0$). Therefore,

$$\text{Rate of oxidation} = k_a(C_R)_{x=0} \quad \text{Eq.3.4}$$

$$\text{Rate of reduction} = k_c(C_O)_{x=0} \quad \text{Eq.3.5}$$

If the potential of the working electrode is made more negative than the equilibrium potential, then in order to establish equilibrium, the surface concentration of O and R have to take up new values in order to satisfy the Nernst equation (Eq.3.2). This will require current to flow through the electrode/solution interface. In the case where the potential of the working electrode goes positive from the equilibrium potential, an anodic current will be observed. The magnitude of the current flowing at any potential will depend on the kinetics of the electron transfer.

3.3.2 Butler-Volmer equation

Considering the reaction from Eq.3.1 where k_{red} and k_{ox} are the rate constants for the reduction and oxidation steps. Assuming that there are amounts of [O] or [R] in the solution, the total current density flowing (i) is the sum of the reductive and of the oxidative currents [3]. These are dependent on the appropriate rate constant, the concentration of the electroactive species (C_O and C_R) at the site of the electron transfer, *i.e.* at the electrode surface.

$$i = i_a + i_c = nFAk_{red} C_R - nFAk_{ox} C_O \quad \text{Eq.3.6}$$

It is found experimentally that k_{red} and k_{ox} vary with potential according to the equations of the form [1]:

$$k_{red} = k_o \exp\left(\frac{-\alpha_c nF}{RT} E\right) \quad \text{Eq.3.7}$$

$$k_{ox} = k_o \exp\left(\frac{\alpha_a nF}{RT} E\right) \quad \text{Eq.3.8}$$

By combining Eq.3.6, Eq.3.7 and Eq.3.8, the deviation of the applied potential from the equilibrium value *i.e.* overpotential (η) can be calculated.

$$\eta = E - E_{eq} \quad \text{Eq.3.9}$$

The magnitude of the anodic and cathodic currents at equilibrium *i.e.* $\eta = 0$ is known as the exchange current density (i). This leads to one of the most fundamental relationships in electrochemistry, the Butler-Volmer equation. The latter describes how the current density varies with the exchange current density, overpotential, and the transfer coefficients [3].

$$i = i_o \left[\exp\left(-\frac{\alpha_a nF}{RT} \eta\right) - \exp\left(-\frac{\alpha_c nF}{RT} \eta\right) \right] \quad \text{Eq.3.10}$$

The current density scales exponentially with the applied overpotential as illustrated in Fig.3.3.

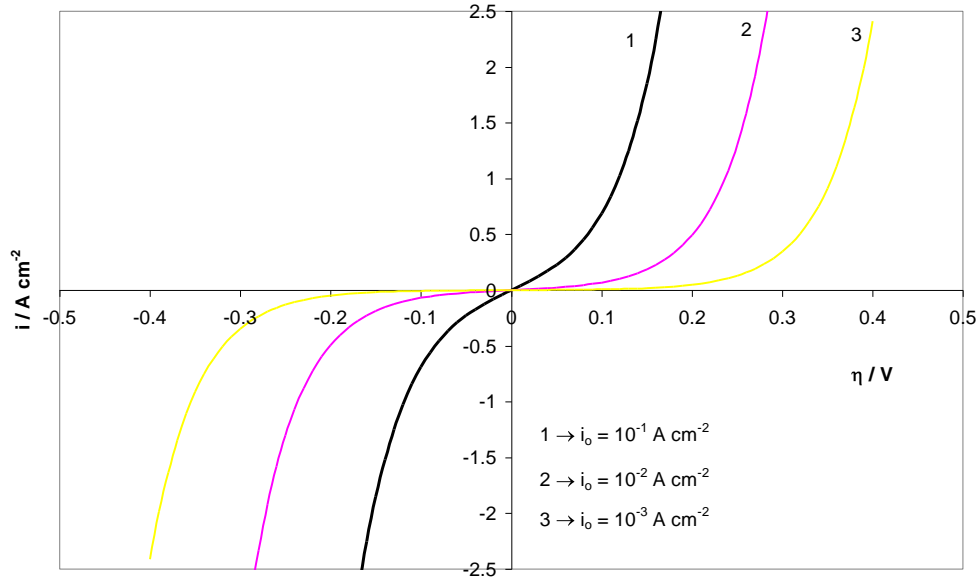


Fig.3.3: Current - voltage characteristics predicted by Eq.3.10 showing the scaling effect of i_0 .

The Butler-Volmer equation is valid in cases where the electrode reaction is controlled by electrical charge transfer at the electrode. There are three limiting forms of the Butler-Volmer equation. At high overpotentials *viz.* $|\eta| \geq 0.1$ V, Eq.3.10 can be simplified to give the anodic and cathodic Tafel equations [1]. The latter, relate the rate of the electrochemical reaction to the overpotential. At large positive and negative overpotentials the anodic and cathodic current densities are given by Eq.3.11 and Eq.3.12 respectively [1].

$$i = i_0 \exp\left(\frac{\alpha_A n F}{RT} \eta\right) \quad \text{Eq.3.11}$$

$$i = -i_0 \exp\left(-\frac{\alpha_C n F}{RT} \eta\right) \quad \text{Eq.3.12}$$

Graphical representations of the Tafel equations are presented in Fig.3.4 together with the full Butler-Volmer equation.

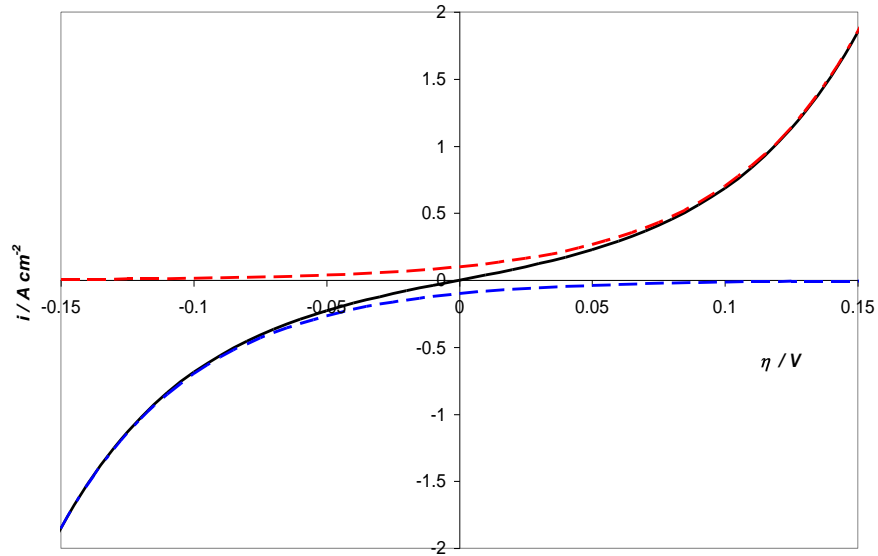


Fig.3.4: Anodic (red) and cathodic (blue) Tafel equations and Butler-Volmer (black) equation over the range $\eta = \pm 150$ mV.

The linearized forms of Eq.3.11 and Eq.3.12, *i.e.* Eq.3.13 and Eq.3.14, form the basis of a simple method for determining the exchange current density and the charge transfer coefficients [1].

$$\log i = \log i_o + \frac{\alpha_A n F}{2.3 RT} \eta$$

Eq.3.13

$$\log |-i| = \log i_o - \frac{\alpha_A n F}{2.3 RT} \eta$$

Eq.3.14

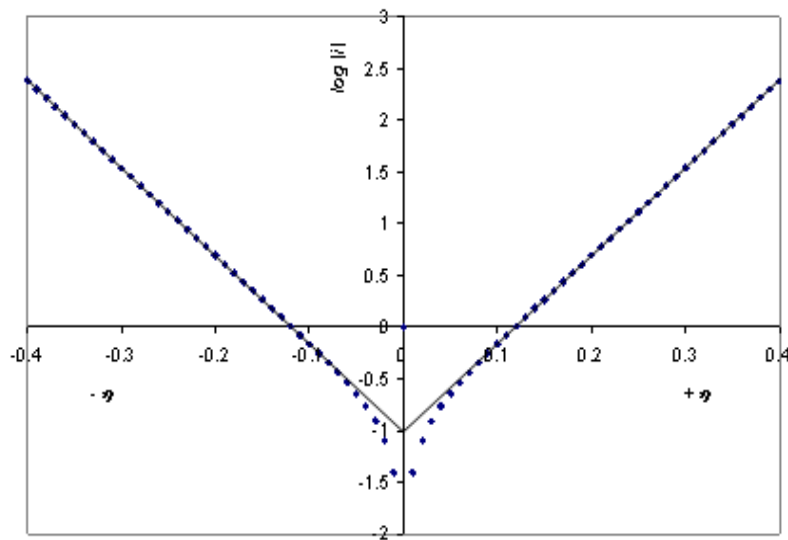


Fig.3.5: Tafel plots of $\log_{10}i$ versus η according to Eq.3.11 and Eq.3.12 showing the region of validity of the equations for $\alpha_C = \alpha_A = 0.5$.

The third limiting form to the Butler-Volmer equation applies at very low values of overpotential, *i.e.* $|\eta| \ll \left(\frac{RT}{\alpha_c nF}\right)$. In this low overpotential region often called the linear polarisation region the current increases linearly with the applied voltage [4]. The polarisation resistance is the ratio of the applied potential and the resulting current response. This resistance is inversely related to the exchange current density.

$$i = i_o \frac{nF}{RT} \Leftrightarrow \eta = \left(\frac{RT}{i_o nF}\right) i$$

Eq.3.15

where the polarisation resistance term (R_p) is equal to $\left(\frac{RT}{i_o nF}\right)$.

3.3.3 Nernst diffusion layer

When a very slow scan is applied to an electrochemical system governed by a reversible reaction (Eq.3.1), the voltammogram recorded will appear like a steady current versus voltage curve, yielding a s-shaped curve. As the sweep rate is increased however, a peak in the current response is found. This can be explained by examining the shape of the concentration profiles of O as a function of the applied potential and thus time. The concentration profile is the driving force mass transport by diffusion.

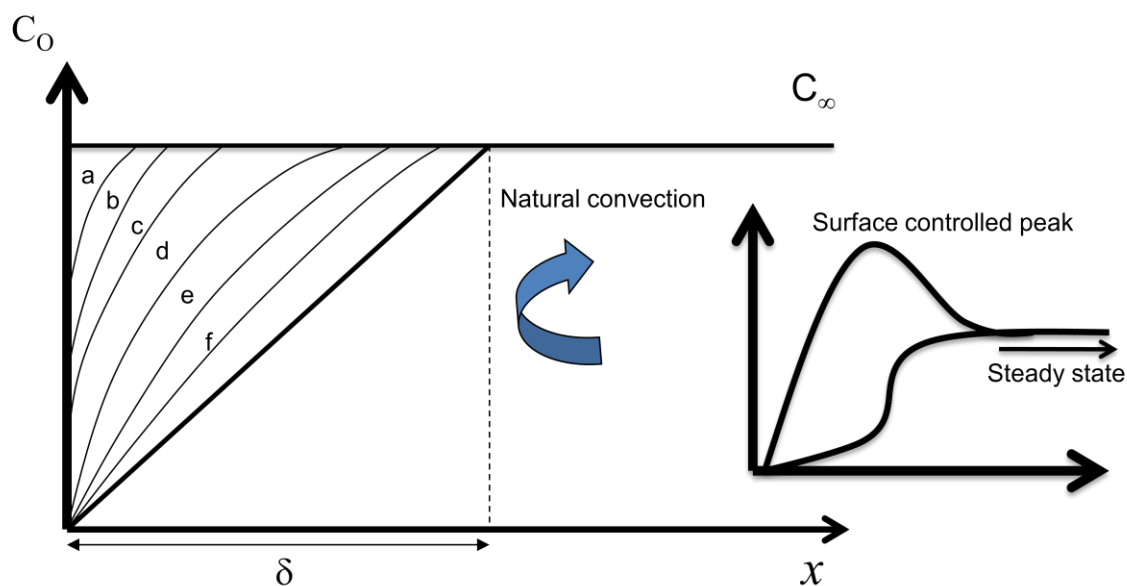


Fig.3.6: Concentration-distance profile for the electroactive species [O] for a reversible reaction (Eq.3.1) during a linear voltage sweep experiment.

Under steady state conditions, concentrations above a certain distance are maintained by natural convection. Within the region next to the electrode, known as the Nernst diffusion layer, the concentration gradient is essentially linear. As the scan rate increases, the diffusion layer does not have enough time to relax at its equilibrium state and hence the concentration profiles are not linear anymore (Fig.3.6). As soon as the potential at which [O] is reduced has been reached, the surface concentration decreases from its bulk according to the Nernst equation and a concentration profile is set up (Fig.3.6 (a)). As the potential is made more negative, the surface concentration of the reactant gradually decreases as a result of diffusion. Meanwhile, the electrode potential is still changing and as a result the surface concentration as well (Fig.3.6 (b) (c)). Eventually the surface concentration of the reactant reaches zero (Fig.3.6 (e)) and the steady state concentration cannot change any further reaching a plateau value (*i.e* system is entirely diffusion controlled). Once the surface concentration reaches zero

the concentration gradient starts to decrease due to a relaxation effect and with it the current flowing also decreases giving the peak shaped-potential response as shown in the voltammogram of Fig.3.3.

The exact form of the cyclic voltammogram can be determined mathematically by solving Fick's second law [5] for C_O and C_R . It predicts how diffusion (D) causes the concentration (C) to change with time (t) (Eq.3.16).

$$\frac{\partial C}{\partial t} = D \frac{\partial^2 C}{\partial \chi^2}$$

Eq.3.16

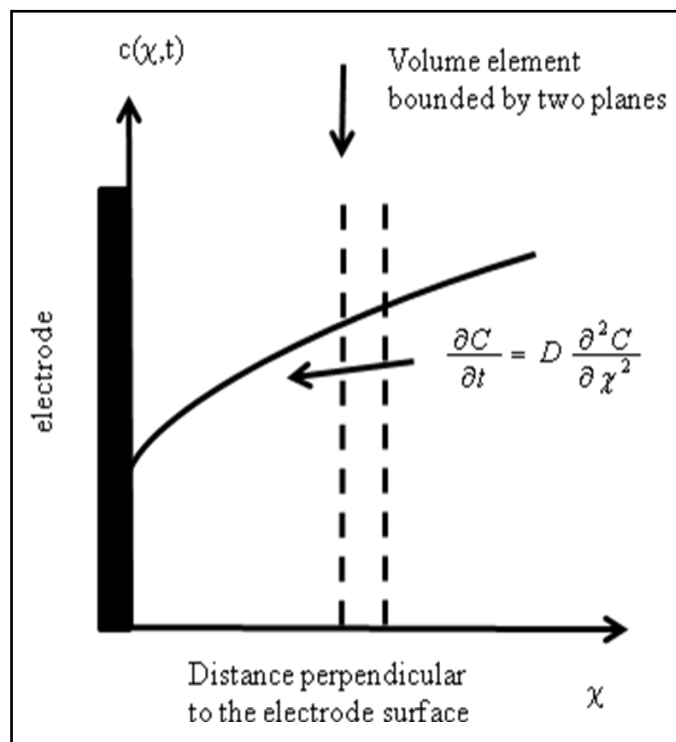


Fig.3.7: Fick's second law of diffusion [5].

3.3.4 Cyclic voltammetry

A cyclic voltammogram is a type of potentiodynamic electrochemical measurement that measures the charge transfer between an electrode (*i.e.* electron conductor) and an electrolyte species in a solution. It is one of the most frequently used electrochemical methods because of its relative simplicity and its high information content. It is mainly used to study the electrochemical properties of a substance or a chemical constituent that is determined in an analytical procedure. In this case, the chemical constituent is an electroactive species, *i.e.*, a species which can undergo reduction or oxidation at the electrode surface [6]. Potential sweep experiments such as cyclic voltammetry are designed to operate under conditions where diffusion is the only mode of mass transport (unstirred solution) and is described by semi-infinite linear diffusion to a planar electrode surface [7]. Thus, the variation in concentration occurs only in the direction perpendicular to the surface.

In a typical cyclic voltammetry experiment, the potential limits are set within the region where the electroactive species can undergo reduction or oxidation at the electrode surface. A solution component is electrolyzed by placing the solution in contact with an electrode surface and then making the surface sufficiently positive or negative to force electron transfer. The current (I) at the working electrode is plotted versus the applied voltage (V) to give the cyclic voltammogram trace. This rate of increase in the potential is known as the experiment's scan rate (ν). The latter, determines the timescale of the experiment and therefore the rate of non-steady state diffusion.

The waveform of the voltage applied to the working electrode versus the reference electrode is triangular shaped. In the cyclic voltammogram of Fig.3.8 the scan begins from the right hand side of the current-voltage plot where no current flows. The choice of the initial potential defines the initial concentration profiles for the reactant, the intermediates and the products. As the voltage is swept further to the left (cathodic scan *viz.* reduction) a current begins to flow and eventually reaches a peak before decreasing as shown in the figure.

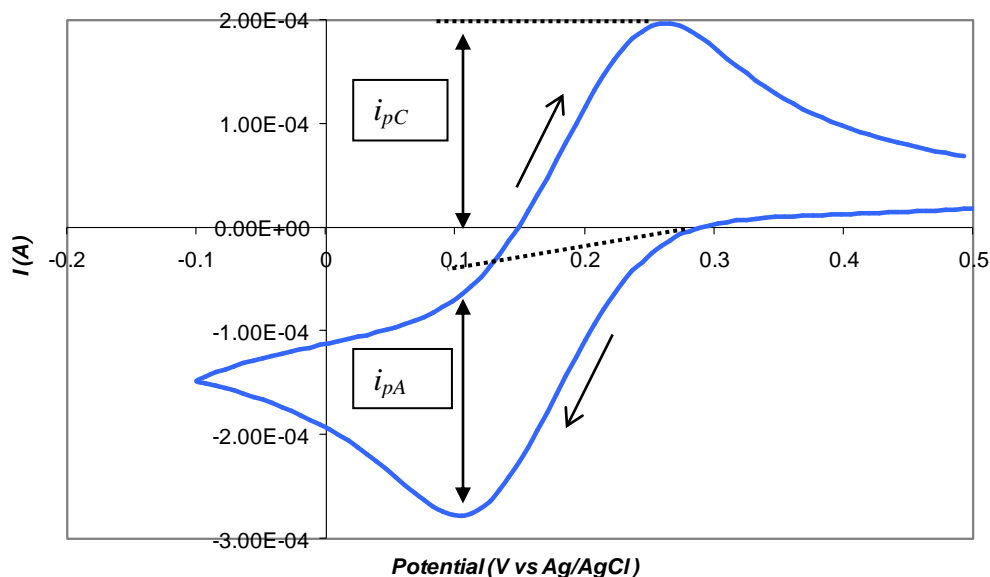


Fig.3.8: Cyclic voltammogram at 40 mV s^{-1} for $5 \times 10^{-3} \text{ mol dm}^{-3} \text{ K}_3 \text{ Fe(CN)}_6 / 1 \times 10^{-1} \text{ mol dm}^{-3} \text{ KCl}$ - Au electrode (0.38 cm^2).

Overall, on a cyclic voltammogram it is possible to observe features such as the number of peaks on forward and reverse scan, the shapes of the peaks, the peak potentials (E_p) and the peak current densities (i_p).

There are generally two types of systems namely reversible and irreversible used to describe the electrochemical processes. They are used to denote whether or not the electron transfer reaction at the electrode is rapid (*i.e* fast kinetics of the reaction) and so the concentration at the electrode surface is at Nernstian equilibrium. If the redox couple is reversible, then when the applied potential is reversed and reached the potential that will reoxidize the product formed in the reduction reaction (the half-wave potential) will be a current of reverse polarity from the forward scan. The oxidation peak usually has a similar shape to the reduction peak at reversible systems as shown in Fig.3.3. This is due to the fact that the oxidation current is only limited by the amount of product formed during the reduction reaction. In the case of irreversible systems, the rate of electron transfer is slow so that the potential no longer reflects the Nernstian equilibrium of the redox couple at the electrode surface leading to large anodic-cathodic peak separations, especially at high scan rates.

3.3.5 Randles-Sevcik equation

The obtained peak shape of the oxidative and reverse current-potential curve is typical for an electrode reaction in which the rate is governed by semi-infinite diffusion to a planar electrode surface [7]. That is, the rate of the electron transfer step is relatively fast compared to that of diffusion. In such a case, the peak current density (i_p) is given by the *Randles-Sevcik* relationship [8].

$$i_p = 0.4463 nFA C_o^* \left(\frac{nFvD}{RT} \right)^{\frac{1}{2}}$$

Eq.3.17

At room temperature (25°C), the Randles-Sevcik equation reduces to the form:

$$i_p = 6.687 \times 10^5 n^{\frac{3}{2}} v^{\frac{1}{2}} A D^{\frac{1}{2}} C_o^*$$

Eq.3.18

The peak current density is proportional to the concentration of electroactive species (C_o^*), the square root of the sweep rate ($v^{1/2}$) and the diffusion coefficient (D). A linear plot of i_p versus $v^{1/2}$ passing through the origin indicates that the electrochemical process is reversible and under diffusion control. A reversible cyclic voltammogram can be observed if both C_o and C_R are stable (*i.e* do not undergo any chemical degradation). Provided that the electron transfer process is in equilibrium, the surface concentration will follow the Nernst equation (Eq.3.2). Other diagnostic tests for cyclic voltammograms of the reversible systems at room temperature are listed below [9]:

- $\Delta E_p = E_p^A - E_p^C = \frac{59}{n} mV .$
- $E_p - E_{\frac{p}{2}} = \frac{59}{n} mV .$
- $\left(\frac{i_p^C}{i_p^A} \right) = 1 .$
- $I_p \sim v^{1/2} .$
- E_p is independent of v .
- At potentials higher than E_p , I vs $t^{-1/2}$.

3.4 Potential step techniques

A potential step experiment is used to initiate the nucleation and growth of the deposits. The potential of the electrode is changed in a step-wise manner, usually from a value where no current flows to one where the desired electrode reaction takes place. Prior to the conduction of the potential step experiment in our case to examine nucleation, the correct potential limits have to be selected where nucleation can occur. These potential limits can be determined by cyclic voltammetry experiments on the system under investigation. The potential is held constant for a fixed period of time at a set potential and the current-time profile is measured. If the electrode surface then needs to be examined *ex-situ* (*i.e.* scanning electrode microscopy) the cell is turned off so as to avoid the stripping of the metal back to the solution (Fig.3.8).

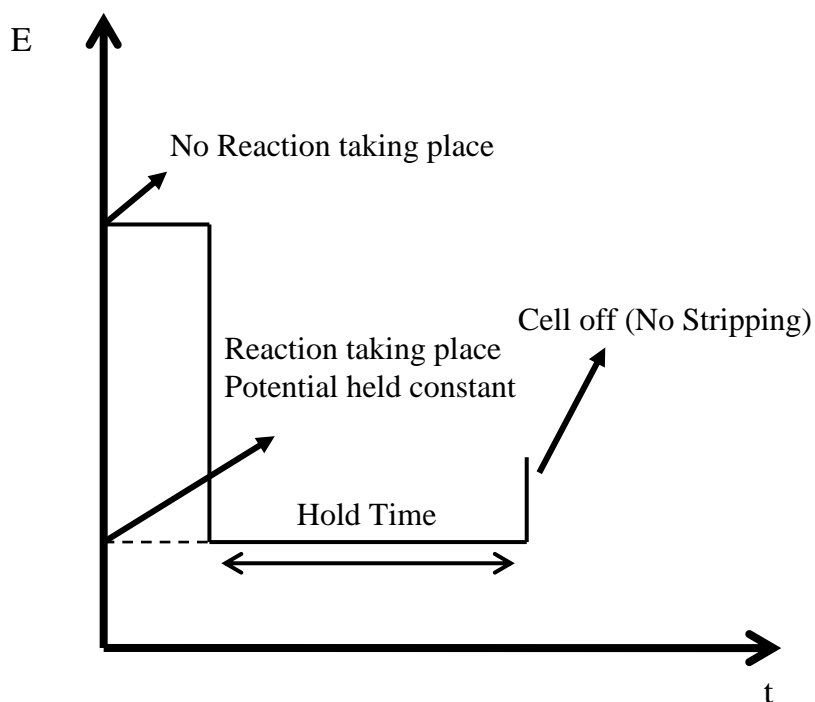


Fig.3.9: Schematic of the potential step experiment with no stripping of electrodeposits.

3.4.1 Instantaneous and progressive nucleation

A fundamental step in the electrodeposition processes is the initial stage of phase formation, called electrocrystallization. Nucleation is the formation of stable centres. The stability originates from the interaction of atoms, ions and molecules in the bulk of the material. The electrodeposition process leads to an increase in current with time as the number of nuclei increase and so the available surface area increases as well. This stage is normally associated with a two or three dimensional growth process where the number of the nuclei formed on the electrode surface depends strongly on the overpotential (η). The merging of these growth centres will lead to a reduction in the current and at longer times the current reaches a limiting value due to the fact that the centres overlap into a continuous layer and the process becomes mass transport controlled. There are two ways of examining the kinetics of the nucleation process namely instantaneous and progressive nucleation. Instantaneous nucleation occurs when a number of nuclei (N_o) are formed instantly at the available sites, *viz.*

$$N(t) = N_o \quad \text{Eq.3.19}$$

whereas in progressive nucleation the number of nuclei increases with time following first order kinetics [10] with A being the first order nucleation constant according to [6]:

$$N(t) = N_o \left[1 - \exp(-At) \right] \quad \text{Eq.3.20}$$

Investigations of instantaneous and progressive nucleation are carried out following initial examinations of the system by cyclic voltammetry. The cyclic voltammogram is first scrutinised for evidence of a nucleation loop (*i.e* the potential at which zinc deposition starts occurring) and a cathodic/anodic charge ratio close to unity, which implies that all the metal deposited on the negative scan is redissolved on the anodic scan. The potential is stepped to a region where nucleation and growth of the new phase occurs. Typically, the applied potential step is just negative of the nucleation loop observed by the cyclic voltammogram.

The data obtained from the step experiment helps us understand if the new phase formation is controlled by instantaneous or by progressive nucleation. In the subsequent analyses of the amperometric data, it is assumed that both instantaneous and progressive nucleation are for three-dimensional centres [11]. Nucleation followed by two-dimensional growth leads to the formation of a monolayer. Overall, the stages of the nucleation process involve the nucleation of the new phase *viz.* formation of stable nuclei, growth of the individual metal centres (growth of nuclei and formation of further stable nuclei in the case of

the progressive nucleation), overlap of the growing centres leading to a complete monolayer for 2-D growth and then thickening of the layer.

The current-time ($I-t$) transients of Fig.3.10 exhibit the typical shape for a nucleation process with three dimensional growth of nuclei limited by the diffusion of the electroactive species at longer times. At short times, an increase in the current density is observed corresponding to the birth and growth of the nuclei. At later stages, the diffusion zones of adjacent nuclei overlap and the current density reaches a maximum followed by a decaying portion which converges to a limiting current (I_L) due to semi-infinite linear diffusion of the electroactive ions to a planar electrode surface.

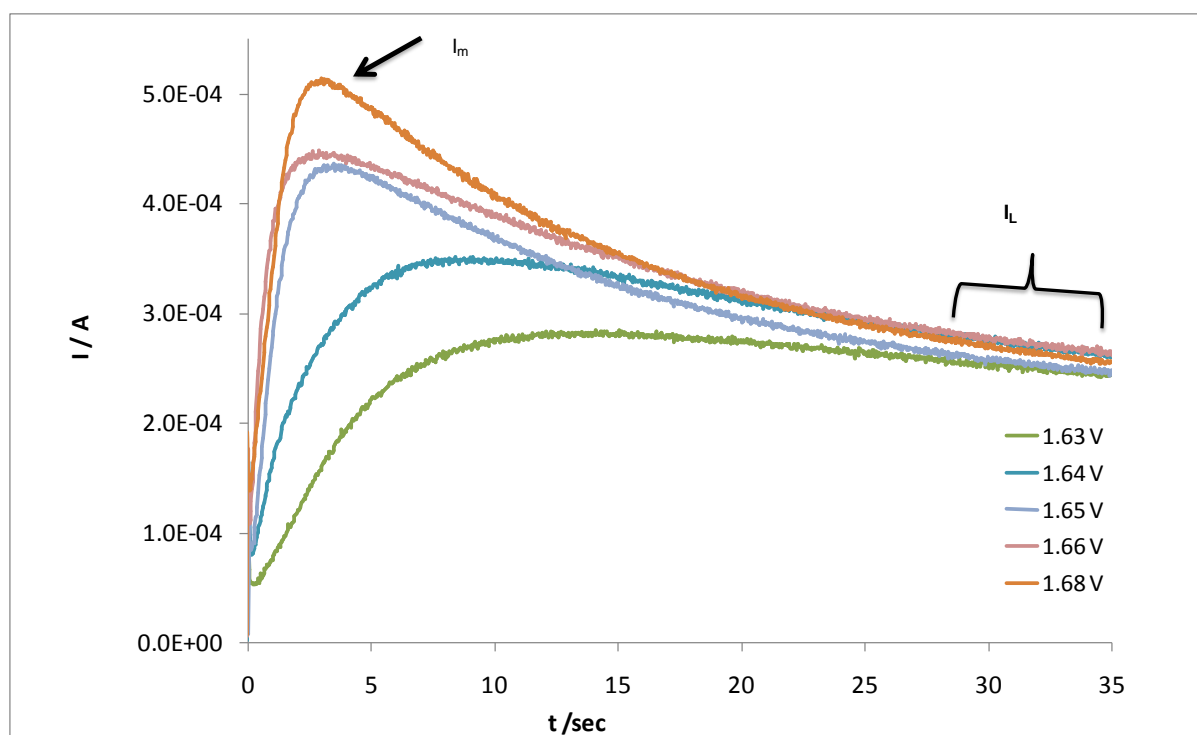


Fig.3.10: I versus t transients in a solution containing $7 \times 10^{-1} \text{ mol dm}^{-3} \text{ Zn(II)}$ and $5.7 \text{ mol dm}^{-3} \text{ CH}_3\text{SO}_3\text{H}$; GC electrode (0.38 cm^2) at 25°C and no rotation.

From Fig.3.10, the maximum current *viz.* I_m and the corresponding time t_m can be determined for each potential step. Analysis of the nucleation data is carried out in terms of the normalised current and time with respect to I_m and t_m respectively. Eq.3.21 is for instantaneous nucleation and Eq.3.22 for progressive nucleation [12]:

$$\left(\frac{I}{I_m}\right)^2 = \left(\frac{t}{t_m}\right) \times \left[1 - \exp\left(-1.256\left(\frac{t}{t_m}\right)\right)\right]^2$$

Eq.3.21

$$\left(\frac{I}{I_m}\right)^2 = \left(\frac{t}{t_m}\right) \times \left[1 - \exp\left(-2.336\left(\frac{t}{t_m}\right)\right)\right]^2$$

Eq.3.22

As noted above, the exact shape of the transient will depend on whether the nucleation process follows the instantaneous or the progressive route, the growth of the nuclei is in two or three dimensions and also on whether the growth of the nuclei occurs under electron transfer or mass transport control. The relationships for instantaneous and progressive nucleation have been derived by Scharifker *et al.* and others [11] [13] [14]. The parameters in which I_m and t_m depend on *viz.* number of nuclei (N_o), diffusion coefficient (D) and the dimensionless constant affecting the growth rate of the diffusion zones (k^*)

For instantaneous nucleation we have:

$$t_m = \left(\frac{1.26}{N_o k^* D \pi}\right)$$

Eq.3.23

and for progressive nucleation

$$t_m = \left(\frac{4.67}{A N_o k^* D \pi}\right)^{\frac{1}{2}}$$

Eq.3.24

The dimensionless constant affecting the growth rate of the diffusion zones (k^*) is defined according to:

$$k^* = \frac{4}{3} \left(\frac{8\pi C_\infty M}{\rho}\right)^{\frac{1}{2}}$$

Eq.3.25

From Eq.3.23 and Eq.3.24, the appropriate graph that determines the nature of the nucleation process can be plotted (Fig.3.11) where a comparison is made to the experimental data at a potential of -1.575 V vs Ag|AgCl.

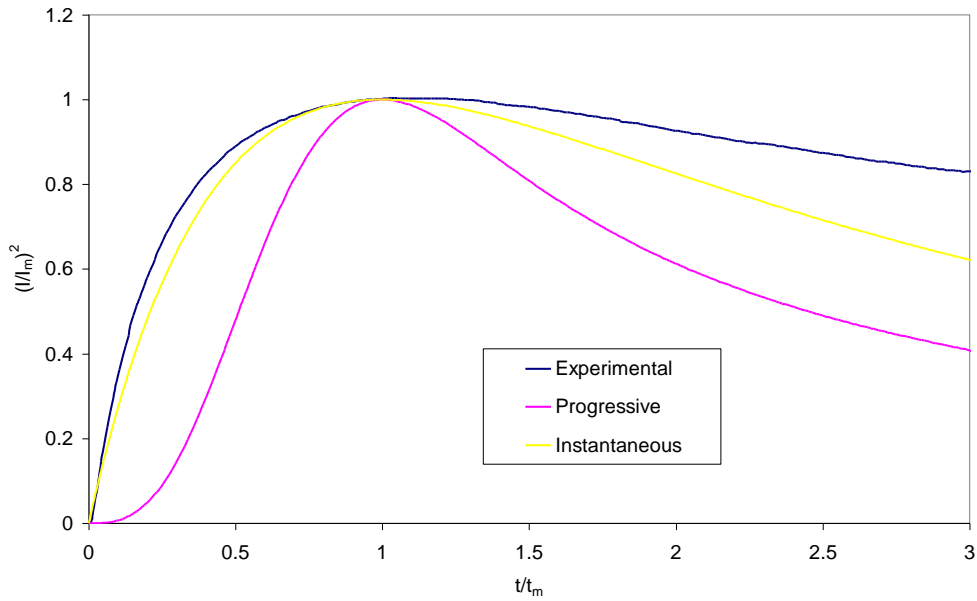


Fig.3.11: Current transients calculated from Eq.3.21 and Eq.3.22 in $7 \times 10^{-1} \text{ mol dm}^{-3} \text{ Zn(II)}$ and $5.7 \text{ mol dm}^{-3} \text{ CH}_3\text{SO}_3\text{H}$ - Glassy carbon electrode (0.38 cm^2) at 25° C - Potential = $-1.575 \text{ V vs Ag|AgCl}$.

At very short times the interaction of the diffusion fields can be assumed to be negligible and the two limiting cases of instantaneous and progressive nucleation of growth centres are linked with the nuclear number density (N_o). As the applied potential increases, the mode of nucleation tends to change from progressive to instantaneous. This seems reasonable as the more negative the potentials are, the more energy is applied to the system and instantaneous nucleation is the more likely process to occur due to the fact that all the available sites become more or less equivalent. The diffusion coefficient can be calculated from the current corresponding to the maximum in each transient [12]. For instantaneous nucleation we have:

$$I_m^2 t_m = 0.163 D n F C_\infty \quad \text{Eq.3.26}$$

For the case of progressive nucleation we have:

$$I_m^2 t_m = 0.260 D n F C_\infty \quad \text{Eq.3.27}$$

3.4.2 Electric Double layer

The study of the electrical double layer is intimately concerned with the concept of the ideally polarized electrode which is defined as an electrode at which no charge transfer can occur, regardless of the potential imposed by an external voltage source (*i.e* no Faradaic current flowing) [15]. The ideally polarized electrode is most commonly studied by measurement of capacitance, C , defined by the change in the electrode surface, q_M , with change in potential [7].

$$C = \frac{dq_M}{dE}$$

Eq.3.28

The capacitance can be measured by either an A.C. capacitance bridge (discussed in Section 3.4.4) or from a cyclic voltammogram where in the absence of Faradaic processes, the observed current density is given by [7]:

$$i = C\nu$$

Eq.3.29

where ν is the scan rate and C is the concentration of the species.

When a potential is applied to an electrode in an electrolyte solution, the electrode surface takes up a characteristic charge and attracts a layer of ions of opposite charge to form a double layer. The structure of the double layer depends on the applied potential, the electrode material and the solution composition. The models used to describe the electrical double layer have become more complicated with time. A model of an electric double layer for a dilute aqueous salt solution is given in Fig.3.12. This model is based on the Gouy-Chapman-Stern model [16].

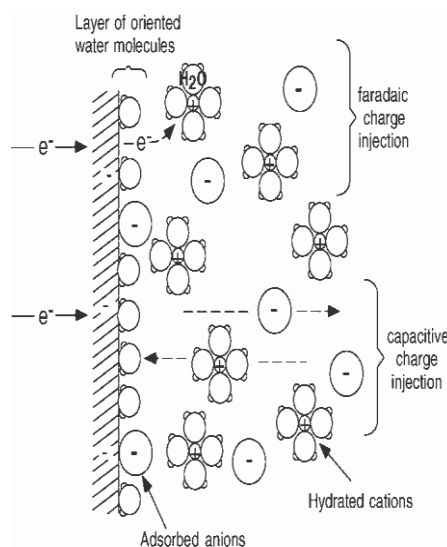


Fig.3.12: Electric double layer for a dilute aqueous solution [7].

From Fig.3.12 it can be seen that due to their dipole moments (*i.e* asymmetrical charge distribution), the water molecules will adsorb on the electrode surface and effectively the ions will compete for the sites on the surface. Negative to the potential of zero charge, the surface layer is made up of hydrated cations and water molecules while the presence of specifically adsorbed cations or anions cannot be ruled out. Positive to the potential of zero charge, both hydrated and specifically adsorbed anions as well as water are likely to exist [17].

Consequently, the charge distribution is altered while also the structure of the compact layer. A double layer will exist at the electrode/solution interface and will interfere with the behavior of the electrode. The double layer charging occurs whenever there is a change in electrode potential and lasts a few tens of milliseconds. This is due to the fact that this short period of time is needed for the ions in the solution to balance the charge on the electrode. The electrons at the surface of the electrode which is solid move instantaneously on the application of an electrode potential. On the other side of the interface, the ions are in solution and thus travel at slower velocities. The double layer at most metals is difficult to characterize due to the presence of Faradaic processes (*i.e* electron transfer reactions) taking place at the surface.

3.4.3 A.C. Impedance

Impedance is defined as the measure of opposition to an A.C. current. It extends the concept of resistance to A.C. circuits describing not only the amplitudes of current and voltage but also the phases. For an electron transfer reaction occurring (Eq.3.1), the simplest electrochemical system to analyze would be that of a rapid reaction at equilibrium, *i.e.* no net current flowing. Under alternating current (A.C.) excitation, (the excitation of the working electrode is by a small A.C. voltage ≤ 10 mV peak to peak) the net current is still zero but the current-potential relationship is linear rather than exponential. In order to examine both the electron transfer and mass transfer (diffusion) for an electrochemical reaction, the following equivalent circuit is used:

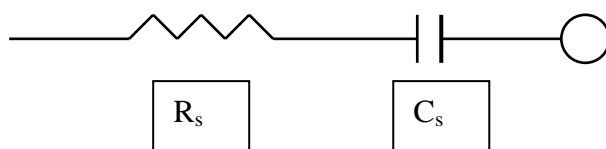


Fig.3.13: Impedance as a combination of a resistor and a capacitor.

Impedance is expressed as a series of a resistor and capacitor. The resistance of the system (R_s) and the pseudo-capacitance (C_s) are given by [7]:

$$R_s = R_{ct} + \frac{\sigma}{\omega^{\frac{1}{2}}} \quad \text{Eq.3.30}$$

$$C_s = \frac{1}{\sigma\omega^{\frac{1}{2}}} \quad \text{Eq.3.31}$$

R_{ct} is the charge transfer resistance (Ω), ω is the angular frequency (Hz) of the A.C. excitation and σ is the Warburg coefficient ($\Omega \text{ s}^{-1/2}$). Since, for small potential perturbations the relationship between current and potential is linear rather than logarithmic and therefore the charge transfer resistance, R_{ct} can be expressed as [7]:

$$R_{ct} = \frac{RT}{nFi_o} \quad \text{Eq.3.32}$$

The charge transfer resistance is thus a measure of the exchange current density (i_o) and therefore of the standard electron transfer rate constant at equilibrium (k°). σ is dependent on the diffusion parameters of the system (Eq.3.33).

$$\sigma = \left(\frac{RT}{2^{\frac{1}{2}} n^2 F^2 A D^{\frac{1}{2}}} \right) \times \left(\frac{1}{C_o} + \frac{1}{C_R} \right)$$

Eq.3.33

As can be seen from Eq.3.33 the overall impedance equation is the sum of two resistive terms, a resistive component which is small when i_o is large and a reactance that can be regarded as a frequency-dependent resistance [7]. This special resistance is called the Warburg impedance (Z_w) as shown in Eq.3.34.

$$Z_w = R_s + \left(\frac{1}{j\omega C_s} \right) = R_{ct} + \left(\frac{\sigma}{\omega^{\frac{1}{2}}} \right) + \left(\frac{\sigma}{j\omega^{\frac{1}{2}}} \right) = z' - jz'' = R_{ct} + \left(\frac{\sigma}{\omega^{\frac{1}{2}}} - \frac{j\sigma}{\omega^{\frac{1}{2}}} \right)$$

Eq.3.34

A realistic model of a simple electrochemical interface can be built by assuming a double layer capacitance (C_{dl}) always parallel to the reaction impedance. The graph of such a circuit is plotted on an Argand diagram of $\hat{z} = z' - jz''$ and gives a semi-circle (Fig.3.14). The Argand diagram represents a series of points at different frequency values where the value of Z'' approaches zero at infinite frequency as the impedance of the capacitor is effectively zero. The double layer capacitance is independent of any Faradaic reaction but contributes to the overall impedance. Furthermore, if there is any solution resistance (R_u) between the point at which the solution potential measured (*viz.* the tip of the luggin capillary) and the working electrode, this will too appear as part of the measured total impedance (Fig.3.14). R_u has the effect of moving the semi-circle along the Z' axis.

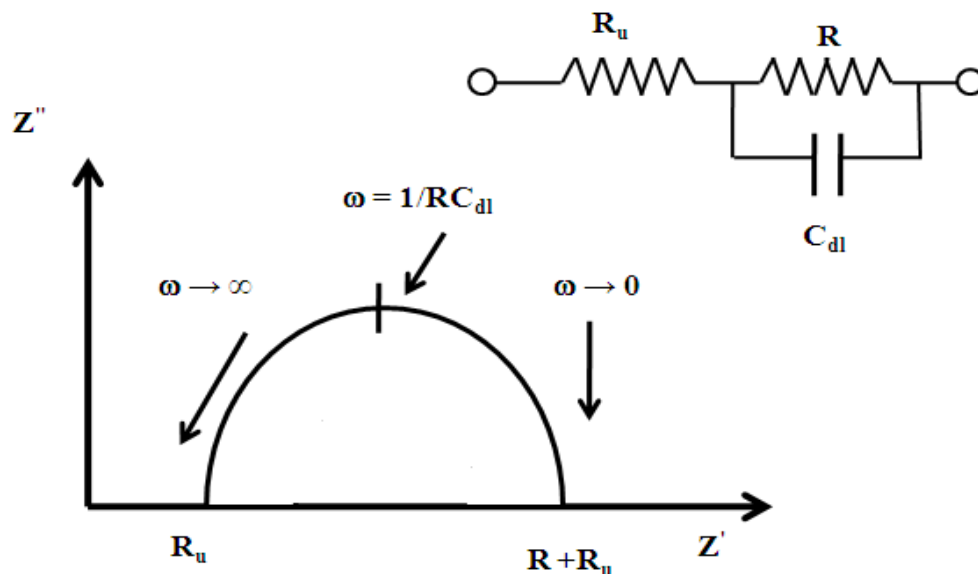


Fig.3.14: Complex plane diagram for a parallel RC circuit with the addition of R_u .

The equivalent circuit for an electrode reaction with double layer capacitance C_{dl} and uncompensated solution resistance R_u and the Faradaic reaction has been resolved into the charge transfer resistance R_{ct} and Warburg impedance is shown in Fig.3.15. When R_{ct} approaches zero (*i.e* fast electrode kinetics), then i_o is very large and thus Z_W dominates the system. The Warburg impedance is used to model semi-infinite linear diffusion *i.e* unrestricted diffusion to a large planar electrode.

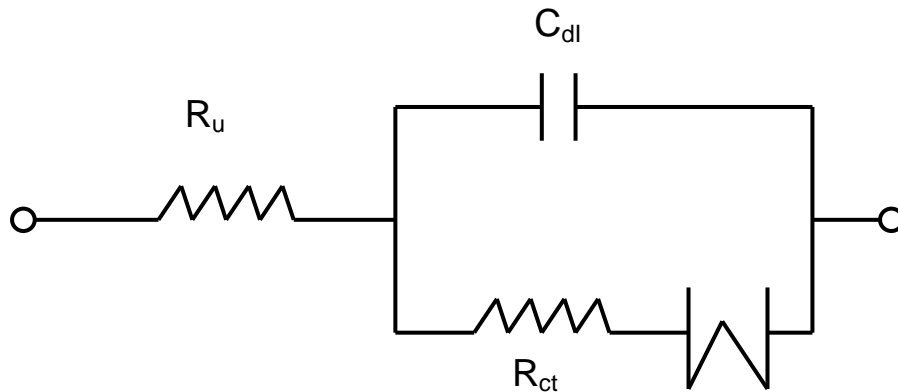


Fig.3.15: Equivalent circuit for an electrode reaction with double layer capacitance C_{dl} , uncompensated solution resistance R_u and the reaction resistance (R_{ct} and Z_W) [1].

The complex plane plot of the circuit of Fig.3.15 is illustrated in Fig.3.16.

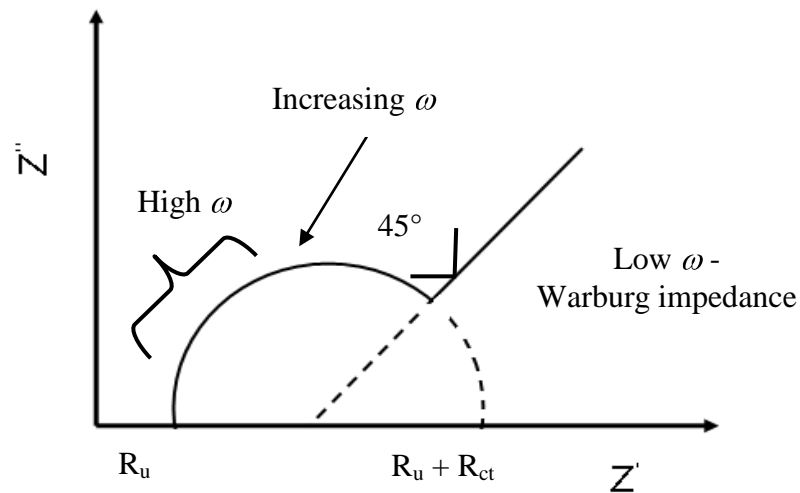


Fig.3.16: Complex plane impedance plot for the circuit of Fig.3.15.

In this plot both the kinetically controlled (semi-circular part of the complex plane impedance plot) and diffusion controlled (linear part of the complex plot) regions are displayed. At low frequencies the impedance is dominated by the diffusion component since this term varies inversely with $\omega^{1/2}$ (Eq.3.34) and this in turn gives a constant phase angle of $\pi/4$ (45°), independent of the frequency.

3.5 Rotating disk electrode

The rotating disk electrode (RDE) is used in electrochemical studies when investigating the reaction mechanisms that involve mass transport of the electroactive species. In a three electrode system (Section 3.2), the working electrode rotates during the experiment thus pushing a flux of analyte to the electrode surface. It consists of a polished disc of the chosen electrode material surrounded by an insulating sheath of substantially larger diameter. The disk's rotation is usually described in terms of angular velocity (rads). The principal movement of electrolyte is towards the disk, perpendicular to the surface. But since the solution cannot pass through the surface of the disc and its sheath, the convection becomes radial close to the surface as illustrated in

Fig.3.17. The rotating electrode therefore acts as a pump. It pulls the solution vertically upwards and throws it outwards as the solution cannot pass through the solid material. This results in a laminar flow of solution passing towards and across the electrode. The rate of the solution flow towards the electrode can be controlled by the angular velocity and has been modelled mathematically by Levich *et al.* [18].

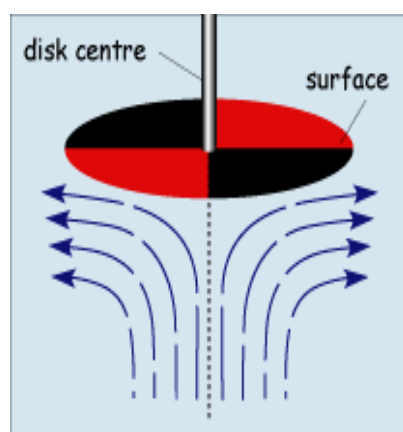


Fig.3.17: Flow pattern close to

RDE surface.

The RDE creates conditions *i.e.* steady state

well-defined hydrodynamic mass transport regime. The

flow created by the rotation can quickly achieve conditions in which the steady state current is controlled by the convective flow rather than by diffusion. There is a minimum rotation rate where the forced convection dominates against natural convection and non-steady state diffusion. As the RDE flow is always laminar, *i.e.* the solution moves forward in a highly organized manner and it can be considered to consist of a sequence of separate, non-mixing elements. At higher rotation rates, the flow regime becomes less organized and hence more difficult to deal with theoretically.

With regards to the Nernst diffusion layer model (Section 3.3.3); if a linear concentration gradient is maintained throughout this increase in potential, then a classic s-shaped steady state current is obtained. The steady state gradient is limited by natural

convection and has a diffusion layer thickness (δ), which depends on the viscosity of the solution into which it extends. The diffusion layer thickness derives from Fick's first law of diffusion [5] [19] as shown in Eq.3.35. It is used for steady state diffusion *viz.* the concentration within the diffusion volume does not change with respect to time, ($J_{in} = J_{out} =$ flux removed by electrode reaction). The negative sign on Eq.3.35 indicates that the direction of the flow is from high to low concentration.

$$J = -D \left(\frac{\partial C}{\partial x} \right)$$

Eq.3.35

where $\frac{\partial C}{\partial x}$ represents the concentration gradient of species [O] and is the driving force that leads to molecular movement and is defined as $\frac{\partial C_R^*}{\partial x} = \frac{\Delta C}{\Delta x} = \frac{C_\infty - C_\sigma}{\delta} = \frac{C_\infty}{\delta}$, since $C_\sigma = 0$ (C_σ : surface concentration [mol dm^{-3}]).

The current density is equal to:

$$i = nFJ = nFD \left(\frac{C_\infty}{\delta} \right) \Leftrightarrow i \propto \frac{1}{\delta}$$

Eq.3.36

and the diffusion layer thickness (δ) at the rotating disk electrode is given by:

$$\delta = \frac{1.61 D^{\frac{1}{3}} \nu^{\frac{1}{6}}}{\omega^{\frac{1}{2}}}$$

Eq.3.37

where ν is the kinematic viscosity ($\text{cm}^2 \text{s}^{-1}$)

By running linear sweep voltammetry or other experiments at various rotation rates, different electrochemical phenomena can be investigated including multi-electron transfer reactions, the kinetics of a slow electron transfer as well electrochemical and chemical reaction mechanisms [18]. Problems that arise during the RDE experiments involve the leakage of solution into any gap between the active disc material and the insulating sheath, while noise can be introduced by poor or dirty electrical contacts on the rotating shaft.

3.5.1 Levich equation

The RDE gives a well defined, steady state mass transport regime. The concept of the Nernst diffusion layer provides a basis for good quantitative models that are able to predict the voltammetric response. When the electrode reaction is mass transport controlled (Fig.3.18), according to the Nernst diffusion layer model, for such potentials the surface concentration of the electroactive species is zero.

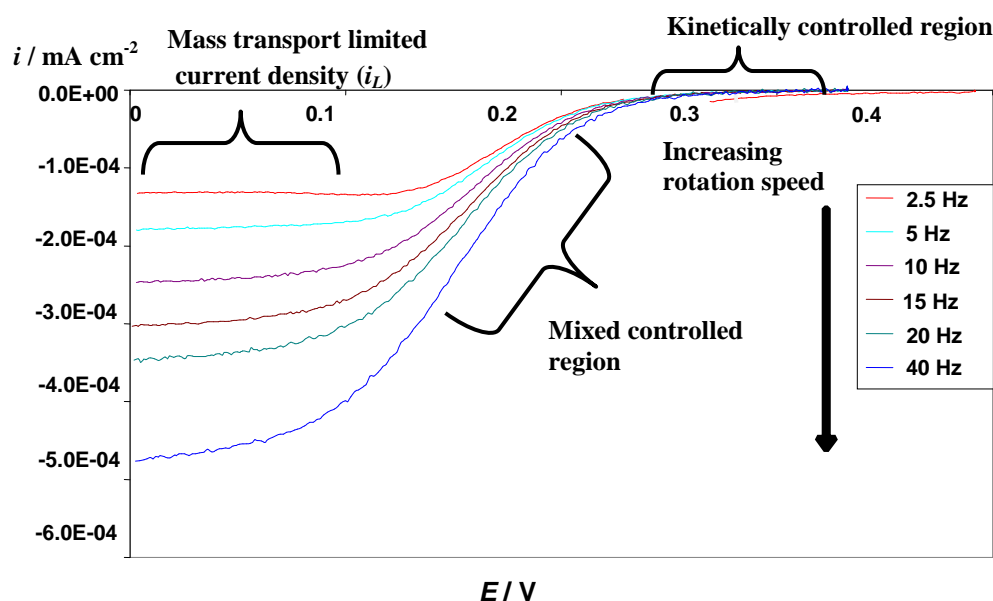


Fig.3.18: Cyclic voltammogram at various rotation rates in a solution consisting of $5 \times 10^{-3} \text{ mol dm}^{-3} \text{ K}_3\text{Fe}(\text{CN})_6$ in $1 \times 10^{-1} \text{ mol dm}^{-3} \text{ KCl}$ - 20 mV s^{-1} - 25° C - Pt electrode.

The equation relating the limiting current density (i_L) for an oxidation to the rotation rate is known as the *Levich* equation [20]. This equation applies to the mass transfer limited condition at the RDE and predicts that i_L is proportional to the concentration of species in bulk solution (C_∞) and to the square root of rotation rate ($\omega^{1/2}$).

$$i = 0.62nFD^{2/3}\nu^{-1/6}\omega^{1/2}C_\infty$$

Eq.3.38

The RDE can also be used to determine the kinetic parameters of an irreversible reaction at the electrode's surface. If the current density is entirely kinetically controlled (*i.e.* electron transfer), it will be independent of the rotation rate of the disk (Fig.3.18). If the reaction is mass transport controlled, the rate of the electrode reaction depends solely on the geometric area as only the species that are passing through a plane parallel to the surface will undergo a reaction.

3.5.2 Koutecky-Levich equation

The Koutecky-Levich equation is used under steady state mass transport regime conditions to calculate heterogeneous electron transfer rate constant (k_o) for the species of interest [21]. This is best done in the mixed control region for the current-voltage curve (Fig.3.18) *i.e* the current is under partial electron transfer and partial mass transport control. Thus by extrapolating the data here to infinite rate of mass transport the current becomes controlled solely by electron transfer and the rate constant can be determined. The rate constant for electron transfer can be calculated as a function of potential. Eq.3.39 describes the expression of the current density under mixed mass transport and kinetic control.

$$\frac{1}{i_L} = \left(\frac{1}{nFkC} + \frac{1}{0.62nFAD^{3/2}v^{1/6}C_\infty\omega^{1/2}} \right)$$

Eq.3.39

The intercept at $\frac{1}{\omega^{1/2}} = 0$ is the inverse of the current density at infinite rotation rate

and thus reflects only the kinetics of the electron transfer reaction. Hence, Eq.3.39 can be written as:

$$\frac{1}{i_L} = \left(\left(\frac{1}{i_k} \right) + \left(\frac{1}{0.62nFAD^{3/2}v^{1/6}C_\infty} \right) \right) \omega^{-1/2}$$

Eq.3.40

where k is the electron transfer rate constant at that potential and is determined as a function of the rotation rate according to Eq.3.41.

$$k = k^\circ \exp\left(-\frac{\alpha nFE}{RT}\right) \Leftrightarrow \ln k = \ln k^\circ - \frac{\alpha nFE}{RT}$$

Eq.3.41

By plotting i^{-1} versus $\omega^{-1/2}$, a line whose y-intercept is equal to i_k^{-1} and is extracted as shown in Fig.3.19 [22].

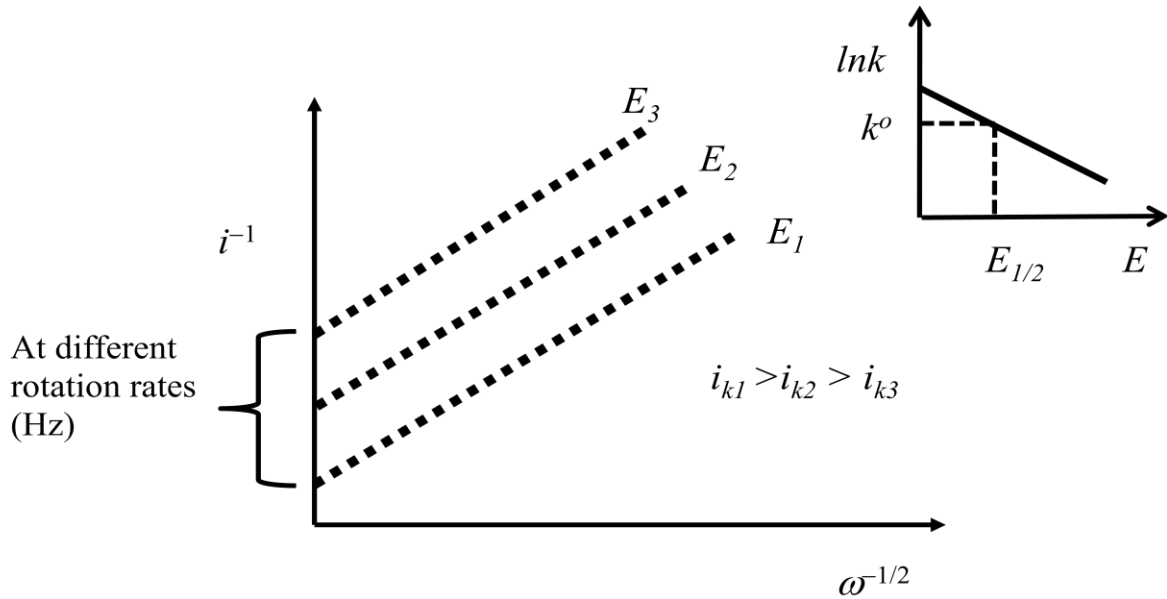


Fig.3.19: i^{-1} versus $\omega^{-1/2}$ plots as a function of potential for a rotating disk electrode.

From Fig.3.19 it can be seen that the slopes of the plots are independent of the potential and this can be used to evaluate the diffusion coefficient. When E is equal to E_1 , the reaction is very fast, *viz.* as the current density is larger. Hence, as the rotation rate tends to infinity, the current density equals to the limiting current density while i^{-1} tends to zero. At E_3 , the reaction is slower and therefore as the rotation rate increases, i^{-1} will equal to $i_k^{\circ -1}$ at high rates of mass transfer. i_k is the activation control current density. The intercepts are used to calculate the heterogeneous rate constant (k^0) for an electron transfer at each potential, *viz.* k^0 is at E^0 , when $E^0 \equiv E_{1/2}$ using the following equation:

$$\frac{1}{i_k^{\circ}} = \frac{1}{nFk^{\circ}C}$$

Eq.3.42

3.6 Galvanic Cycles - General remarks and methodology

A typical charge discharge curve involves the application of a set charge current over a certain amount of time. Then, during the discharge part of the cycle, a current of reverse polarity is introduced to discharge the system. A potential limit is usually set during discharge so that when this is reached (corresponding to a fully or nearly fully discharged system) then immediately another charge cycle commences. Exceeding the cut-off potential can significantly damage the electrodes in the cell and lead to gas evolution. The controlling parameters on the charge/discharge cycles are the current density, flow rate, temperature and electrolyte composition.

The charge discharge cycles on the zinc half cell reaction ($1.5 \text{ mol dm}^{-3} \text{ Zn(II)}$ in $5.7 \text{ mol dm}^{-3} \text{ CH}_3\text{SO}_3\text{H}$) are shown in Fig.3.20 for the BAC2 carbon based electrode while for the zinc cerium flow cell a graphical representation is shown in Fig.3.21. The open circuit potential (OCP) is the reversible potential of the zinc deposit in contact with the 1.5 mol dm^{-3} zinc (II) solution *viz.* $-1.44 \text{ V vs Hg|Hg}_2\text{SO}_4(\text{sat.})$.

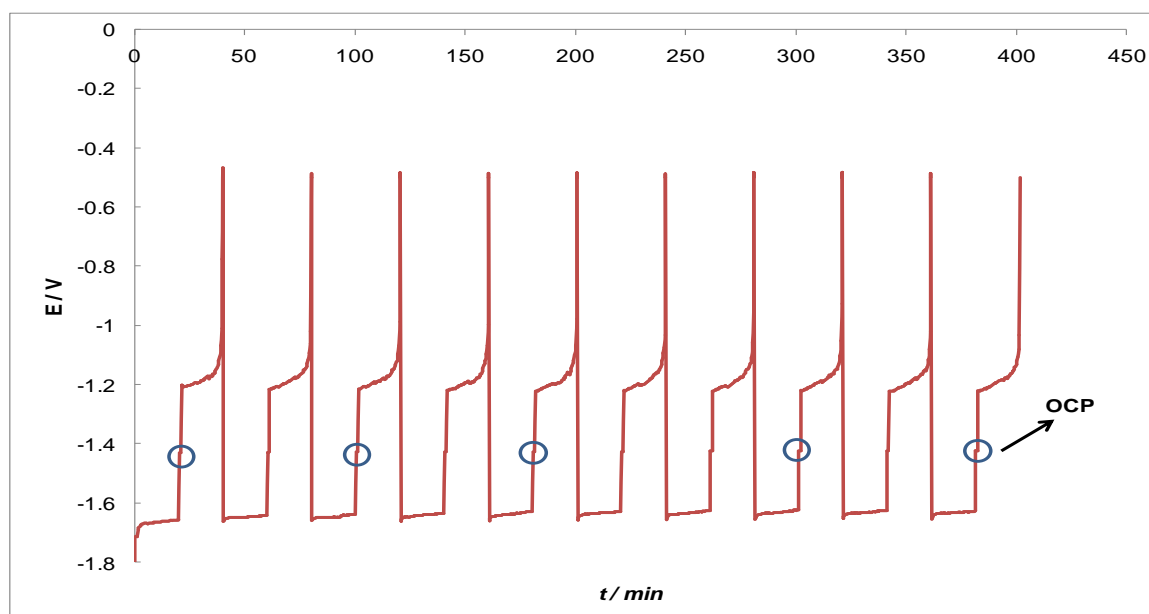


Fig.3.20: Voltage-time responses to galvanostatic charge/discharge cycles for the BAC2 electrode in $1.5 \text{ mol dm}^{-3} \text{ Zn(II)}$ & $5.7 \text{ mol dm}^{-3} \text{ CH}_3\text{SO}_3\text{H}$ at 30°C & 10 Hz . Charging time: 20 minutes at $\pm 50 \text{ mA cm}^{-2}$

During charging *viz.* electrodeposition of the zinc at the negative electrode, the potential decreased to -1.66 V and stayed there for the duration of the charging time. Then, the electrode was switched to open circuit (no current passing through the system) for a fixed amount of time prior to the application of the discharge current. When discharging at 50 mA cm^{-2} , the voltage falls immediately to a value of -1.18 V . This value increases slightly as the

zinc is anodically dissolved back into solution and when all the zinc is exhausted from the electrode surface, the potential quickly moves more positive to find another reaction but the cut-off potential is reached.

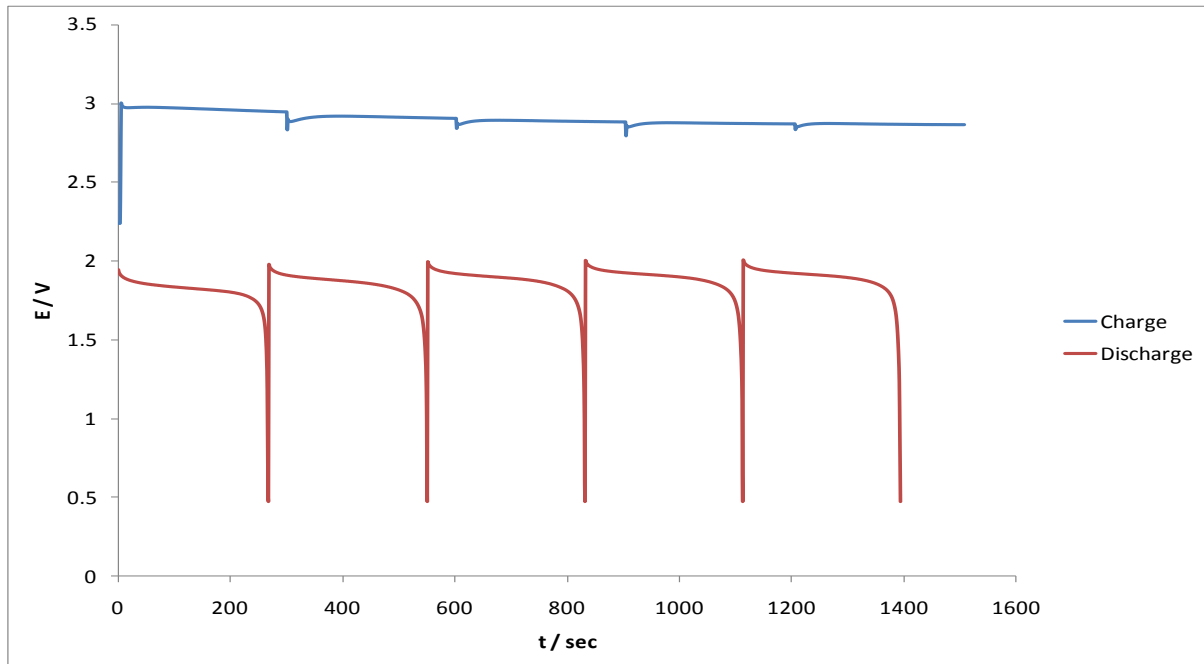


Fig.3.21: Voltage-time responses to galvanostatic charge/discharge cycles on $1.5 \text{ mol dm}^{-3} \text{ Zn(II)}$ and $5.7 \text{ mol dm}^{-3} \text{ CH}_3\text{SO}_3\text{H}$ on the negative side (polyvinyl ester carbon composite electrode) and $5.9 \times 10^{-1} \text{ mol dm}^{-3} \text{ Ce(IV)}$ $8 \times 10^{-1} \text{ mol dm}^{-3} \text{ Zn(II)}$ and $6.9 \text{ mol dm}^{-3} \text{ CH}_3\text{SO}_3\text{H}$ on the positive side (Pt-Ti mesh).

The coulombic efficiency (η_c) of each cycle on the flow cell is evaluated simply as the ratio of the anodic to cathodic charge while the voltage efficiency (η_v) is the ratio of the potential during charging over the potential during discharge.

$$\eta_c = \frac{Q \times t_{\text{discharge}}}{Q \times t_{\text{charge}}}$$

Eq.3.43

$$\eta_v = \frac{V_{\text{discharge}}}{V_{\text{charge}}}$$

Eq.3.44

The overall energy efficiency of the system (η_e) is simply the multiplication of the coulombic and voltage efficiencies during charge and discharge.

$$\eta_e = \frac{Q \times t_{\text{discharge}}}{Q \times t_{\text{charge}}} \times \left(\frac{V_{\text{discharge}}}{V_{\text{charge}}} \right) = \frac{E_{\text{discharge}}}{E_{\text{charge}}} = \frac{Q_C \times \eta_v \times t_{\text{discharge}}}{Q_C \times \eta_v \times t_{\text{charge}}}$$

Eq.3.45

3.7 Hydrogen evolution reaction

The study of the hydrogen evolution reaction (HER) has been central to the development of modern concepts of electrochemistry. It is an electrochemical process that has received wide attention due to its great importance in both fundamental and technological electrochemistry [23] [24]. Applications of the HER can be found in water electrolysis, the chlor-alkali industry [25] and in the fuel cell technologies [26]. Two criteria play an important role in selecting catalytically active materials for hydrogen evolution. The first one is the actual electrocatalytic effect of the material while the second one is its long-term stability. In some circumstances such as water electrolysis, a low overpotential is desirable while in others the inhibition of hydrogen evolution is essential. The latter, is the situation in the zinc cerium system.

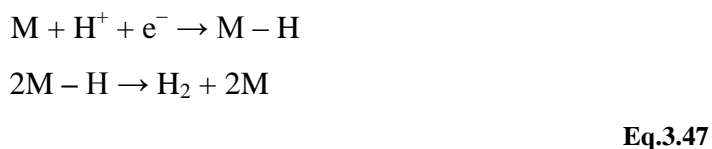
For the zinc-cerium flow cell, hydrogen evolution is a competing reaction during the electrodeposition of zinc. The standard potential of the hydrogen electrode is $E_{\text{H}}^{\circ} = 0$, while the standard potential of zinc is $-0.76 \text{ V vs S.H.E.}$ Hence, from a purely thermodynamic point of view, hydrogen evolution will always occur before any zinc deposition and this will be present during the zinc reduction reaction.

The overall hydrogen evolution reaction in an aqueous acid is represented simply by:

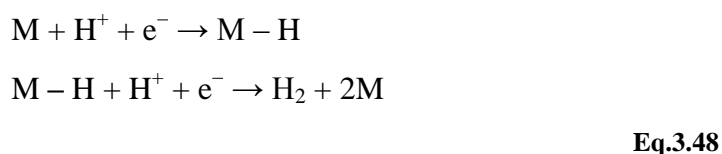


Two mechanisms outlined below I and II for the HER involving adsorbed hydrogen atoms, have been described. In both, an adsorbed hydrogen atom is first formed on the surface of a metal cathode (M) by the reduction of a single proton [17]. The key intermediate of the HER is the adsorbed hydrogen atom formed during the reaction.

Mechanism I (Volmer-Tafel) [27]:



Mechanism II (Volmer-Heyrovsky) [28]:



In each pathway, either the first or the second step can be the rate-determining step. Both pathways require the formation and then the cleavage of the M-H bonds. Mechanism *I* assumes that the formation of the adsorbed hydrogen atom is followed by the combination of two such entities and the release of hydrogen gas. In mechanism *II*, the second step involves the discharge of a proton at a surface site already covered by an adsorbed hydrogen atom. If the Gibbs free energy of adsorption is too small, the coverage of the adsorbed hydrogen atoms will be low, while if it is too large the first step will lead to the formation of a monolayer of adsorbed hydrogen atoms, which in turn will slow the second step. The extent of the reaction is limited by the number of sites available as only a monolayer of hydrogen atoms can be formed during the reaction. The number of sites and the Gibbs free energy of adsorption are determined by the cathode material as shown in Table 3.1 [29].

Metal	$-\log(i_o / \text{A cm}^{-2})$
Ag	5.4
Au	5.5
Cr	7.4
Cu	6.7
Hg	12.5
Ni	5.2
Pb	12.2
Pt	3.6
Rh	2.1
Zn	10.5

Table 3.1: Exchange current densities for the hydrogen evolution reaction in 1 mol dm⁻³ H₂SO₄ at 25°C.

3.8 Oxygen evolution reaction

Oxygen evolution and reduction reactions are of great importance in water electrolysis [30], fuel cells [31] and also in batteries using air cathodes [32]. For the zinc-cerium cell, the oxygen evolution could potentially take place during the oxidation of Ce(III) to Ce(IV) as the standard potential of the OER in acid solution (1.23 V vs *S.H.E*) is lower than the standard potential of the Ce(III)/Ce(IV) oxidation reaction (1.44 V vs *S.H.E*).

The OER is a significantly more complex reaction than the HER. The product can be hydrogen peroxide (H_2O_2), a two-electron reaction having a standard potential of 0.69 V vs *S.H.E* or water in a four electron reduction. The $4e^-$ reduction can occur through two types of pathways as illustrated in Fig.3.22. The first pathway involves formation of water where the O-O bond is cleaved early in the reaction sequence. Surface-oxygen bonds are formed simultaneously with weakening of the O-O bond. This pathway offers the best chance for effective electrocatalysis. The second pathway involves the formation of hydrogen peroxide as a discrete intermediate. In both cases, the equilibrium potential is determined by the $\text{O}_2/\text{H}_2\text{O}$ couple.

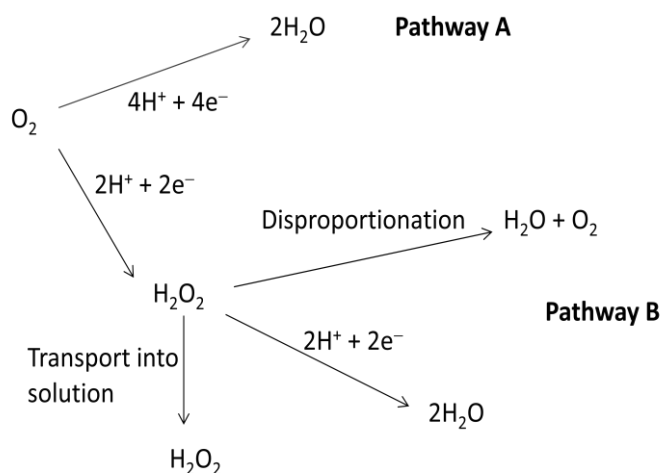


Fig.3.22: Reaction pathways for the reduction of oxygen in acid solution [17].

The exchange current densities for the oxygen evolution reaction on platinum and graphite electrodes in acid solutions *viz.* $1 \text{ mol dm}^{-3} \text{H}_2\text{SO}_4$ is *c.a.* $<10^{-7} \text{ mA cm}^{-2}$ [33] [34].

3.9 Scanning electron microscope

The scanning electron microscope (SEM) is a type of electron microscope that images the sample surface by scanning it with a high-energy beam of electrons. The electrons interact with the atoms that make up the sample producing signals that contain information about the sample's surface topography composition, electrical conductivity and deposit morphology. The types of signals produced by an SEM include secondary electrons, back scattered electrons, characteristic x-rays, specimen current and transmitted electrons [35].

The electron beam, which typically has an energy ranging from a few hundred eV to 40 keV is focused by one or two condenser lenses to a spot about 0.4 to 5 μm in diameter. The beam passes through pairs of scanning coils or pairs of deflector plates in the electron column, which deflect the beam in the x and y axes. Their function is to focus the beam to a spot and not to image the specimen [36]. Magnification between 10 and 10^5 times can be achieved allowing examination of areas as small as 100 nm.

For the zinc cerium RFB, the scanning electron microscope will provide valuable information about the zinc morphology on the various working carbon based electrodes investigated. Features such as dendritic and nodular growth, grain size and zinc adhesion can be determined by the SEM analysis. A diagram of the main components of the SEM instrument is given in Fig.3.23.

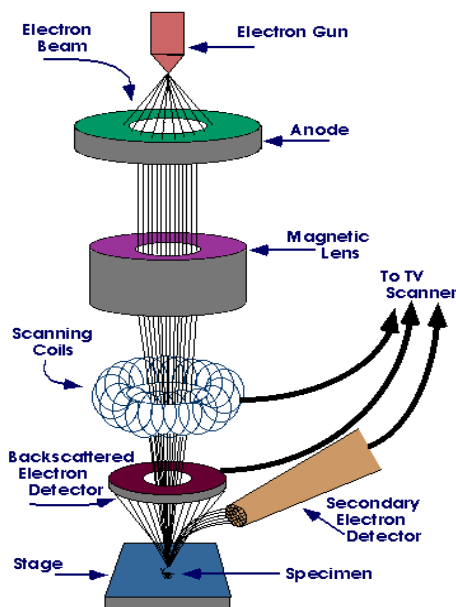


Fig.3.23: Scanning Electron Microscope Schematic [37].

3.10 Thermogravimetric analysis

Thermogravimetric analysis (TGA) is a widely used thermal analytical method for determining changes in the mass of the material with relation to change with temperature. It involves a high degree of precision in mass and temperature change. It is extensively employed in testing and measuring the characteristics of materials such as polymers. These characteristics include degradation temperature, absorbed moisture content of materials, solvent residues and also the level of organic and inorganic components in material can be determined [38]. The analyzer consists of a high-precision balance with a pan made of platinum loaded with the sample. The latter is placed in a small electrically heated oven with a thermocouple to accurately record the temperature. In some cases, the atmosphere is purged with inert gas so as to prevent oxidation or other undesired reaction. A TGA thermal curve is displayed from the left to right in Fig.3.24. The x -axis represents either time or temperature while in the y -axis the mass (mg) or mass percent (%) is displayed. The curve of Fig.3.24 shows the Ce(III) carbonate weight loss that occurs on heating to 250°C, depicting loss of water crystallization from the sample. This allows the number of moles of water of crystallization in the compound to be evaluated. A more in-depth investigation of the thermal decomposition of the cerium (III) carbonate is given by Padeste *et al.* [39].

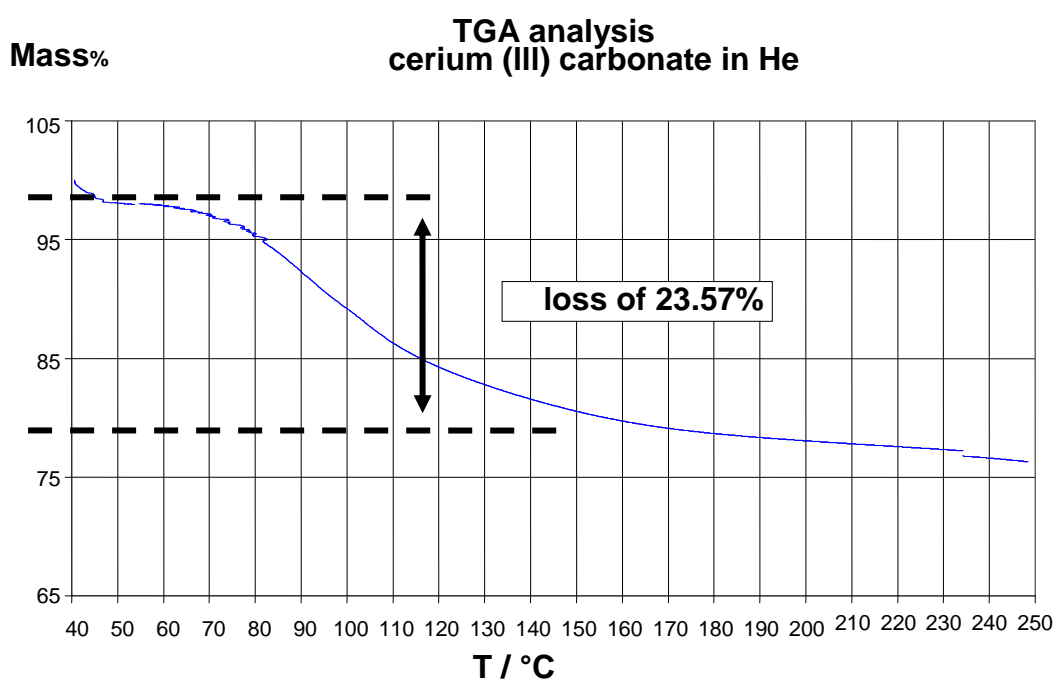


Fig.3.24: Thermal decomposition of $\text{Ce}_2(\text{CO}_3)_3 \cdot x\text{H}_2\text{O}$; heating rate: 10 K min^{-1} .

3.11 ICP-MS

ICP - MS (inductively couple plasma - mass spectroscopy) is considered as the method of choice for elemental speciation due to the fact that it can attain low detection limits, give isotope information and finally, achieve multi-element capacity [40] [41] [42] [43]. Compared to other atomic absorption techniques, ICP-MS has greater speed, precision and sensitivity.

ICP-MS separates and measures ultra-trace levels of metals and organo-metallic compounds at concentration below one part per 10^{12} (ppt). An ICP is plasma that holds a sufficient concentration of ions and electrons to make gas electrically conductive. It is sustained in a torch that consists of three concentric tubes which are made of quartz. The end of the torch is placed inside an induction coil supplied with radio-frequency electric current. The torch consists of a set of three concentric tubes. A flow of argon gas is introduced between the two outermost tubes of the torch while an electric spark is introduced to supply free electrons into the gas stream. These electrons are accelerated and collide with the argon atoms while the temperature of the plasma reaches 10.000 K. Due to the high temperatures occurring in the plasma each atom losing its most loosely-bound electron to form a singly charged ion. Focused by an ion lens system, analyte isotopes are separated according to their mass/charge ratio by either a quadrupole or magnetic sector mass analyzer. The ion detection and counting system of an electron multiplier use in a dual-gain pulse counting mode or low gain analog mode depending on the ion beam intensity.

For the zinc cerium flow cell, the ICP MS was used in to verify the concentrations of the Ce(III)/Ce(IV) concentrations in the solution prepared and obtained from Plurion Ltd.

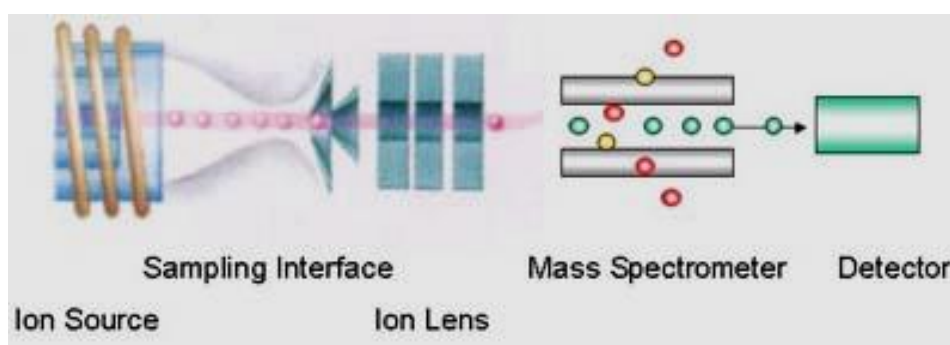


Fig.3.25: ICP-MS structure [44].

-
- [1] A.J. Bard, L.R. Faulkner, *Electrochemical Methods: Fundamentals and Applications*, 2nd Edition, John Wiley & Sons, pp 26, 99, (2001).
- [2] Thermo Fisher Scientific Ltd., Russell Electrode, Operating and maintenance data
- [3] J.A.V. Butler, *Trans. Faraday Soc.*, **19**,734, (1924).
- [4] M. Stern, A.L. Geary, *J. Electrochem. Soc.*, **104**, 1, 56, (1957).
- [5] A. Fick, *Phil. Mag.*, **10**, 30, (1855).
- [6] A.J. Bard, L.R. Faulkner, *Electrochemical Methods: Fundamentals and Applications*. New York, John Wiley & Sons, pp. 91-95, 291-298, 539-540, (1980).
- [7] Southampton Electrochemistry Group, *Instrumental Methods in Electrochemistry*. Ellis Horwood Series in Physical Chemistry, 2nd Edition, pp.23, 33, 121-126, (1990).
- [8] R.S. Nicholson, I. Shain, *Anal. Chem.*, **36**, 706, (1964).
- [9] R.S. Nicholson, *Anal. Chem.*, **37**, 1351, (1964).
- [10] K.A. Connors, *Chemical Kinetics, the study of reaction rates in solution*, VCH Publishers, (1991).
- [11] B.R. Scharifker, G.J. Hills, *Electrochim. Acta.*, **28**, 879, (1983).
- [12] J.O.M. Bockris, G.A. Razumney. *Fundamental Aspects of Electrocrystallization*, Plenum Press, New York, (1967).
- [13] B.R. Scharifker, J. Mostavy, *J. Electroanal. Chem.*, **177**, 13-23, (1984).
- [14] G. Gunawardena, G. Hills, I. Montenegro, B. Scharifker, *J. Electrochem. Soc.*, **138**, 225, (1982).
- [15] A. Softer, *J. Electroanal. Chem.*, **40**, 153, (1972).
- [16] K.B. Oldham, *J. Electroanal. Chemistry.*, **613**, 131-138, (2008).
- [17] D. Pletcher. *A first Course in Electrode Process*. The Electrochemical Consultancy, 139-140, (1991).
- [18] V.G. Levich, *Physicochemical Hydrodynamics.*, Prentice Hall, (1962).
- [19] G.L. Flynn, S.H. Yalkowsky, T.J. Roseman, *J. Pharm. Sci.*, **63**, (4), 479-510, (1974).
- [20] D.P. Gregory, A.C. Riddiford, *J. Chem. Soc.*, 3756, (1956).
- [21] J. Koutecky, V.G. Levich, *Zh. Fiz. Khim.*, **32**, 1565, (1956).
- [22] Z. Rongfeng, D.H. Evans, *J. Electroanal. Chem.*, **201**, 385, (1995).
- [23] R. Parsons, *Trans. Faraday Soc.*, **56**, 1340-1350, (1960).
- [24] R. Parsons, *Trans. Faraday Soc.*, **54**, 1053, (1958).
- [25] H. Zheng, J.Huang, W. Wang, C. Ma, *Electrochem. Commun.*, 7, 1045-1049, (2005).

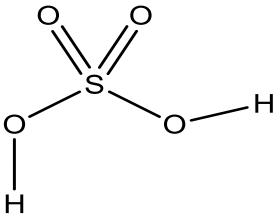
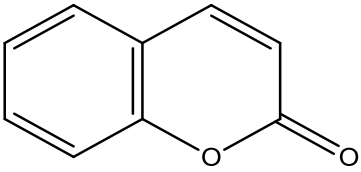
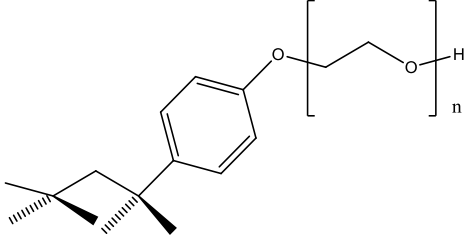
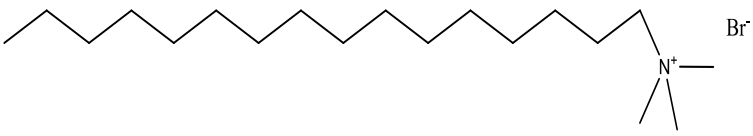
-
- [26] B. Sorensen. *Hydrogen and fuel cells, Emerging technologies and applications*, Elsevier Academic Press, pp.77, 113-151, (2005).
- [27] M.C. Tavares, S.A.S. Machado, L.H. Mazo, *Electrochim. Acta.*, **46**, 4359-4369, (2001).
- [28] B.E. Cornway, M. Salomon, *Electrochim. Acta.*, **9**, 1599, (1964).
- [29] A.J. Appleby, M. Chemla, H. Kita, G. Bronoel, *Encyclopedia of the Electrochemistry of the Elements*, Volume IXA, Edited by A.J. Bard, Marcel, Dekker, New York, pp. 383, (1982)
- [30] M.E.G. Lyons, M.P. Brandon, *Int. J. Electrochem. Sci.*, **3**, 1386-1424, (2008).
- [31] Y. Liang, Y. Li, H. Wang, J. Zhou, J. Wang, T. Regier, H. Dai, *Nature Materials.*, **10**, 780-786, (2011).
- [32] A.T. Marshall, S. Sunde, M. Tsyppkin, R. Tunold, *Int. J. Hydrogen Energy.*, **32**, 2320-2324, (2007).
- [33] A. Damjanovic, A.Dey, J.O.M. Bockris, *Electrochim. Acta.*, **11**, 7, 791-814, (1966).
- [34] S.M. Lipka, G.L. Cahen Jr, G.E. Stoner, L.L. Scribner Jr, E. Gileadi, *Electrochim. Acta.*, **33**, 6, 753-760, (1988).
- [35] M. Von Ardenne. Improvements in electron microscopes. GB patent 511204, Germany, 18 Feb 1937.
- [36] J. Tunncliffe, S.J.C. Irvine, O.D. Dosser, J.B. Mullin, *J. Cryst. Growth.*, **68**, 245, (1984).
- [37] <http://www.purdue.edu/REM/rs/sem.htm> assessed Nov. (2011).
- [38] E. Mansfield, A. Kar, T.P. Quinn, S.A. Hooker, *Anal. Chem.*, **82**, 24, (2010).
- [39] C. Padeste, N.W. Cant, D.L. Trimm, *Catalysis Letters.*, **24**, 95-105, (1994).
- [40] Harris, C. Daniel, *Gas Chromatography, Quantitative chemical analysis*, 5th edition, W. H. Freeman & Company, pp. 675-712, (1999).
- [41] L. Donald, G.M. Lampman, G.S. Kritz, G. Engel, *Introduction to Organic Laboratory Techniques* (4th edition.). Thomson Brooks/Cole. pp. 797-817, (2006).
- [42] <http://www.speciation.net/Public/Document/2007/08/11/2930.html> assessed Sept. (2011).
- [43] G.K. Zoorob, J.W. McKiernan, J.A. Caruso, *Microchim. Acta.*, **124**, 145-168, (1998).
- [44] http://www.siint.com/en/products/icp/tec_descriptions/descriptions2_e.html assessed December 2011.

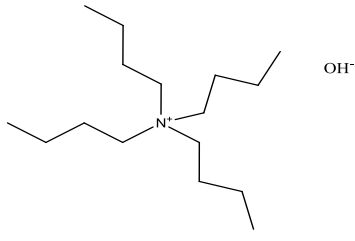
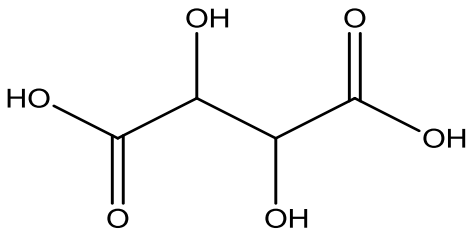
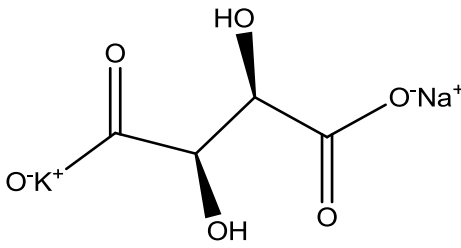
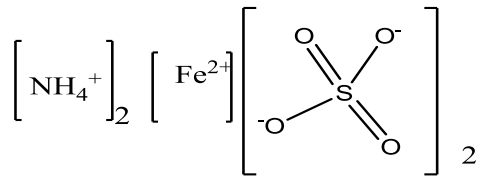
Chapter 4

4.1 Chemical reagents

All chemicals reagents shown in Fig.4.1 were used as received from the supplier without further purification. All solutions were prepared using Milli-Q deionised water (resistivity: $18.2 \text{ M}\Omega \text{ cm}^{-1}$ at 25°C) [1].

Chemical reagents	Comment	Supplier
Zinc Oxide	99.5 % purity Molecular mass = 81.39 g mol^{-1}	Fisher Chemicals [2]
Cerium (III) carbonate	$\text{Ce}_2(\text{CO}_3)_3 \cdot 5\text{H}_2\text{O}$, 99.9 % purity Molecular mass = 550 g mol^{-1}	Sigma Aldrich [3]
Cerium (III) carbonate	$\text{Ce}_2(\text{CO}_3)_3 \cdot 4\text{H}_2\text{O}$, 98 % purity Molecular mass = 532 g mol^{-1}	Zibo Jiahua Advanced Material Resources Co. Ltd.
Cerium (IV) sulfate	$\text{Ce}_2(\text{SO}_4)_2 \cdot x \text{H}_2\text{O}$, 99.5 % purity Molecular mass = $332.24 \text{ g mol}^{-1}$	WVR [4]
Sodium carbonate 10-hydrate		
	$\text{Na}_2\text{CO}_3 \cdot 10 \text{H}_2\text{O}$, 99.8 % purity Molecular mass = $105.99 \text{ g mol}^{-1}$	Fisher Chemicals [2]
Methanesulfonic acid		
	$\text{CH}_3\text{SO}_3\text{H}$, 70 vol. % Molecular mass = 96.1 g mol^{-1}	Lutropur® BASF [5] Alfa Aesar [6]

Sulfuric Acid		
	H_2SO_4 , 97 % purity Molecular mass = 98.07 g mol^{-1}	Sigma-Aldrich [3]
Coumarin		
	$\text{C}_9\text{H}_6\text{O}_2$ Molecular mass = $146.15 \text{ g mol}^{-1}$	Sigma-Aldrich [3]
Triton X-100		
	$\text{C}_{14}\text{H}_{22}\text{O}(\text{C}_2\text{H}_4\text{O})_n$ (n=9-10) $\rho = 1.07 \text{ g cm}^{-3}$	Sigma-Aldrich [3]
Cetyltrimethyl- ammonium bromide (CTABr)		
	$\text{C}_{19}\text{H}_{42}\text{BrN}$, 99.5 % purity Molecular mass = 364.5 g mol^{-1}	Sigma-Aldrich [3]

Tetrabutyl-ammonium hydroxide (TBAOH)		
	$C_{16}H_{37}NO$ Puriss. 1 mol dm ⁻³ in water Molecular mass = 259.48 g mol ⁻¹	Sigma-Aldrich [3]
Tartaric acid		
	$C_4H_6O_6$, 99.5 % purity Molecular mass = 150.09 g mol ⁻¹	WVR [7]
Potassium sodium tartarate		
	$KNaC_4H_4O_6 \cdot 4H_2O$, 99% Molecular mass = 282.23 g mol ⁻¹	Fisons [8]
Indium oxide	In_2O_3 99.995 % purity (metal basis) Molecular mass = 277.64 g mol ⁻¹	Alfa Aesar [6]
Ammonium Ferrous Sulfate		
	$(NH_4)_2Fe(SO_4)_2 \cdot 6H_2O$, 98 % purity Molecular mass = 392.14 g mol ⁻¹	Fisons [8]

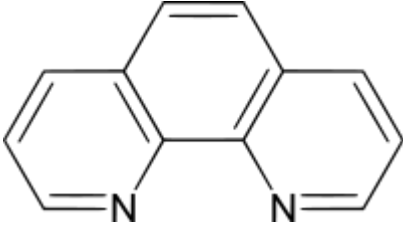
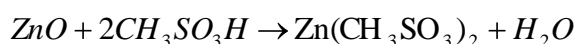
1,10 Phenanthroline		
	$C_{12}H_{10}N_2O$ Molecular mass = 198.22 g mol ⁻¹	
Iron (II) sulfate	$FeSO_4 \cdot 7H_2O$, Assay 98 % min Molecular mass = 278.02 g mol ⁻¹	Fisons [8]
Iso-Propanol	C_3H_8O , > 99.5 % purity Molecular mass = 60.03 g mol ⁻¹	Sigma-Aldrich [3]
Acetone	C_3H_6O , > 99 % purity Molecular mass = 58.03 g mol ⁻¹	Sigma-Aldrich [3]
Polishing powder	0.3 μm Al ₂ O ₃	Buehler [9]
Polishing cloth	10' microcloth PSA	Buehler [9]
Nitrogen (oxygen free)	99.99 % purity	BOC Gases [10]

Table 4.1: List of chemical reagents and their suppliers.

4.2 Zinc and cerium electrolytes

Since there were no commercial available salts for electroactive species of zinc and cerium for the flow battery, the cerium and zinc methanesulfonate solutions were prepared by stirring the metal carbonate and oxide respectively, in deionized water and then adding concentrated methanesulfonic acid to convert the carbonate and oxide into methanesulfonate salts via the following reactions R.4.1 and R.4.2 correspondingly.

Zinc (II) methanesulfonate



R.4.1

Cerium (III) methanesulfonate



R.4.2

According to R.4.1, one mole of zinc oxide reacts with two moles of methanesulfonic acid to produce two moles of zinc methanesulfonate. For the preparation of 250 mL of 1.5 mol dm⁻³ zinc methanesulfonate the following procedure was used:

1. 30.375 g of zinc carbonate was added into 80 mL deionized water (composing of 90% of the total water content for the solution *i.e* 71 mL).
2. 159.8 mL of methanesulfonic acid was added to the solution with continuous stirring.
3. Upon completely dissolution, the remaining amount of deionized water was added (9 mL).

From R.4.2, the stoichiometry indicates that one mole of cerium carbonate requires 6 moles of methanesulfonic acid to make two moles of cerium methanesulfonate releasing three moles of carbon dioxide and three moles of water. The exact amount of water content in the cerium carbonate and hence the exact molecular weight was determined from Thermogravimetric analysis (TGA 7 Perkin Elemer), as described in Chapter 3, Section 3.10. For the preparation of 250 mL of the 8×10^{-1} mol dm⁻³ cerium methanesulfonate, the following procedure was carried out:

1. 64.92 g of cerium (III) carbonate was added into 80 mL deionized water (90% of the total water content).
2. 159.8 mL of methanesulfonic acid was added into the solution with continuous stirring at 40°C.

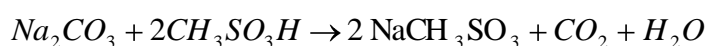
3. As the reaction produced CO₂, the addition was carefully controlled so that there was no loss of reactants. The remaining deionized water (8 MI) was added to the solution.

For the case where the electrolyte compositions contained both cerium and zinc species *viz.* mixed electrolytes (*e.g.* $5 \times 10^{-1} \text{ mol dm}^{-3}$ Ce(III), 1.5 mol dm^{-3} Zn(II) and 3 mol dm^{-3} CH₃SO₃H) the following procedure was carried out.

1. 90% of the required deionized water (*viz.* 80 MI) was placed in a flask containing a Teflon stir bar.
2. The cerium (III) carbonate was added to the flask with stirring.
3. From 40%-50% of the methanesulfonic acid was slowly added, giving time for the solution to evolve carbon dioxide, without overflowing the flask.
4. The addition of the methanesulfonic acid was stopped when further gas evolution was found from the solution.
5. The zinc oxide was added in 4 to 5 portions each time followed by methanesulfonic acid addition. The solution temperature did not exceed 45°C in order to avoid CeO₂ precipitation. The remaining 10% of the required water was added.
6. Stirring was maintained until all the cerium (III) carbonate was completely dissolved.

4.2.1 Sodium methanesulfonate solutions

Sodium methanesulfonate was prepared by stirring the sodium carbonate in deionized water and then adding the concentrated methanesulfonic acid.



R.4.3

One mole of sodium carbonate reacts with two moles of methanesulfonic acid to give two moles of sodium methanesulfonate, 1 mole of carbon dioxide and 1 mole of water. For the preparation of the 250 ml of 1.5 mol dm^{-3} sodium methanesulfonate the following procedure was used:

1. 86.3 g of sodium carbonate was added to 200 mL of deionized water.
2. This was then titrated using 114.9 mL of methanesulfonic acid (9 mol dm^{-3}) into the solution with continuous stirring.
3. Add the remaining deionized water to make-up the volume to 250 mL.
4. Check the pH of the solution.

4.3 Carbon composite materials for the zinc-cerium RFB

The carbon composite materials used in both negative and in some trials for the positive half cell reactions of the zinc cerium cell are presented in Table 4.2. The majority of these materials are widely used in the PEM fuel cells [11].

Carbon composite material	Comment	Supplier
BMA5 (PVDF)	Polyvinylidene difluoride (Fluoro polymer) 3-5 mm thickness - Bulk density: 2.1 g m^{-3} Thermal conductivity through plane: $20 \text{ W m}^{-1} \text{ K}^{-1}$ Permeability coefficient: $10^{-5} \text{ cm}^2 \text{ s}^{-1}$	SGL Carbon GmbH [12] [13]
BMA5 PVDF oxidised*	Polyvinylidene difluoride 3-5 mm thickness	SGL Carbon GmbH [12] [13]
PE20	20 w% Polyvinylidene difluoride, cured 1 mm thickness - Bulk density: 1.85 g m^{-3} Thermal conductivity through plane: $14 \text{ W m}^{-1} \text{ K}^{-1}$ Permeability coefficient: $7 \times 10^{-6} \text{ cm}^2 \text{ s}^{-1}$	SGL Carbon GmbH [12] [13]
Carbon Foil	Resin Formulation TF4 - 1 mm thickness Thermal conductivity through plane: $23 \text{ W m}^{-1} \text{ K}^{-1}$ Permeability coefficient: $5 \times 10^{-6} \text{ cm}^2 \text{ s}^{-1}$	SGL Carbon GmbH [12] [13]
PVE	Polyvinyl ester - 3-5 mm thickness Thermal conductivity through plane: $18.5 \text{ W m}^{-1} \text{ K}^{-1}$ Diffusivity: $1.15 \times 10^{-1} \text{ cm}^2 \text{ s}^{-1}$ Specific heat through plane: $8 \times 10^{-1} \text{ J g}^{-1} \text{ K}^{-1}$	Entegris Inc. [14] [15]
PVE Roughened**	Polyvinyl ester - 3-5 mm thickness	Entegris Inc. [14] [15]
HDPE-1	Uncured High density polyethylene - 1 mm thickness Thermal conductivity through plane: $20 \text{ W m}^{-1} \text{ K}^{-1}$ Permeability coefficient: $8 \times 10^{-6} \text{ cm}^2 \text{ s}^{-1}$ Bulk density: 1.97 g m^{-3}	SGL Carbon GmbH [12] [13]

HDPE-2	High density polyethylene - 3-5 mm thickness	GE [16]
BAC2	Conductive polymer - acid-cure version (10-20% carbon)	Bac2 Ltd. [17]
Glassy carbon	Non-graphitizing carbon Density: 1.45 g m ⁻³	Alfa Aesar [18] [19]

Table 4.2: Carbon composite materials used for the negative side of the zinc cerium RFB.

*: Same properties as PVDF BMA5

** : Same properties as PVE

Aside from the glassy carbon, the composite materials have been made using thermoplastic (poly(vinylidene difluoride), high density polyethylene) or thermosetting resins (epoxies and vinyl esters (chemical formula: [RCOOCHCH₂])). A detailed study on the effect of vinyl ester resins on expanded graphite is given by Fu *et al.* [20] while the electrical properties of the poly(vinylidene difluoride) were investigated by Cunningham *et al.* [21], Del Rio *et al.* [22] and Chunhui *et al.* [23]. The BAC2 electrode is made from organic polymers (*i.e* either polyacetylene or polypyrrole). The key material properties of such electrodes include chemical resistance, good electrical conductivity, compactness, durability and mechanical strength. Some of the electrodes had been treated further (anodized, roughened) in order to enhance the properties of the carbons such as acid resistance and surface porosity. The electrical resistance of the carbon composite materials was reported to be measured between $5 \times 10^{-1} \Omega \text{ cm}$ and $8 \times 10^{-1} \Omega \text{ cm}$ [13][15] [17].

For the electrochemical studies, these materials were cut into cylinders of suitable diameter (7 mm) which could be mounted using electrically conducting paint (silver conducting paint (RS 186-36000)) onto an Oxford Electrodes[®] rotating disc electrode set up (Fig.4.1) and sealed with a glue resin (Loctite 3430 A+B Hysol[®]) so as to prevent any unwanted contact of the solution with the support. The surface of the carbon composites was rinsed with ethanol prior to use and dried in an air stream, while care was also taken to ensure that the samples did not suffer any mechanical damage to the exposed surface.

The glassy carbon electrode was used in order to compare the electrochemical behaviour of the composite materials with a standard electrode material (*i.e* glassy carbon). It is a non-graphitizing carbon that combines the glassy and ceramic properties of the graphite while in the same time shows similar conductivity values ($k_{\text{itreous carbon}} = 1 \times 10^2 \text{ S cm}^{-1}$ - $4 \times 10^2 \text{ S cm}^{-1}$ while $k_{\text{graphite}} = 2 \times 10^2 \text{ S cm}^{-1}$ - $20 \times 10^2 \text{ S cm}^{-1}$ [24]). The most relevant

properties here are extreme resistance to chemical attack and impermeability to gases and liquids. Mechanical polishing of the glassy carbon surface was carried out using a polishing cloth (Buehler) with 0.3 μm alumina powder (Buehler).



Fig.4.1: (a) Carbon composite sample electrodes - (b) mounted on a RDE holder.

A standard 3-electrode configuration was employed (Figure 3.1 Chapter 3) with a platinum gauze acting as the counter electrode, while the reference electrode was a $\text{Hg}|\text{Hg}_2\text{SO}_4|\text{K}_2\text{SO}_4(\text{sat.})$ (Russell pH Ltd.). The electrolyte was contained in a jacketed cell which enabled its temperature to be controlled ($\pm 2^\circ\text{C}$) by means of a thermostated water bath (Gallenkamp thermostirrer 95).

The cyclic voltammograms and galvanic cycles were carried out using an EG & G M100A Potentiostat/Galvanostat controlled by custom written software in LabVIEW. A 1286 Electrochemical Interface, Solatron Instruments, Schlumberger Ltd., controlled by the Corrware[®] software (Corrware electrochemistry, Schribner Associates, Inc [25]) was also used for the measurements. Both systems were also employed for examining charge and discharge efficiencies for the zinc half-cell reaction. The morphology of the zinc electrodeposits was examined using a scanning electron microscopy (Cambridge Instruments Spectroscan 90) while the morphology of the composite carbon surfaces following repeated cycling was monitored by an Olympus SZ-CTV optical microscope controlled by DP12[®] software.

4.3.1 Correlation of electrode rotation rate with Re for the electrodes used on the negative half cell reaction of the zinc cerium flow cell

The Re is given by [26] [27]:

$$Re = \frac{r^2 \omega}{\nu} \quad \text{Eq.4.1}$$

where:

ω : Angular velocity (Hz)

r_c : Radius of carbon electrodes viz. 7 mm = 7×10^{-3} m

f / Hz	Re
5	62
10	123
15	185
20	247
25	308
30	370

Table 4.3: Correlation between Re and electrode rotation speed for the electrodes used in the negative half cell reaction of the zinc-cerium system.

4.4 Pt based substrates for the positive side of the zinc cerium RFB

For the Ce(IV)/Ce(III) reaction at the positive side of the zinc cerium flow cell several platinum and platinum iridium based electrodes were tested as shown in Table 4.4. The calculation of the specific electrochemical area of the Pt and Pt-Ir substrates is shown in Section 4.4.1.

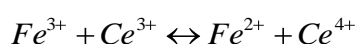
Substrate name	Description	Specific electrochemical area ($\text{cm}^2 \text{ Pt mg}^{-1}$ or $\text{cm}^2 \text{ Pt /Ir mg}^{-1}$)
BMM1	Pt Ir composition: 30/70 - 9.9 g Pt/Ir m^{-2} [375°C]	99
BMM2	Pt Ir composition: 50/50 - 9.25 g Pt/Ir m^{-2} [500°C]	92.5
BMM3	Pt Ir composition: 30/70 - 10 g Pt/Ir m^{-2} [375°C]	100
BMM4	Pt Ir composition: 50/50 - 10.23 g Pt/Ir m^{-2} [375°C]	102
BMM6	Pt Ir composition: 50/50 - 9.25 g Pt/Ir m^{-2} [500°C]	92.5
BMM11	Pt Ir composition: 30/70 - 10 g Pt/Ir m^{-2} [375°C]	100
BMM12	Pt Ir composition: 50/50 - 10 g Pt/Ir m^{-2} [375°C]	100
BMM13	Pt Ir composition: 30/70 - 10 g Pt/Ir m^{-2} [375°C]	100
BMM14	Pt Ir composition: 50/50 - 10 g Pt/Ir m^{-2} [375°C]	100
BMM15	Pt Ir composition: 30/70 - 10 g Pt/Ir m^{-2} [500°C]	100
Pt-Ti mesh	10 g Pt m^{-2}	100
SL1	5 g Pt m^{-2}	50
SL2	3 g Pt m^{-2}	30
SL3	(Etched) 5 g Pt m^{-2}	50
SL4	(Etched) 3 g Pt m^{-2}	30
SL5	(Sandblasted & etched) 3 g Pt m^{-2}	30
SL6	(Sandblasted & etched) 3 g Pt m^{-2}	30
SL7	(Sandblasted & etched) 3 g Pt m^{-2}	30

Table 4.4: Pt- based substrates for the positive side of the zinc cerium flow cell.

All the substrates employed in this study were supplied by Plurion Ltd. From Table 4.4 it can be seen that for the BMM series, the composition of the platinum and iridium as well as the temperature at which these electrodes were prepared, varied. The SL substrates had different platinum loadings as well as surface treatment *viz.* time of etching and/or sandblasting. Sandblasting involves the propelling of a stream of abrasive material against a surface under high pressure so as to roughen the surface. Etching is the process of utilizing a strong acid to cut into certain unprotected parts of the metal surface and so create a more roughened and active surface. For comparison purposes, a Pt disk electrode (Oxford Electrodes[®]) was used with an electrical conductivity of *ca.* $1 \times 10^5 \text{ S cm}^{-1}$ [24]. Mechanical polishing of its surface was carried out using a polishing cloth (Buehler) with $0.3 \mu\text{m}$ alumina powder (Buehler) prior to trials. Although no details of the Pt-Ti mesh were given, there are various ways of depositing Pt on a titanium support such as electrodeposition in hydrofluoric (HF) [28] or chloroplatinic acid (H_2PtCl_6) [29] [30] or by vacuum deposition techniques [31].

As with the electrodes used for the negative side of the zinc cerium flow cell, the materials were cut into squares of suitable dimensions ($1 \text{ cm} \times 1 \text{ cm}$) and mounted onto an Oxford Electrodes[®] rotating disc electrode using silver conductive paint (RS 186-3600) and araldite (Loctite 3430 A+B, Hysol[®]) to seal the mounted electrode. The cyclic voltammograms, polarisation resistance, Tafel, A.C. impedance and galvanic cycle measurements were conducted using the 1286 Electrochemical Interface, Solatron Instruments, Schlumberger Ltd., controlled by the Corrware[®] software and the Z-plot impedance software (Scribner Associates, Inc). In order to determine the electroactive surface area of the substrates listed in Table 4.4, cyclic voltammograms in 1 mol dm^{-3} sulfuric acid under nitrogen (BOC gases) were conducted and recorded by the EG & G M100A Potentiostat/Galvanostat.

The cerium (IV) concentration was monitored by colourimetric redox titration [32] apart from ICP-MS as mentioned previously. The indicator used to evaluate the Ce(IV) concentration, was a 1:10 phenanthroline-ferrous-sulfate complex solution, titrated against standardised ferrous ammonium sulfate according to R.4.4.



R.4.4

50 mL of the 1:10 phenanthroline-ferrous sulfate complex were made by adding 1 g of 1:10 phenanthroline hydrate and 4×10^{-1} g of iron (II) sulfate into 50 ml of sulfuric acid (1.5 mol dm^{-3}).

4.4.1 Determining the specific electrochemical area of the Pt and Pt/Ir electrodes

From Table 4.3, the Pt-Ti mesh substrate has a platinum loading of *ca.* 10 g m^{-2} .

Hence, converting g m^{-2} to mg cm^{-2} we get:

$$\frac{10 \times 10^3 \text{ mg}}{10^2 \times 10^2 \text{ cm}^2} = 1 \text{ mg / cm}^2$$

The electroactive platinum surface area of this electrode was determined by conducting cyclic voltammograms in 1 mol dm^{-3} sulfuric acid (The determination of the electroactive platinum or platinum/iridium surface areas of the substrates in Table 4.4 is discussed in detail in Chapter 6, Section 6.2). The electroactive platinum surface area for the Pt-Ti mesh was *ca.* 100 cm^2 . Therefore, the roughness factor can be determined.

$$\text{Roughness factor: } \frac{100 \text{ cm}^2}{1 \text{ cm}^2} = 100$$

Knowing the roughness factor, the specific electrochemical area was determined as it is simply the roughness factor multiplied by the loading of platinum of the electrode under investigation, in this case the platinised titanium mesh.

$$\text{Specific electrochemical area: } 100 \times \frac{1}{1 \text{ mg / cm}^2} = 100 \text{ cm}^2 \text{ Pt / mg}$$

For the samples containing platinum and iridium the same methodology was used but instead of platinum, the specific electrochemical area was measured in $\text{cm}^2 \text{ Pt-Ir mg}^{-1}$.

4.4.2 Correlation of electrode rotation rate with Re for the electrodes on the positive half cell reaction of the zinc cerium cell

From Eq.4.1 the correlation between Re and electrode rotation rate for the electrodes used in the cerium half cell reaction studied is shown in Table 4.5. In this case, the radius of the Pt and Pt-Ir electrodes (r_{Pt} / r_{Pt-Ir}) was *ca.* 1 mm = 1×10^{-3} m.

f / Hz	Re
5	114
10	227
15	341
20	454
25	568
30	681

Table 4.5: Correlation between Re and electrode rotation speed for the electrodes used in the positive half cell reaction of the zinc-cerium system.

4.5 Batch Cell

The batch reactor consisted of two ground glass joints (Quickfit Ltd.) separated by a Nafion[®] 117 membrane in the middle and kept in position by a spherical bracket (

Fig.4.2). Each side of the cell contained 250 mL of solution. The surface area of the negative side carbon electrodes tested was always set to 6 cm² while a platinized titanium mesh (10 g Pt m⁻²) with dimensions 10 cm × 1 cm was used for the positive side of the cell. Prior to each experiment, the surface of the carbon electrodes was rinsed with iso-propanol (Sigma Aldrich) and dried in an air stream. Throughout the trials, the solution was stirred by two IKA[®] mini magnetic stirrers pointed at '2' indicator. All batch cell experiments were conducted at room temperature (25°C).

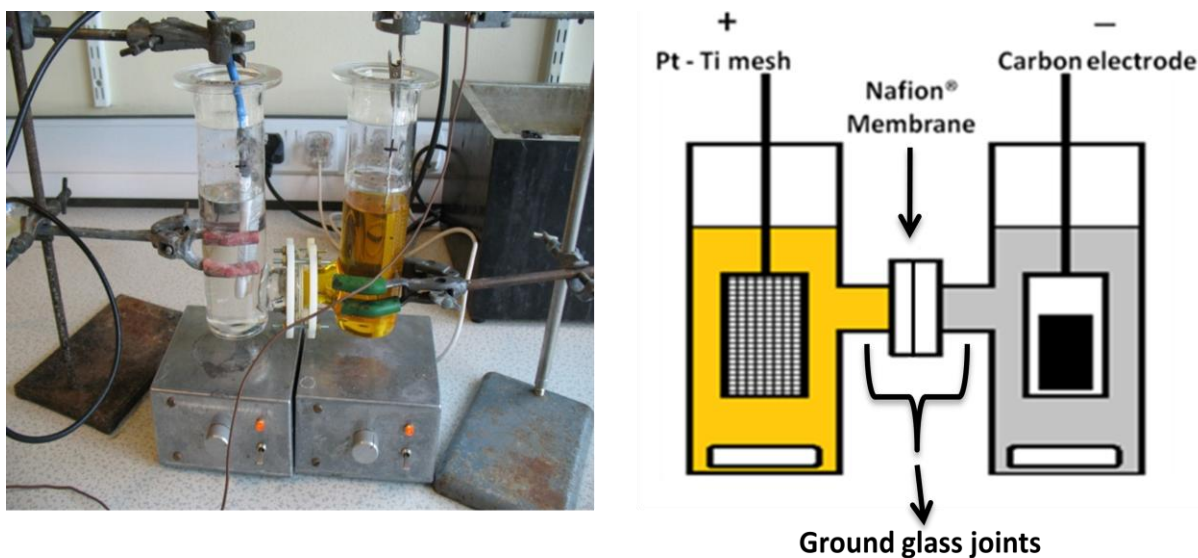


Fig.4.2: Picture and schematic of an experimental set up of the zinc cerium batch reactor.

The galvanic cycles were conducted by using either an EG & G M100A Potentiostat/Galvanostat, which was controlled by custom written software in LabVIEW and/or by the 1286 Electrochemical Interface controlled by the Corrware[®] software. Each charge discharge cycle involved the application of a constant charge and discharge current for a set amount of time.

4.6 Flow cell

Fig. 4.3 shows the various components of the half flow cell going from the outside parts of the cell to the centre of the plate (working electrode).

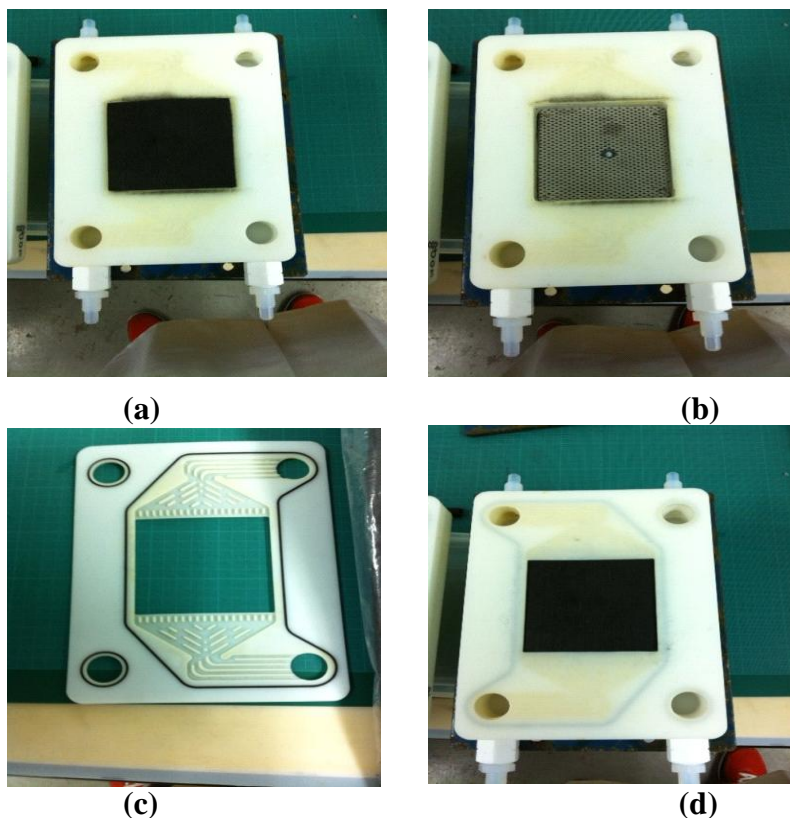


Fig.4.3: Pictures of (a) the negative side of the zinc cerium cell (carbon cloth), (b) the positive side (Pt-Ti mesh), (c) the flow field plate, (d) the flow field plate on top of the carbon cloth.

The plastic plate was acetyl polymer based (Fig.4.3 (a)). The gasket was used in order to maintain uniform pressure whilst putting all the components of the cell together and prevent leaks. It was ethylene propylene diene monomer (EPDM) based and it comes in various thicknesses depending on the thickness of the positive electrode. EPDM is a type of synthetic rubber, an elastomer with ethylene content between 45% and 75%. The higher the ethylene content the higher the loading possibilities of the polymer. The dienes (*viz.* hydrocarbons containing two double bonds) comprise from 2% to 15% by weight of the composition and serve as crosslinks when curing sulfur with resin [33]. The geometric dimensions of both positive and negative working electrodes were 10 cm \times 10 cm. The flow field plate gave the electrolyte a set flow pattern over the electrodes (Fig.4.3 (c)). It was made of the same material as the external plastic plates (EDPM). Similar pieces were used on the negative half-cell side and finally the metal plates were used in the final assembly (Fig.4.4 (d)) to compress the cell in order to prevent any leakage.

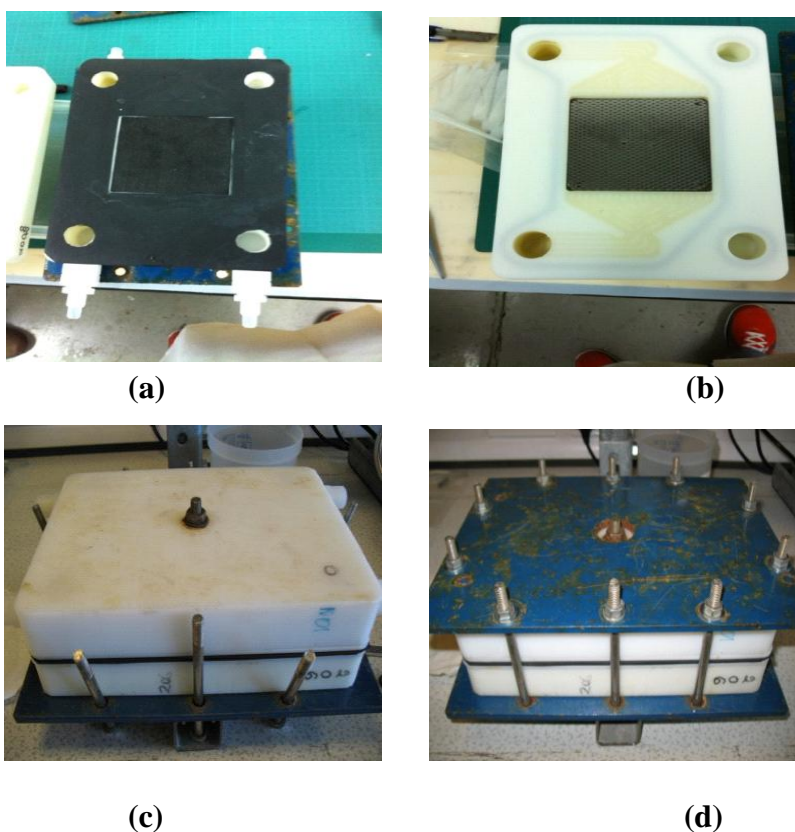


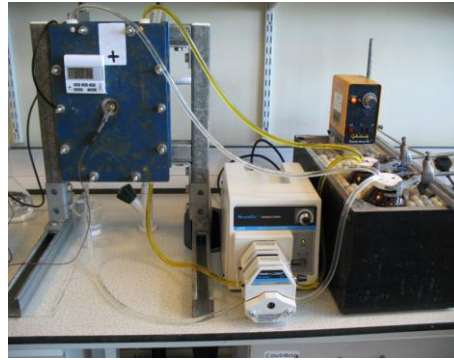
Fig.4.4: Pictures of (a) the gasket, (b) the flow field plate on top of the Pt-Ti mesh, (c) the cell without the metal plate, (d) the zinc cerium cell with the metal plates.

The membrane, which is hygroscopic, was placed on the top of the gasket to complete the half cell. The membrane used for the flow cell experiments was a Nafion[®] 117 membrane Dupont[®] [34]. Nafion[®] membranes consist of ionomers with a perfluorinated backbone such as Teflon. The equivalent weight was *ca.* 1100 g while the thickness was 175 μm [34]. The area resistance of the Nafion[®] 117 membrane was reported to be equal to $2.5 \times 10^{-1} \Omega \text{ cm}^2$ in $6 \times 10^{-1} \text{ mol dm}^{-3}$ KCl while the conductivity was *ca.* $7 \times 10^{-2} \text{ S cm}^{-1}$ [35].

A peristaltic pump (Masterflex[®]) was employed to flow the solutions into and out of the flow cell with the aid of Masterflex[®] precision tubing. The flow rate ranges employed are given in Chapter 7. Polyflon - PVDF straight male-female connectors were used to fit and connect the inlet/outlet ports to the electrolyte containers. Two 500 mL amber packer jars (FisherBrand) with a Teflon face lined cap were used as reservoirs for the flow cell. The operating temperature was controlled by a thermostated water bath (Gallenkamp thermostirrer 95) (Fig.4.5 (b)).



(a)



(b)

Fig.4.5: (a) Side view of the zinc cerium flow cell (b) flow cell during operation.

The charge discharge cycles were carried out using an EG & G M100A Potentiostat/Galvanostat controlled by custom written software in LabVIEW. For the application of higher charge currents (3 A) a power supply (Farnell Ltd.) was used.

4.6.1 Cell velocity of the zinc cerium flow cell

The characteristics of the zinc cerium flow cell used in this study are summarised in Table 4.6.

Symbol	Definition	Equation	Units
f	Flow velocity		cm s^{-1}
d	Cell gap		0.2 cm
ω	Cell width		10 cm
d_e	Equivalent diameter	$d_e = \frac{\omega d}{\omega + d}$ Eq.4.2	0.391 cm
CSA	Cross sectional area:	$CSA = \omega \times d$ Eq.4.3	2 cm^2
Q	Flow rate	$Q = \frac{f \times 1000 \times CSA}{60}$ Eq.4.4	L min^{-1}
Re	Reynolds number	$Re = \frac{\rho u d}{\mu} = \frac{d_e f}{\nu}$ Eq.4.5	

Table 4.6: Characteristics of the zinc cerium flow cell.

Prior to the conduction of the galvanic cycles at the flow cell, the peristaltic pump was first calibrated. Fig.4.6 shows the relationship of flow rate ($\text{cm}^3 \text{s}^{-1}$) to the pump “settings” viz. from 2 to 5. Hence, from the data of Fig.4.6 and of Table 4.6, the relationship between the flow rate (Q) and the flow velocity (f) with regards to the pump “settings” is shown in Table 4.7.

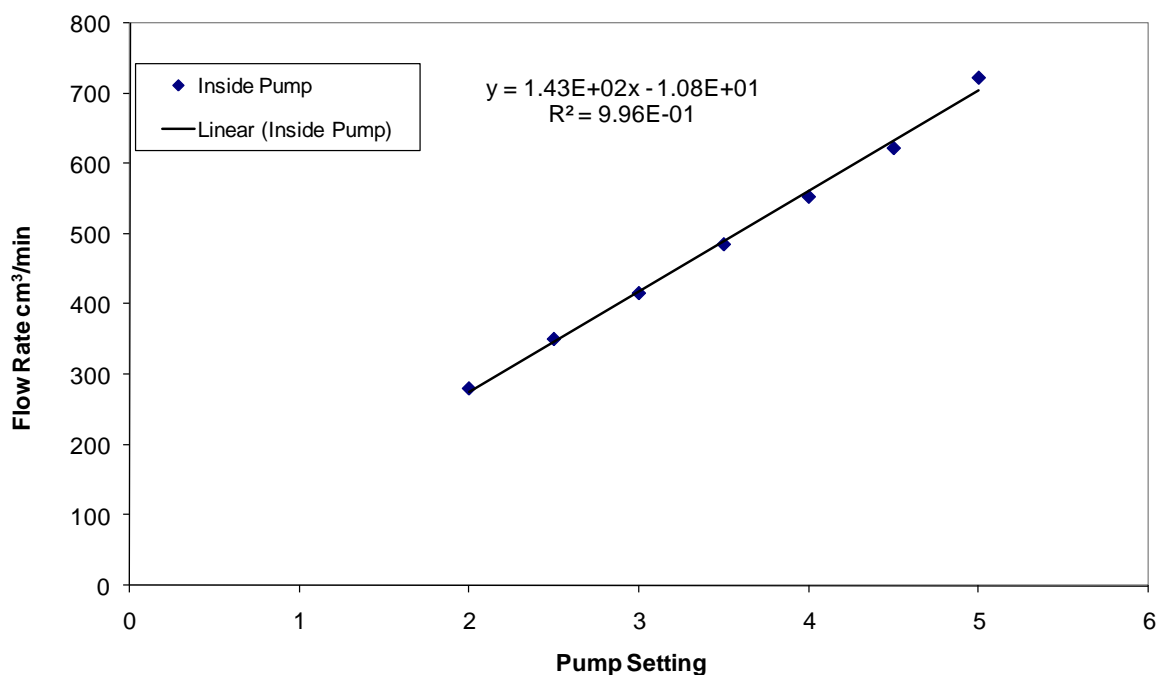


Fig.4.6: Calibration of peristaltic pump used in the zinc cerium flow cell.

Setting in peristaltic pump	$Q / \text{cm}^3 \text{min}^{-1}$	$f / \text{cm s}^{-1}$	Re
2	280	2.5	25
2.5	350	5	49
3	416	7.5	75
3.5	485	10	99
4	552	12.5	124
4.5	631	15	148
5	701	17.5	172

Table 4.7: Correlation between flow velocity, flow rate and Re for the zinc cerium RFB.

4.7 Undivided zinc-cerium redox cell

Fig.4.7 shows the apparatus used in the undivided cell experiment. The surface area of the carbon electrodes used for the negative side was 6 cm^2 and held in place at a distance less than 20 mm from the positive side where a $10\text{ cm} \times 1\text{ cm}$ platinized titanium mesh (10 g Pt m^{-2}) was used. The electrodes used for both sides of the cell were rinsed with iso-propanol prior to experimentation and dried in an air stream. For each experiment, 400 ml of electrolyte was placed in the batch cell. The bath solution was stirred and heated by an IKA RCT hot plate thermostat. The PTFE-coated (Fisherband, UK, 1 cm diameter, 3 cm length) magnetic stirrer pointed between '3 and 4'.

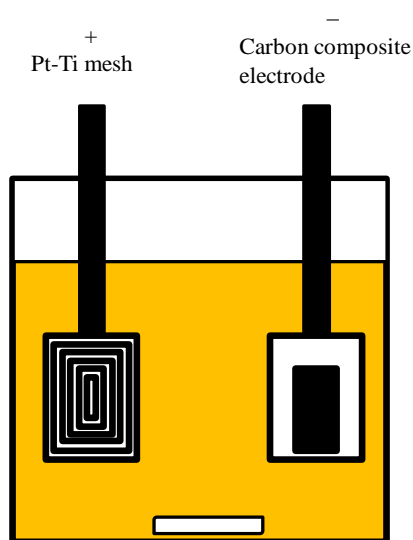


Fig.4.7: Illustration of an experimental set up of the zinc cerium undivided cell

The galvanic cycles were conducted by using an EG & G M100A Potentiostat/Galvanostat controlled by custom written software in LabVIEW or by the 1286 Electrochemical Interface controlled by the Corrware[®] software. Each charge-discharge cycle involved the application of a constant charging and discharge current for a set amount of time. Once the experiment at one concentration was completed, the cell was carefully cleaned and the next set of conditions was introduced to the batch cell.

-
- [1] <http://www.millipore.com/> accessed: Dec. 2011
- [2] <http://www.fisher.co.uk/> accessed: Dec. 2011
- [3] <http://www.sigmaaldrich.com/united-kingdom.html> accessed: Dec. 2011
- [4] <https://uk.vwr.com/app/Home> accessed: Nov. 2011
- [5] <http://www.basf.com/group/corporate/en/innovations/innovation-award/2008/an-old-favorite> accessed: Dec. 2011
- [6] <http://www.alfA.C.om/en/gh100w.pgm> accessed: Dec. 2011
- [7] https://sg.vwr.com/app/Header?tmpl=/research_development/analar_normapur_hgp.htm accessed: Dec. 2011
- [8] <http://en.sanofi.com/> accessed: Sept. 2011
- [9] <http://www.buehler.com/> accessed: Dec. 2011
- [10] <http://www.boconline.co.uk/> accessed: Nov. 2011
- [11] A. Hermanna, T. Chaudhuria, P. Spagnolb, *Int. J. of Hydrogen Energy*,. **30**, 1297-1302, (2005).
- [12] http://www.sglgroup.com/cms/international/products/product-groups/eg/sigracet-bipolar-plates/index.html?__locale=en accessed: Dec. 2011
- [13] http://www.eisenhuth.de/pdf/SIGRACET_Datenblaetter.pdf accessed: Dec. 2011
- [14] <http://www.entegris.com/Index.aspx> accessed: Dec. 2011
- [15] <http://www.entegrisfuelcells.com/Documents/BMCI8649.pdf> accessed: Dec. 2011
- [16] www.ge.com accessed: Dec. 2011
- [17] <http://www.bac2.co.uk/> accessed: Oct. 2011
- [18] P.J.F. Harray, *Philosophical Magazine*., **84**, (29), 3159-3167, (2004).
- [19] <http://www.alfA.C.om/content/msds/british/38024.pdf> accessed: Dec. 2011
- [20] J. Fu, H. Xu, Y. Wu, Y. Shen, C. Du, *J. Reinforced Plastics & Composites*., **3**, 31, (2012).
- [21] B.D. Cunningham, D.G. Baird, *J. Power Sources*., **168**, 418-425, (2007).
- [22] C. Del Rio, M.C. Ojeda, J.L.Acosta, M.J. Escudero, E. Hontanon, I. Daza, *J. Appl. Polym. Science*., **83**, 2817-2822, (2002).
- [23] S. Chunhui, P. Mu, Y. Runzhang, *Int. J. Hydrogen Energy*., **33**, 1035-1039, (2008).
- [24] D. Pletcher. *A first Course in Electrode Process*. The Electrochemical Consultancy, 49 (1991).
- [25] <http://www.scribner.com/> accessed: Dec. 2011
- [26] O. Reynolds, *Phil. Trans. R. Soc. Lond.* **174**, 935-982, (1883).

-
- [27] N. Rott, *Note on the History of the Reynolds number*, Annual review of Fluid Mechanics, Vol.22: 1-12, (1990) doi: 10.1146/annurev.fl.22.010190.000245
- [28] G. Kokkinidis, A. Papoutsis, D. Stoychev, A. Milchev, *J. Electroanal. Chem.*, **486**, 48-55, (2000).
- [29] H. Yu, K. Scott, *Electrochem. Commun.*, **6**, 361-365, (2004).
- [30] S.V. Mentus, *Electrochim. Acta.*, **50**, 3609-3615, (2005).
- [31] K. Tammeveski, M. Arulepp, T. Tenno C. Ferraterb, J. Claret, *Electrochim. Acta.*, **42**, 19, 2961-2967, (1997).
- [32] P. Patnaik, *Dean's Analytical Chemistry Handbook*, 2nd Edition, McGraw-Hill, (2004).
- [33] K. L. Douglas. "Elastomers". *Handbook of sulphuric acid manufacturing*. Richmond Hill, Canada: DKL Engineering, Inc. pp. 16–116 (2005).
- [34] Z.Q. Mao, *Fuel Cell, Chemical Industry Press.*, **63**, 33-47, (2005).
- [35] S. Slade, S.A. Campbell, T.R. Ralph, F.C. Walsh, *J. Electrochem. Soc.*, **149**, 12, 1556-1564, (2002).

Chapter 5

Zinc half cell reaction

5.1 Cyclic Voltammetry

Cyclic voltammetry is useful to understand the electrochemistry of zinc reactions and electrode kinetics under different operating conditions. Zinc electrodeposition from an additive free acid electrolyte can be described by:



Eq.5.1

Fig.5.1 shows the voltammetric behaviour of 1.5 mol dm^{-3} zinc methanesulfonate electrolyte for the reduction of Zn(II) species from the bulk of the solution (pH between 0 and 1). In this study, the sweep rate (50 mV s^{-1}) was reversed when the potential approached a value of $-1.8 \text{ V vs. Hg|Hg}_2\text{SO}_4|\text{K}_2\text{SO}_4 \text{ (sat.)}$ for a HDPE carbon electrode. At more negative potentials (*viz.* $>-2 \text{ V}$) solvent breakdown leads to the hydrogen evolution reaction and large currents are observed.

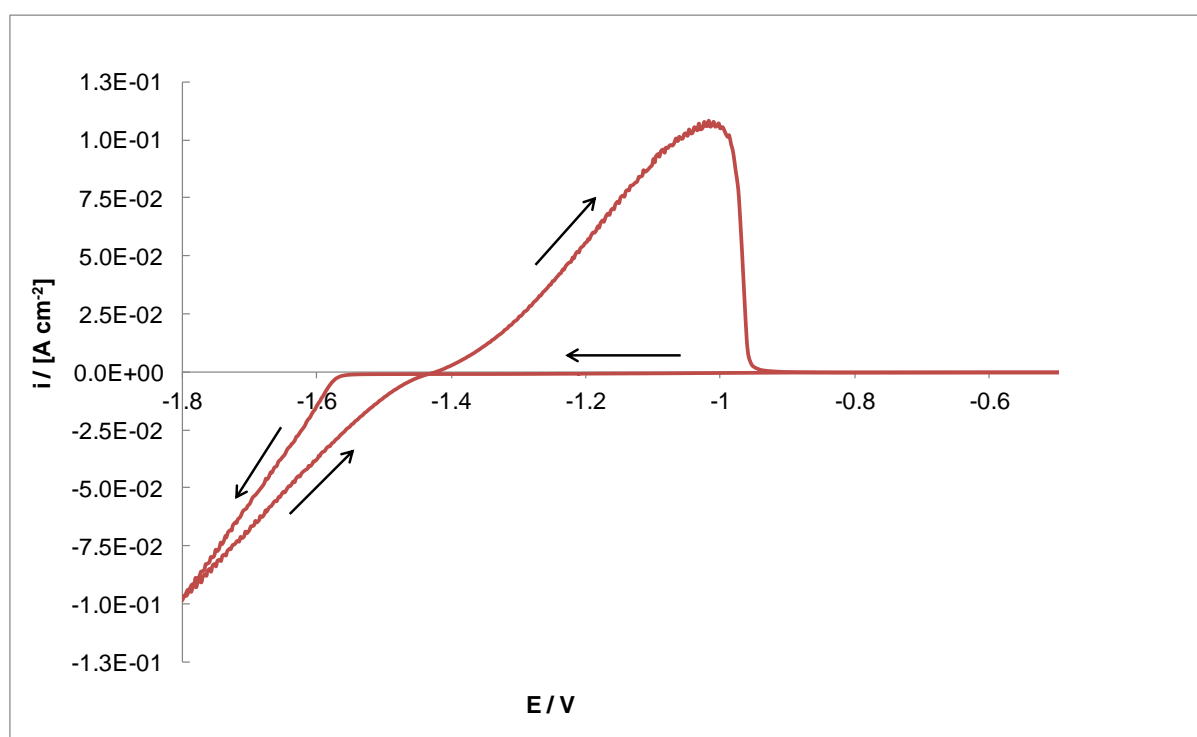


Fig.5.1: Cyclic voltammetry of the zinc(II)/zinc (0) couple onto a HDPE-2 carbon electrode (0.38 cm^2) in 1.5 mol dm^{-3} Zn(II) and 5.7 mol dm^{-3} $\text{CH}_3\text{SO}_3\text{H}$ at 50 mV s^{-1} ; 5 Hz and 60°C .

The potential at which zinc started depositing (*i.e* onset potential) was equal to -1.58 V. Since the system was under hydrodynamic control, the introduction of rotation should have led to a plateau limiting current density (i_L) indicating a mass transport controlled system according to the Levich theory [1]. In this case the zinc deposition process does not give a limiting current indicating that it is accompanied by hydrogen evolution (HER) even at these potentials. This is because of the fact that the reduction potential of zinc is more negative than that of hydrogen [2].

The current density achieved during the zinc deposition was *ca.* -9.39×10^{-2} mA cm⁻² at 5 Hz. It is controlled in part by the reaction rate at the surface of the electrode rather than wholly by mass transport. Leung *et al.* [3] also reported that at high concentrations of methanesulfonic acid (pH between 0 and 1) in the presence of Zn(II) ions, the current is mainly due to the HER process. The HER process is inhibited on the electrodeposited zinc surface, as can be gleaned from the exchange current density values for the hydrogen evolution reaction on zinc, which is only 3.16×10^{-11} A cm⁻² from Table 3.1 p.69 [4].

As the potential was swept towards more positive values on the reverse sweep, the solid zinc deposit was no longer thermodynamically stable on the electrode surface and re-dissolved into the aqueous solution. It is worth noting that the reverse and forward curves for zinc deposition did not pass through the same potential indicating that deposition is far easier on the reverse sweep. This feature is called a nucleation loop. The pronounced stripping peak implies that fast zinc dissolution occurred during the oxidation process than the reduction one. This is due to the layer of zinc coated on the top of the electrode surface, which implies that dissolution is a thermodynamically and kinetically favourable process. The zinc stripping efficiency was found to be *ca.* 81% from this study suggesting a poor adhesion of zinc on the surface of the carbon composite electrode. Another more unlikely explanation is that the HER process is present at these negative potentials.

5.1.1 Effect of mass transport

Fig.5.2 shows the effect of increasing mass transport for the reduction reaction of zinc (II) to zinc (0). The potentials for this system were scanned from -0.6 V to -1.8 V for a PVE carbon composite at 20 mV s^{-1} and 60°C .

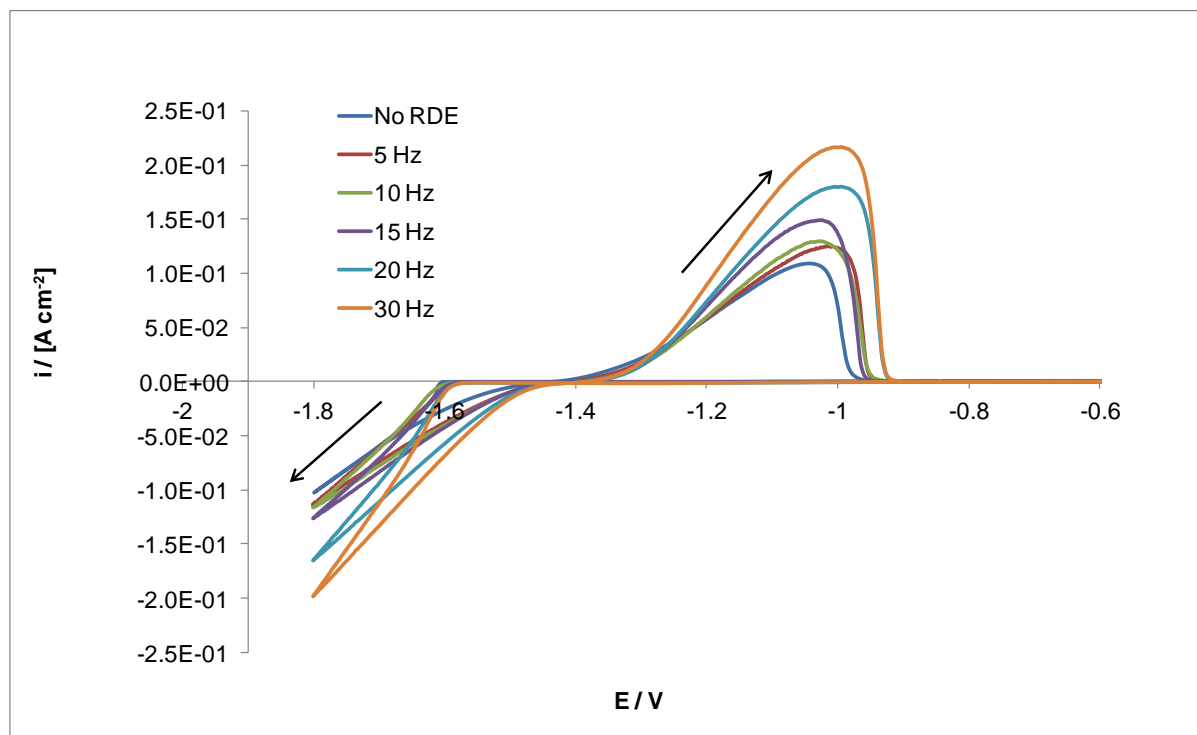


Fig.5.2: Effect of rotating disk speed on the cyclic voltammetry of the zinc (II)/zinc (0) couple onto a carbon PVE electrode; $1.5 \text{ mol dm}^{-3} \text{ Zn}(\text{CH}_3\text{SO}_3)_2$ and $5.7 \text{ mol dm}^{-3} \text{ CH}_3\text{SO}_3\text{H}$ at 20 mV s^{-1} and 60°C .

At each rotation speed, the deposition of zinc was observed due to the presence of a nucleation loop at the forward scan and of course the stripping peak at the reverse. The current density values obtained under high rotation rates for deposition were *ca.* -1.62×10^{-1} mA cm^{-2} at 20 Hz and -1.91×10^{-1} mA cm^{-2} at 30 Hz. For the dissolution reaction the current densities were *ca.* 1.81×10^{-1} mA cm^{-2} at 20 Hz and 2.22×10^{-1} mA cm^{-2} at 30 Hz. For both processes, these values were considerably higher than the one in the absence of solution flow rates, suggesting that mass transport to the electrode surface appears to have an impact even at these relatively low overpotentials (*i.e.* limit of voltammogram: -1.8 V). It was observed that at low rotation rates, the bubbles formed during the deposition process remained on the electrode surface and were not swept away.

At rotation rates between 5 and 10 Hz, the mass transport effect did not seem to be that significant as the current densities were quite similar (1.15×10^{-1} A cm^{-2}), even when compared with the voltammogram at the absence of rotation speed *ca.* 1.02×10^{-1} A cm^{-2} .

These observations suggested that although mass transport of the Zn(II) species will be enhanced at higher rotation rates, it is more likely that it was the shearing action of the convective flow removing hydrogen bubbles from the electrode surface which controls the zinc deposition process. This finding was in accordance with the work of Van Parys *et al.* [5] on an aqueous acidic sulfate solution *viz.* $1 \times 10^{-1} \text{ mol dm}^{-3} \text{ ZnSO}_4$ and $1 \text{ mol dm}^{-3} \text{ Na}_2\text{SO}_4$ with a pH of 2.5.

Since the potential at which the zinc dissolution process occurred is the same for all rotation speeds *viz.* -1.40 V , the different rates and amount of zinc dissolution must come therefore from the nature of the solid deposit formed in the presence or absence of rotation. This suggests that solution flow had an impact on the morphology of the deposit formed, with the one formed at rotation rates greater than 15 Hz ($Re > 190$) being more inhibited towards anodic dissolution. High convective flow did not increase the overpotential range over which deposition can take place but allowed higher current densities to be achieved.

At high rotation rates the zinc deposition took place slightly earlier (Fig.5.2). For a rotation speed of 5 Hz the onset potential value was *ca.* -1.60 V , 200 mV more negative when compared to the rotation speed of 20 Hz (-1.58 V). The effect of electrode rotation on the onset potential for zinc deposition is shown in Table 5.1 for several carbon based substrates. The error factor of the onset potentials was less than $\pm 10 \text{ mV}$.

$E_{onset} / \text{V vs. Hg Hg}_2\text{SO}_4 \text{K}_2 \text{SO}_4 \text{ (sat)}$					
Rotation rate / Hz	0	5	10	20	30
<i>Re</i>	0	62	123	257	370
Electrode					
PVDF	-1.55	-1.55	-1.55	-1.54	-1.53
PVE	-1.60	-1.60	-1.60	-1.58	-1.58
HDPE - 1	-1.52	-1.52	-1.51	-1.51	-1.51
HDPE - 2	-1.55	-1.55	-1.54	-1.53	-1.53
BAC2	-1.66	-1.62	-1.62	-1.61	-1.60
PE20	-1.55	-1.54	-1.54	-1.53	-1.53

Table 5.1: Effect of electrode rotation on the onset potential for zinc deposition onto various carbon based substrates in $1.5 \text{ mol dm}^{-3} \text{ Zn}(\text{CH}_3\text{SO}_3)_2$ and $5.7 \text{ mol dm}^{-3} \text{ CH}_3\text{SO}_3\text{H}$ at 20 mV s^{-1} and 60°C .

From the data of Table 5.1 it would appear that the higher the rotation speed the earlier the zinc nuclei formed on the surface of the electrodes. The HDPE-1 polymer had the more positive onset potentials for the range of the rotation speed tested, indicating that the zinc deposition process was more favourable at the surface of this electrode. However, it has been previously reported that this foil type electrode is accompanied by the physical deterioration in the electrode surface in such acidic media [6]. Positive onset potentials were also reported for the PVDF, HDPE-2 and BAC2 carbon composites.

5.1.2 Effect of temperature

The electrolyte temperature is a very important operating parameter for any electrochemical process. Fig.5.3 shows the effect of elevated temperatures on a carbon PVDF based electrode in 1.5 mol dm^{-3} zinc methanesulfonate with 2.7 mol dm^{-3} excess methanesulfonic acid. The potential was swept from 0.4 V to -2 V at 20 mV s^{-1} .

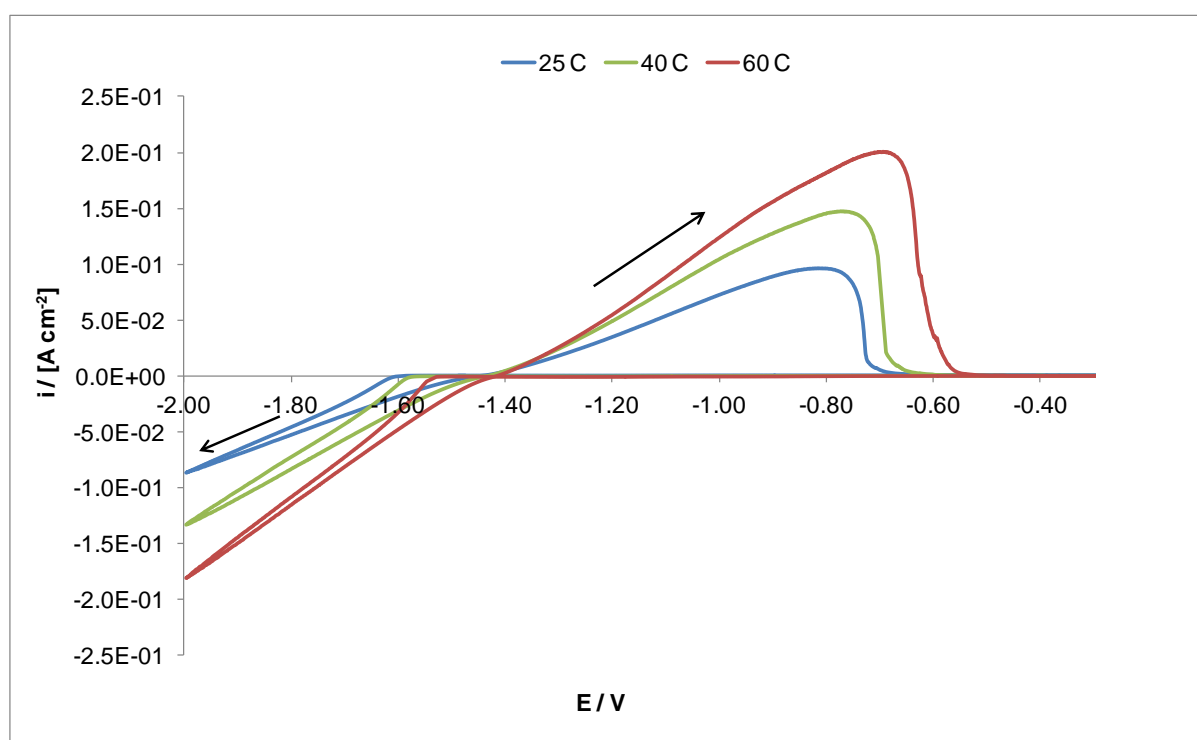


Fig.5.3: Effect of T on the overpotential for the zinc (II)/zinc (0) couple in the solution of 1.5 mol dm^{-3} $\text{Zn}(\text{CH}_3\text{SO}_3)_2$ and 5.7 mol dm^{-3} $\text{CH}_3\text{SO}_3\text{H}$ at 20 mV s^{-1} and 20 Hz - PVDF based electrode (0.38 cm^2).

From Fig.5.3, the current densities achieved during deposition at the potential limit (-2 V) are higher by a factor of approximately 2 at 60°C *viz.* $-1.88 \times 10^{-1} \text{ A cm}^{-2}$ compared to 25°C ($-8.4 \times 10^{-2} \text{ A cm}^{-2}$). In addition, higher dissolution current densities were observed at elevated temperatures, indicating that overall the zinc reaction is more favourable at higher

temperatures. The data gleaned from Fig.5.3 are in agreement with other studies conducted in zinc methanesulfonate solutions regarding the effect of temperature on current density during zinc deposition and dissolution [3].

When the electrolyte temperature increased, the onset potentials shifted to more positive potentials. From Fig.5.3 it can be seen that at 25°C, $E_{onset} = -1.61$ V while at 60°C the E_{onset} is *ca.* -1.52 V. The change in the electrode potential obeyed the Nernst equation according to which elevated temperatures reduce the driving force for zinc electrodeposition and hydrogen evolution. The effect of temperature on E_{onset} is shown in Table 5.2 for two rotation rates *viz.* 10 Hz and 20 Hz for several carbon composite materials in a solution consisting of 1.5 mol dm^{-3} zinc(II) in 2.7 mol dm^{-3} excess methanesulfonic acid. The error factor of the onset potentials was less than ± 10 mV.

$E_{onset} / \text{V vs. Hg Hg}_2\text{SO}_4 \text{K}_2\text{SO}_4 (\text{sat})$						
	10 Hz	20 Hz	10 Hz	20 Hz	10 Hz	20 Hz
Electrode	25°C		40°C		60°C	
PVDF	-1.60	-1.59	-1.58	-1.57	-1.55	-1.54
PVE	-1.60	-1.61	-1.57	-1.57	-1.60	-1.60
HDPE - 1	-1.58	-1.57	-1.58	-1.56	-1.52	-1.51
HDPE - 2	-1.65	-1.63	-1.60	-1.60	-1.54	-1.53
BAC2	-1.69	-1.68	-1.65	-1.64	-1.62	-1.61
PE20	-1.59	-1.58	-1.62	-1.61	-1.54	-1.53

Table 5.2: Effect of T on E_{onset} for the zinc deposition reaction onto various carbon electrodes, $1.5 \text{ mol dm}^{-3} \text{ Zn}(\text{CH}_3\text{SO}_3)_2$ in $5.7 \text{ mol dm}^{-3} \text{ CH}_3\text{SO}_3\text{H}$ at 20 mV s^{-1} ; 10 Hz and 20 Hz.

From Table 5.2, the potential at which the zinc nucleation process occurred decreased significantly at elevated temperatures for all the substrates examined. This could be due to the fact that elevated temperatures increased the kinetics of the zinc deposition reaction. The effect of temperature on the zinc reaction kinetics is being discussed in detail in Section 5.2.4. Hence, for the majority of the carbon substrates elevated temperatures make the zinc deposition reaction thermodynamically more favourable. The HDPE-1 carbon composite showed the more positive onset potentials as the temperature increased for both rotation speeds *viz.* 10 Hz and 20 Hz.

5.1.3 Effect of carbon composite materials

For the purposes of this study, several carbon substrates were investigated for the zinc deposition and dissolution reactions. As shown in Fig.5.4 the potentials in this study were scanned from 0.8 V to -1.8 V at 20 mV s^{-1} while the temperature was maintained at 25°C .

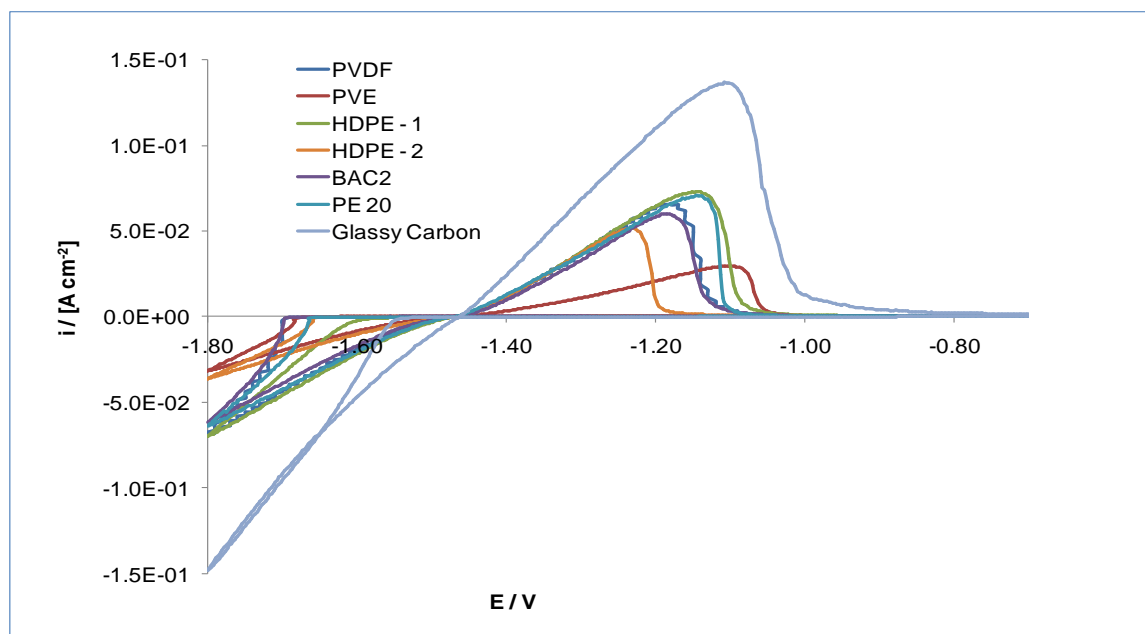


Fig.5.4: Cyclic voltammetry of the zinc (II)/zinc (0) couple onto various carbon electrodes in 1.5 mol dm^{-3} Zn(II) and 5.7 mol dm^{-3} $\text{CH}_3\text{SO}_3\text{H}$ at 20 mV s^{-1} ; 10 Hz and 25°C .

When comparing the different electrodes, the highest current density achieved during the deposition and the dissolution of the zinc species was for the glassy carbon electrode at 10 Hz . Indeed, the rate of growth of the zinc layer at the glassy carbon surface was the fastest of all the electrode materials examined. This can be attributed to the different resistivity of the carbon materials as well as to the fact that pure carbon offers negligible porosity and good mechanical rigidity [7]. It has been reported in the literature that glassy carbon attracts zinc much more easily than any type of composite material due to its large number of active surface sites it contains [8]. Moreover, the high current densities of the glassy carbon can also be due to the fact that the competing hydrogen evolution reaction has a bigger impact on the carbon composite electrodes than on the pure carbon at the rotation speed of 10 Hz . As well as the higher current densities, the onset potential for zinc deposition was lower for the glassy carbon, as expected. From Fig.5.4 the current density found at the negative potential limit for the glassy carbon electrode was *ca.* $-1.5 \times 10^{-1} \text{ A cm}^{-2}$. The onset potential during the zinc deposition at the glassy carbon was equal to -1.54 V , significantly smaller than at the HDPE

based electrode ($E_{onset} = -1.61$ V) and also the BAC2 and PVDF composite materials ($E_{onset} = -1.69$ V).

5.1.4 Effect of zinc (II) ion concentration

Fig.5.5 shows the cyclic voltammogram of zinc electrodeposition from different zinc concentrations *viz.* 7×10^{-1} mol dm⁻³, 1 mol dm⁻³, 1.5 mol dm⁻³ and 2 mol dm⁻³ at a rotating speed of 10 Hz and at 60°C. The range of the zinc concentration was not very wide but it is more than adequate for demonstrating the effect of higher zinc concentrations in the methanesulfonic acid medium on the PVDF carbon composite. The methanesulfonic acid concentration was the same for all solutions *viz.* total 5.7 mol dm⁻³. In this voltammetric study, potentials were linearly swept from +0.5 to -1.8 V at a sweep rate of 40 mV s⁻¹.

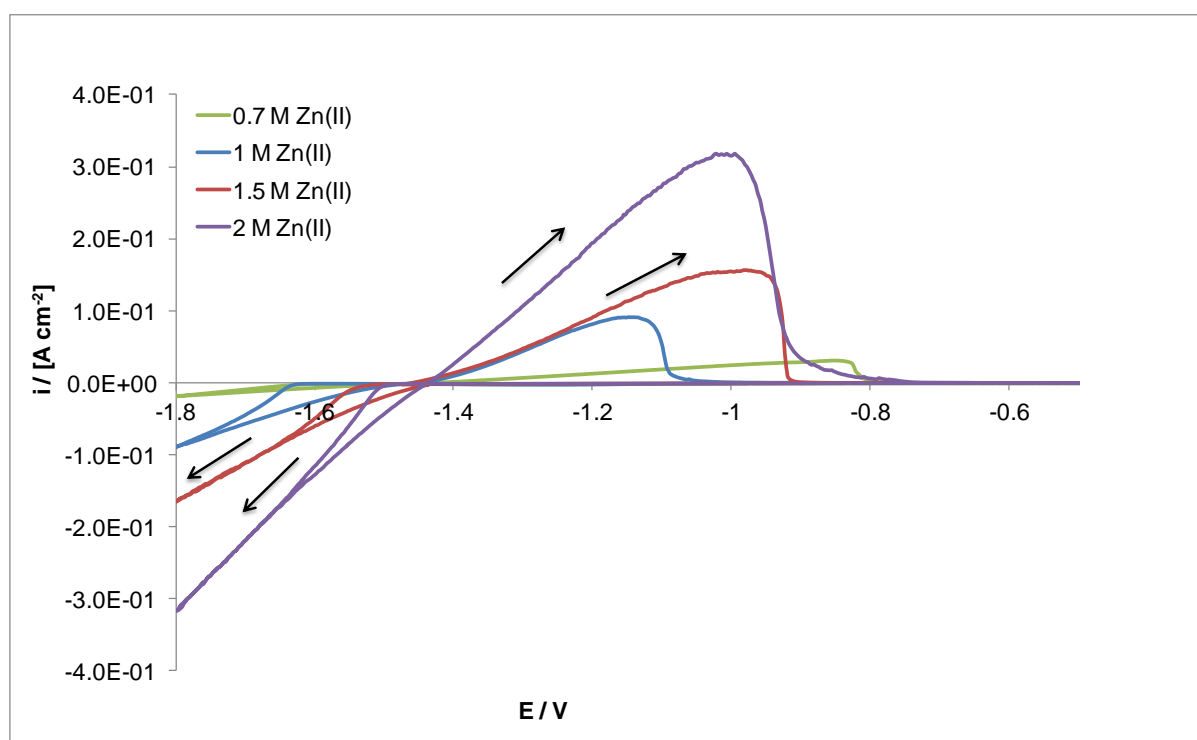


Fig.5.5: Effect of zinc concentration on the zinc deposition and dissolution reaction in 5.7 mol dm⁻³ CH₃SO₃H at 40 mV s⁻¹, 60°C and 10 Hz; PVDF electrode (0.38 cm²).

The current densities for the zinc deposition and dissolution reactions were significantly enhanced at higher concentrations of zinc methanesulfonate. However, the current density did not increase by a factor of two with the doubling of the zinc concentration. This clearly suggests that this system is not mass transport controlled and even at high zinc concentrations the parallel HER reaction still influences the zinc deposition reaction. On the contrary, as confirmed from the Nernst equation, the onset potentials for the

zinc deposition and dissolution reactions were found to be more positive at higher zinc concentrations. For instance, between the voltammograms of 1 mol dm^{-3} and 2 mol dm^{-3} $\text{Zn}(\text{CH}_3\text{SO}_3)_2$ the onset potential difference was *ca.* 125 mV.

5.1.5 Effect of methanesulfonic acid concentration

Cyclic voltammetry of zinc electrodeposition in 1.5 mol dm^{-3} zinc (II) under different methanesulfonic acid concentrations was carried out in this study. The potential sweep rate was 40 mV s^{-1} and the potential limit range was from -0.5 V to -1.8 V at the optimum rotating speed of 10 Hz and the operating temperature of 60°C .

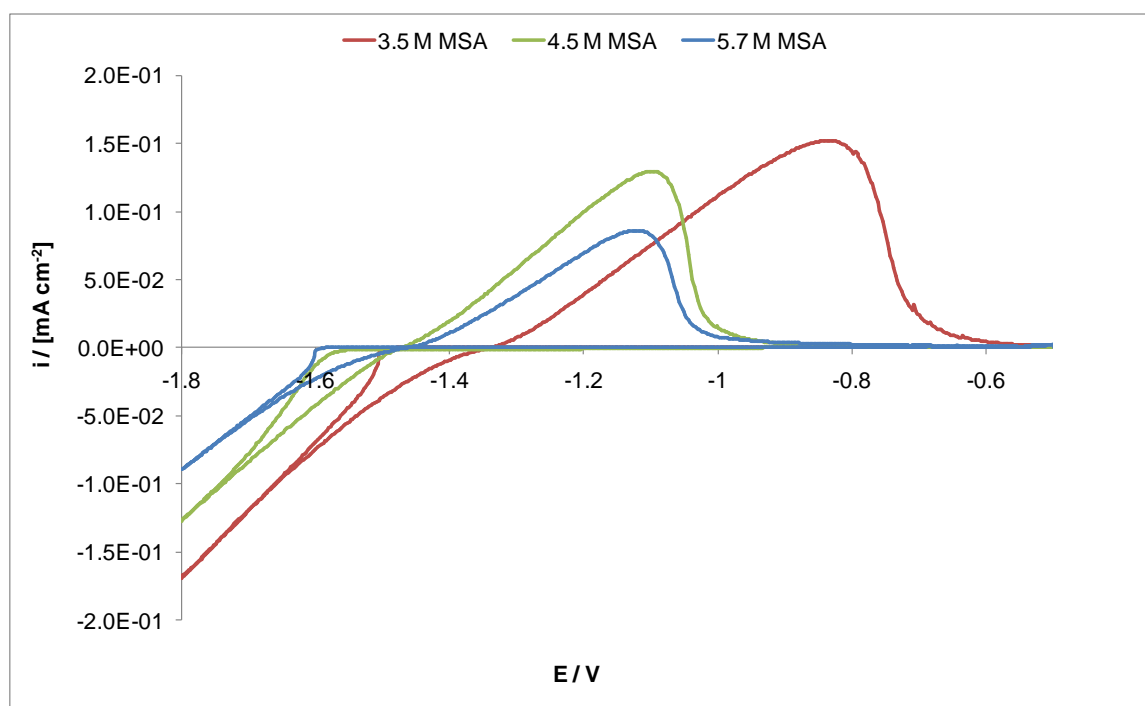


Fig.5.6: Effect of methanesulfonic acid concentration (3.5, 4.5 and 5.7 mol dm^{-3}) on the zinc deposition and dissolution process in 1.5 mol dm^{-3} $\text{Zn}(\text{CH}_3\text{SO}_3)_2$ at 40 mV s^{-1} , 10 Hz and 60°C ; PVE electrode.

The zinc deposition current density for the voltammogram containing less acid concentration (3.5 mol dm^{-3}) was *ca.* $-1.8 \times 10^{-1} \text{ A cm}^{-2}$ at -1.8 V , considerably larger than the one containing 5.7 mol dm^{-3} methanesulfonic acid ($i = -8.6 \times 10^{-2} \text{ A cm}^{-2}$). According to Cachet *et al.* [9] the discharge of Zn(II) ions is firstly inhibited by hydrogen adsorption followed by the hydrogen evolution on the surface of the zinc deposit. Higher methanesulfonic acid concentrations result in the minimization of the hydrogen absorption as the concentration of the zinc ions on the surface of the electrode is low. Therefore, the majority of the current is used for the HER process, leading to lower current densities during the zinc deposition and dissolution reactions. The onset potential was also more positive for

the zinc deposition reaction at lower acid concentrations ($E_{onset} = -1.49$ V) while it was *ca.* -1.57 V for 4.5 mol dm^{-3} of methanesulfonic acid and -1.60 V for 5.7 mol dm^{-3} following the obeying the Nernst equation.

5.1.6 Effect of additives on zinc electrodeposition

The electrodeposition of zinc was investigated in the presence of several additives, which included traditional brighteners, surface active agents and inorganic additives under mass transport control (*i.e.* 10 Hz). The majority of these additives have been reported to enhance the zinc deposition reaction as discussed in Chapter 2, Section 2.4.1. The scan rate was 20 mV s^{-1} and the potential limits were between -0.5 V and -1.8 V for the PVDF based carbon substrate at 60°C . The additives were found to give different onset potentials for zinc deposition and their characteristics are summarized in Table 5.3.

Additives	Concentration / $\times 10^{-3} \text{ mol dm}^{-3}$	Onset potential during Zn deposition / V	Zn stripped off during dissolution	$i_{deposition}$ at -1.8 V $\times 10^{-1} \text{ A cm}^{-2}$	Evaporation	Froth	Colour
No additive	0	-1.55	✖	-1.32	✓	✓	✓
Coumarin	2	-1.52	✖	-1.10	✖	✖	✖
Triton X-100	2	-1.80	✖	-0.34	✖	✖	✓
Cetyltrimethyl-ammonium bromide	1	-1.67	✖	-0.83	✖	✓	✓
Cetyltrimethyl-ammonium bromide	5	-1.69	✖	-0.34	✖	✖	✓
Tetrabutyl- ammonium hydroxide	2	-1.63	✖	-1.07	✓	✓	✓
Tartaric acid	2	-1.56	✖	-0.84	✓	✓	✓
Potassium sodium tartarate	2	-1.50	✖	-0.04	✖	✓	✓
Indium oxide	2	-1.49	✖	-0.25	✓	✓	✓

Table 5.3: Characteristics of different additives during zinc electrodeposition in 1.5 mol dm^{-3} $\text{Zn}(\text{CH}_3\text{SO}_3)_2$ and 5.7 mol dm^{-3} $\text{CH}_3\text{SO}_3\text{H}$ at 60°C , 20 mV s^{-1} and 10 Hz; PVDF electrode.

✖: poses the problem. ✓: does not pose the problem.

The presence of indium oxide, potassium sodium tartarate and coumarin all gave smaller onset potentials when compared to the additive-free electrolyte ($1.5 \text{ mol dm}^{-3} \text{ Zn(II)}$ and $5.7 \text{ mol dm}^{-3} \text{ CH}_3\text{SO}_3\text{H}$). Indium oxide as well as potassium sodium tartarate have been reported to suppress the HER [3]. According to Leung *et al.* [3], potassium sodium tartarate and indium oxide showed a charge discharge ratio during cyclic voltammetry of *ca.* 88% on a solution containing $1 \times 10^{-2} \text{ mol dm}^{-3} \text{ Zn(CH}_3\text{SO}_3)_2$ and $5 \times 10^{-1} \text{ mol dm}^{-3} \text{ NaCH}_3\text{SO}_3$ at 25°C . However, potassium sodium tartarate as well as $5 \times 10^{-3} \text{ mol dm}^{-3}$ CTABr and Triton X-100 revealed poor current densities during zinc deposition, *i.e.* smaller by a factor of 10 when compared with the additive free electrolyte. This could be due to the fact that these additives are adsorbing at the surface of the electrode, blocking part of it, thereby reducing the number of active sites for the formation of zinc nuclei and causing a decline in the nucleation rate [10]. Another reason could be the high acidic environment (2.7 mol dm^{-3}) not having the expected effect (*i.e.* uniformity) on the zinc deposition as has been reported elsewhere [11].

In addition, Triton X-100 was found to generate excessive foam leading to evaporation issues at 60°C . The same occurred for CTABr at concentrations of ($1 \times 10^{-3} \text{ mol dm}^{-3}$). These two additives have been widely used in the alkaline Zn-MnO₂ batteries [12]. It has been reported that CTABr can act as a hydrogen evolution suppressant in sulfuric acid solutions [13] [14]. Here though, during experimentation it was found that zinc did not re-dissolve back in the solution during the reverse scan suggesting that another reaction carried the current at these potentials (either the hydrogen evolution reaction occurring at 0 *vs* *S.H.E* or the oxygen reduction reaction occurring at 0.69 *vs* *S.H.E*).

Coumarin yielded the highest current densities during zinc deposition. However, it turned the clear electrolyte solution into pale yellow at temperatures higher than 40°C . This colouration has been reported in acetonitrile solutions ($1 \times 10^{-1} \text{ mol dm}^{-3}$) [15]. In that case, the colouration occurred with the reduction of the carbonyl group. Finally, the tetrabutyl ammonium hydroxide current densities of *ca.* $-1 \times 10^{-1} \text{ A dm}^{-3}$ at -1.8 V *vs* $-1.32 \times 10^{-1} \text{ A dm}^{-3}$ of the additive free solution were observed. However, the onset potential for the zinc deposition reaction was 700 mV more negative suggesting that the presence of this additive did not enhance the zinc deposition reaction on the surface of the PVDF electrode.

5.2 Kinetic parameters on the negative side of the zinc - cerium RFB

5.2.1 Introduction

The zinc half cell reaction was investigated by using Tafel extrapolation and linear polarisation methods in the negative half cell electrolyte of the zinc cerium redox flow cell (*viz.* 1.5 mol dm^{-3} Zn(II) and 5.7 mol dm^{-3} methanesulfonic acid). The exchange current density (i_o) and the equilibrium potential (E°) were measured for a variety of carbon composite materials (HDPE, BAC2, PVE and PVDF) at two different temperatures, *viz.* 25°C and 60°C . The exchange current density is expressed in terms of projected or geometric surface area and expresses the amount of current flowing at the equilibrium potential. It depends upon the surface roughness and the concentration of both oxidised and reduced species at the surface. The equilibrium potential is the potential at which the current changes polarity and corresponds to the open circuit potential of the system when electrodeposited zinc is in contact with Zn(II) ions in solution.

In order to plate zinc on the surface of the carbon composites, a current density of 50 mA cm^{-2} was applied to the system for 10 minutes under an electrode rotation rate of 10 Hz. The counter electrode was a platinum “gauze” electrode. Tafel extrapolation and polarization resistance techniques were employed with no rotation of the electrode.

5.2.2 Tafel extrapolation

The potential sweep rate used in the study was 1 mV s^{-1} and the potential limits were set at $\pm 0.15 \text{ V}$ from the open circuit potential ($> -1.45 \text{ V vs. Hg|Hg}_2\text{SO}_4|\text{K}_2\text{SO}_4 \text{ (sat.)}$). From Fig.5.7, the Tafel slopes obtained were 149 mV/decade and $-138 \text{ mV per decade}$ for the zinc dissolution and zinc deposition reactions respectively. These values are larger than the expected ones for a 2-electron process *viz.* 60 mV per decade as reported from the literature [16] [17] [18]. Still, they are in accordance with the values of Martyak *et al.* [19] for zinc methanesulfonate and zinc chloride solutions.

It must be borne in mind that at this equilibrium potential, the HER is not absent and furthermore complexation of the zinc ions by the methanesulfonic acid would affect the rate limiting step for both deposition and dissolution reactions and in turn change the charge transfer coefficient. This suggests that the open circuit potential corresponds to a mixed electrical potential but the measured value of -1.45 V indicates that this corresponds to the Zn(0)/Zn(II) equilibrium rather than zinc corrosion in acid medium. The i_o obtained from the fitting of the Tafel extrapolation data was *ca.* $3.80 \times 10^{-3} \text{ A cm}^{-2}$.

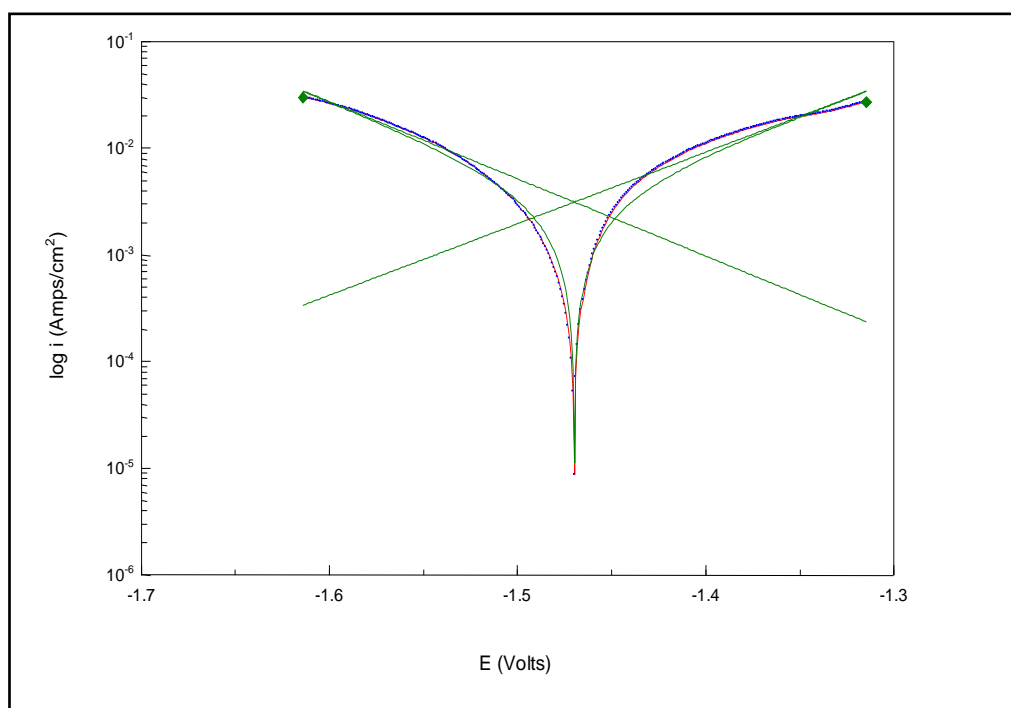


Fig.5.7: Tafel extrapolation measurements in a solution containing $1.5 \text{ mol dm}^{-3} \text{ Zn(II)}$ in $5.7 \text{ mol dm}^{-3} \text{ CH}_3\text{SO}_3\text{H}$ at 25°C ; Scan rate = 1 mV s^{-1} ; PVE carbon electrode (0.38 cm^2).

5.2.3 Polarisation resistance

For the linear polarisation experiment, the scan rate employed was 0.1667 mV s^{-1} . At low values of polarization *viz.* in-between $\pm 0.015 \text{ V}$, the dependence of the current on voltage is linear and not exponential. A polarization resistance plot for this system is shown in Fig.5.8. The i_o found here is double than that found in the Tafel measurements. A possible explanation for this discrepancy could be the dependence of the i_o calculated from the polarisation resistance (R_p) on the Tafel slopes. The low values of polarisation do not take into account the HER. In the case of the Tafel measurements though, the latter is most likely to be taken into consideration resulting thus in different i_o values.

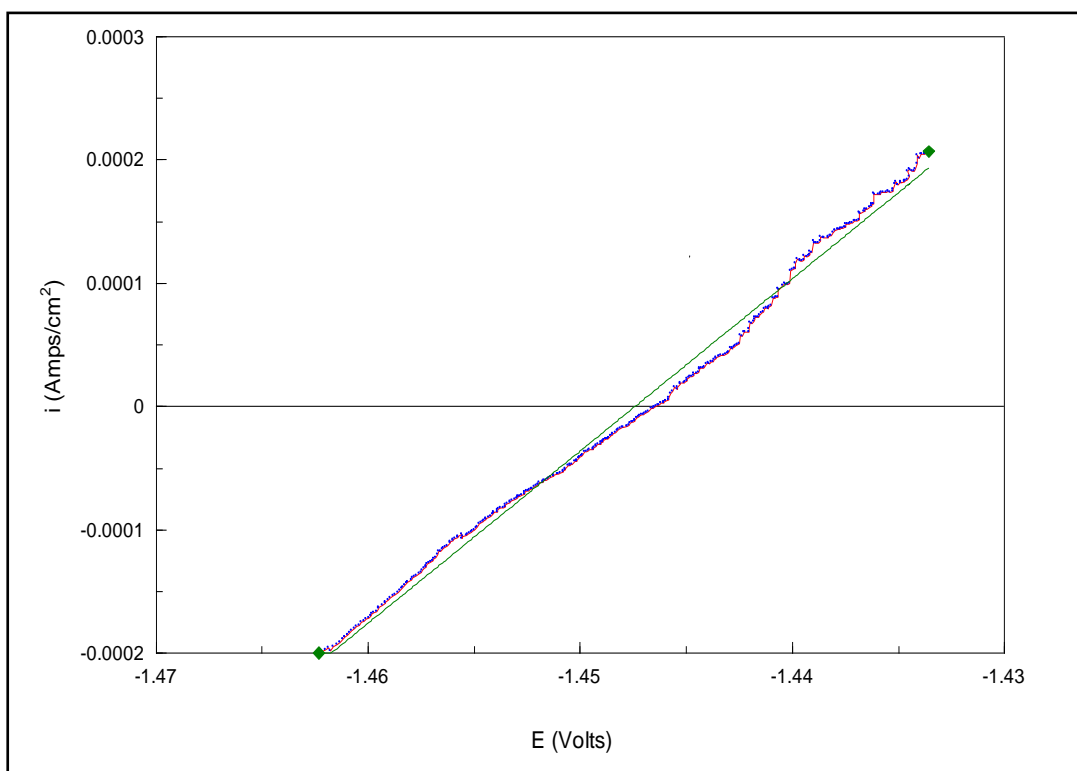


Fig.5.8: Polarization resistance measurements in a solution containing $1.5 \text{ mol dm}^{-3} \text{ Zn(II)}$ in $5.7 \text{ mol dm}^{-3} \text{ CH}_3\text{SO}_3\text{H}$ at 60°C ; Scan rate = 0.167 mV s^{-1} ; PVE carbon electrode (0.38 cm^2).

5.2.4 Exchange current density of zinc in methanesulfonic acid

The results of i_o for the several carbon substrates are summarised in Table 5.4.

$i_o / (10^{-3} \text{ A cm}^{-2})$				
Electrode	Polarization resistance		Tafel extrapolation	
	25°C	60°C	25°C	60°C
PVE	0.22	0.41	0.53	0.92
PVDF	0.58	1.88	1.31	3.03
HDPE-2	0.36	0.68	0.97	1.31
BAC2	0.48	1.24	1.03	2.06

Table 5.4: i_o as a function of T for various carbon electrodes in a solution consisting of $1.5 \text{ mol dm}^{-3} \text{ Zn(II)}$ and $5.7 \text{ mol dm}^{-3} \text{ CH}_3\text{SO}_3\text{H}$.

Table 5.4 clearly shows that for all four carbon substrates tested, i_o increases along with temperature. Higher i_o values indicate faster kinetics and so the system can respond rapidly to a potential change. The highest i_o values were recorded for the PVDF composite electrode *ca.* $3.03 \times 10^{-3} \text{ A cm}^{-2}$ at 60°C . The difference in i_o between the two techniques can be attributed to changes in the surface of the electrode upon which i_o is dependent and the HER as mentioned in Section 5.2.2. The i_o values gleaned from the polarisation technique are consistent with literature values for zinc deposition in acidic medium *viz.* between 2 mA cm^{-2} and 3.6 mA cm^{-2} [20] [21].

Finally, the equilibrium potential values shifted to more positive values by $\pm 2 \times 10^{-2} \text{ V}$ obeying the Nernst equation. However, this shift was insignificant and it can be assumed the E° values remained constant at $-1.44 \text{ V vs Hg|Hg}_2\text{SO}_4 \text{ (sat.)}$ over the temperatures examined.

5.3 Zinc deposition from a sodium methanesulfonate solution containing $10 \times 10^{-3} \text{ mol dm}^{-3} \text{ Zn(II)}$

5.3.1 RDE study

The highly acidic environment of the electrolyte studied above (2.7 mol dm^{-3} excess MSA) did not allow the investigation of the diffusion of the zinc (II) species during the deposition process (Eq.5.1). This is because of the HER process competing with the zinc deposition reaction. Therefore, a less acidic solution was made involving the addition of sodium carbonate to neutralise the methanesulfonic acid. The cyclic voltammogram of the zinc deposition reaction from a solution containing $1 \times 10^{-2} \text{ mol dm}^{-3} \text{ Zn(II)}$ and $2.5 \times 10^{-1} \text{ mol dm}^{-3} \text{ Na(CH}_3\text{SO}_3)$ at 60°C is shown in Fig.5.9. The pH of the solution was 3.5.

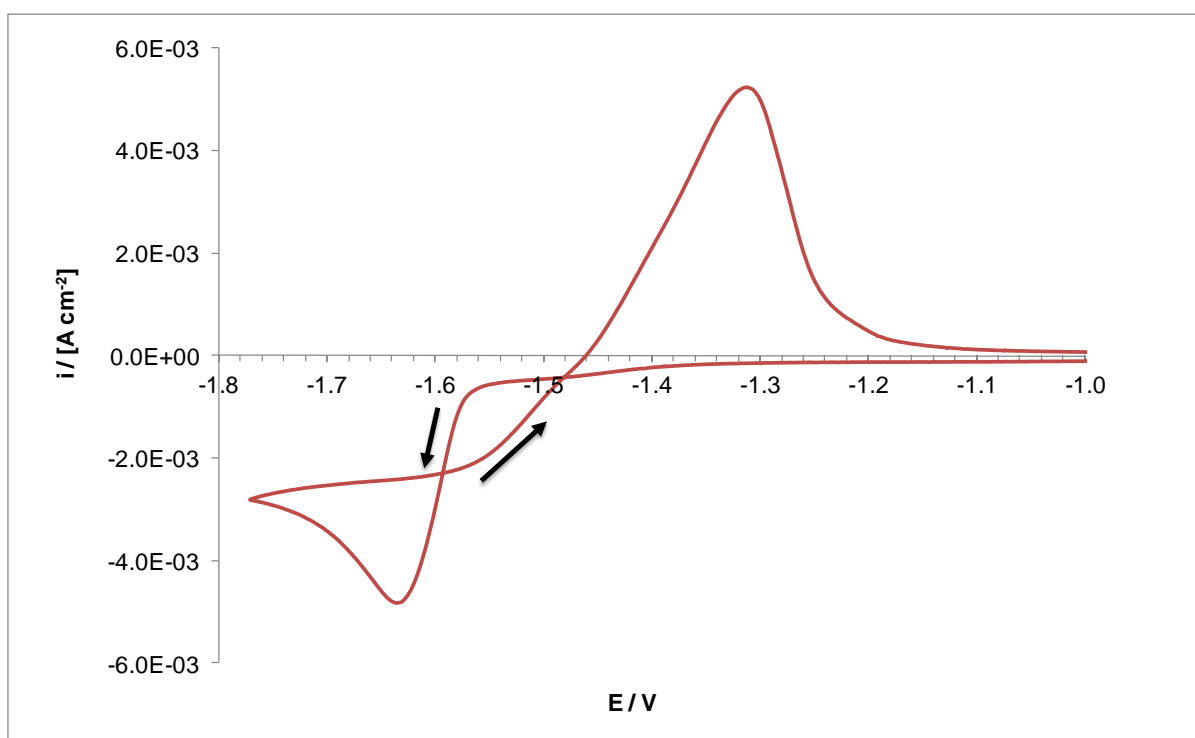


Fig.5.9: Cyclic voltammogram of a PVDF electrode (0.38 cm^2) in $1 \times 10^{-2} \text{ mol dm}^{-3} \text{ Zn(II)}$ and $2.5 \times 10^{-1} \text{ mol dm}^{-3} \text{ Na(CH}_3\text{SO}_3)$ at 60°C ; Scan rate: 20 mV s^{-1} .

From Fig.5.9 it can be seen that the onset for zinc deposition occurred at -1.58 V and the diffusion-controlled deposition peak at -1.68 V . As the potential was swept towards more positive values, the solid zinc deposit was no longer thermodynamically stable on the electrode surface and re-dissolved back into the aqueous species. The classic nucleation loop between -1.56 V and -1.63 V indicates the formation of the nuclei of the zinc metal phase onto the carbon PVDF electrode surface (overpotential of *ca.* 70 mV). The zinc dissolution

process leads to a very symmetrical peak, characteristic of a surface controlled process. It is symmetrical as the charge for zinc deposition is limited by the amount of zinc plated. The zinc stripping efficiency for this voltammogram was found to be 56%. The low stripping efficiency could be attributed to the poor activity of the PVDF carbon sites of this particular sample.

The data from a rotating disc electrode study on the deposition process is shown in Fig.5.10 for the HDPE-1 electrode. Neutralizing the zinc methanesulfonate solution would shift the hydrogen evolution reaction to more negative potentials, allowing a plateau to occur for the zinc deposition process. The potentials were scanned from -1.2 V and reversed at -1.9 V. For each rotation rate, the reduction of zinc was observed as a well defined constant current plateau instead of a peak. This is due to the constant steady state supply of the zinc ions to the electrode surface under mass transport control. Increased rotation speed extended the Tafel region and shortened the region of electrode potential for complete mass transport before the hydrogen evolution reaction dominated the current. Hence, for the rotation rates of 15 Hz and 20 Hz the i_L was selected at the potential of -1.85 V.

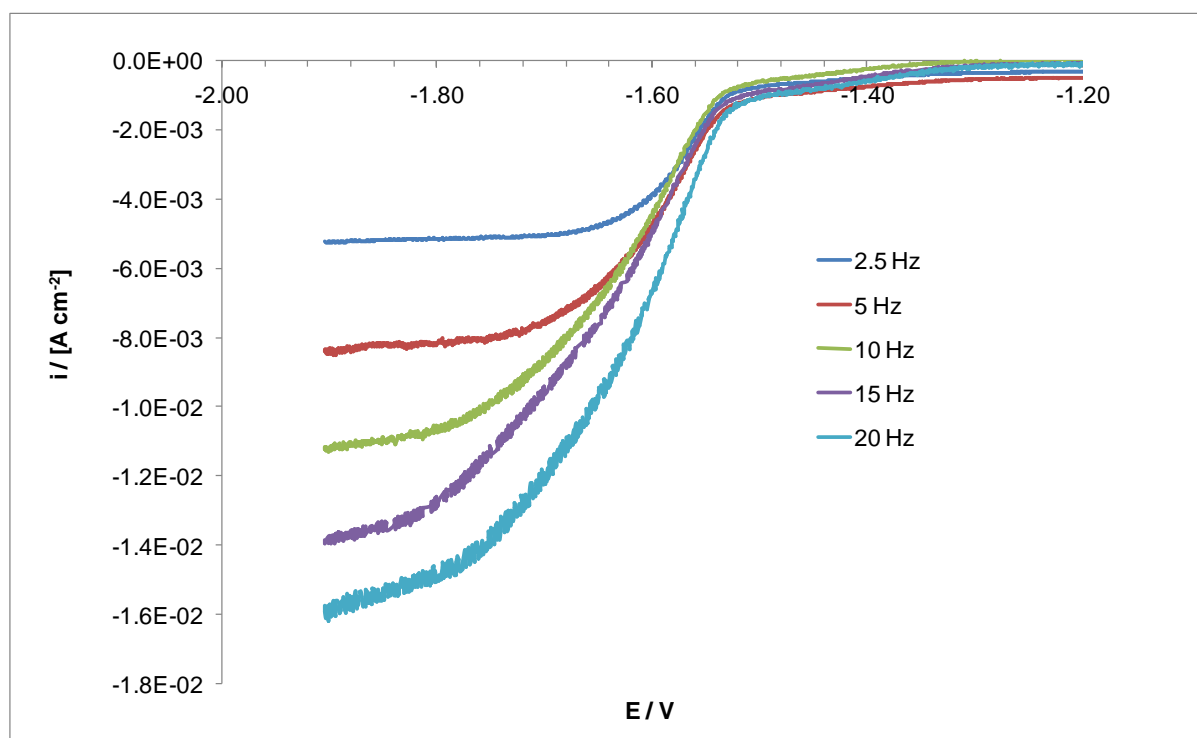


Fig.5.10: Rotating disc electrode study of a HDPE -1 electrode (0.54 cm^2) in $1 \times 10^{-2} \text{ mol dm}^{-3} \text{ Zn(II)}$ in $2.5 \times 10^{-1} \text{ mol dm}^{-3} \text{ Na(CH}_3\text{SO}_3)$ at 60°C ; Scan rate: 10 mV s^{-1} .

Through the use of the Levich equation (Eq.3.49, Chapter 3) the limiting current densities (i_L) were plotted as a function of the square root of the rotation speeds (Fig.5.11). The linear plot confirms that the system was under mass transport limiting conditions. The diffusion coefficient values of the zinc-methanesulfonate species at three different temperatures, *viz.* 25°C, 40°C and 60°C were determined for this system and presented in Table 5.5.

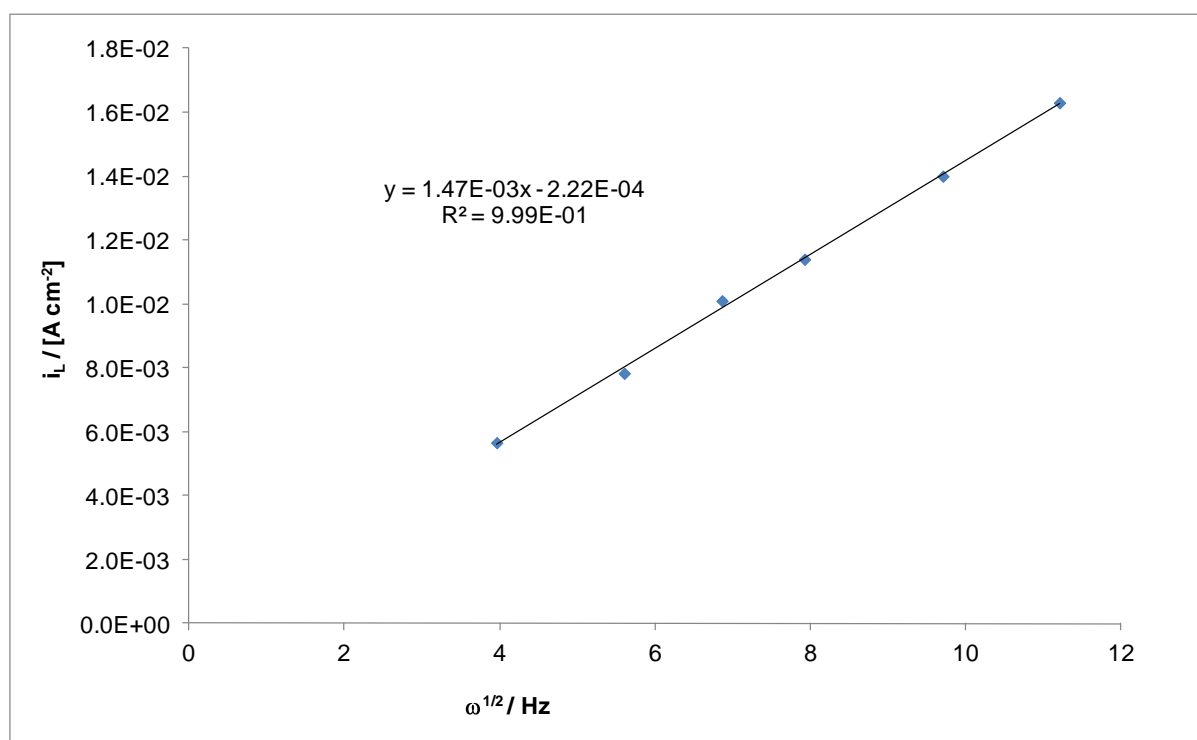


Fig.5.11: Levich plot at an RDE for the zinc (II)/zinc (0) couple in $1 \times 10^{-2} \text{ mol dm}^{-3} \text{ Zn(II)}$ and $2.5 \times 10^{-1} \text{ mol dm}^{-3} \text{ Na(CH}_3\text{SO}_3)$ at 60°C; PVE based electrode (0.38 cm^2).

	$D / (10^{-5} \text{ cm}^2 \text{ s}^{-1})$				
	Glassy Carbon	PVE	PVDF	HDPE - 1	HDPE - 2
25°C	0.79	0.51	0.24	0.41	0.46
40°C	0.95	1.35	0.53	0.97	0.75
60°C	1.21	1.38	0.81	1.27	1.23

Table 5.5: D values obtained as a function of T for various carbon substrates from the RDE in $1 \times 10^{-2} \text{ mol dm}^{-3} \text{ Zn(II)}$ and $2.5 \times 10^{-1} \text{ mol dm}^{-3} \text{ Na(CH}_3\text{SO}_3)$.

The values obtained for the diffusion coefficient are in good agreement with literature values [3] [22] [23] (i.e in the range of $10^{-5} \text{ cm}^2 \text{ s}^{-1}$) and as expected, increase with temperature. From the Stokes-Einstein equation [24], the increase in temperature results in higher kinetic energies of the zinc atoms leading to lower viscosities and higher velocities, which in turn increase the speed of diffusion. The highest diffusion coefficient value recorded was for the PVE electrode at 60°C , *ca.* $1.38 \times 10^{-5} \text{ cm}^2 \text{ s}^{-1}$ with the HDPE-1 and HDPE-2 carbon composites following in close range. The surprising variations in the D values between the different electrodes would suggest that the active area of these electrodes were not identical and although the diffusion field will become semi-infinite planar, diffusion at longer times the actual surface area for deposition will differ for the same geometric area.

The rotating disk electrode study also allowed the heterogeneous standard rate constant (k°) for the zinc reduction process to be obtained at the different carbon-based materials employed in this study through the use of the Koutechy-Levich relationship (Eq. 3.42 Chapter 3). Plotting the reciprocal of the limiting current density ($1/i_L$) versus the reciprocal of the square root of the rotation rate ($1/\omega^{1/2}$) gives a line whose y-intercept is equal to $1/i_k$ (Fig.5.12). From Eq. 3.41 Chapter 3, the heterogeneous standard rate constant (k°) was calculated for a variety of carbon substrates at three different temperatures as shown in Table 5.6.

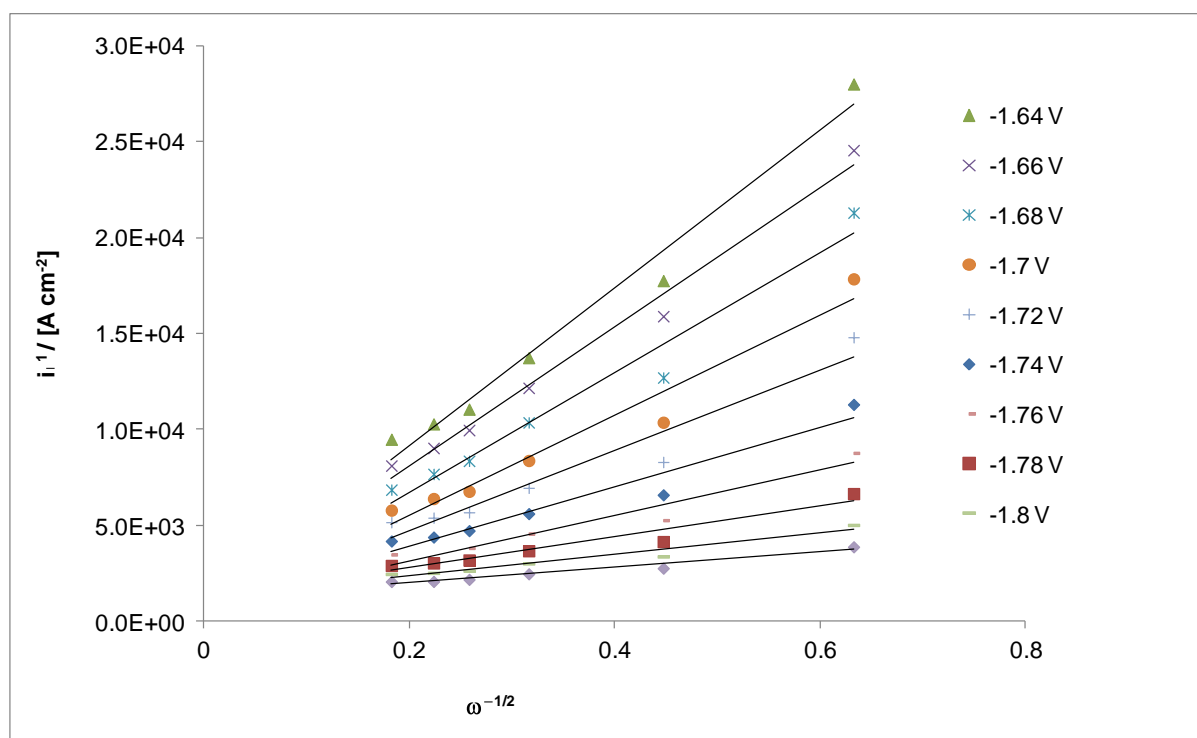


Fig.5.12: $1/i_L$ versus $1/\omega^{1/2}$ for the zinc (II)/zinc (0) couple in $1 \times 10^{-2} \text{ mol dm}^{-3} \text{ Zn(II)}$ and $2.5 \times 10^{-1} \text{ mol dm}^{-3} \text{ Na(CH}_3\text{SO}_3)$ at 40°C ; PVDF electrode (0.38 cm^2).

	$k^{\circ} / (10^{-3} \text{ cm s}^{-1})$				
	Glassy Carbon	PVE	PVDF	HDPE - 1	HDPE - 2
25°C	0.16	0.45	0.69	1.11	1.57
40°C	0.33	0.96	1.16	1.34	1.94
60°C	0.97	2.16	2.32	1.52	3.40

Table 5.6: Rate constants obtained as a function of T for various carbon substrates from the RDE in $1 \times 10^{-2} \text{ mol dm}^{-3} \text{ Zn(II)}$ and $2.5 \times 10^{-1} \text{ mol dm}^{-3} \text{ Na(CH}_3\text{SO}_3)$.

As expected, the k° values increased with higher temperatures for all the electrodes investigated. This trend is in agreement with the one of Table 5.5 for the estimation of the diffusion coefficients. Assuming that the active surface of these electrodes were not the same it is expected that the carbon electrodes will yield different standard rate constants. The HDPE-2 carbon composite exhibited slightly faster kinetics when compared to the other electrodes. For the PVDF, glassy carbon and HDPE-2 carbon substrates, the rate constant increased by a factor greater than two when the temperature increased from 40°C to 60°C. The standard rate constant of the PVE electrode was smaller by a factor of 10 compared to the one of the HDPE-2 carbon, indicating that kinetics on this electrode surface are slow even at 60°C.

Interestingly, the values of Mendoza *et al.* [23] in chloride solution ($5 \times 10^{-1} \text{ mol dm}^{-3} \text{ ZnCl}_2$ and $4 \times 10^{-1} \text{ mol dm}^{-3} \text{ H}_3\text{BO}_3$) for the standard rate constant are lower by a factor of 10, *viz.* $8.73 \times 10^{-3} \text{ cm s}^{-1}$ for the glassy carbon electrode thus emphasising the important role played by the counter ions (*viz.* Cl^-) in the adsorption, complexation and transport of the depositing species.

5.3.2 Scan rate dependence in $1 \times 10^{-2} \text{ mol dm}^{-3} \text{ Zn(II)}$ and $2.5 \times 10^{-1} \text{ mol dm}^{-3} \text{ Na(CH}_3\text{SO}_3)$

The peak shape of the oxidative and reverse current-potential curve in Fig.5.9 is typical for an electrode reaction in which the rate is governed by diffusion to a planar electrode surface. Fig.5.13 shows the cyclic voltammograms from the zinc deposition reaction of $2.5 \times 10^{-1} \text{ mol dm}^{-3}$ sodium methanesulfonate in $1 \times 10^{-2} \text{ mol dm}^{-3}$ zinc methanesulfonic acid using a carbon HDPE-2 based electrode, which were scanned from -1.40 V to -1.92 V vs. $\text{Hg}|\text{Hg}_2\text{SO}_4|\text{K}_2\text{SO}_4$ (sat.) at 60°C .

With regards to the Randles-Sevcik equation, (Eq. 3.17, Chapter 3) the cathodic peak current densities (i_p) for the zinc sodium methanesulfonate solution were plotted as a function of the square root of the sweep rates (i_p vs. $v^{1/2}$) as shown in Fig.5.14. It has to be mentioned that the potential where i_p occurred during the zinc deposition process increased with scan rate from 1.556 V at 5 mV s^{-1} to 1.698 V at 200 mV s^{-1} suggesting that the surface of the HDPE-2 electrode changed with each voltammogram. As a result, the plot of i_p as a function of $v^{1/2}$ was linear but did not pass through the origin as theory suggests for a system that is under diffusion control (Chapter 3, Section 3.3.5). Nonetheless, the diffusion values of this system were calculated for three different temperatures, viz. 25°C , 40°C and 60°C and the data are presented in Table 5.7.

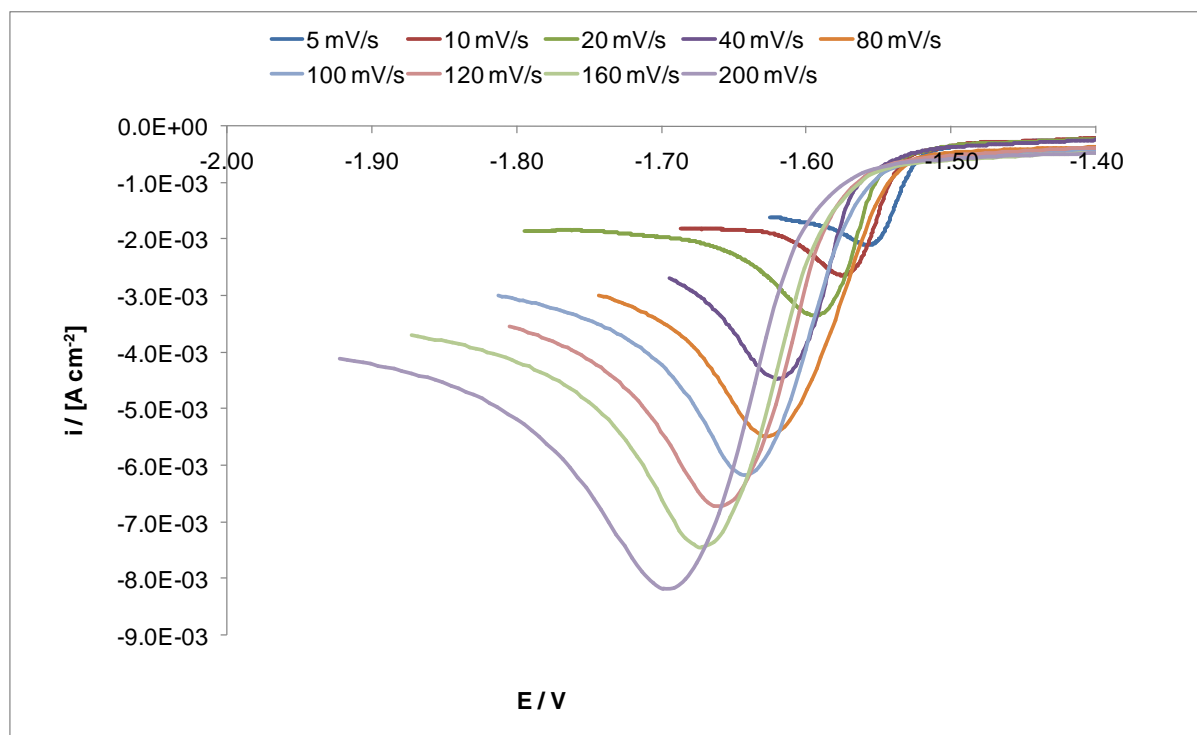


Fig.5.13: Cyclic voltammetry at different sweep rates zinc (II)/zinc (0) couple in $1 \times 10^{-2} \text{ mol dm}^{-3} \text{ Zn(II)}$ and $2.5 \times 10^{-1} \text{ mol dm}^{-3} \text{ Na(CH}_3\text{SO}_3)$ at 60°C ; HDPE-2 electrode (0.38 cm^2).

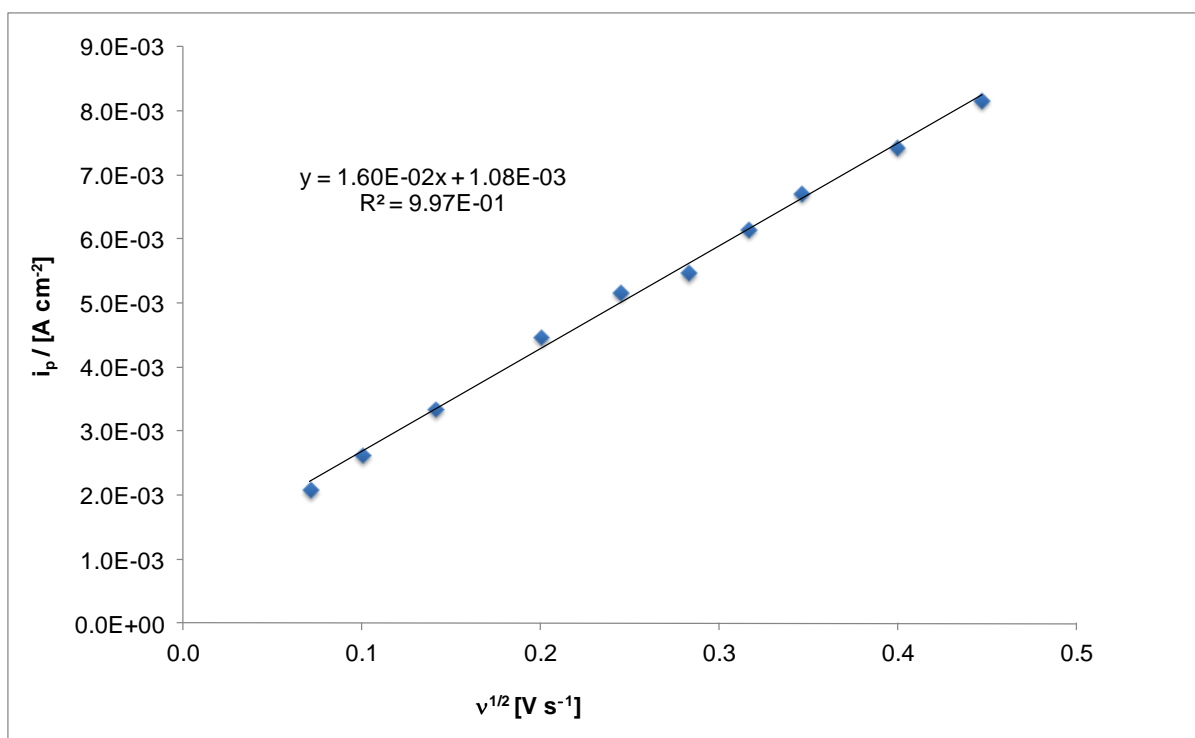


Fig.5.14: Randles-Sevcik plot zinc (II)/zinc (0) couple in $1 \times 10^{-2} \text{ mol dm}^{-3} \text{ Zn(II)}$ and $2.5 \times 10^{-1} \text{ mol dm}^{-3} \text{ Na(CH}_3\text{SO}_3)$ at 60°C ; PVDF electrode (0.38 cm^2).

	$D / (10^{-6} \text{ cm}^2 \text{ s}^{-1})$				
	Glassy Carbon	PVE	PVDF	HDPE - 1	HDPE - 2
25°C	3.57	0.72	1.17	1.12	1.17
40°C	4.39	1.11	1.75	1.98	2.79
60°C	5.92	1.24	1.95	2.34	4.51

Table 5.7: D values obtained as a function of T for various carbon substrates from the steady state study in $1 \times 10^{-2} \text{ mol dm}^{-3} \text{ Zn(II)}$ and $2.5 \times 10^{-1} \text{ mol dm}^{-3} \text{ Na(CH}_3\text{SO}_3)$.

By far the highest diffusion coefficients were obtained at the glassy carbon electrode for all the temperatures investigated. Even if the geometric area is the same for all of the substrates the results of Table 5.7 clearly suggest that the actual surface area (*i.e.* carbon sites on the surface of the electrode) is different for the substrates. The higher D values of the glassy carbon can be attributed to its smooth surface area and hence a greater number of active sites for diffusion. The values obtained from the glassy carbon electrode are in slightly lower than the values reported by Leung *et al.* [3] *ca.* $7.20 \times 10^{-6} \text{ cm}^2 \text{ s}^{-1}$ in the same medium, Meas *et al.* [25] ($7.27 \times 10^{-6} \text{ cm}^2 \text{ s}^{-1}$) in hydrochloric acid, Yu *et al.* [26] [27] in

sulfuric acid ($5.5 \times 10^{-6} \text{ cm}^2 \text{ s}^{-1}$) and Mendoza *et al.* [23] ($7.14 \times 10^{-6} \text{ cm}^2 \text{ s}^{-1}$) in chloride solutions.

It is interesting to note the relation in the effective diffusion coefficient between these different electrode surfaces. Normally, the diffusion coefficient should be independent of the properties of the electrode surface as it is concerned with the movement of the species in the solution. The measured current is proportional to the active area of the electrode and in these measurements the geometric area was always chosen to be equivalent to this. Clearly, in the composite electrodes there will be parts of the surface which will be non-conductive due to the binding polymer matrix and so they will have a reduced electroactive area. The diffusion field will merge becoming (semi-infinite) at large overpotentials but this will be coming from a reduced area of the composites electrodes. This may partially explain why the diffusion coefficient values for the composite electrodes are generally lower than that found for the glassy carbon.

5.3.3 Note - comparison of D values from sections 5.3.1 and 5.3.2

There is a difference by as much as a factor of 10 when comparing the D values obtained from the RDE analysis and the ones obtained from the Randles-Sevcik relationship for the glassy carbon electrode while for the other carbon electrodes the difference was smaller but still significant. The RDE technique is a steady state technique in which the concentration gradient is fixed by the electrode rotation as opposed to the technique of the scan rate dependence from cyclic voltammetry where the profile changes with time (*i.e* non-steady state).

Furthermore, as discussed previously there was a significant shift on the potential of the i_p during the scan rate dependence study for the zinc deposition leading to Randles-Sevcik plot that does not pass through the origin suggesting that the system is not entirely diffusion controlled. As expected, this would lead to an error on the diffusion values calculated from this method.

5.4 Nucleation studies on the formation of zinc nuclei during zinc deposition

5.4.1 Nucleation studies in a solution consisting of various concentrations of Zn(II) in $5.7 \text{ mol dm}^{-3} \text{ CH}_3\text{SO}_3\text{H}$

Nucleation studies on the glassy carbon electrode were carried out using potential steps in the range from -1.60 V to -1.85 V at 60°C . The normalised plot for the nucleation of zinc at -1.65 V on the glassy carbon electrode is presented in Fig.5.15. Superimposed on the experimental data are the simulated plots for instantaneous and progressive nucleation according to (Eq 3.21 and Eq. 3.22, Chapter 3). The zinc nucleation process on the glassy carbon seems to occur via the instantaneous route.

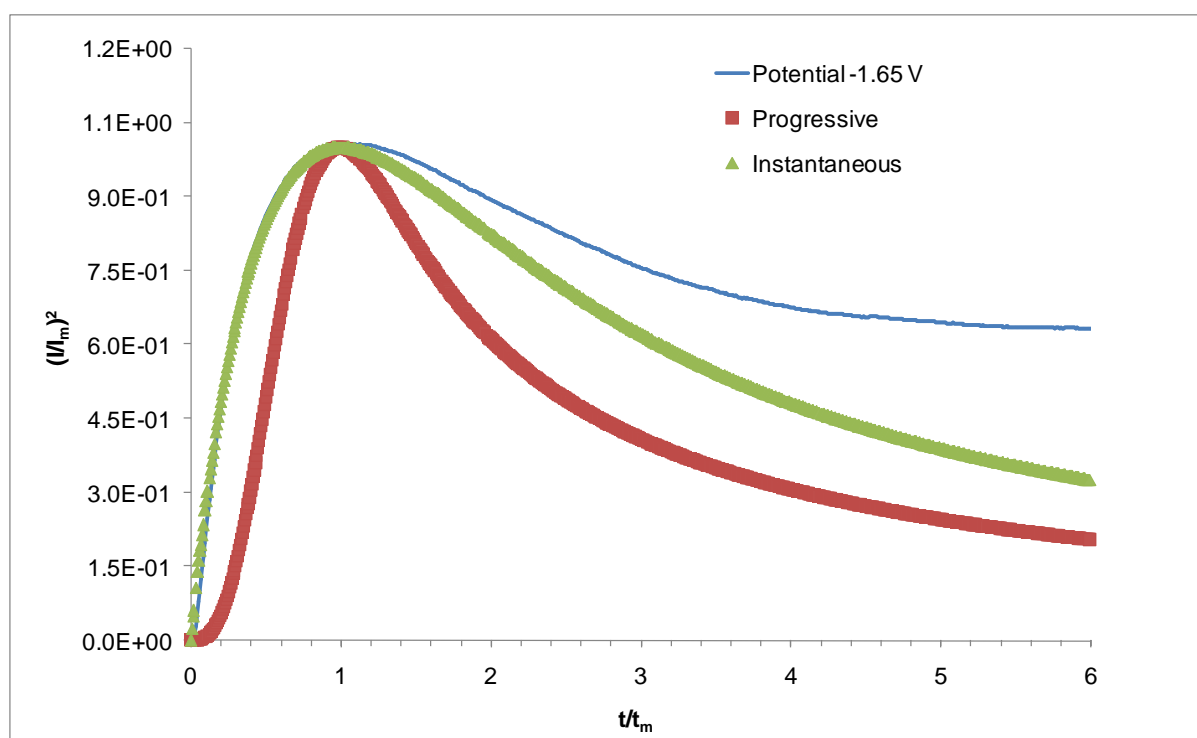


Fig.5.15: Normalised experimental current-time plots at -1.65 V for zinc electrodeposition in $7 \times 10^{-1} \text{ mol dm}^{-3} \text{ Zn(II)}$ and $5.7 \text{ mol dm}^{-3} \text{ CH}_3\text{SO}_3\text{H}$ at 60°C on a glassy carbon electrode (0.34 cm^2) compared to simulated curves for instantaneous and progressive nucleation.

From Fig.5.15 it is clear that there is a very good fit to the data during the initial portion of the curve, *viz.* at $t/t_m < 1.5$. At the final portions of the curve though, a considerable deviation of the experimental data from the theory beyond the current maximum was noticed. This is due to the increasing contribution of the HER to the measured current density. The deviation becomes more significant at more negative potentials as the HER dominates the

current measured, as shown in Fig.5.16. It has to be mentioned that in this system only the glassy carbon was able to exhibit the classic response for a nucleation and growth process. On all the other composite carbon electrodes (Table 4.2 Chapter 4), the current was dominated by the HER process and therefore the experimental nucleation plot deviated from the instantaneous and progressive nucleation plot even in the initial portions of the curve.

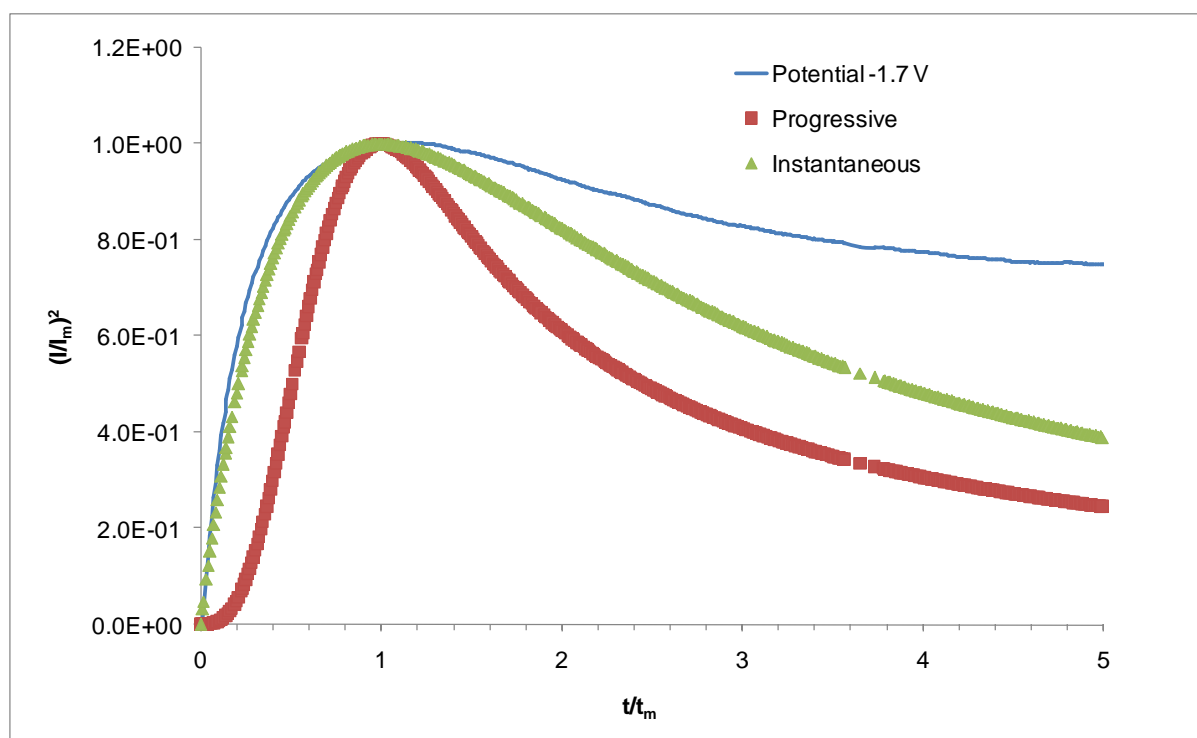


Fig.5.16: Normalised experimental current-time plots at -1.7 V for zinc electrodeposition in 7×10^{-1} mol dm^{-3} Zn(II) plus 5.7 mol dm^{-3} $\text{CH}_3\text{SO}_3\text{H}$ at 60°C on a glassy carbon electrode compared to simulated curves for instantaneous and progressive nucleation.

Table 5.8 shows the evaluated nuclei density as a function of the applied potential as obtained from Eq.3.50 and Eq.3.51, Chapter 3 for the growth of the zinc deposits from a solution containing in each case 7×10^{-1} mol dm^{-3} and 1.5 mol dm^{-3} Zn(II) in total 5.7 mol dm^{-3} methanesulfonic acid onto the glassy carbon electrode.

$7 \times 10^{-1} \text{ mol dm}^{-3} \text{ Zn(II)}$		$1.5 \text{ mol dm}^{-3} \text{ Zn(II)}$	
E / V	$N_o / (10^6 \text{ cm}^{-2})$	E / V	$N_o / (10^6 \text{ cm}^{-2})$
-1.6	0.92	-1.56	3.17
-1.625	1.66	-1.58	2.75
-1.65	2.61	-1.59	2.94
-1.675	3.42	-1.61	3.86
-1.70	5.34	-1.63	4.11
-1.725	64	-1.64	4.37
-1.75	6.72	-1.66	4.55
-1.80	12.4	-1.68	4.72
		-1.7	6.30

Table 5.8: N_o as a function of potential for a glassy carbon electrode (0.34 cm^2) in 7×10^{-1} and $1.5 \text{ mol dm}^{-3} \text{ Zn(II)}$ and $5.7 \text{ mol dm}^{-3} \text{ CH}_3\text{SO}_3\text{H}$ solution at 60°C .

The data from Table 5.8 showed that as the potentials become more negative, the nuclei density values increase in both cases. For example, a 100 mV change in potential (from -1.6 V to -1.7 V) in the solution containing $7 \times 10^{-1} \text{ mol dm}^{-3}$ zinc(II) results in the change in N_o by a factor of 6. More negative potentials imply that more energy is introduced to the system. At these potentials instantaneous nucleation is more likely to occur because of the fact that all the available sites become more or less equivalent. The N_o values obtained from this study are in good agreement with the values found by Wu *et al.* [28] from zinc chloride solutions following instantaneous nucleation, Yu *et al.* [27] in $1 \times 10^{-1} \text{ mol dm}^{-3} \text{ Zn(Ac)}_2$ and $5 \times 10^{-1} \text{ mol dm}^{-3} \text{ NaAc}$ and also by Sonneveld *et al.* [29] in an alkaline zincate solution ($2.5 \times 10^{-1} \text{ mol dm}^{-3} \text{ K}_2\text{Zn(OH)}_4$). Interestingly, a study of zinc deposition on glassy carbon electrodes by Plata-Torres *et al.* [30] in $10^{-2} \text{ mol dm}^{-3} \text{ ZnCl}_2$ revealed initial nuclei densities as low $3.9 \times 10^3 \text{ cm}^{-2}$ following progressive nucleation.

5.4.2 Nucleation studies in a solution consisting of various concentrations of Zn(II) in sodium methanesulfonate solutions

Since in highly acidic media the zinc nucleation is hindered by the HER process on the carbon composite electrodes, a neutralized solution was implemented instead in order to define the nature of nuclei growth on these substrates. The current density-time transients recorded from this study in $1 \times 10^{-2} \text{ mol dm}^{-3} \text{ Zn(II)}$ in $2.5 \times 10^{-1} \text{ mol dm}^{-3} \text{ Na(CH}_3\text{SO}_3)$ are shown in Fig.5.17 for the PVE carbon electrode at 25°C . The normalised plot for the nucleation of zinc at -1.62 V on the PVDF carbon electrode is shown in Fig.5.18.

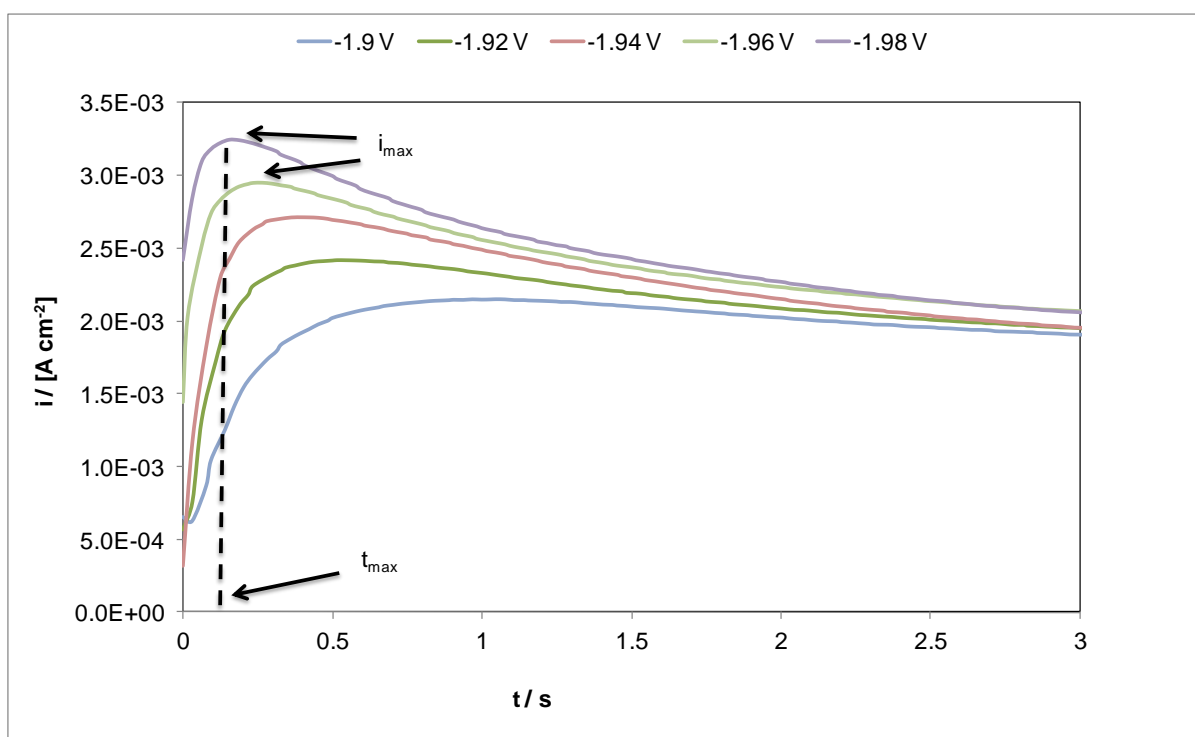


Fig.5.17: $i-t$ transients recorded for potential step experiments in $2.5 \times 10^{-1} \text{ mol dm}^{-3} \text{ Na(CH}_3\text{SO}_3)$ at 25°C on a PVE electrode containing $5 \times 10^{-3} \text{ mol dm}^{-3} \text{ Zn(II)}$; No RDE.

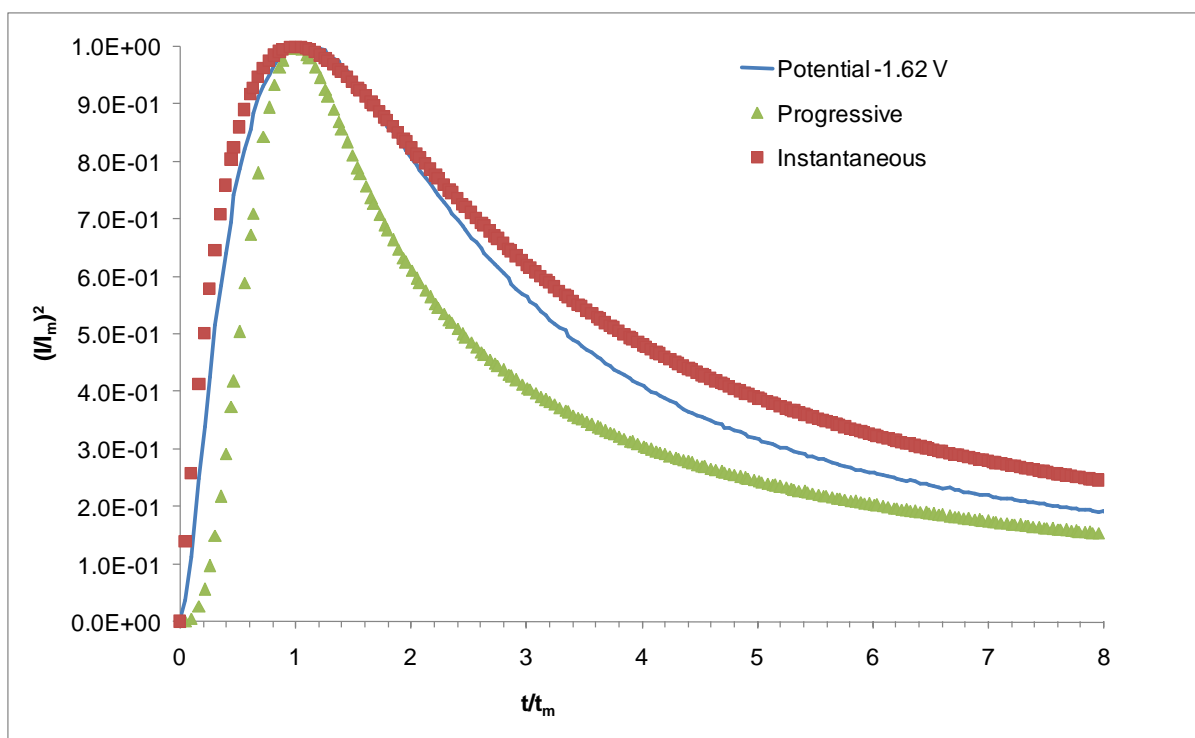


Fig.5.18: Normalised experimental I-t plots at -1.62 V for zinc electrodeposition in $2.5 \times 10^{-1}\text{ mol dm}^{-3}$ $\text{Na}(\text{CH}_3\text{SO}_3)$ containing $1 \times 10^{-3}\text{ mol dm}^{-3}$ $\text{Zn}(\text{II})$ at 25°C on a PVDF electrode compared to simulated curves for instantaneous and progressive nucleation.

From Fig.5.18 it can be clearly seen that of the two nucleation and growth mechanisms examined here, that for instantaneous nucleation is a better fit to the experimental data. This was the case for all the carbon composite materials tested in this solution, irrespective of the zinc concentration and temperature. It is important to note that the compactness and physical stability of the layer grown depends not only on the adherence of the deposit to the substrate but also on the number of nuclei formed and the rate of evolution of these growth centres.

The nuclei densities as a function of the potential from two solutions in $2.5 \times 10^{-1}\text{ mol dm}^{-3}$ $\text{Na}(\text{CH}_3\text{SO}_3)$ and different concentrations of zinc between $1 \times 10^{-3}\text{ mol dm}^{-3}$ and $5 \times 10^{-3}\text{ mol dm}^{-3}$ onto various carbon substrates are presented in Table 5.9 and Table 5.10. The nucleation study of the solution containing $5 \times 10^{-3}\text{ mol dm}^{-3}$ zinc(II) ($\text{pH} = 3.2$) was conducted at 25°C while the solution containing $1 \times 10^{-2}\text{ mol dm}^{-3}$ zinc (II) ($\text{pH} = 3.5$) was conducted at 60°C .

	PVDF	Glassy Carbon	PVE	PE-20	
E / V	$N_o / (10^4 \text{ cm}^{-2})$	$N_o / (10^4 \text{ cm}^{-2})$	$N_o / (10^5 \text{ cm}^{-2})$	E / V	$N_o / (10^5 \text{ cm}^{-2})$
-1.58	1.04	1.24	1.34	-1.61	1.43
-1.59	1.74	1.47	1.53	-1.62	3.96
-1.6	2.47	2.42	3.36	-1.63	4.42
-1.61	4.98	6.57	3.64	-1.64	6.28
-1.62	8.25	13.	4.84	-1.65	15.4
-1.65	24.0	17.9	7.42	-1.66	19.4

Table 5.9: N_o as a function of potential for various carbon electrodes in $2.5 \times 10^{-1} \text{ mol dm}^{-3} \text{ Na}(\text{CH}_3\text{SO}_3)$ and $5 \times 10^{-3} \text{ mol dm}^{-3}$ of Zn(II) at 25°C .

HDPE-2		PVE		HDPE-1		PVDF	
E / V	$N_o / (10^5 \text{ cm}^{-2})$	E / V	$N_o / (10^5 \text{ cm}^{-2})$	E / V	$N_o / (10^6 \text{ cm}^{-2})$	E / V	$N_o / (10^4 \text{ cm}^{-2})$
-1.53	1.36	-1.84	3.21	-1.62	6.09	-1.72	3.38
-1.55	1.91	-1.85	4.99	-1.63	6.98	-1.73	6.86
-1.56	2.18	-1.88	6.13	-1.64	12.8	-1.74	8.58
-1.575	4.24	-1.9	7.25	-1.65	18.2	-1.75	12.0
-1.6	8.22	-1.92	13.2	-1.67	34.3	-1.76	12.2
-1.61	9.55	-1.94	19.3	-1.69	67.4	-1.78	15.4
		-1.96	29.3			-1.8	22.0
		-1.98	67.4			-1.82	24.7

Table 5.10: N_o as a function of potential for various carbon electrodes in $2.5 \times 10^{-1} \text{ mol dm}^{-3} \text{ Na}(\text{CH}_3\text{SO}_3)$ and $1 \times 10^{-2} \text{ mol dm}^{-3}$ of Zn(II) at 60°C .

The data from Table 5.9 and Table 5.10 clearly indicate that the N_o values increase at more negative potentials as the energy applied to the system is greater. Hence, following the initial formation of the zinc centres, higher energies lead to the overlapping of the growing centres, which in turn lead to the formation of a compact zinc deposit.

At 25°C , there was a considerable difference between the N_o values formed on the PVE electrode and the PVDF and glassy carbon electrodes. The potentials here were the same so a direct comparison can be made. The data suggest that the surface of the PVE composite enhances the formation of more zinc nuclei through the instantaneous route. This

can be attributed to the fact that the solution used in this study was not that acidic resulting in the HER being suppressed. Thus, there is no competing reaction when the zinc nuclei are formed. The N_o values found for the solution containing $1 \times 10^{-2} \text{ mol dm}^{-3} \text{ Zn(II)}$ are in a similar range with the ones found by Marquez *et al.* [31] for silver nucleation on glassy carbon electrodes from silver cyanide solutions and also by Yu *et al.* [32] for zinc nucleation on glassy carbon from sulfate, chloride and acetate solutions at 25°C.

When the temperature was increased to 60°C, the potentials where the instantaneous nucleation took place were considerably higher for the PVE and PVDF electrodes, albeit with a lower zinc composition in this case. For the PVE electrode the difference was 310 mV while for the PVDF composite it was *ca.* 140 mV. This unusual behaviour may be linked to the nature of the composite electrode material. The higher temperature could lead to the expansion of the matrix which in turn will reduce the electrode conductivity and so necessitating the need for the higher potential observed. Yu *et al.* [27] however showed that elevated temperatures resulted in the increase of the N_o values in an alkaline Zn/MnO₂ battery.

5.5 Galvanic Cycles

5.5.1 Effect of rotation rate

The effect of electrode rotation rate (f) on the η_c values was clear, as can be gleaned from the data of Fig.5.19. The methodology on the galvanic cycles is discussed in p.64.

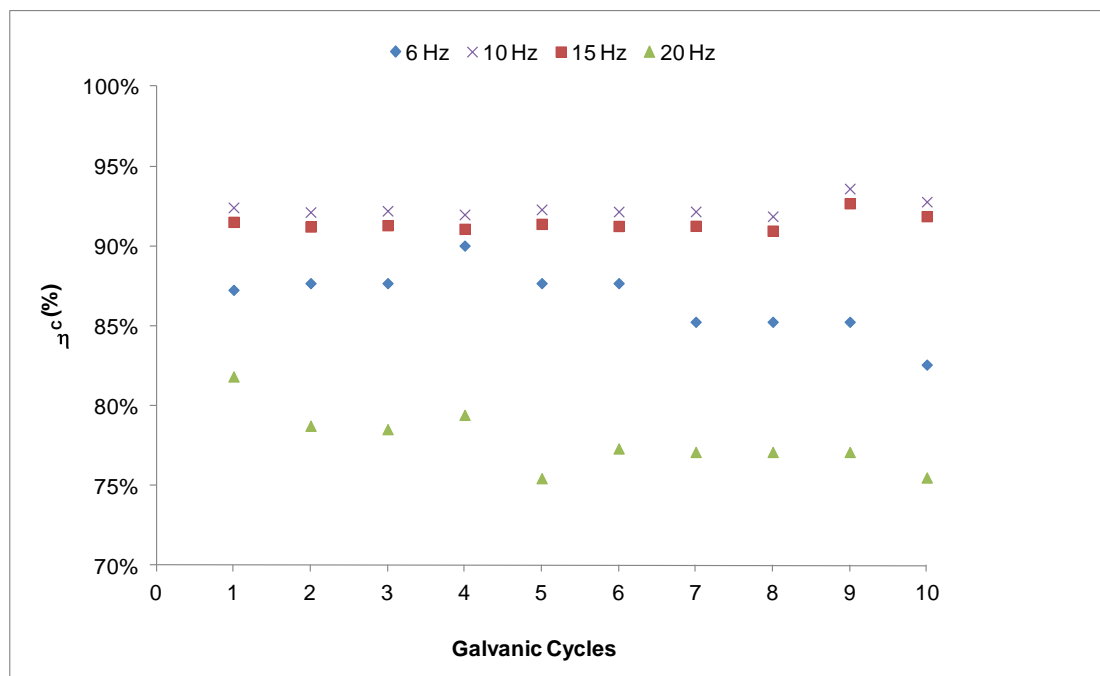


Fig.5.19: Effect of electrode rotation rate on the η_c for the HDPE-2 electrode in $1.5 \text{ mol dm}^{-3} \text{ Zn(II)}$ and $5.7 \text{ mol dm}^{-3} \text{ CH}_3\text{SO}_3\text{H}$ solution at 60°C ; charge at -50 mA cm^{-2} for 2 minutes / discharge at 50 mA cm^{-2} .

The majority of the galvanic cycles conducted at lower rotation rates *viz.* $<10 \text{ Hz}$ ($Re < 120$) showed a decrease in η_c by 5% to 15% for all of the carbon materials. The lower efficiencies could be due to bubble formation occurring/present during both charge and discharge periods as there was insufficient flow velocity to remove the bubbles from the electrode surface. At higher angular velocities, *i.e.* $10\text{--}15 \text{ Hz}$ ($200 < Re < 300$), there appeared to be very little dependence on this parameter indicating that mass transport of the electrode species does not have a major impact on the deposition/dissolution rates ($\pm 50 \text{ mA cm}^{-2}$), at least over the solution flow and deposition rates examined here. This can be explained as the deposition reaction using the constant current density ranges employed in this study is well below that mass transport limiting current density of the zinc ion concentration, which can be readily evaluated as 1.4 A cm^{-2} at 10 Hz . At 20 Hz ($Re = 247$), the efficiency is significantly lowered and this can be attributed to the shearing effect of the solution flow on any loosely adhered deposit particles ($\eta_c = 76\%$). The effect of electrode rotation rate on the η_v is summarised in Table 5.11.

Rotation speed (Hz)	5	10	15	20
<i>Re</i>	62	123	185	247
Electrode	η_V			
PVE	39%	40%	40%	33%
HDPE-1	26%	33%	33%	28%
HDPE-2	34%	39%	38%	27%
PVDF	39%	45%	46%	40%
GC	23%	22%	21%	20%
BAC2	59%	62%	63%	60%
Carbon Foil TF4	25%	35%	34%	27%
PE20	33%	46%	52%	45%

Table 5.11: Effect of electrode rotation rate on the η_V for the various carbon electrodes in 1.5 mol dm^{-3} Zn(II) and 5.7 mol dm^{-3} $\text{CH}_3\text{SO}_3\text{H}$ solution at 60°C ; charge at -50 mA cm^{-2} for 2 minutes / discharge at 50 mA cm^{-2} .

The galvanic cycles conducted at low rotation rates, *i.e.* 5 Hz, varied with regards to the type of the electrode material. The rotation rates that yielded the highest η_V values were between 10 Hz and 15 Hz indicating that these rotation speeds were the most favourable for the conduction of the galvanic cycles at 60°C . The BAC2 electrode showed the highest η_V values at 10 Hz equal to 63%. These high values stem from the fact that for the BAC2 electrode the polymer used for binding it is conductive, which is not the case for the rest of the carbon composite materials. Furthermore, the low η_V values of the glassy carbon can be attributed to the smooth surface of the latter leading to poor adhesion during charging. These findings are consistent with the values of Leung *et al.* [3] over the same media (1.5 mol dm^{-3} zinc methanesulfonate). At higher rotation rates η_V decreased for all of the carbon materials suggesting that high flow rates did not benefit the system, neither in terms of the η_C nor in terms of η_V , and of course in terms of extra energy costs.

5.5.1.1 Calculation of limiting current density (i_L) for the zinc deposition reaction containing $1.5 \text{ mol dm}^{-3} \text{ Zn(II)}$ ions.

The equation of the limiting current density is given by:

$$i_L = nFk_L C_O^*$$

Eq.5.2

Where:

$$k_L = \frac{D}{\delta} = 0.62D^{\frac{2}{3}}\omega^{\frac{1}{2}}\nu^{-\frac{1}{6}}$$

Eq.5.3

$$C_o^* = 1.5 \times 10^{-3} \text{ mol cm}^{-3}$$

$$\omega = 2\pi \times f = 62.8 \text{ s}^{-1} \text{ (for } f = 10 \text{ Hz)}$$

$$\nu: \text{ Kinematic viscosity of methanesulfonic acid (m}^2 \text{ s}^{-1}) = \mu/\rho = 3.97 \times 10^{-2} \text{ cm}^2 \text{ s}^{-1}$$

From the rotation rate study in $2.5 \times 10^{-1} \text{ mol dm}^{-3} \text{ Na(CH}_3\text{SO}_3)$ (Chapter 5, Table 5.5), $D = 1.38 \times 10^{-5} \text{ cm}^2 \text{ s}^{-1}$.

Substituting the values we get:

$$k_L = 4.83 \times 10^{-3} \text{ cm s}^{-1} \text{ and therefore } \underline{i_L = 1.40 \text{ A cm}^{-2}}$$

5.5.2 Effect of temperature

The galvanic cycles were conducted at a rotation speed of 10 Hz onto five different carbon substrates and at two different temperatures, 25°C and 60°C. The average η_C and η_V values from 10 galvanic cycles are displayed in Fig.5.12. The charge and discharge operating conditions were $\pm 50 \text{ mA cm}^{-2}$ respectively. Fig.5.12 showed that the effect of temperature on the η_C is not as considerable as it is with the η_V for the carbon electrodes tested.

Charging time (minutes)		1		5		10		20	
Electrode		η_C	η_V	η_C	η_V	η_C	η_V	η_C	η_V
PVE	25°C	95%	74%	93%	74%	91%	73%	79%	73%
	60°C	95%	42%	96%	41%	92%	42%	81%	41%
HDPE-1	25°C	94%	72%	93%	73%	90%	72%	78%	73%
	60°C	96%	32%	96%	33%	92%	33%	81%	33%
HDPE-2	25°C	93%	83%	91%	82%	89%	83%	78%	82%
	60°C	94%	38%	93%	38%	90%	39%	80%	38%
PVDF	25°C	94%	81%	93%	80%	91%	81%	81%	80%
	60°C	95%	46%	90%	47%	89%	46%	84%	47%
BAC2	25°C	91%	76%	88%	77%	86%	76%	77%	76%
	60°C	92%	61%	91%	62%	87%	62%	79%	62%

Table 5.12: Effect of temperature on η_C and η_V for various carbon electrodes in $1.5 \text{ mol dm}^{-3} \text{ Zn(II)}$ and $5.7 \text{ mol dm}^{-3} \text{ CH}_3\text{SO}_3\text{H}$ at 10 Hz; charge at -50 mA cm^{-2} / discharge at 50 mA cm^{-2} .

A decrease in η_C is observed as the charging times are increased from 1 minute to 20 minutes for all the electrode materials tested. The η_C values at room temperature were still considerably high (>93% for 1 and 5 minute charging). Calvani *et al.* [33] reported that elevated temperatures can enhance the HER in favour of the zinc deposition reaction due to stronger depolarizing effects (*i.e* the electron transfer process is easier for the/a reaction to happen).

As far as the η_V is concerned, the values were significantly higher (>30%) when the galvanic cycles were conducted at room temperature *viz.* 25°C. From Table 5.12, the highest η_V values recorded were for the HDPE-2 composite *viz.* 83% for all charging times giving an overall energy efficiency (η_E) of *ca.* 77%. The results of the PVDF electrode were similar to the HDPE-2 electrode with η_V values averaging at 81% and η_E values equal to 76%. Higher

η_V imply that the potentials at which charging and discharging occur are very similar, meaning negligible overpotential and ohmic losses for the charge and discharge reactions. An example is shown in Fig.5.20 for a PVDF composite. In this case, the open circuit potential (-1.41 V vs Hg|Hg₂SO₄ (sat.)) does not change significantly with temperature and number of cycles. However, the charging potential at 25°C and an $i_{discharge}$ of -50 mA cm⁻² was *ca.* -1.68 V while at 60°C it was equal to -1.965 V. The discharging potential at 60°C and 50 mA cm⁻² was at -0.81 V whereas at 25°C it was -1.29 V. This trend (*i.e.* effect of temperature on η_V) was found for all electrodes tested for zinc deposition and dissolution. Since this is unlikely to originate from the overpotential term, this increased overpotential loss must come from the ohmic term.

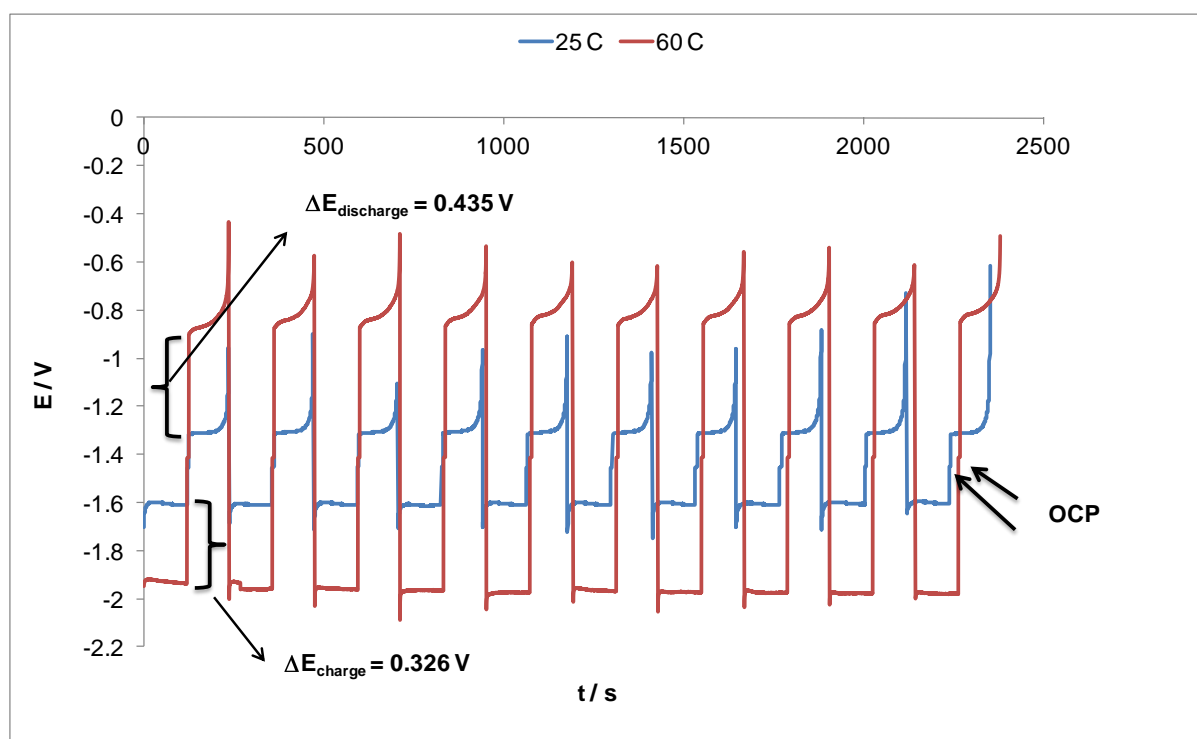


Fig.5.20: Charge discharge curves at different T for the PVDF electrode in 1.5 mol dm⁻³ Zn(II) and 5.7 mol dm⁻³ CH₃SO₃H solution at 10 Hz; charge at -50 mA cm⁻² for 2 minutes / discharge at 50 mA cm⁻².

A possible explanation of this trend could be that at 60°C, the expansion of the matrix might lead to loss of contact between the carbon particles and so to loss of electrical conductivity. Leung *et al.* [3] has also reported that higher temperatures have a stronger depolarising effect on hydrogen evolution than zinc deposition leading to poorer zinc deposits at elevated temperatures.

5.5.3 Different carbon composite materials

5.5.3.1 Effect of carbon composite materials on η_c and η_v

According to Frackowiak *et al.* [34] the key parameters for the selection of carbon materials are the following: pore geometry, size distribution, average pore size, wettability (*i.e* when a liquid spreads on a solid substrate) and presence of electroactive species. Fig.5.21 compares the different electrode material performances directly in terms of the η_c . In this case, the conditions of the galvanic cycles involved charging for one minute at -50 mA cm^{-2} under a rotation speed of 10 Hz at 60°C . The discharge current density was 50 mA cm^{-2} .

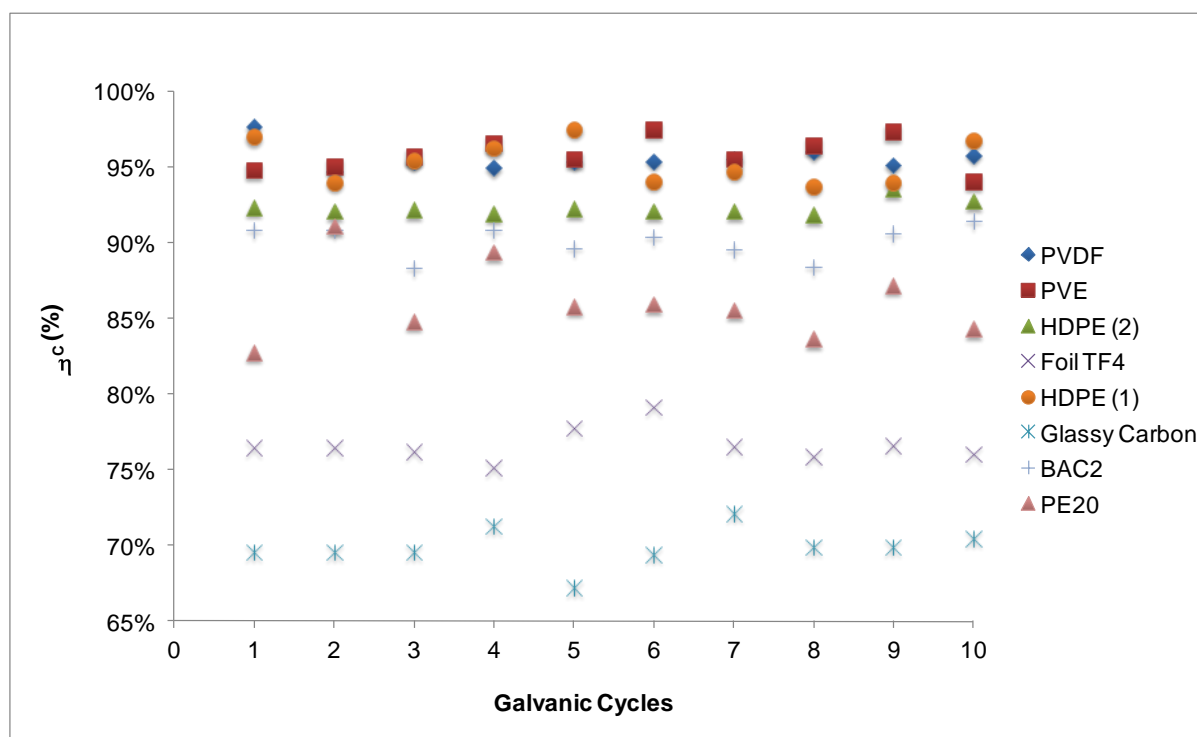


Fig.5.21: Comparison of various carbon substrates in $1.5 \text{ mol dm}^{-3} \text{ Zn(II)}$ and $5.7 \text{ mol dm}^{-3} \text{ CH}_3\text{SO}_3\text{H}$ solution at 60°C and 10 Hz; charge at -50 mA cm^{-2} for 1 minute / discharge at 50 mA cm^{-2} .

The results from Fig.5.21 indicated that the PVDF and the HDPE-1 carbon materials showed the best performance of all the carbon composite materials examined here with η_c equal to 96%. The PVE and HDPE-2 electrodes exhibited η_c values averaging 95% and 93% respectively. The results of the other three carbon electrodes investigated (glassy carbon, PE 20 and BAC2) are displayed in Table 5.13.

Charging time (minutes)		1		5		10		20	
		η_C	η_V	η_C	η_V	η_C	η_V	η_C	η_V
PE20 (0.54 cm ²)	25°C	83%	55%	73%	55%	66%	56%	52%	55%
	60°C	85%	30%	75%	31%	67%	30%	55%	29%
Glassy Carbon (0.34 cm ²)	25°C	70%	42%	60%	44%	<50%	54%	40%	44%
	60°C	72%	22%	63%	23%	<50%	24%	40%	23%
Carbon Foil TF4 (0.38 cm ²)	25°C	78%	58%	70%	60%	62%	60%	54%	59%
	60°C	79%	34%	81%	34%	65%	34%	55%	34%

Table 5.13: Effect of temperature on η_C and η_V for various carbon electrodes in 1.5 mol dm⁻³ Zn(II) and 5.7 mol dm⁻³ CH₃SO₃H solution at 10 Hz; charge at -50 mA cm⁻² / discharge at 50 mA cm⁻².

Clearly, it can be seen that there is a significant fall in both η_C and η_V values by 10% to 20% when compared with the results of Table 5.12. But, as with the electrodes of Table 5.12, lower temperatures (*viz.* 25°C) yielded higher η_V . The drop in η_C here would indicate that there might be issues with the adhesion of the zinc deposit to the substrate surface or with the increase in the HER process on these surfaces.

One possible explanation for the difference in both η_C and η_V could be the increased hydrophobicity of the composite due to the presence of the -C-F bond in the PVDF electrode compared to the -C-H- bond in the HDPE polymer. In the strong acidic electrolyte employed here, it is very likely that the HDPE layer may have undergone a delamination process leading to a weakening of the binding properties of the polymer and in turn to degradation in the structure of the composite electrode. This naturally affects the morphology of the zinc deposited on the materials.

5.5.3.2 Effect of cycling on carbon composites

The composite materials that exhibited the greatest long term stability to cycling were the PVE and PVDF based electrodes as shown in Table 5.14. No deterioration was observed in η_C or indeed in the physical structure of the electrode surface with prolonged cycling (>200 cycles). This is in contrast with the results obtained for both the HDPE-2 and PE-20 and carbon foil electrodes, which degraded substantially after 70 cycles. Under the highly acidic environment, it is very likely that the thin carbon layers of the carbon foil, PE20 and HDPE-1 electrodes may undergo a delamination process. The binding and structural properties of these electrodes cannot withstand the acidic environment and thus the surface decomposes and becomes rough (Fig.5.22). This will in turn lead to lower η_C and η_V values.

Number of Galvanic cycles			
	Electrode degradation after	η_C decreased after	η_V decreased after
PVE	200	>200	180
HDPE-1	180	150	140
HDPE-2	70	60	50
PVDF	200	>200	185
PE20	85	80	75
Carbon Foil TF4	70	60	50
BAC2	120	100	100

Table 5.14: Effect of prolonged cycling onto various carbon electrodes in a solution containing $1.5 \text{ mol dm}^{-3} \text{ Zn(II)}$ and $5.7 \text{ mol dm}^{-3} \text{ CH}_3\text{SO}_3\text{H}$.

The optical microscopy examination for the HDPE-2 and BAC2 electrodes as well as the SEM images of the PVE carbon surface shown in Fig.5.22 clearly confirmed the roughness of the carbon composite electrode surfaces. The surface of these carbon composites cannot endure repeated cycling in such high acid concentrations (2.7 mol dm^{-3} excess H^+) and as a result the surface degraded. It is worth mentioning that the η_V decreased much faster over the cycling period than the η_C for the majority of the carbon composite materials tested signifying that the kinetics of the zinc reaction have become more inhibited.

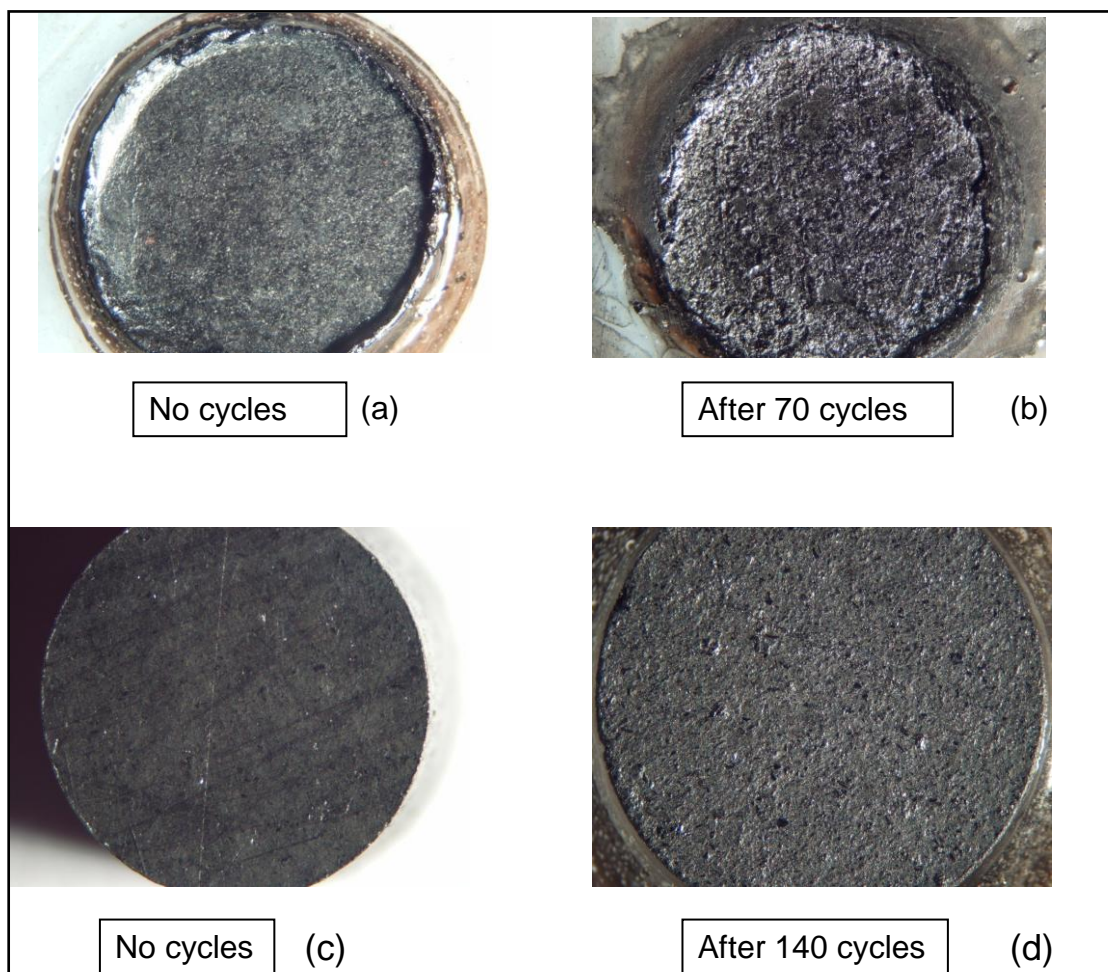


Fig.5.22: Optical microscopy of (a) (b) HDPE-2 and (c) (d) BAC2 electrode surfaces before and after conducting galvanic cycles in $1.5 \text{ mol dm}^{-3} \text{ Zn(II)}$ and $5.7 \text{ mol dm}^{-3} \text{ CH}_3\text{SO}_3\text{H}$ ($\phi=2.5$).

The effect of cycling on the carbon composite materials was also investigated by means of cyclic voltammetry. Fig.5.23 shows the voltammetric behaviour of the HDPE-1 based electrode in 1.5 mol dm^{-3} zinc methanesulfonate measured after the conduction of 100 cycles and again after a further 70 cycles. The scan rate (20 mV s^{-1}) was reversed when the potential reached a value of -2 V resulting in zinc dissolution. The anodic scan of the voltammogram stopped at -0.4 V at 10 Hz and 60°C .

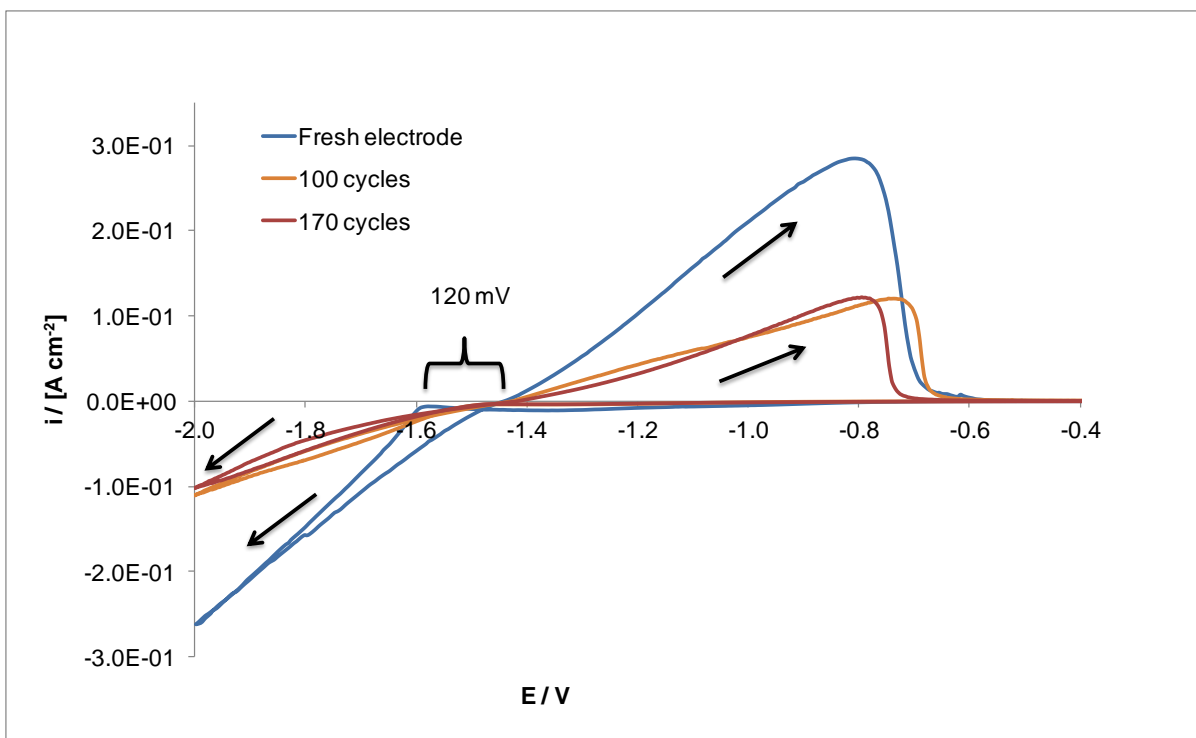


Fig.5.23: Cyclic voltammetry of zinc deposition onto a carbon HDPE-1 composite electrode in $1.5 \text{ mol dm}^{-3} \text{ Zn(II)}$ and $5.7 \text{ mol dm}^{-3} \text{ CH}_3\text{SO}_3\text{H}$ at 20 mV s^{-1} , 10 Hz and 60°C .

The potential at which zinc started depositing on the fresh electrode was equal to -1.59 V , around 120 mV more negative compared to the potentials required for the electrode after galvanic cycling. However, the current density increases much more slowly than for the fresh electrode, indicating that although nucleation occurs easier on the roughened electrode there are fewer sites available for zinc deposition. This stems to the delamination of the surface severely affecting the integrity, structure and conductivity of the electrode material. For the remaining electrodes, the onset potential shifted to more negative potentials as the electrodes under examination were under a larger number of galvanic cycles.

5.5.4 Effect of charging time on η_C and η_V

The dependence of the η_C on the duration of the charging period is shown in Fig.5.24 for the BAC2 based electrode at 10 Hz and 60°C . The trend here shows that shortest deposition times (from 1 minute to 5 minutes) give the highest η_C values, *ca.* 96% while at longer periods of charging (40 minutes) η_C reduces to $\sim 70\%$. The effect of charging on the η_C and the η_V for the other composite carbon electrodes is already given in the previous sections, *viz.* Table 5.12 and Table 5.13. The trend generally for these electrodes is the same as with the BAC2 electrode.

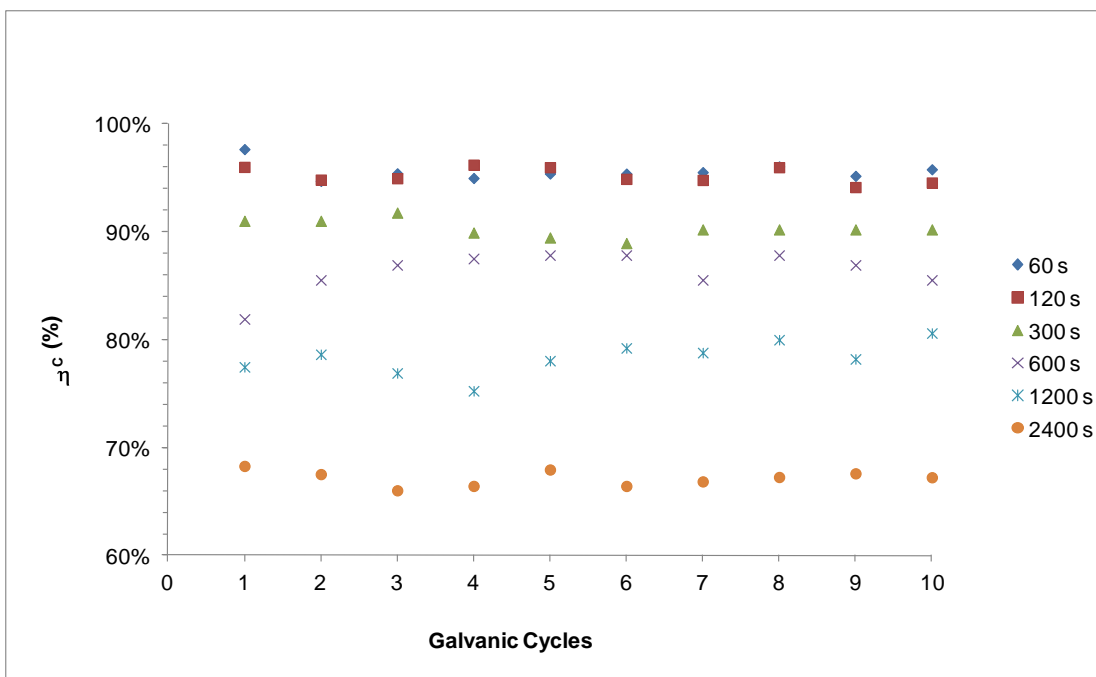


Fig.5.24: Effect of charging time on η_c in $1.5 \text{ mol dm}^{-3} \text{ Zn(II)}$ and $5.7 \text{ mol dm}^{-3} \text{ CH}_3\text{SO}_3\text{H}$ solution at 60°C and 10 Hz ; charge at -50 mA cm^{-2} for 1 minute / discharge at 50 mA cm^{-2} ; BAC2 electrode.

For the HDPE-2, PE20 and carbon foil TF4 electrodes the corresponding variation in η_c was greater, with the η_c decreasing to between 55% and 65% at the longest deposition time *i.e.* 40 minutes. The η_v however does not appear to be dependent on charging time as this represents simply the overpotentials for the deposition and dissolution reaction and should not therefore be a function of film thickness.

The decrease in η_c with increasing charging time could not be attributed to the HER and/or a change in the nature of the zinc deposit during charging since zinc inhibits the HER. A more likely explanation is that as the deposit increases in thickness, the surface morphology changes giving rise to dendritic and non-uniform growth, which can be more easily removed from the surface, especially at higher rotation rates. Zhang *et al.* [35] reported that for a zinc bromine battery, prolonged cycling increased the growth of zinc platelets which in turn increased the reaction area for zinc deposition leading to a decrease in the real current density under constant current.

5.5.5 Effect of discharge current density

So far, only galvanostatic charge/discharge cycles at -50 mA cm^{-2} during charge and 50 mA cm^{-2} during discharge were conducted on these carbon-based electrodes for which the η_C as well as the η_V values were evaluated. Table 5. summarises the efficiencies at a rotation speed of 10 Hz for different charge and discharge current densities *viz.* from $\pm 25 \text{ mA cm}^{-2}$ to $\pm 100 \text{ mA cm}^{-2}$. The operating temperature in all cases was 60°C while the charging period was set to one minute.

$i_{\text{charge}}/i_{\text{discharge}} / \text{mA cm}^{-2}$	± 25		± 50		± 100	
	η_C	η_V	η_C	η_V	η_C	η_V
PVE	87%	52%	96%	41%	97%	22%
HDPE-1	88%	59%	96%	33%	97%	15%
HDPE-2	86%	60%	94%	38%	95%	19%
PVDF	80%	56%	92%	47%	95%	27%
BAC2	82%	51%	90%	62%	92%	45%
PE20	49%	68%	75%	31%	78%	19%
Glassy Carbon	60%	34%	70%	23%	-*	-*
Carbon Foil TF4	68%	34%	81%	34%	82%	11%

Table 5.15: Effect of charge and discharge current density on η_C and η_V on various carbon substrates in $1.5 \text{ mol dm}^{-3} \text{ Zn(II)}$ and $5.7 \text{ mol dm}^{-3} \text{ CH}_3\text{SO}_3\text{H}$ at 10 Hz and 60°C ; charging time: 1 minute.

*: Very low value

The results from Table 5. evidently suggested that the charge and discharge current densities have a strong influence on the measured efficiencies for all carbon substrates. In the case where the charge and discharge current densities were reduced to $\pm 25 \text{ mA cm}^{-2}$, the η_V increased due to the less ohmic resistance losses and the charge-transfer losses obtained, as expected. The observation that the highest η_C was found at the highest charge/discharge current density would indicate that the HER process is reduced at these high current levels. This could be because the surface of the electrode here became rapidly covered by the zinc and so suppressed the HER process. The effect on η_V and η_C when maintaining the charge current constant at 50 mA cm^{-2} but varying the discharge current density is presented in Table 5.. The operating conditions were the same as with Table 5. except for the charging time that was set on 2 minutes.

$i_{discharge} / \text{mA cm}^{-2}$	25		50		100		150	
	η_c	η_v	η_c	η_v	η_c	η_v	η_c	η_v
PVE	83%	52%	93%	41%	92%	25%	92%	19%
HDPE-1	85%	40%	93%	33%	92%	24%	92%	18%
HDPE-2	78%	54%	93%	38%	92%	25%	90%	15%
PVDF	80%	56%	92%	47%	90%	31%	89%	22%
BAC2	80%	61%	91%	62%	90%	49%	88%	40%
PE20	55%	68%	75%	31%	77%	30%	78%	20%
Glassy Carbon	60%	34%	70%	23%	68%	>15%	-*	-*
Carbon Foil TF4	56%	34%	81%	34%	80%	23%	79%	>8%

Table 5.16: Effect of discharge current density on η_c and η_v on various carbon substrates in a solution consisting of $1.5 \text{ mol dm}^{-3} \text{ Zn(II)}$ in $5.7 \text{ mol dm}^{-3} \text{ CH}_3\text{SO}_3\text{H}$ at 10 Hz and 60°C ; charging time: 2 minutes.

*: Very low value

The data gleaned from Table 5. do not show any significant change in η_c compared with the data of Table 5.. As expected, the dependence on the $i_{discharge}$ was found to be very significant for the η_v . Elevated $i_{discharge}$ values led to the increase of the overpotential which in turn resulted into lower η_v values because of larger ohmic losses. This dependence on $i_{discharge}$ could also stem from a decreasing competition at high discharge currents from the corrosion of the zinc in the acid solution. However over the time scale of these experiments, corrosion of zinc is not a serious issue even at the lowest of the current densities employed for the PVDF electrode.

5.5.6 Effect of zinc methanesulfonate concentration

The effect of the zinc (II) concentration on η_V and η_C for a PVE based electrode at 60°C and a charging period of 5 minutes is shown in Fig.5.25. The rotation speed was 10 Hz while 50 mA cm⁻² of constant current was applied to the system during charge and discharge. The zinc methanesulfonate concentration in the solutions was between 7 × 10⁻¹ mol dm⁻³ and 2 mol dm⁻³ as shown in Table 5.17. Since the total methanesulfonic acid concentration was not changed in these solutions increasing the zinc (II) concentration resulted in a decrease in the acid content.

[Zn(II)] / mol dm ⁻³	Free acid concentration [H ⁺] / mol dm ⁻³
0.7	2
1	1.7
1.5	1.2
1.8	0.9
2	0.7

Table 5.17: Zinc(II) and free acid concentrations of the zinc methanesulfonate solutions used for the charge-discharge cycles.

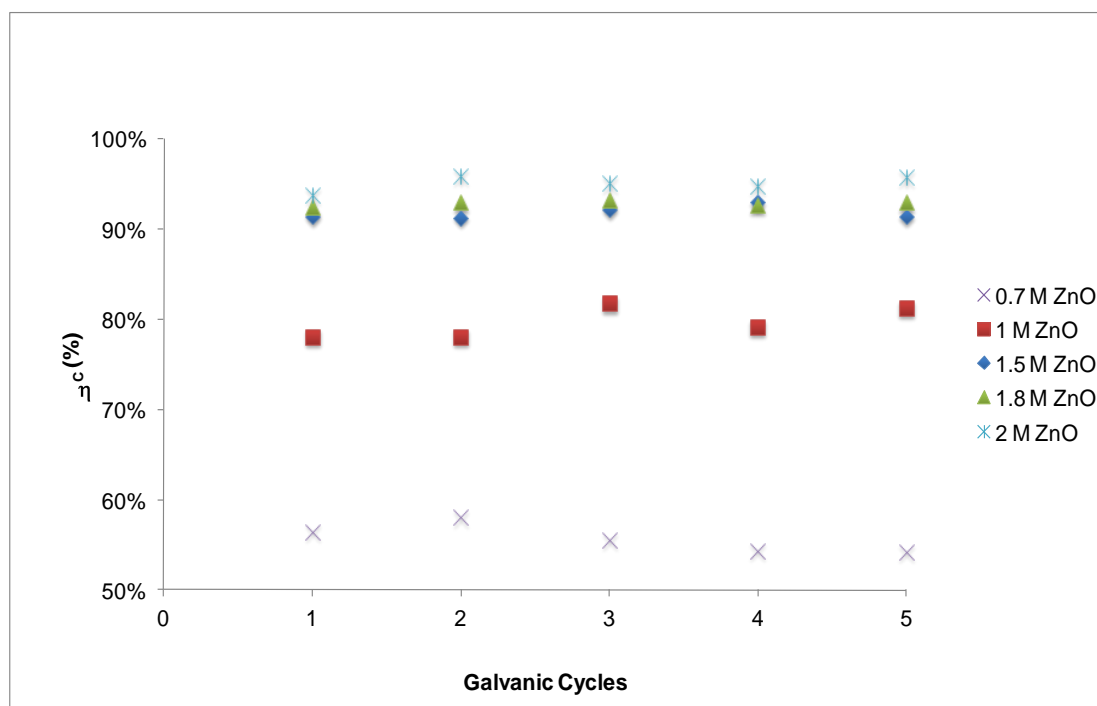


Fig.5.25: Effect of zinc methanesulfonate concentration on η_C in 5.7 mol dm⁻³ CH₃SO₃H at 60°C and 10 Hz; charge at -50 mA cm⁻² for 5 minutes / discharge at 50 mA cm⁻², PVE electrode (0.38 cm²).

At 5.7 mol dm⁻³ of methanesulfonic acid, the η_C of the high zinc methanesulfonate concentrations (*i.e.* > 1.5 mol dm⁻³) was greater than 95% \pm 2%. The difference in η_C between 1.5 mol dm⁻³ and 2 mol dm⁻³ zinc (II) was insignificant. At lower zinc (II) concentrations the η_C values decreased to 80% for 1 mol dm⁻³ zinc methanesulfonate and to 55% for 7×10^{-1} mol dm⁻³.

Here, the η_C of the system was reduced due to the fact that at 7×10^{-1} mol dm⁻³, the free acid concentration was higher and this favours the competing HER process. At these low Zn(II) concentrations, the amount of zinc available for deposition is much lower which means that the HER becomes more dominant at this high current density. The above data are in agreement with the results from Leung *et al.* [3] in the same medium. Also, according to Alfantazi *et al.* [36], increasing the zinc(II) sulfate concentration to 1.4 mol dm⁻³ in sulfuric acid resulted in higher deposition efficiencies which were not affected by the acid concentration.

Regarding the η_V , Table 5.18 shows that the lowest values were obtained from the 2 mol dm⁻³ of zinc methanesulfonate solution for all three composite electrodes. Indeed, the η_V values for the PVE and HDPE-1 electrodes are at the same level at concentrations above 1.5 mol dm⁻³. At first hand, this would appear counter intuitive as the higher zinc concentration should make the deposition easier. However, the zinc dissolution reaction now has to occur in a more concentrated zinc solution and it is very likely that it is this process which is affecting the η_V .

Electrode	[Zn(II)] / mol dm ⁻³				
	0.7	1.0	1.5	1.8	2.0
PVE	30%	35%	41%	40%	38%
HDPE-1	32%	38%	33%	34%	33%
PVDF	45%	29%	47%	41%	43%
PE-20	25%	28%	30%	33%	35%
HDPE-2	30%	33%	39%	38%	37%

Table 5.18: Effect of zinc methanesulfonate concentration on η_V onto various carbon substrates in 5.7 mol dm⁻³ CH₃SO₃H at 10 Hz and 60°C; charging time: 5 minutes.

5.5.7 Effect of methanesulfonic acid concentration

The effect of the methanesulfonic acid concentration on η_c and η_v is summarised in Table 5.19 for the PVE, PVDF, BAC2 and HDPE-1 carbon composites. The charge and discharge current density was *ca.* $\pm 50 \text{ mA cm}^{-2}$ and the operating temperature was 60°C for a charging period of 10 minutes. The total methanesulfonic concentration in the solutions was between 3.5 mol dm^{-3} and 5.7 mol dm^{-3} (equivalent to free acid concentration: $5 \times 10^{-1} \text{ mol dm}^{-3}$ and 2.7 mol dm^{-3}) respectively.

[CH ₃ SO ₃ H] / mol dm ⁻³		3.5		4.5		5.7	
Electrode		η_c	η_v	η_c	η_v	η_c	η_v
PVE	25°C	92%	72%	91%	74%	91%	73%
	60°C	91%	37%	91%	40%	92%	42%
PVDF	25°C	93%	70%	91%	58%	91%	81%
	60°C	90%	30%	88%	36%	89%	46%
HDPE-1	25°C	91%	70%	91%	77%	90%	72%
	60°C	93%	22%	90%	33%	92%	33%
BAC2	25°C	90%	68%	91%	73%	86%	76%
	60°C	89%	58%	87%	69%	87%	62%

Table 5.19: Effect of methanesulfonic acid concentration on η_c and η_v in $1.5 \text{ mol dm}^{-3} \text{ Zn(II)}$ at 10 Hz and 60°C ; charging time: 10 minutes.

The data from Table 5.19 suggested that at 25°C , both the η_c and η_v are generally higher than at 60°C . The η_c values at 25°C were *ca.* $91\% \pm 2\%$, while at 60°C the values were in the range of $87\% \pm 3\%$. It would have been expected that lower methanesulfonic acid concentrations should yield higher η_c values due to the lower number of protons in the solution. Here however, this trend was not observed for all the carbon composites tested suggesting that the HER was greatly inhibited on the zinc surface as has been noted previously.

A clear impact of temperature in these acid solutions was found in the η_v values. Elevated temperatures decreased η_v and this was observed for the PVE, PVDF and HDPE-1 electrodes. Overall, higher electrolyte concentrations led to higher η_v values and this can be attributed to the possible intercalation of the ions increasing the conductivity of the matrix.

5.5.8 Effect of operating conditions on zinc deposit morphologies

5.5.8.1 Zinc deposition at the edges of the substrate

The morphology of the zinc electrodeposits was studied by scanning electron microscopy (SEM). Fig 5.27 shows the coatings of two electrodes (HDPE-1 and PVE carbon composites) after charging at 50 mA cm^{-2} for 2 minutes at 10 Hz and 60°C . These pictures were concentrated at the edges of the electrode's surface. The dendritic growth found implied non-uniform potential and current distribution to the electrode surface leading to a deposit which can be easily dislodged. Evolution of dendritic growth tends to concentrate at certain region of the electrodes, typically at the edges where the local overpotential (ohmic drop) is higher than in the centre due to the higher electrode field [37]. The latter is the driving force for roughness evolution. Once roughness elements are formed they propagate extremely rapidly and so it is then difficult to terminate these features which lead to dendritic growth.

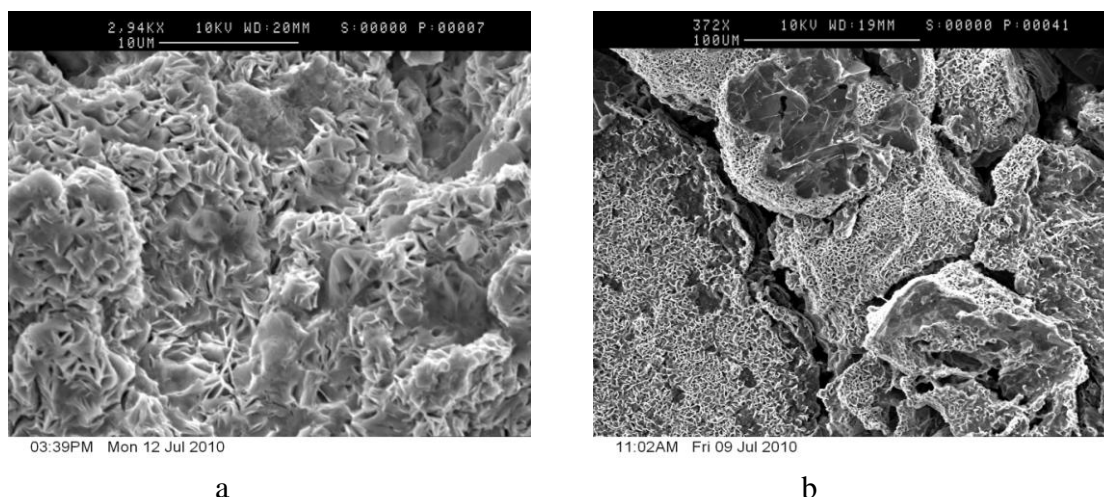


Fig.5.26: SEM pictures of zinc deposit from a solution containing $1.5 \text{ mol dm}^{-3} \text{ Zn(II)}$ and $5.7 \text{ mol dm}^{-3} \text{ CH}_3\text{SO}_3\text{H}$; 2 minutes charge at -50 mA cm^{-2} (a) HDPE-1, (b) PVE at 60°C and 10 Hz.

The SEM images for the HDPE-1 electrode (Fig.5.26 (a)) however do not show any signs of dendritic growth. There was a large formation of spikes (length $\sim 1 \mu\text{m}$) and also a bright overall deposition. Leung *et al.* [3] reported that the microstructure of zinc deposited from the methanesulfonic acid electrolyte is smooth without any nodular and dendritic growth. For the PVE electrode (Fig.5.26 (b)), the formation of needle-shaped structures was evident. A rough and non uniform surface distribution was observed with long size grains ($100 \mu\text{m}$). The same structure was found in the study of Hu *et al.* [38] in zinc chloride and zinc sulfate solutions. According to Baik *et al.* [39], the nucleation sites are more abundant on fine and oriented zinc surfaces than unidirectionally grown large crystalline surface.

5.5.8.2 Hydrogen evolution along with zinc deposition

Another illustration of the zinc deposits is shown in Fig.5.27 for the HDPE-1 and PVE electrodes. The operating conditions were the same as in Fig.5.26, except that in this case the charging time was 5 minutes.

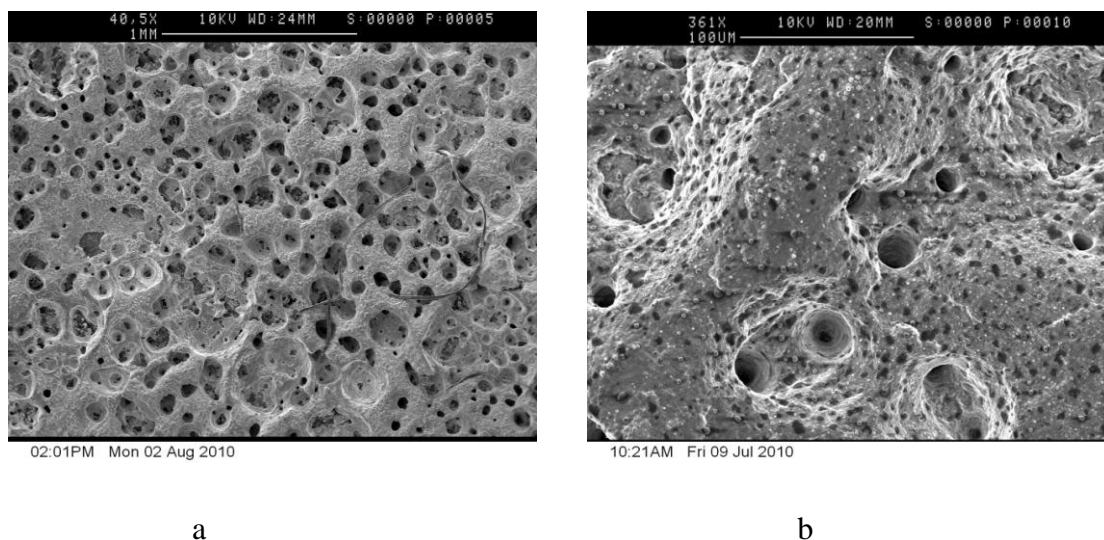


Fig.5.27: SEM pictures of zinc deposit in $1.5 \text{ mol dm}^{-3} \text{ Zn(II)}$ and $5.7 \text{ mol dm}^{-3} \text{ CH}_3\text{SO}_3\text{H}$; 5 minutes charge at -50 mA cm^{-2} (a) HDPE-1, (b) PVDF at 60°C and 10 Hz .

The pinholes observed in Fig.5.27 derive from the HER at these sites, preventing the adhesion of the zinc to that surface. The presence of the holes may also serve to explain the detachment of the zinc deposit beyond a certain time (thickness) as the hydrogen evolution could undercut and dislodge the layer. Hydrogen bubbles can also cover the cathode surface decreasing the number of sites available for the nucleation and growth of the zinc deposits. Bressen *et al.* [40] as well as Ichino *et al.* [41] have described the mechanisms for the evolution of hydrogen on zinc surfaces (Volmer-Tafel and Volmer-Heyrovsky mechanisms Eq.3.47 & Eq. 3.48 Chapter 3). These findings are similar to those reported in the study of Recendiz *et al.* [42] in a solution containing $1.3 \text{ mol dm}^{-3} \text{ Zn(II)}$ and 1.1 mol dm^{-3} sulfuric acid.

5.5.8.3 SEM of zinc deposits with prolonged cycling

The impact of prolonged cycling on the zinc deposits is illustrated in Fig.5.28 for the BAC 2 electrode at 60°C and a constant charging current of -50 mA cm^{-2} .

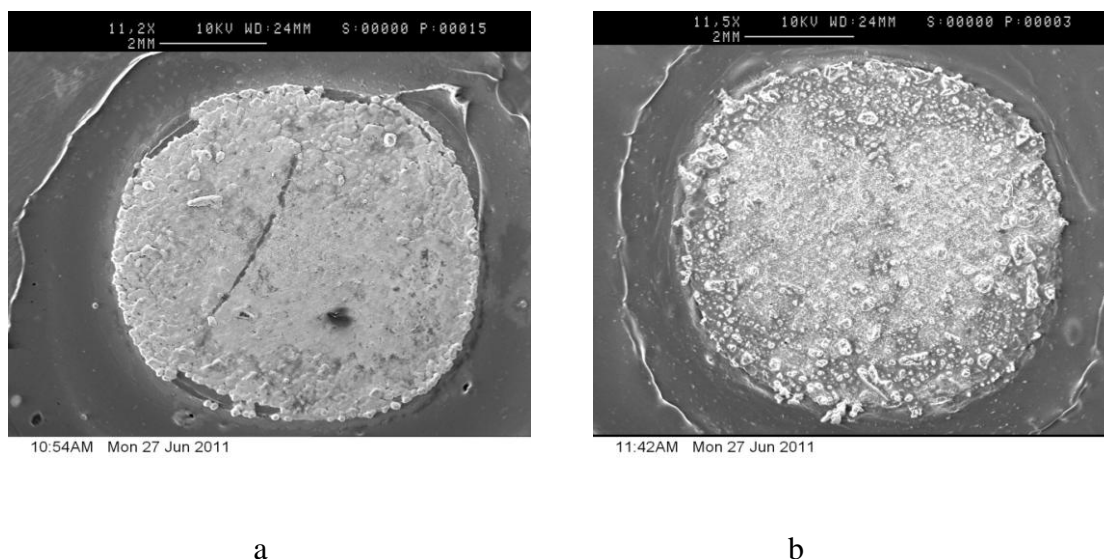


Fig.5.28:SEM pictures of zinc deposit in $1.5 \text{ mol dm}^{-3} \text{ Zn(II)}$ and $5.7 \text{ mol dm}^{-3} \text{ CH}_3\text{SO}_3\text{H}$ and at 60°C, 10 Hz and -50 mA cm^{-2} onto a BAC2 electrode; (a) 10 minutes (b) 1 hour.

From the SEM pictures of Fig.5.28, it can be seen that smaller charging times resulted in thinner coatings of zinc (Fig.5.28 (a)). The deposit looks uniform with a small number of clusters at the top of the zinc layer. The deposit obtained after 1 hour charging (Fig.5.28 (b)) is shinier but shows more evidence of clusters/grains of zinc deposited on a smoother surface. The grain shape pattern is clearly irregular, as was observed in the study of Ye *et al.* [32] in $1 \times 10^{-1} \text{ ZnCl}_2$ and $5 \times 10^{-1} \text{ NaCl}$ on a glassy carbon electrode. This morphology (*i.e* hexagonal pellets with moderate size randomly orientated) of the zinc deposits was also reported by Das *et al.* [43] from an acidic sulfate solution ($55 \text{ g dm}^{-3} \text{ Zn(II)}$ and 150 g dm^{-3} sulfuric acid).

5.5.8.4 Effect of rotation rate on PVDF electrodeposits

The effect of rotation rate on the morphology of the zinc deposits is illustrated on a PVDF electrode in Fig.5.29. Here, non-uniform growth was found to be the most severe at the edges where the local overpotentials prevailed [37] for both rotation rates investigated *viz.* 10 Hz and 20 Hz ($Re = 123$ and 247 respectively). It may well be that higher rotation rates will have removed the clusters on the top surface due to shearing effects. Such nodular zinc growth has been observed by Lacovangelo *et al.* [44] at Re between 62 and 308 (5 to 25 Hz) and a current density of 25 mA cm^{-2} . It is worth mentioning that the spikes observed here are larger in length by a factor of 10 (*i.e.* $10 \mu\text{m}$) when compared with the data of Fig.5.26 for the PVE and HDPE-1 electrodes.

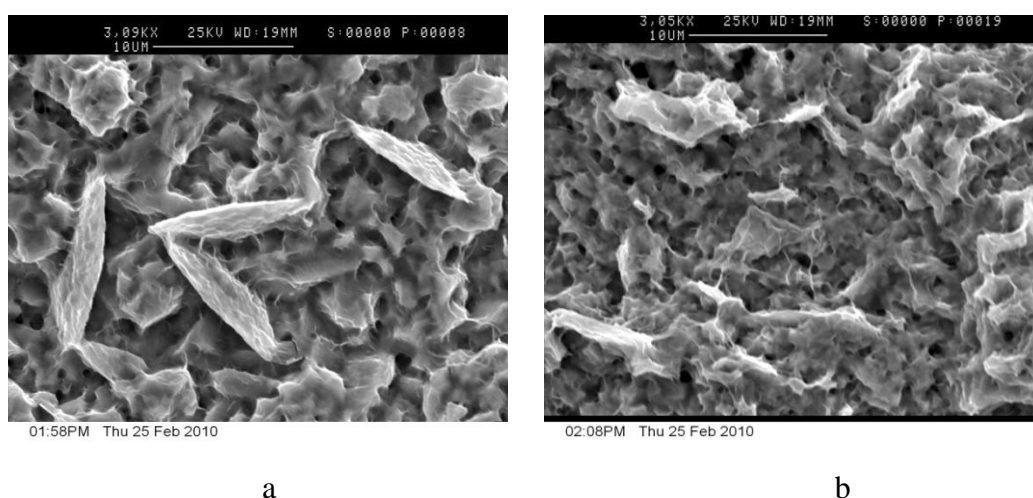


Fig.5.29: SEM pictures of zinc deposit in $1.5 \text{ mol dm}^{-3} \text{ Zn(II)}$ and $5.7 \text{ mol dm}^{-3} \text{ CH}_3\text{SO}_3\text{H}$ at 60°C and -50 mA cm^{-2} onto a PVDF electrode; charge for 2 minutes at (a) 10 Hz (b) 20 Hz.

5.5.8.5 Summary

The behaviour of the carbon composite electrodes is summarised in Table 5.20.

Electrode	Nodules-Spikes	Dendrites	Grains / Clusters	Zinc adhesion	Full coverage of surface area
PVE	✗	✓	✓	✓	✓
HDPE-1	✗	✓	✓	✓	✓
HDPE-2	✗	✗	✓	✗	✗
PVDF	✗	✓	✓	✓	✓
BAC2	✓	✗	✓	✗	✓
PE20	✗	✗	✓	✗	✗
Glassy Carbon	✓	✗	✓	✗	✗
Carbon Foil TF4	✓	✗	✓	✗	✓

Table 5.20: Characteristics of zinc deposits of various carbon electrodes in $1.5 \text{ mol dm}^{-3} \text{ Zn(II)}$ and $5.7 \text{ mol dm}^{-3} \text{ CH}_3\text{SO}_3\text{H}$ at 60°C , 10 Hz and -50 mA cm^{-2} ; ✓: Present. ✗: Not present.

The differences in the zinc morphologies stem not only from the different operating conditions such as rotation rate, charging time but also from the different carbon composite materials. Overall, the zinc deposits of the PVE, HDPE-1 and PVDF electrodes displayed the best properties. The deposits were compact, adhered well and covered fully the surface area of the electrode suggesting the presence of more uniform active sites during the zinc deposition. Still, these electrodes showed signs of nodules, spikes and clusters of different dimensions depending on the charging time especially at the edges of the deposits. But here, the non-uniform deposition of the zinc increased with charging time.

5.5.9 Effect of additives on galvanic cycles

The effect of the additives on η_C and η_V on the negative half cell electrolyte (1.5 mol dm^{-3} in 2.7 mol dm^{-3} excess methanesulfonic acid) is summarised in Table 5.21 for a deposition current density of $\pm 50 \text{ mA cm}^{-2}$.

		PVDF		PVE		HDPE-1	
<i>Additives</i>	$\times 10^{-3}$ mol dm^{-3}	η_C	η_V	η_C	η_V	η_C	η_V
-	0	93%	45%	93%	41%	93%	33%
Coumarin	2	88%	28%	85%	29%	81%	29%
Triton X-100	2	<20%	32%	<20%	62%	30%	35%
CTABr	1	80%	<20%	82%	<20%	75%	<20%
CTABr	5	82%	62%	82%	60%	79%	59%
TBAOH	2	69%	76%	50%	75%	58%	71%
Tartaric acid	2	87%	34%	86%	63%	82%	78%
Potassium Sodium Sulfate	2	60%	67%	63%	65%	55%	59%

Table 5.21: Effect of additives on η_C and η_V onto various carbon substrates in 1.5 mol dm^{-3} Zn(II) and 5.7 mol dm^{-3} $\text{CH}_3\text{SO}_3\text{H}$ at 10 Hz and 60°C ; charging time: 5 minutes.

The η_V values increased in the presence of three additives namely cetyltrimethyl-ammonium bromide ($5 \times 10^{-3} \text{ mol dm}^{-3}$), tetrabutyl-ammonium hydroxide and potassium sodium tartarate by $>20\%$. CTABr has been previously used as a surfactant in zinc electrodeposition [45]. Li *et al.* [46] has reported that CTABr brightens and smoothens the zinc deposits. The highest energy efficiency obtained was *ca.* 49% for the PVDF carbon composite material and a solution containing $5 \times 10^{-3} \text{ mol dm}^{-3}$ cetyltrimethyl - ammonium bromide.

It is worth noting that increasing the CTABr concentration from $1 \times 10^{-3} \text{ mol dm}^{-3}$ to $5 \times 10^{-3} \text{ mol dm}^{-3}$ led to a large increase in η_V , suggesting that the action of the CTA^+ species changes with concentration. This concentration effect is commonly found for the action of inhibitors which actually work only in a narrow concentration range [47] [48]. Here, the data suggest that there could be better participation in the electron transfer step by the presence of these ions. For the potassium sodium tartarate the values recorded for η_C and η_V were between 55% and 67% for all three electrodes yielding η_e of *ca.* 38%. Leung *et al.* [3] has reported that in the presence of potassium sodium tartarate, rough irregular-plate like structures were observed for the same medium while the η_e of the system was *ca.* 73% in methanesulfonic acid media. The same irregular pattern of zinc deposits was found in this study.

The use of TBAOH yielded the highest η_v , *viz.* 76% for the PVDF electrode. It is worthwhile noting that the OH^- is instantly neutralized and so, it is the TBA^+ cation which is acting as the active agent. At the same time though, the η_C decreased by 25% suggesting that the HER reaction is not hindered with this chemical present. Poor η_C could also suggest poor zinc adhesion. This same trend was noticed for the other two carbon electrodes used in this study namely, PVE and HDPE-1. Coumarin and $1 \times 10^{-3} \text{ mol dm}^{-3}$ cetyltrimethyl-ammonium bromide maintained the η_C values at high levels, *i.e.* $>80\%$ for all three carbon composites but at the same time the voltage efficiencies dropped dramatically ($<20\%$) indicating an increase in energy required for the deposition. Thus, the species are acting as cathodic inhibitors. It has been previously reported that coumarin produced a zinc deposit with a finer grain size [49].

Finally, studies using the RDE (from 10 to 20 Hz) showed that mass transport did not have a great impact to the efficiencies as the values were similar for all the carbon materials and additives tested.

5.6 Conclusion

The zinc deposition process from the sodium sulfonate electrolyte appears to follow the instantaneous nucleation route with nuclei densities (from 10^4 to 10^5 cm^{-2}) obtained from the $5 \times 10^{-3} \text{ mol dm}^{-3}$ zinc solution in this medium. Nucleation for the zinc deposition process from the methanesulfonic acid electrolyte was found to be affected by the HER at more negative potentials. The diffusion values for the 1.5 mol dm^{-3} zinc electrolyte on the glassy carbon electrode were between $3 \times 10^{-6} \text{ cm}^{-2}$ to $6.3 \times 10^{-6} \text{ cm}^{-2}$. Higher methanesulfonic acid concentrations shifted the nucleation potentials towards more negative values, due to the higher conductivity of the electrolyte (k) and the increased excess proton concentration.

The diffusion coefficients from the methanesulfonate electrolyte increased with temperature from $4.6 \times 10^{-6} \text{ cm}^2 \text{ s}^{-1}$ to $1.38 \times 10^{-5} \text{ cm}^2 \text{ s}^{-1}$ as well as the standard rate constants (*i.e* from $1.6 \times 10^{-4} \text{ cm s}^{-1}$ to $3.4 \times 10^{-3} \text{ cm s}^{-1}$). The HDPE-2 based carbon composite exhibited slightly faster kinetics compared to other materials. The same dependence with temperature was found for the Zn(II)/Zn(0) reaction as well as cyclic voltammetry onto 1.5 mol dm^{-3} methanesulfonate electrolyte.

The carbon PVE, HDPE-2 and PVDF electrode materials showed the best performance in terms of η_c (>96 %), robustness and stability (>200 cycles). The HDPE-1 and graphite foil type electrodes such as the TF4 degraded considerably after 70 cycles. Higher zinc (II) concentrations and lower cell operating temperatures (25°C) favoured η_v with values ranging from 75% to 85% depending on the electrode substrate. The optimum charge and discharge current densities were found to be between $\pm 50 \text{ mA cm}^{-2}$ and 100 mA cm^{-2} as η_e values of *ca.* 78% were achieved for the HDPE-2 electrode. The nature of the zinc deposit was found to change with different charging periods.

With regards to the flow velocity, the outcome of the cyclic voltammetry RDE studies and galvanic cycles suggested that the optimum rotation rate for the zinc reduction and oxidation reactions was between 10 Hz and 15 Hz. Lower rotation rates led to bubble formation due to the HER while higher angular velocities resulted in loosely adhered shearing off the surface.

-
- [1] V.G. Levich, *Physicochemical Hydrodynamics.*, Prentice Hall, (1962).
- [2] M. Pourbaix, *Atlas of Electrochemical Equilibria in Aqueous Solutions*, Pergamon, London (1966).
- [3] P.K. Leung, C. Ponce-de-León, C.T.J. Low, F.C. Walsh, *Electrochim. Acta.*, **56**, 6536-6546, (2011).
- [4] D. Pletcher, F.C. Walsh, *Industrial Electrochemistry*, Blackie Academic and Professional, London (1993).
- [5] H. Van Parys, G. Teliás, V. Nedashkivskyi, B. Mollay, I. Vandendael, S. Van Damme, J. Deconinck, A. Hubin, *Electrochim. Acta.*, **55**, 20, 5709-5718, (2010).
- [6] G. Nikiforidis, L. Berlouis, D. Hall, D. Hodgson, *J. Power Sources.*, **206**, 497- 503, (2012).
- [7] J. Wang, *Electroanalytical Chemistry*, 2nd edition, Wiley, New York, (2000).
- [8] R.L Mc. Creery, *Carbon electrodes: Structural effects on electrotransfer kinetics in: A.J. Bard . Electroanalytical*, vol. 18, Dekker, New York, (1991).
- [9] C. Cachet, R. Wiart, *Electrochim. Acta.*, **44**, 4743, (1999).
- [10] L. Simanavicus, A. Stakenas, A. Sarkis, *Electrochim. Acta.*, **42**, 1581, (1997).
- [11] E. Michailova, I. Vitanova, D. Stoychev, A. Milchev, *Electrochim. Acta*, **38**, 2455, (1993).
- [12] R.K. Ghavami , Z. Rafiei, *J. Power Sources.*, **162**, 893-899, (2006).
- [13] A. Gomes, M.I. da Silva Pereira, *Electrochim. Acta.*, **52**, 863, (2006).
- [14] A. Recendiz, I. Gonzalez, J. Nava, *Electrochim. Acta.*, **52**, 6880-6887, (2007).
- [15] S.H. Kim, E.J. Jung, E.M. So, C.Z. Shen, H.J. Chun, Y.M. Kim, I.K. Kim, *Bull. Korean Chem. Soc.*, **27**, 9, 1329, (2006).
- [16] A.J. Bard, L.R. Faulkner, *Electrochemical Methods: Fundamentals and Applications*. New York: John Wiley and Sons, pp. 100-106, (2001).
- [17] M.A.M. Ibrahim, *J. Chem. Technol. Biotechnol.*, **75**, 745, (2000).
- [18] E. Guerra, *Evaluation of Zinc Electrodeposition Kinetics from Acidic Zinc Sulfate Solutions using a UPD Modified Platinum Substrate*, University of British Columbia, 2003. <https://circle.ubc.ca/handle/2429/16770>.
- [19] N.M Martyak, *Surf. Coat. Technol.*, **88**, 139, (1996).
- [20] D.S. Baik, D.J. Fray, *J. Appl. Electrochem.*, **31**, 1141-1147, (2001).
- [21] L.E. Morón, A. Méndez, F. Castaneda, J.G. Flores, L. Ortiz-Frade, Y. Meas, G. Trejo, *Surface & Coatings Technology.*, **205**, 4985-4992, (2011).

-
- [22] W.E. Price, H. Weingärtner, *J. Phys. Chem.*, **95**, 8933, (1991).
- [23] L.H. Mendoza-Huizar, C.H. Rios-Reyes, M.G. Gómez-Villegas, *J. Mex. Chem. Soc.*, **53**, (4), 243-247, (2009).
- [24] J.T. Edward, *J. Chem. Education.*, **47**, 4, 261-269, (1970).
- [25] G. Trejo, H. Ruiz, R. Ortega Borges, Y. Meas, *J. Appl. Electrochem.*, **31**, 685, (2001).
- [26] J. Yu, H. Yang, X. Ai, Y. Chen, *Russian J. Electrochem.*, **38**, 321, (2002).
- [27] J. Yu, L. Wang, L. Su, X. Ai, H. Yang, *J. the Electrochemical Society.*, **150**, 1, 19-23, (2003).
- [28] H.H. Wu, S.K. Xu, S.M. Zhou, *Acta Physico-Chim. Sin (Chn).*, **1**, 357-364, (1985).
- [29] P.J. Sonneveld, W. Visscher, E. Barendrecht, *Electrochim. Acta.*, **37**, 7, 1199-1205, (1992).
- [30] M. Plata-Torres, S.L. Olvera-Vázquez, C. Ramírez-Rodríguez, A. Ezeta-Mejía, H. Dorantes-Rosales, E.M. Arce-Estrada, *ECS Transactions.*, **3**, 25, 25-33, (2007).
- [31] K. Marquez, G. Staikov, J.W. Schultze, *Electrochim. Acta.*, **48**, 875-882, (2003).
- [32] J. Yu, H. Yang, X. Ai, Y. Chen, *Russian J. Electrochem.*, **38**, 3, 363-367, (2002).
- [33] I.A. Carlos, F. Galvani, *J. Met. Finish.*, **95**, 70, (1997).
- [34] E. Frackowiak, F. Beguin, *Carbon.*, **39**, 937-950, (2001).
- [35] L. Zhang, J. Cheng, Y. Yang, Y. Wen, X. Wang, G. Caob, *J. Power Sources.*, **179**, 381-387, (2008).
- [36] A.M. Alfantazi, D.B. Dreisinger, *J. Appl. Electrochem.*, **31**, 41, (2001).
- [37] U. Landau, J.H. Shyu, *Roughness evolution and dendritic growth on zinc electrodeposition from halide electrolytes*, Care Western Reserve University, (1983).
- [38] C. Hu, C. Chang, *Materials Chemistry and Physics.*, **86**, 195-203, (2004).
- [39] D.S. Baik, D.J. Fray, *J. Appl. Electrochem.*, **31**, 1141-1147, (2001).
- [40] J. Bressen, R. Wiart, *J. Appl. Electrochem.*, **9**, 43, (1979).
- [41] R. Ichino, C. Cachet, R. Wiart, *Electrochim. Acta.*, **41**, 1031, (1996).
- [42] A. Recendiz, I. Gonzalez, J.L. Nava, *Electrochim. Acta.*, **52**, 6880-6887, (2007).
- [43] S.C. Das, P. Singh, G.T. Hefter, *J. Appl. Electrochem.*, **27**, 738, (1997).
- [44] C.D. Lacovangelo, F.G. Will, *Hydrogen Evolution Reaction Velocity.*, **132**, 4, 851-857, (1985).
- [45] K.O. Nayana, T.V. Venkatesha, B.M. Praveen, K. Vathsala, *J. Appl. Electrochem.*, **41**, 39, (2011).

-
- [46] M. Li, S. Luo, Y. Qian, W. Zhang, L. Jiang, J. Shen, *J. Electrochem. Soc.*, **154**, 567, (2007).
- [47] D. Wilcox, P.J. Mitchell, *J. Power Sources.*, **28**, 345-359, (1989).
- [48] J. Torrent-Burgue's, E. Guaus, *J. Appl. Electrochem.*, **37**, 643-651, (2007).
- [49] M. Mouanga, L. Ricq, L. Ismaili, B. Refouvelet, P. Berçot, *Surface & Coatings Technology.*, **201**, 7143-7148, (2007).

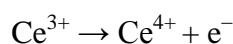
Chapter 6

Cerium half cell reaction

6.1 Introduction

In this study, the cerium half cell reaction (R.6.1 and R.6.3) of the zinc cerium redox flow battery was examined on a variety of electrode substrates such as platinum, platinum-iridium and carbon-based substrates in order to assess the electron transfer kinetics of the reaction. All the experiments were performed over the temperature range of 25°C to 60°C in different methanesulfonic acid concentrations.

At the positive electrode during charging, the primary reaction is the oxidation of the Ce(III) to form Ce(IV). The standard electrode potential for this reaction lies between 1.28 V and 1.72 V vs. Ag|AgCl [1]. Due to the high potential of the Ce(III)/Ce(IV) couple the electron transfer reaction taking place inevitably occurs on the oxidised metal catalyst surface. The majority of the substrates investigated were platinum coated but it must be noted that platinum is also a good catalyst for the oxygen evolution reaction (R.6.2). The latter is a secondary reaction taking place at the anode.



R.6.1

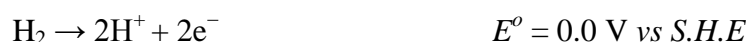


R.6.2

During discharge, the reduction of Ce(IV) to Ce(III) occurs while the secondary reaction thermodynamically should be the oxygen reduction (reverse of (R.6.2)) as the standard potential of the ORR is *ca.* 0.69 V vs *S.H.E.* However, the ORR current is very small *viz.* $K_{sp}[\text{O}_2] = 8.24 \text{ mg L}^{-1}$, at 25°C and 1 atm giving an $[\text{O}_2] = 2.5 \times 10^{-4} \text{ mol dm}^{-3}$ [2]. Therefore, the hydrogen evolution reaction (R.6.4) is the most likely reaction to occur.



R.6.3



R.6.4

The techniques of cyclic voltammetry, Tafel extrapolation, polarisation resistance, electrochemical impedance spectroscopy (EIS) and rotating disk electrode (RDE) studies were employed on the different substrates containing different coatings to investigate the Ce(III)/Ce(IV) reaction.

6.2 Determination of the Pt surface area for the electrodes for the positive half cell electrolyte

The electroactive platinum and platinum-iridium surface area of the substrates was determined by conducting cyclic voltammograms in 1 mol dm^{-3} sulfuric acid. This was necessary because the techniques of Tafel extrapolation, linear polarisation resistance and electrochemical impedance would depend on the electroactive active surface and not on the geometric area. The potential was repeatedly swept between the limits of -0.75 V and $+1.0 \text{ V}$ at 200 mV s^{-1} vs $\text{Hg}|\text{Hg}_2\text{SO}_4(\text{sat.})$ in order to obtain a clean Pt surface.

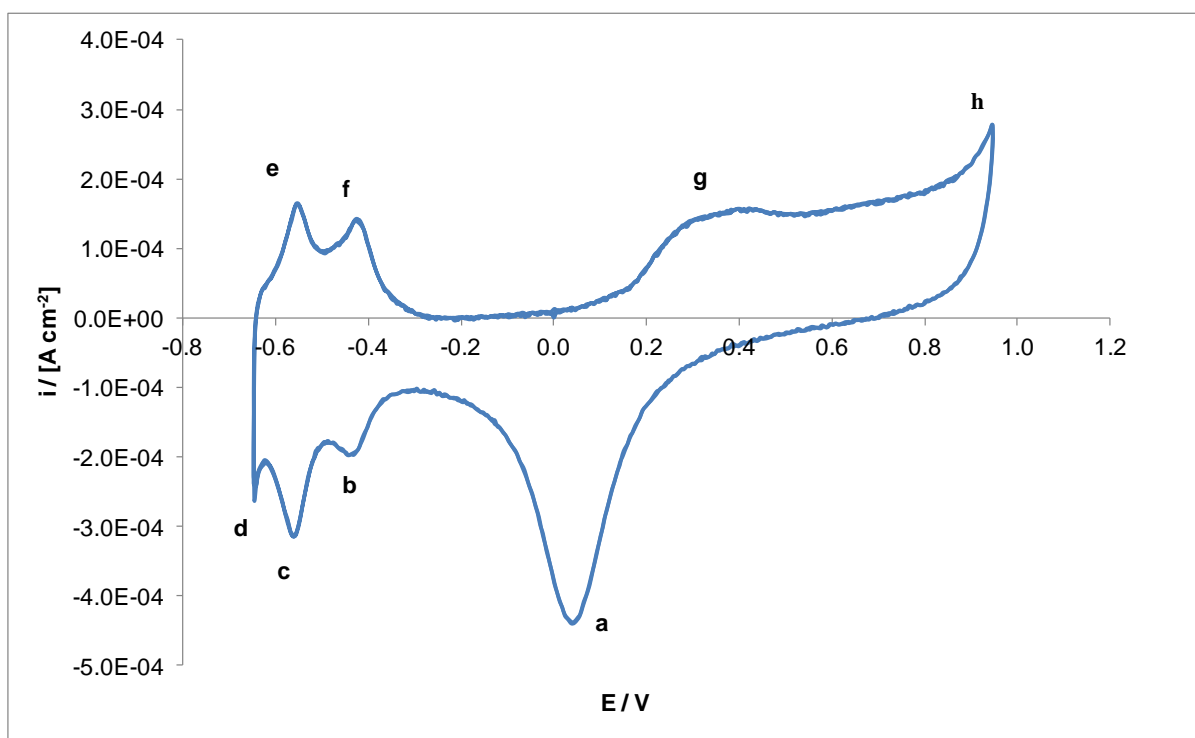
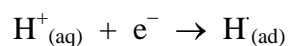


Fig.6.1: Cyclic voltammogram of Pt a disk electrode (0.44 cm^2) in $1 \text{ mol dm}^{-3} \text{ H}_2\text{SO}_4$ at 25°C and 200 mV s^{-1} .

The stages of the cyclic voltammogram on a Pt disk electrode (Fig.6.1) are listed as follows:

- | | |
|--|---|
| <i>a</i> : Pt oxide reduction; | <i>e</i> : Desorption of weakly bound hydrogen; |
| <i>b</i> : Strongly absorbed hydrogen; | <i>f</i> : Desorption of strongly bound hydrogen; |
| <i>c</i> : Weakly absorbed hydrogen; | <i>g</i> : Pt oxide monolayer formation; |
| <i>d</i> : Hydrogen evolution region; | <i>h</i> : Oxygen evolution; |

The characteristic features of the voltammogram in Fig.6.1 are well defined in the literature [3] [4]. On the cathodic scan, the first peak represents a surface controlled reaction (Fig.6.1 (a)) in which the adsorbed oxygen layer is reduced. For a surface controlled reaction there is a linear dependence with scan rate. The next two peaks represent the hydrogen adsorption (strong (Fig.6.1 (b)) and weak (Fig.6.1 (c)) chemisorbed hydrogen atom that takes place in the cathodic part of the forward scan, according to the following reaction:



R.6.5

Hydrogen was adsorbed more strongly at the first peak than at the second due to the fact that less energy was needed to absorb hydrogen at the first peak than for the second one. At more negative potentials *viz.* > -0.55 V the system is lead to the HER region. As expected, more energy was required to desorb the first layer on the reverse scan (Fig.6.1 (e)) than the second layer (Fig.6.1 (f)). Furthermore, a Pt oxide monolayer was formed during the anodic scan (Fig.6.1 (g)) while at more positive potentials the oxygen evolution reaction dominates the current *i.e* solvent breakdown (Fig.6.1 (h)). It is this hydrogen adsorption region (Fig.6.1 (b)) and (Fig.6.1 (c)) that was employed to determine the active surface area of the Pt based materials. This corresponded to the two cathodic peaks, from the double layer charging region to just before the onset for the HER process. The total monolayer charge of the strongly and weakly adsorbed hydrogen (Fig.6.1 (b) and (Fig.6.1 (c)) in the Pt disk electrode was *ca.* $210 \mu\text{C cm}^{-2}$ [3] [4] [5] and this corresponds to 77% of a full monolayer of adsorbed hydrogen on polycrystalline platinum [6].

The cyclic voltammogram of the Pt-Ti mesh in 1 mol dm^{-3} sulfuric acid at 25°C is shown in Fig.6.2. As expected, all the essential features from Fig.6.1 are also present in this cyclic voltammogram. A key difference though is the ratio between the strong and weak chemisorbed hydrogen for the data of Fig.6.2. This suggests a strong alteration of the adsorption sites of the Pt resulting from coating onto the Ti substrate. The charge from the adsorption peaks at this electrode was found to be equal to 493 mC giving a Pt surface area of *ca.* 131 cm^2 . This indicates that the surface area of the deposited Pt nanoparticles determined from the voltammetric charge is approximately 287 times larger than that of the Pt disk electrode.

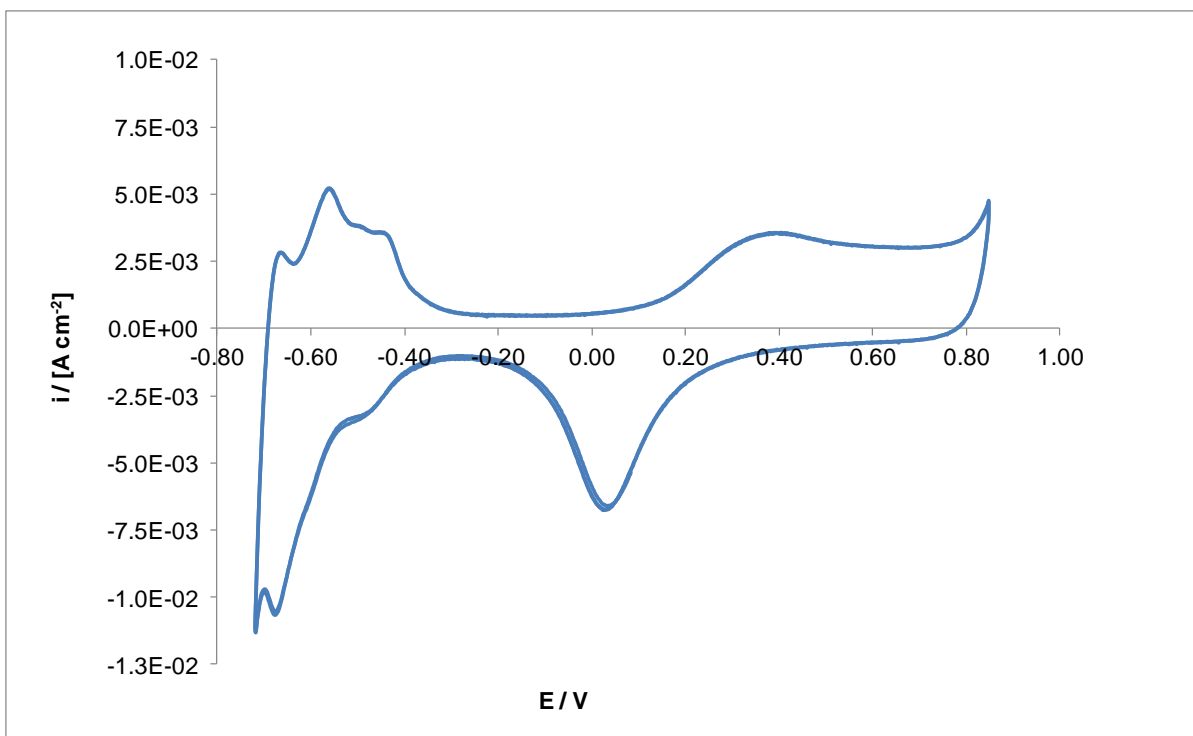


Fig.6.2: Cyclic voltammogram of Pt-Ti mesh electrode in $1 \text{ mol dm}^{-3} \text{ H}_2\text{SO}_4$ at 25°C and 200 mV s^{-1} .

In Table 6.1, the various platinum surface areas of the substrates used for this study are given for a nominal geometric electrode area of 1 cm^2 . For the Pt based electrodes (SL), as expected, an increase in platinum loading resulted in higher surface areas (SL1 - SL2), while etching of this surface seemed to have no great impact (SL3 - SL1). Some of the substrates were sandblasted prior to etching (SL5 - SL7). Sandblasting and etching create a rough and porous surface area but do not increase the actual geometric surface area [7]. No clear trends were found here regarding the surface area but we would have expected a small decrease in the Pt surface area of the SL electrodes following sandblasting and etching as some Pt particles could be removed during these processes. For the BMM series of electrodes the key factor in obtaining large Pt/Ir active areas appeared to be the temperature at which the coatings were fired, with 500°C being better than the lower temperature of 375°C treatment. The specific electrochemical area of the Pt and Pt-Ir substrates is also included in Table 6.1. The calculation for estimating the specific electrochemical area of the substrates is shown in Section 4.4.1, Chapter 4.

Substrate Name	Description	Surface area in $1 \text{ mol dm}^{-3} \text{ H}_2\text{SO}_4$ Cm^2	Specific electrochemical area ($\text{cm}^2 \text{ Pt mg}^{-1}$ or $\text{cm}^2 \text{ Pt /Ir mg}^{-1}$)
Pt-Ti mesh	10 g Pt m^{-2}	131	100
BMM1	Pt Ir composition: 30/70 - $9.9 \text{ g Pt/Ir m}^{-2}$ [375°C]	101	99
BMM2	Pt Ir composition: 50/50 - $9.25 \text{ g Pt/Ir m}^{-2}$ [500°C]	200	92.5
BMM3	Pt Ir composition: 30/70 - $10 \text{ g Pt/Ir m}^{-2}$ [375°C]	82	100
BMM4	Pt Ir composition: 50/50 - $10.2 \text{ g Pt/Ir m}^{-2}$ [375°C]	209	102
BMM6	Pt Ir composition: 50/50 - $9.25 \text{ g Pt/Ir m}^{-2}$ [500°C]	162	92.5
BMM11	Pt Ir composition: 30/70 - $10 \text{ g Pt/Ir m}^{-2}$ [375°C]	136	100
BMM12	Pt Ir composition: 50/50 - $10 \text{ g Pt/Ir m}^{-2}$ [375°C]	80	100
BMM13	Pt Ir composition: 30/70 - $10 \text{ g Pt/Ir m}^{-2}$ [375°C]	86	100
BMM14	Pt Ir composition: 50/50 - $10 \text{ g Pt/Ir m}^{-2}$ [375°C]	153	100
BMM15	Pt Ir composition: 30/70 - $10 \text{ g Pt/Ir m}^{-2}$ [500°C]	111	100
SL1	5 g Pt m^{-2}	120	50
SL2	3 g Pt m^{-2}	83	30
SL3	(Etched) 5 g Pt m^{-2}	111	50
SL4	(Etched) 3 g Pt m^{-2}	85	30
SL5	(Sandblasted & etched) 3 g Pt m^{-2}	106	30
SL6	(Sandblasted & etched) 3 g Pt m^{-2}	71	30
SL7	(Sandblasted & etched) 3 g Pt m^{-2}	185	30

Table 6.1: Surface area of materials used in positive half cell of the zinc cerium cell; cyclic voltammograms in $1 \text{ mol dm}^{-3} \text{ H}_2\text{SO}_4$ at 25°C and 200 mV s^{-1} .

6.3 Cyclic Voltammetry in $8 \times 10^{-1} \text{ mol dm}^{-3} \text{ Ce(III)}$ and $6.9 \text{ mol dm}^{-3} \text{ CH}_3\text{SO}_3\text{H}$

6.3.1 Different electrode materials

Cyclic voltammetry is a useful tool for the understanding of the electrochemistry of the cerium reaction and also of the electrode kinetics under different operating conditions. The voltammograms of the carbon and the platinum based electrodes in a solution containing $8 \times 10^{-1} \text{ mol dm}^{-3} \text{ Ce(III)}$ and 6.9 mol dm^{-3} total methanesulfonic acid at 60°C are shown in Fig.6.3 and Fig.6.4. In this study, the sweep rate (20 mV s^{-1}) was reversed when the potential reached $+1.3 \text{ V vs. Hg|Hg}_2\text{SO}_4|\text{K}_2\text{SO}_4 \text{ (sat.)}$. This highly acidic medium was investigated under static conditions, *i.e.* no rotation. It has to be noted that the above mentioned carbon materials had been chemically treated (*i.e.* oxidized and roughened surface) in order to withstand the highly acidic and oxidizing environment and also to provide a surface where the cerium reactions are more favorable.

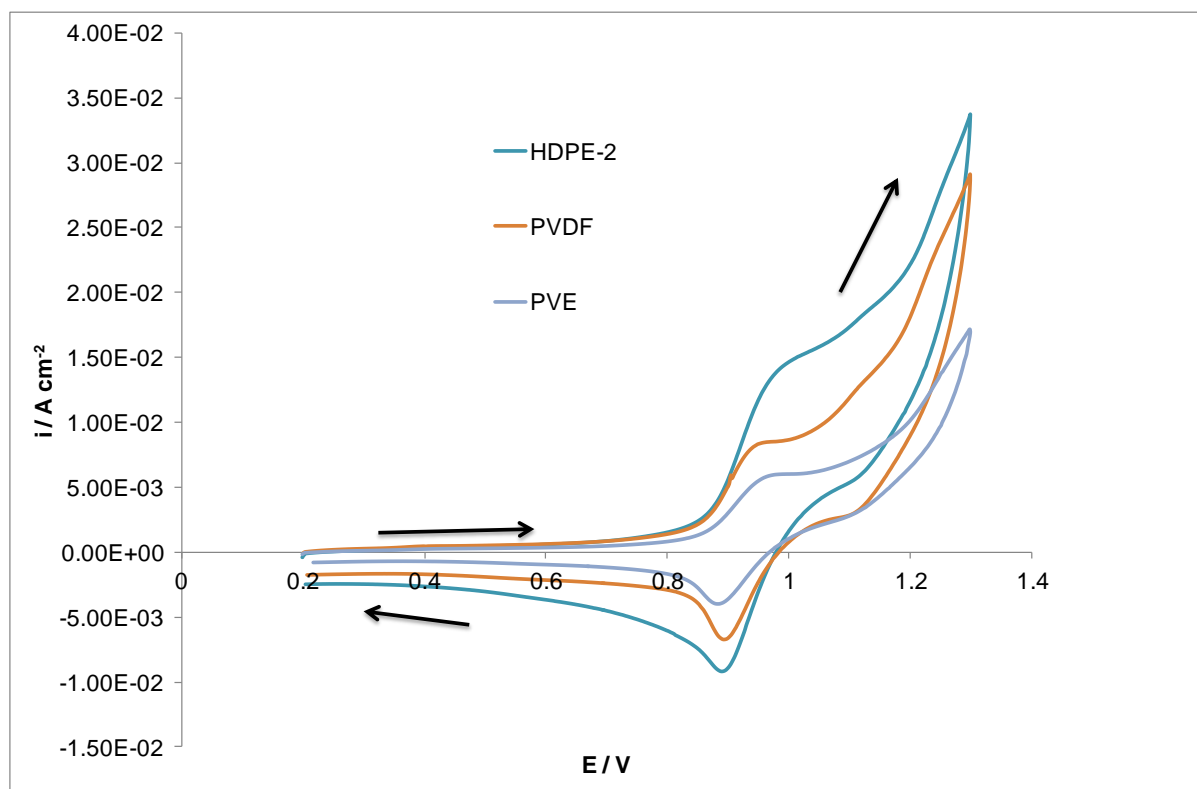


Fig.6.3: Cyclic voltammograms of various carbon electrodes (0.38 cm^2) in $8 \times 10^{-1} \text{ mol dm}^{-3} \text{ Ce(III)}$ and $6.9 \text{ mol dm}^{-3} \text{ CH}_3\text{SO}_3\text{H}$ at 25°C and 20 mV s^{-1} .

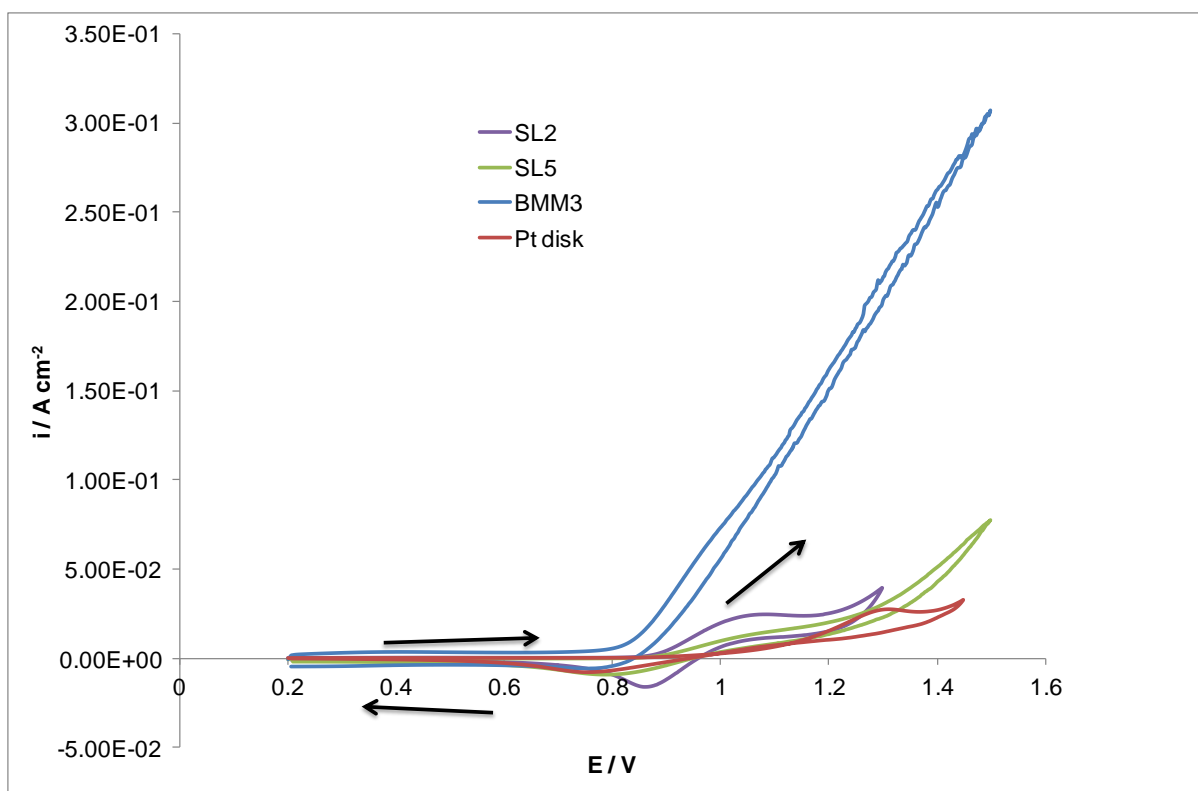


Fig.6.4: Cyclic voltammograms of Pt based electrodes in $8 \times 10^{-1} \text{ mol dm}^{-3} \text{ Ce(III)}$ and $6.9 \text{ mol dm}^{-3} \text{ CH}_3\text{SO}_3\text{H}$ at 60°C and 20 mV s^{-1} .

When comparing Fig.6.3 with Fig.6.4, it is clear that the voltammograms of the carbon based materials displayed higher reversibility for the cerium reactions than the platinum disk electrode and the platinum based electrodes.

For the PVDF based electrode, a distinct oxidation peak was observed at 1.08 V while the reduction peak was at *ca.* 0.80 V. In this case the peak separation (400 mV) suggested that the cerium reaction had faster kinetics here. A peak separation of *ca.* 400 mV was also observed for the HDPE and PVE electrodes. These findings are in accordance with the work of Leung *et al.* [8] and Raju *et al.* [9] in the same medium. For the platinum based electrodes, on the forward scan the current density of the Pt disk electrode increased rapidly beyond 1.1 V to give a small peak at 1.35 V. The considerably large peak separation (>750 mV) for this electrode suggests that the reaction had slow kinetics. For the BMM3 and SL5 electrodes at potentials beyond 1.4 V the current rise due to the oxygen evolution reaction [10] and therefore an oxidation peak could not be obtained. The cathodic peak using platinum was observed at *ca.* 0.63 V while for the carbon materials this was more positive, at 0.83 V for the PVE carbon, 0.84 V for the HDPE-1 and at 0.80 V for the PVDF electrode indicating that cerium is reduced more easily on platinum than on these carbon composites. The reversibility

of the cerium reaction has been found to be dependent on the type of the carbon material used [11].

The current densities of these carbon materials based on the geometric area during the oxidation process (*viz.* $\text{Ce}^{3+} \rightarrow \text{Ce}^{4+} + \text{e}^-$) were in the same order with the of the Pt disk electrode (*i.e.* $\sim 8.5 \times 10^{-3} \text{ A cm}^{-2}$) but smaller by a factor of 2.5 when compared to the i_{pC} of the SL2 electrode (*i.e.* $\sim 2.23 \times 10^{-2} \text{ A cm}^{-2}$). The current densities on the Ce(IV) reduction for the BMM3 and SL5 electrodes were smaller than the ones of the carbon electrodes. For the reduction process (*i.e.* $\text{Ce}^{4+} + \text{e}^- \rightarrow \text{Ce}^{3+}$), the SL2 electrode showed the highest current densities ($\sim -1.6 \times 10^{-2} \text{ A cm}^{-2}$) for this medium, as expected.

Regarding the carbon composite electrodes, there was an obvious change in their surface appearance following the cyclic voltammograms indicating that despite the prior treatments, they were affected by the highly acidic and oxidising environment. The surface of the substrates deteriorated severely with prolonged cyclic voltammetry trials, leading to a degradation of the surface. Small carbon parts were detaching from the electrodes' surface and their presence became apparent in the electrolyte. Fig.6.5 illustrates this for a PVE roughened carbon electrode (a) and a PVDF oxidised electrode (b) following repeated oxidation/reduction cycles.

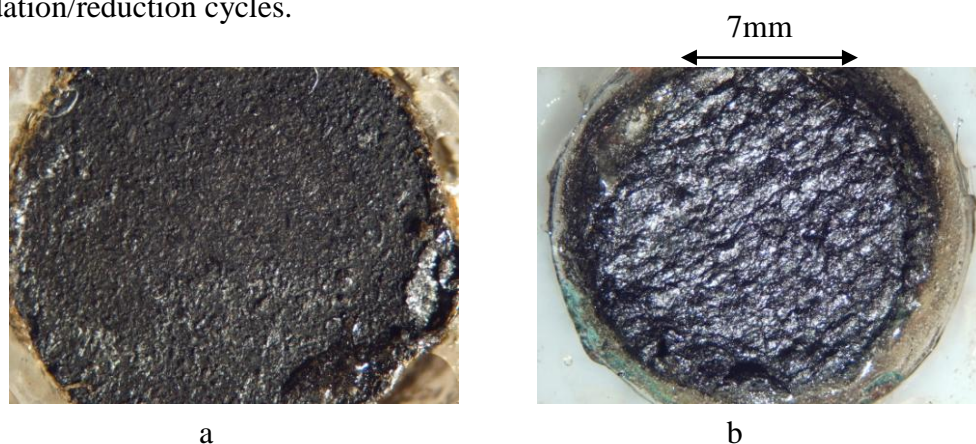


Fig.6.5: Optical microscopy of (a) PVE roughened (magnification = 3) and (b) PVDF oxidised (magnification = 2.5) electrode surfaces before and after conducting cyclic voltammograms in $8 \times 10^{-1} \text{ mol dm}^{-3} \text{ Ce(III)}$ and $6.9 \text{ mol dm}^{-3} \text{ CH}_3\text{SO}_3\text{H}$ ($\phi = 7 \text{ mm}$).

It is clear that since the carbon composite materials degraded in the solution containing 4.5 mol dm^{-3} methanesulfonic acid these materials were not a viable option for the cerium reaction in the flow cell. It has been reported in the literature that the cerium reaction appears to have high reversibility on carbon felt electrodes in methanesulfonic acid medium [12] and in nitric acid medium [13]. Paulenova *et al.* [14] reported that glassy carbon

degraded at temperatures higher than 40°C in sulfuric acid concentrations greater than 2 mol dm⁻³. Spotnitz *et al.* [15] examined several materials for Ce(IV) generation from 1.5 × 10⁻¹ mol dm⁻³ Ce(III) in 2 mol dm⁻³ methanesulfonic acid including a ruthenium oxide dimensionally stable anode (DSA), a glassy carbon electrode and a iridium oxide on titanium electrode. They found that the platinum electrodes showed the highest conversion current efficiency and hence the highest oxygen overvoltage.

Finally, as the pure platinum electrodes are very expensive, the need for cheaper electrode materials that can exhibit the same behaviour as the above materials (carbon and platinum) as the positive electrolyte of the zinc cerium cell were investigated, namely the platinum coated (SL) and Pt-Ir coated (BMM) substrates.

6.3.2 Effect of rotation speed

The cyclic voltammograms carried out with (5 Hz and 10 Hz) and without rotation in 6.9 mol dm⁻³ CH₃SO₃H containing 8 × 10⁻¹ mol dm⁻³ Ce(III) on the platinum (Pt) disk electrode at 60°C are shown in Fig.6.6. The transformation of Ce(III) occurred during charging (positive scan) as the solution at that time turned from transparent to yellow indicating the presence of Ce(IV).

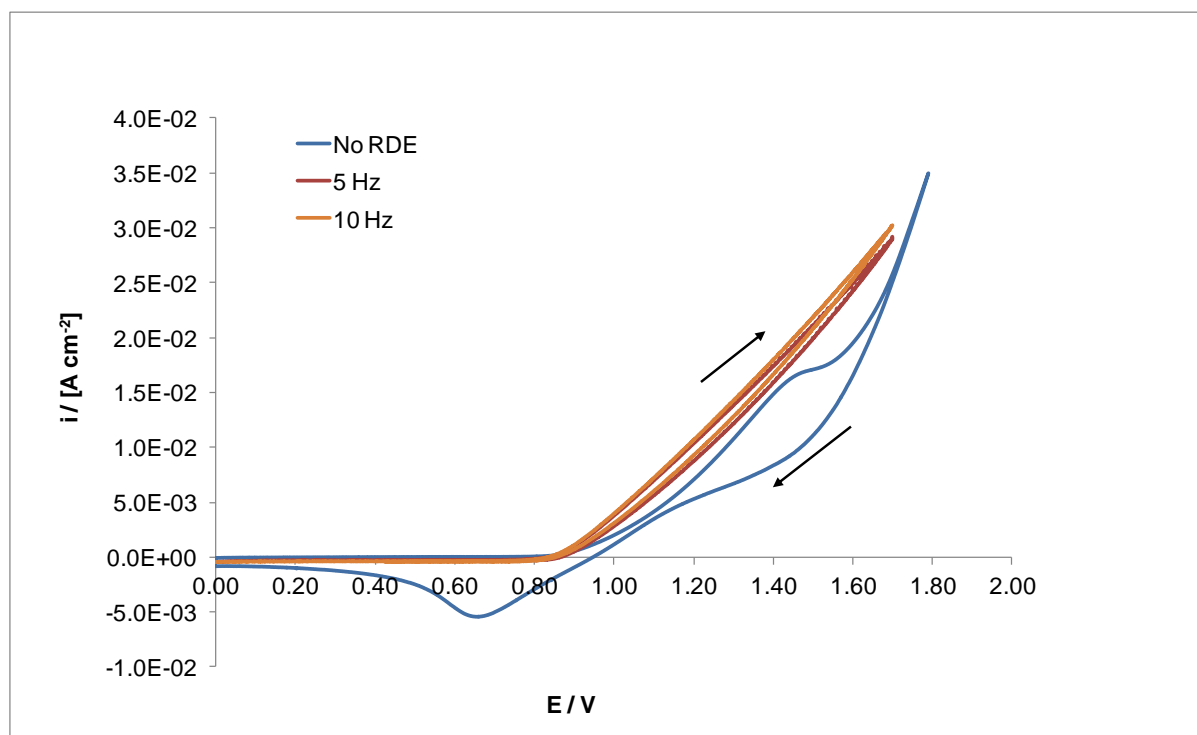


Fig.6.6: Rotating disc electrode study of a Pt electrode (0.44 cm²) in 8 × 10⁻¹ mol dm⁻³ Ce(III) and 6.9 mol dm⁻³ CH₃SO₃ at 60°C and 10 mV s⁻¹.

It can be observed that for the case of the static RDE (*i.e.* no rotation), the anodic and cathodic current peaks corresponding to the Ce(IV)/Ce(III) reaction were located between 1.44 V and 0.65 V respectively. According to the voltammogram, when using the platinum electrode, cerium oxidation took place at the same time with the evolution of oxygen. The peak current density values for the reduction and oxidation process are smaller than the ones of Fig.6.4 due to the larger surface area (0.44 cm^2) of the electrode used for this experiment.

Due to the OER, the Pt and Pt/Ir electrodes listed in Table 6.1 did not exhibit an oxidation peak on their voltammograms under static conditions (*i.e.* no rotation). Nzikou *et al.* [16] have reported that the oxidation of cerous salts appeared to be slower at a Pt/Ti electrode than at a pure platinum surface in a solution containing Ce(III) and $5 \times 10^{-1} \text{ mol dm}^{-3}$ sulfuric acid. The potential at which cerium oxidation took place (between 1.1 V and 1.2 V) was smaller than that at the platinised surface ($>1.25 \text{ V}$). According to Chen *et al.* [7] a sharp increase in the current density was observed at high potentials for a Pt/Ir electrode in $5 \times 10^{-1} \text{ mol dm}^{-3}$ sulfuric acid, due to the high activity of iridium to the OER. The charge transfer coefficient for the cerium oxidation reaction onto the platinum disk electrode was *ca.* 0.41 and in good agreement with the values reported in literature in a sulfuric acid medium [10] [17] [18].

Under rotation, there was no limiting current (i_L) observed during the oxidation process because the increased mass transfer extends the Tafel region for the process and pushes the plateau (mass transport limited) into the oxygen evolution region at the more positive potentials ($>1.40 \text{ V}$). The same was found for the carbon-based substrates and the other Pt and Pt/Ir coated electrodes listed in Table 6.1. As expected, on the reverse scan with the RDE, the reduction peak current density was absent, as no Ce(IV) was present at the electrode surface. It is worth noting that due to the high redox potential of the Ce(IV)/Ce(III) couple, the metal electrode even including a noble metal such as platinum the reaction takes place on the metal oxide rather than on a pure metal surface [19] [20] [21].

6.3.3 Effect of temperature

Fig.6.7 shows the cyclic voltammograms for the cerium reduction and oxidation reaction in $8 \times 10^{-1} \text{ mol dm}^{-3}$ cerium methanesulfonate with 6.9 mol dm^{-3} methanesulfonic acid solution using a platinum disk electrode at three different temperatures *viz.* 25°C, 40°C and 60°C at 20 mV s^{-1} .

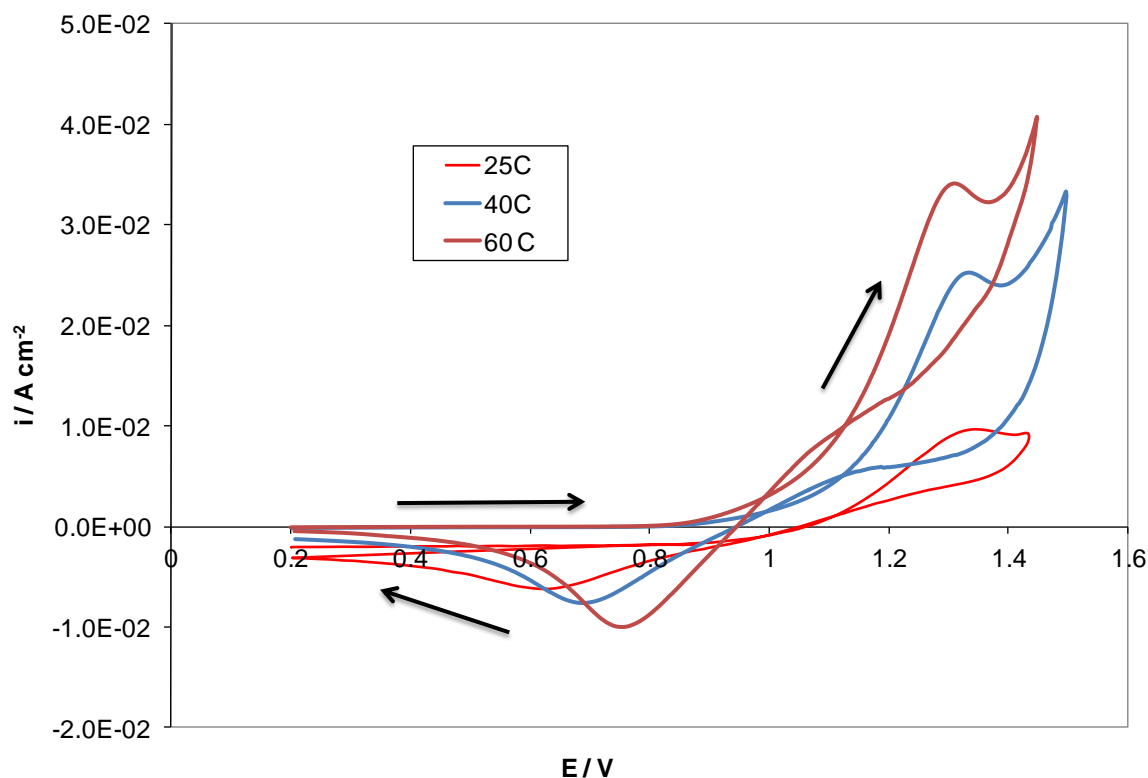


Fig.6.7: Effect of T on a Pt disk electrode (0.44 cm^2) in $8 \times 10^{-1} \text{ mol dm}^{-3}$ Ce(III) and 6.9 mol dm^{-3} CH_3SO_3 at 20 mV s^{-1} .

The potential where the cerium oxidation reaction started occurring (*viz.* the onset potential) shifted to more negative potentials with the increase of temperature from 1.2 V at 25°C to 1.15 V at 60°C. Also, higher temperatures shifted the oxidation peak to more negative values and they gave a higher peak intensity. Indeed, both anodic and cathodic peak current densities were found to increase at higher temperature. For example for the reduction reaction i_{pc} at 25°C was *ca.* $5.7 \times 10^{-3} \text{ A cm}^{-2}$ while at 60°C it was $9.9 \times 10^{-3} \text{ A cm}^{-2}$. The data are consistent with literature values for the cerium reduction in methanesulfonic acid [8]. Numerous studies have confirmed the effect of temperature on the current density of the Ce(III)/(IV) reaction in different acidic media such as nitric acid [22] and sulfuric acid [23].

According to Xie *et al.* [24] the change of the Ce(III)/Ce(IV) redox potential with temperature is due to the non-equal complexation of the Ce(III)/Ce(IV) redox species with the methanesulfonate anion. Vijayarathi *et al.* [25] suggested that the Ce(III)/Ce(IV) redox couple could exist as methanesulfonate complexes in methanesulfonic acid solutions. More precisely, for the Ce(III) species, Ce^{3+} , $[\text{Ce}(\text{CH}_3\text{SO}_3)]^{2+}$, $[\text{Ce}(\text{CH}_3\text{SO}_3)_2]^+$ are involved in the electrode process [26] while the oxidized species were found to be Ce(IV), $[\text{Ce}(\text{CH}_3\text{SO}_3)]^{3+}$, $[\text{Ce}(\text{CH}_3\text{SO}_3)_2]^{2+}$ [27]. In addition, the viscosity of cerium decreases with the increase of temperature, from 13.55 cS at 22°C to 7.2 cS at 45°C and to 4.73 cS at 60°C [28] [29]. The molecules attain more kinetic energy as the temperature increases and are able to move more freely. Hence, the ability to slide past each molecule is improved as the shear forces decreases leading to lower values of kinematic viscosity.

6.3.4 Scan rate dependence on the reduction of Ce(IV)

Since the Ce(III) oxidation peak was not always apparent or distinct enough from the cyclic voltammogram, it was decided to investigate the reduction of the Ce(IV) produced in order to obtain the diffusion coefficient of the Ce(III)/Ce(IV) species. Fig.6.8 shows the cyclic voltammograms of the Ce(IV) reduction reaction in $4 \times 10^{-1} \text{ mol dm}^{-3}$ cerium methanesulfonate and 6.9 mol dm^{-3} methanesulfonic acid using a platinum disk electrode. The voltammograms were scanned from +0.2 V to +1.2 V at 25°C and the reduction curves were recorded.

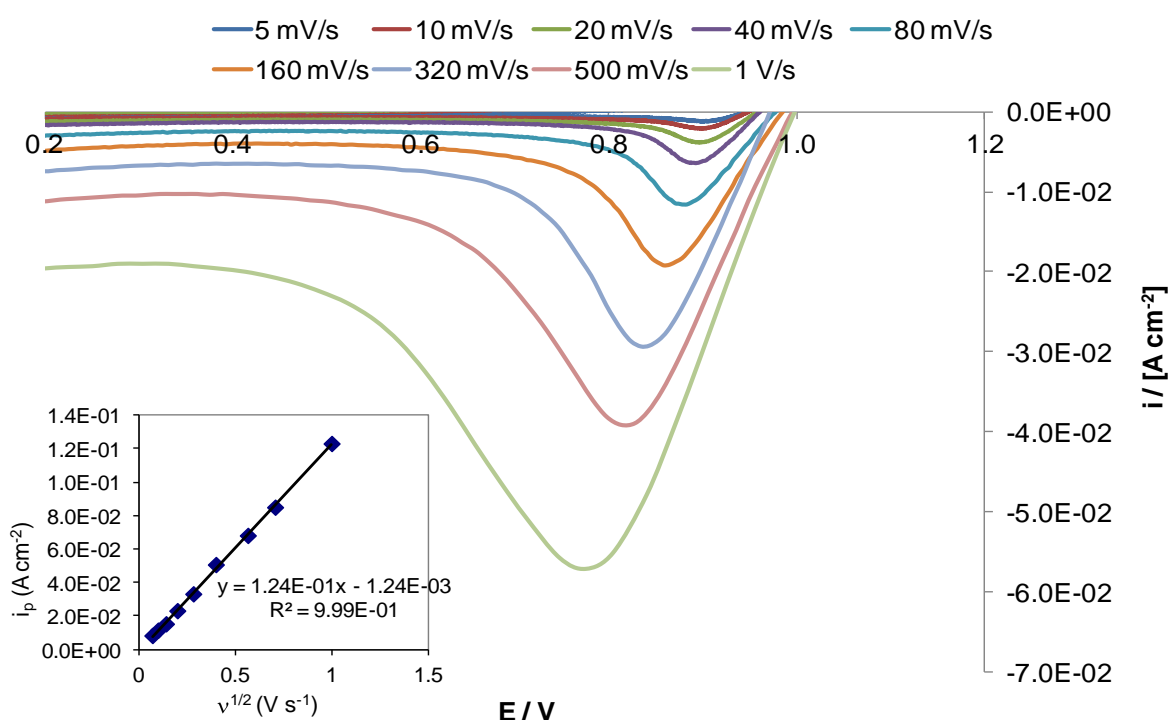


Fig.6.8: Effect of potential scan rate onto a Pt disk electrode (0.44 cm^2) in a solution containing $8 \times 10^{-1} \text{ mol dm}^{-3}$ Ce(III) and 6.9 mol dm^{-3} $\text{CH}_3\text{SO}_3\text{H}$ at 25°C; inset the Randles-Sevcik plot confirming diffusion limited conditions.

For the Pt disk electrode, the reduction peak current density increased linearly with the square root of the potential sweep rate indicating that the reaction is diffusion controlled. The calculated diffusion coefficients for the cerium methanesulfonate were $4.63 \times 10^{-7} \text{ cm}^2 \text{ s}^{-1}$ and $1.32 \times 10^{-6} \text{ cm}^2 \text{ s}^{-1}$ at 25°C and 60°C respectively. The above values are in agreement with previous measurements made in cerium methanesulfonate in the presence of methanesulfonic acid from Spotnitz *et al.* [15]. He reported a diffusion coefficient from a rotating ring disk study equal to $1.0 \times 10^{-6} \text{ cm}^2 \text{ s}^{-1}$ at ambient temperature in a solution containing $2.5 \times 10^{-2} \text{ mol dm}^{-3}$ Ce(III) in 5.9 mol dm^{-3} methanesulfonic acid.

6.4 Cyclic Voltammetry in various Ce(IV) solutions in $6.9 \text{ mol dm}^{-3} \text{CH}_3\text{SO}_3\text{H}$

6.4.1 Pt electrode in $5.9 \times 10^{-1} \text{ mol dm}^{-3} \text{Ce(IV)}$ / $7 \times 10^{-2} \text{ mol dm}^{-3} \text{Ce(III)}$, $7 \times 10^{-1} \text{ mol dm}^{-3} \text{Zn(II)}$ and $6.9 \text{ mol dm}^{-3} \text{CH}_3\text{SO}_3\text{H}$

In this case, the addition of zinc in the positive electrolyte was done in order to reduce the excess acid concentration (*i.e.* 3 mol dm^{-3} excess H^+). The excess acid concentration is well within the limit that was suggested from Clarke *et al* [30]. Thermodynamically, the zinc deposition/dissolution reaction takes place in far more negative potentials than the ones examined for the Ce(III)/Ce(IV) reaction (-0.76 V vs 1.44 V vs *S.H.E*) and therefore does not interfere with the later. It has to be mentioned that the high Ce(IV) concentration was achieved by electrolysis of Ce(III) carbonate in methanesulfonic acid with Pt-Ti mesh electrode.

6.4.1.1 Scan rate dependence on the oxidation and reduction of Ce(IV)

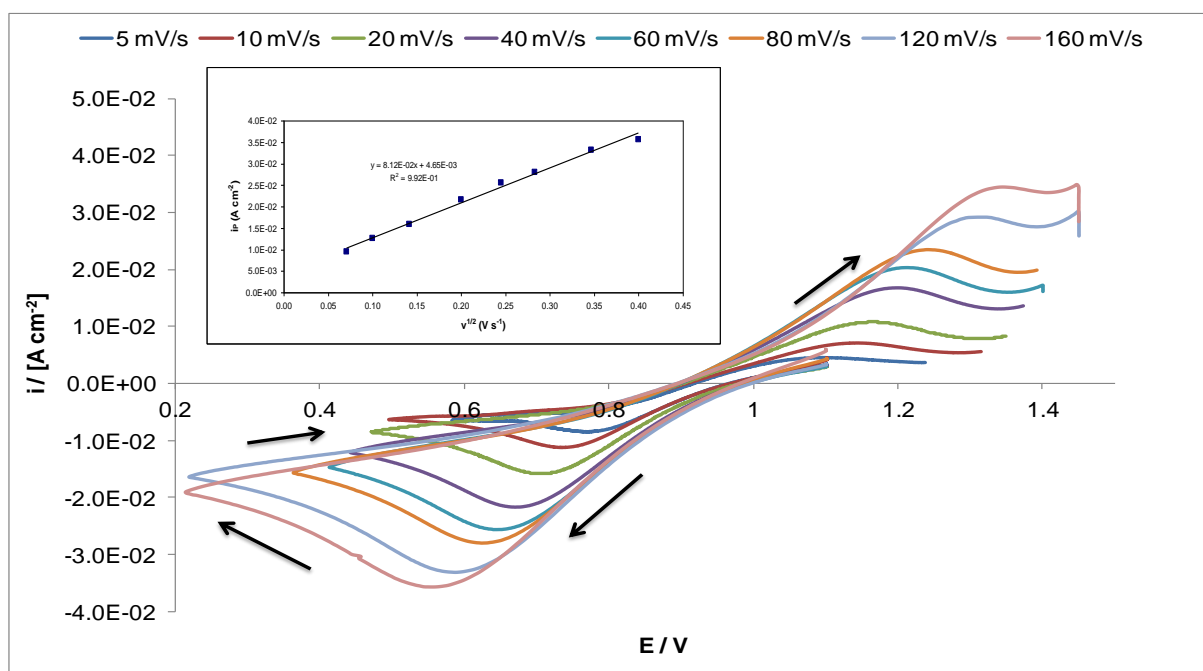


Fig.6.9 shows the cyclic voltammograms for the Ce(IV) oxidation and reduction reaction for a Pt disk electrode at 60°C . The voltammograms were scanned from 1.1 V for to 0.2 V and then reversed to 1.5 V vs $\text{Hg}|\text{Hg}_2\text{SO}_4 (\text{sat.})$. Since there is a high content of Ce(IV) in this solution ($7 \times 10^{-1} \text{ mol dm}^{-3}$), the Ce(IV) reduction process occurs first and then the oxidation reaction.

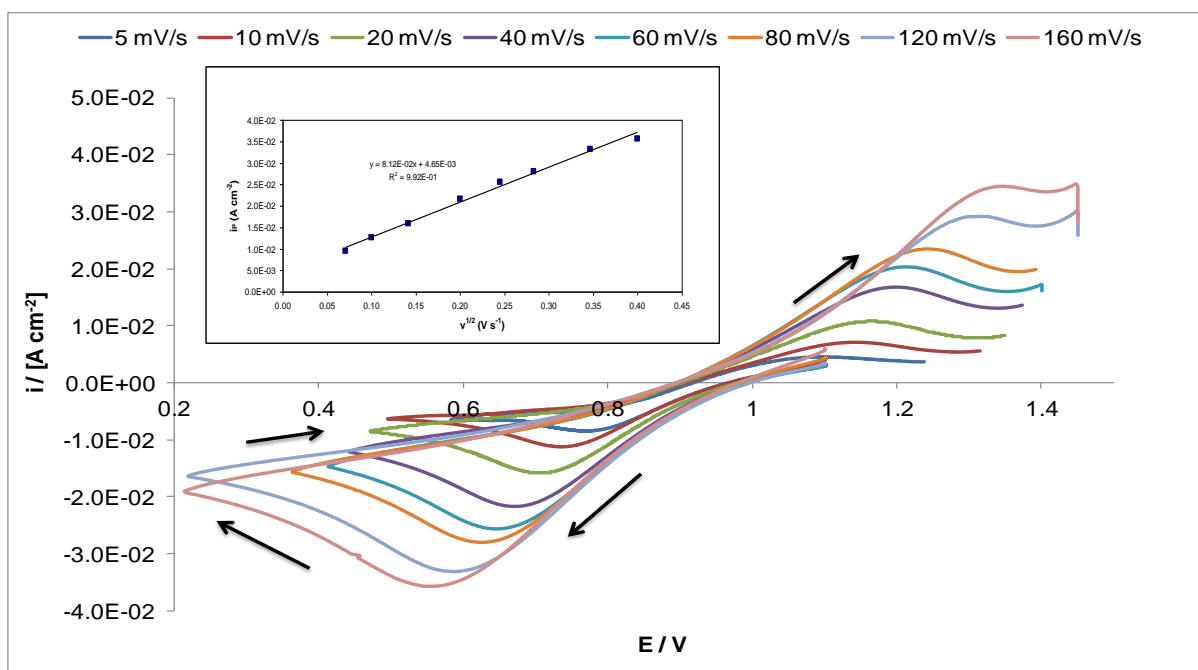


Fig.6.9: Cyclic voltammetry of the Ce(IV)/Ce(III) couple in a solution consisting of $5.9 \times 10^{-1} \text{ mol dm}^{-3}$ Ce(IV) | $7 \times 10^{-2} \text{ mol dm}^{-3}$ Ce(III), $7 \times 10^{-1} \text{ mol dm}^{-3}$ Zn(II) and 6.9 mol dm^{-3} CH₃SO₃H; Pt disk.

Both the reduction and oxidation peak current densities increased linearly with the square root of the potential sweep rate indicating that the reaction was diffusion controlled. The calculated D values for the reduction of cerium methanesulfonate were evaluated as $1.12 \times 10^{-7} \text{ cm}^2 \text{ s}^{-1}$ and $2.62 \times 10^{-7} \text{ cm}^2 \text{ s}^{-1}$ at 25°C and 60°C respectively, from the Randles-Sevcik plot inset Fig.6.9. For the oxidation reaction they were *ca.* $1.93 \times 10^{-7} \text{ cm}^2 \text{ s}^{-1}$ and $3.18 \times 10^{-7} \text{ cm}^2 \text{ s}^{-1}$ at 25°C and 60°C. In both cases, the diffusion coefficient increased with temperature. The above values are in agreement with the findings of Abbaspour *et al.* [31] for the same medium, *viz.* methanesulfonic acid. The effect of temperature on the diffusion coefficient was also confirmed for the substrates of Table 6.1. The values of the BMM3, SL2 and SL5 were between $4 \times 10^{-8} \text{ cm}^2 \text{ s}^{-1}$ and $6 \times 10^{-8} \text{ cm}^2 \text{ s}^{-1}$ at 25°C and at 60°C between $6.5 \times 10^{-8} \text{ cm}^2 \text{ s}^{-1}$ and $8 \times 10^{-8} \text{ cm}^2 \text{ s}^{-1}$, lower by a factor of 2 when compared with the values obtained for the Pt disk electrode.

6.4.1.2 RDE study

The data from a rotating disc electrode study on the cerium reduction process is shown in Fig.6.10 for the Pt disk electrode at 25°C. The potentials were scanned from +0.0 V and reversed at -0.25 V. For each rotation rate, the reduction of Ce(IV) was observed as a well defined constant current plateau instead of a peak.

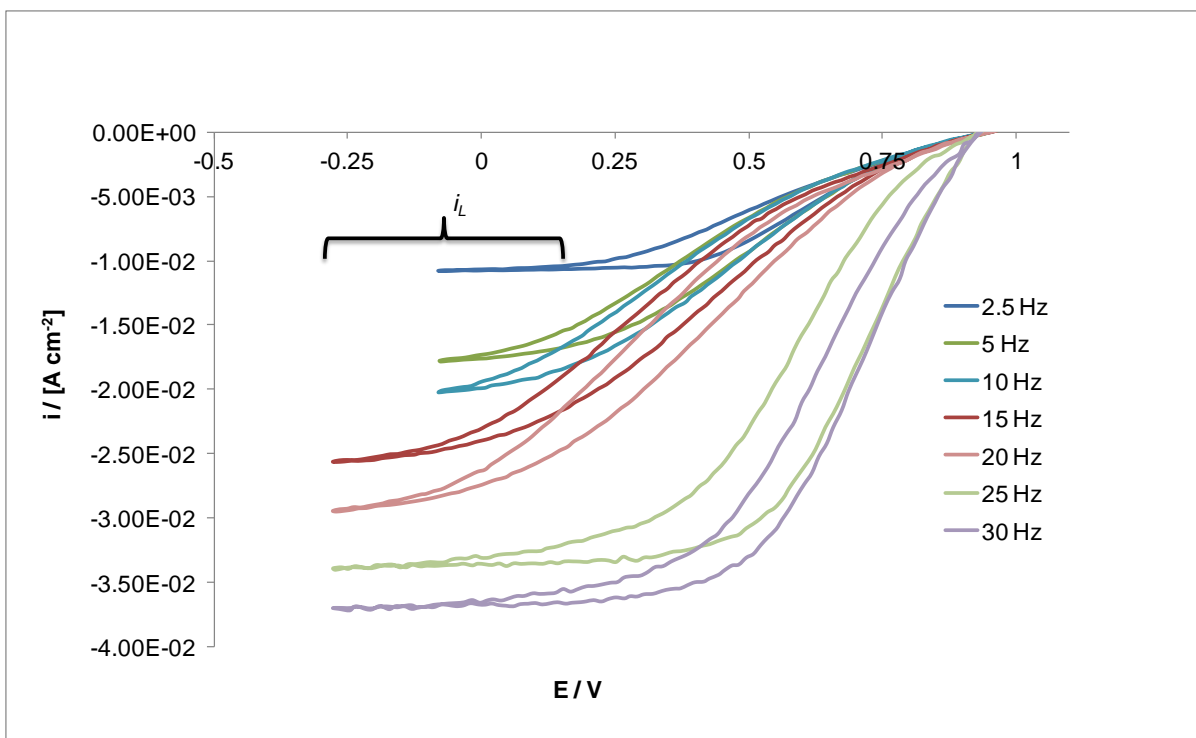


Fig.6.10: Rotating disc electrode study on the Ce(IV)/Ce(III) couple in $5.9 \times 10^{-1} \text{ mol dm}^{-3} \text{ Ce(IV)}$ / $7 \times 10^{-2} \text{ mol dm}^{-3} \text{ Ce(III)}$, $7 \times 10^{-1} \text{ mol dm}^{-3} \text{ Zn(II)}$ and $6.9 \text{ mol dm}^{-3} \text{ CH}_3\text{SO}_3\text{H}$; Pt disk (0.44 cm^2) at 25°C .

From the Levich equation, (Eq. 3.38, Chapter 3) the limiting current densities (i_L) were plotted as a function of the square roots of the rotation speeds. The linear plot confirms that the systems were under mass transport control.

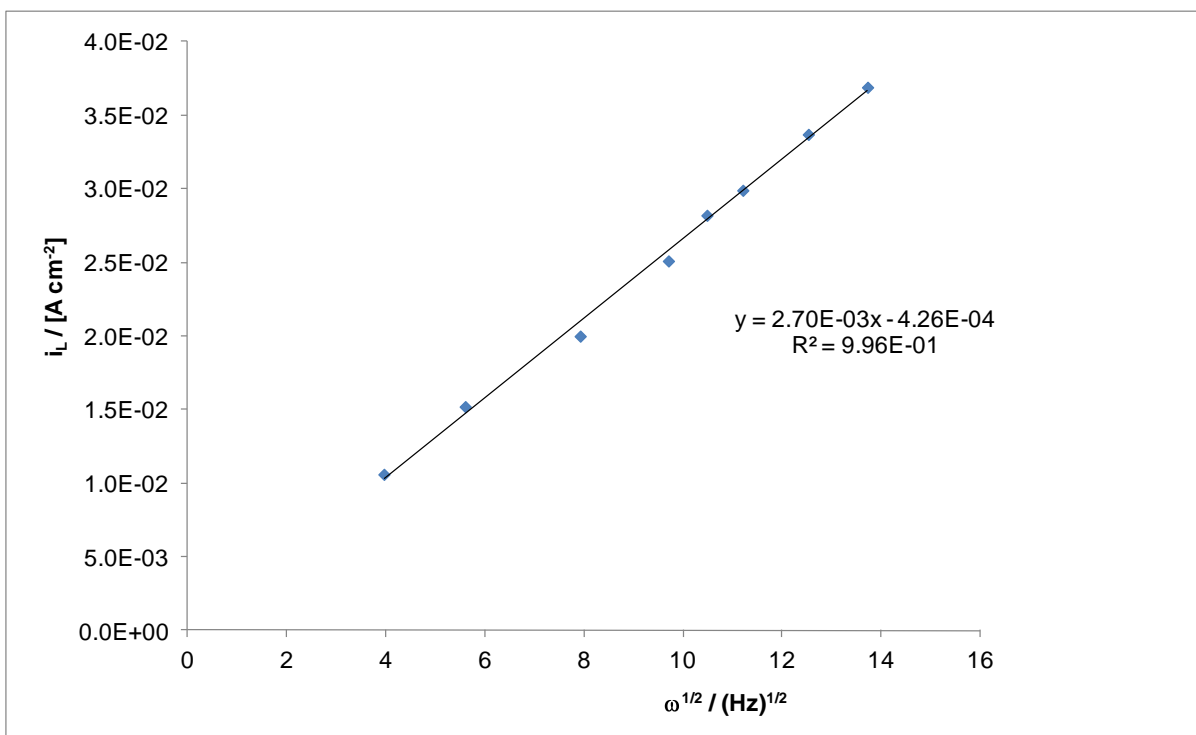


Fig.6.11: Levich plot at an RDE for the Ce(IV)/Ce(III) couple in $5.9 \times 10^{-1} \text{ mol dm}^{-3} \text{ Ce(IV)}$ / $7 \times 10^{-2} \text{ mol dm}^{-3} \text{ Ce(III)}$, $7 \times 10^{-1} \text{ mol dm}^{-3} \text{ Zn(II)}$ and $6.9 \text{ mol dm}^{-3} \text{ CH}_3\text{SO}_3\text{H}$; Pt disk (0.44 cm^2) and 25°C .

The D values of the cerium methylsulfonate species were evaluated as *c.a.* 2.17×10^{-7} $\text{cm}^2 \text{s}^{-1}$ and 4.17×10^{-7} $\text{cm}^2 \text{s}^{-1}$ at 25°C and 60°C respectively. From the Stokes-Einstein equation for diffusion of spherical particles through liquid [16], the increase in temperature results in higher kinetic energies of the cerium atoms and thus higher velocities, which in turn increases the speed of diffusion.

The Stokes-Einstein equation is given by: $D = \mu k_B T$ **Eq. 6.1**

where μ is the mobility for spherical particles, defined as $\mu = \frac{1}{6\pi\eta r}$ and k_B is the Boltzmann constant (1.38×10^{-23} J K^{-1})

The D values obtained from this study are in accordance with the values found from the scan rate dependence study in the same medium (Section 6.4.1.1) and with the work of Abbaspour *et al.* [31]. Furthermore, from the Koutechy-Levich relationship [32] the heterogeneous standard rate constant (k°) for the cerium reduction process was *c.a.* 1.16×10^{-3} cm s^{-1} and 3.42×10^{-3} cm s^{-1} at 25°C and 60°C respectively.

6.4.2 Pt electrode in 5×10^{-3} mol dm^{-3} Ce(IV) in 6.9 mol dm^{-3} $\text{CH}_3\text{SO}_3\text{H}$

A rotating disk study was also carried out in a solution containing 5×10^{-3} mol dm^{-3} Ce(IV) in 6.9 mol dm^{-3} methanesulfonic acid at a Pt disk electrode at two different temperatures *viz.* 25°C and 60°C . The scan rate employed was 20 mV s^{-1} . The sweep rate was reversed when the potential approached $+0.5 \text{ V}$ for the rotational speeds between 2.5 Hz and 12.5 Hz and $+0.4 \text{ V}$ for 15 Hz and 20 Hz.

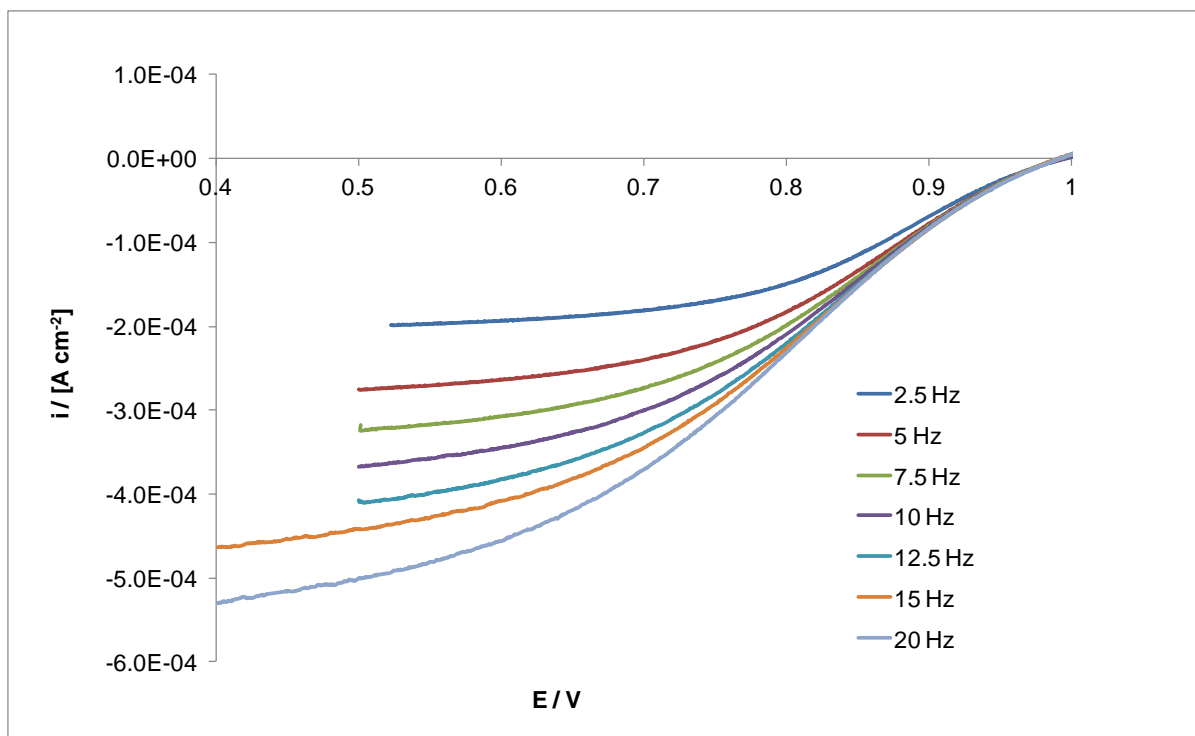


Fig.6.12: Rotating disc electrode study of the Pt electrode in $5 \times 10^{-3} \text{ mol dm}^{-3} \text{ Ce(IV)}$ and $6.9 \text{ mol dm}^{-3} \text{ CH}_3\text{SO}_3\text{H}$ at 60°C , scan rate: 20 mV s^{-1} .

The diffusion coefficients obtained from the Levich analysis at 25°C and 60°C were $4.71 \times 10^{-7} \text{ cm}^2 \text{ s}^{-1}$ and $7.65 \times 10^{-7} \text{ cm}^2 \text{ s}^{-1}$ respectively. Higher temperatures resulted in higher D , as expected from the Stokes-Einstein equation [Eq.6.1]. The D values reported from Randle *et al.* [33] and Nzikou *et al.* [16] in sulfuric acid media ($5 \times 10^{-1} \text{ mol dm}^{-3}$ to 1.5 mol dm^{-3}) are smaller by a factor of 10, *viz.* $5 \pm 0.12 \times 10^{-6} \text{ cm}^2 \text{ s}^{-1}$. This could be due to the higher solution viscosity of the methanesulfonic acid (4.73 cP at 60°C) compared to sulfuric acid (1.02 cP at 60°C [34]). The diffusion coefficients calculated from the RDE tend to be more reliable than the diffusion coefficients obtained from the cyclic voltammogram (scan rate dependence study) as the former is a steady state technique where the current is entirely mass transport controlled.

The rate constants gleaned from the Koutecky-Levich analysis [32] were *ca.* $2.20 \times 10^{-4} \text{ cm}^2 \text{ s}^{-1}$ and $5.47 \times 10^{-4} \text{ cm}^2 \text{ s}^{-1}$ at 25°C and 60°C respectively. These values are in accordance with literature values for the cerium reduction reaction in methanesulfonic acid media [9] (*i.e.* $3.5 \times 10^{-4} \text{ cm}^2 \text{ s}^{-1}$) and also in sulfuric acid media (from 5×10^{-1} to 2 mol dm^{-3}) [16] [33] [35]. Furthermore, Been *et al.* [36] reported limiting current density values for the Ce(IV) reduction reaction between $8 \times 10^{-3} \text{ A cm}^{-2}$ and $6.6 \times 10^{-2} \text{ A cm}^{-2}$ at rotation rates of

3 Hz to 16 Hz in a solution containing $1.2 \times 10^{-1} \text{ mol dm}^{-3}$ Ce(IV), 2.8×10^{-1} Ce(III) and 1.6 mol dm^{-3} sulfuric acid. The values obtained in the voltammograms of Fig.6.12 are considerably lower (*i.e* by a factor of 10^{-2}) and this can be attributed to the different acidic medium.

6.4.3 Platinised-titanium mesh in $8 \times 10^{-2} \text{ mol dm}^{-3} \text{ Ce(IV)}$ / $7.2 \times 10^{-1} \text{ mol dm}^{-3} \text{ Ce(III)}$ and $6.9 \text{ mol dm}^{-3} \text{ CH}_3\text{SO}_3\text{H}$ - effect of temperature

The cyclic voltammograms of the Ce(III)/Ce(IV) species at $8 \times 10^{-2} \text{ mol dm}^{-3}$ to 1.2 and 6.9 mol dm^{-3} methanesulfonic acid using the Pt-Ti mesh were carried out over the potential range +0.5 V to +1.35 V. Fig.6.13 clearly illustrates the effect of temperature on the onset potential for the reduction process, *i.e.* it became easier as it shifted to more positive values with increasing temperatures. For the oxidation process, the peaks remained at the same potential *viz.* 1.10 V vs Hg|Hg₂SO₄ (sat.). In addition, the current density increased with temperature from $-1.51 \times 10^{-3} \text{ A cm}^{-2}$ at 25°C to $-2.62 \times 10^{-3} \text{ A cm}^{-2}$ at 60°C clearly indicating that this reaction was more favorable at higher temperatures. The potential where the oxidation reaction occurs showed no significant variation but the current density values increased at higher temperatures. Therefore, it is clear that the system became more reversible with increasing temperature. The effect of temperature on an electrolyte solution containing for this solution is summarized Table 6..

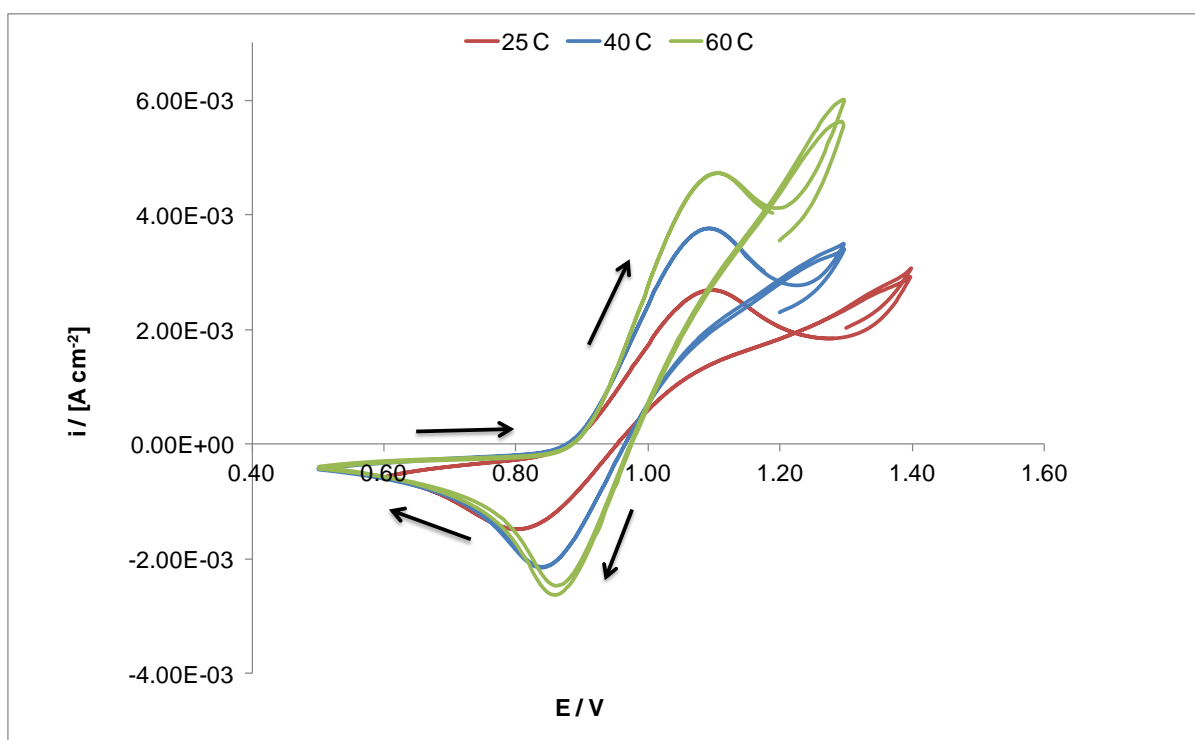


Fig.6.13: Effect of T on the Ce(IV)/Ce(III) couple in a solution consisting of $8 \times 10^{-2} \text{ mol dm}^{-3} \text{ Ce(IV)}$ and $6.9 \text{ mol dm}^{-3} \text{ CH}_3\text{SO}_3\text{H}$ at 40 mV s^{-1} ; Pt-Ti mesh (131 cm^2).

25°C			40°C			60°C		
$i_c / 10^{-3} \text{A cm}^{-2}$	$\Delta E_{C-A} / \text{V}$	$i_A / 10^{-3} \text{A cm}^{-2}$	$i_c / 10^{-3} \text{A cm}^{-2}$	$\Delta E_{C-A} / \text{V}$	$i_A / 10^{-3} \text{A cm}^{-2}$	$i_c / 10^{-3} \text{A cm}^{-2}$	$\Delta E_{C-A} / \text{V}$	$i_A / 10^{-3} \text{A cm}^{-2}$
-1.51	0.29	2.71	-2.11	0.25	3.75	-2.62	0.24	4.70

Table 6.2: Effect of T on ΔE_{C-A} and current density for the cerium reduction-oxidation reactions onto a platinised titanium mesh (131 cm^2) in a solution consisting of $8 \times 10^{-2} \text{ mol dm}^{-3}$ Ce(IV) and 6.9 mol dm^{-3} $\text{CH}_3\text{SO}_3\text{H}$ at 40 mV s^{-1} ; No rotation.

For the oxidation process, the peak current density (i_p) was similar as it was dominated by the bulk Ce(III) concentration rather than the Ce(III) generated at the electrode surface. The peak separation decreased with increasing temperature making the system more reversible. This trend has been confirmed by Raju *et al.* [9] as well as Leung *et al.* [8] in the same medium. Matheswaran *et al.* [37] reported that elevated temperatures increased the oxidation rate of Ce(III) in a solution containing $2 \times 10^{-1} \text{ mol dm}^{-3}$ Ce(III) and 2 mol dm^{-3} methanesulfonic acid.

The average diffusion coefficient as a function of temperature is shown in Table 6.. The large error is due to the small amount of Ce(IV) generated at the surface of the electrode just prior to the start of the scan in the negative direction. The D values increased with temperature for this diffusion control system indicating that higher temperatures favour the cerium reduction reaction in the presence of highly acidic media, (*i.e.* 6.9 mol dm^{-3} total methanesulfonic acid). This is again expected from the Stokes-Einstein equation (Eq.6.1). These values are in good agreement with the data of Yei *et al.* [38] in a solution containing $2 \times 10^{-2} \text{ mol dm}^{-3}$ and 6 mol dm^{-3} HNO_3 for all three temperatures investigated, *viz.* 25°C , 40°C and 60°C .

	$D / (10^{-7} \text{ cm}^2 \text{ s}^{-1})$
25°C	0.83 ± 0.3
40°C	2.20 ± 0.5
60°C	3.15 ± 0.5

Table 6.3: Average D values obtained as a function of T for the Pt-Ti mesh (131 cm^2) from the steady state study in $8 \times 10^{-2} \text{ mol dm}^{-3}$ Ce(IV), $7.2 \times 10^{-1} \text{ mol dm}^{-3}$ Ce(III) and 6.9 mol dm^{-3} $\text{CH}_3\text{SO}_3\text{H}$.

6.4.4 Pt|Ir substrates in $2 \times 10^{-1} \text{ mol dm}^{-3} \text{ Ce(IV)}$ and $6.9 \text{ mol dm}^{-3} \text{ CH}_3\text{SO}_3\text{H}$

The voltammetric behaviour of the platinum-iridium based substrates (BMM series) at three different temperatures (25°C, 40°C and 60°C) was investigated by cyclic voltammetry. From Fig.6.4 it has already been noted that at positive potentials (*i.e.* $> 1 \text{ V vs Hg|Hg}_2\text{SO}_4$ (sat.)), the current increased due to the OER and an oxidation peak could not be observed. Nonetheless, the data for the Ce(IV) reduction are summarized in Table 6.4.

		25°C	40°C	60°C
Electrode	Description	$i_{red} / (10^{-4} \text{ A cm}^{-2})$	$i_{red} / (10^{-4} \text{ A cm}^{-2})$	$i_{red} / (10^{-4} \text{ A cm}^{-2})$
BMM 1	Pt Ir composition: 30/70 - 9.9 g Pt/Ir m ⁻² [375°C]	-0.91	-1.21	-2.08
BMM 2	Pt Ir composition: 50/50 - 9.25 g Pt/Ir m ⁻² [500°C]	-0.43	-0.68	-0.91
BMM 3	Pt Ir composition: 30/70 - 10 g Pt/Ir m ⁻² [375°C]	-0.78	-1.13	-2.23
BMM 4	Pt Ir composition: 50/50 - 10.2 g Pt/Ir m ⁻² [375°C]	-0.33	-0.74	-1.15
BMM 6	Pt Ir composition: 50/50 - 9.25 g Pt/Ir m ⁻² [500°C]	-0.19	-0.45	-0.49
BMM 11	Pt Ir composition: 30/70 - 10 g Pt/Ir m ⁻² [375°C]	-1.19	-1.84	-2.44
BMM 13	Pt Ir composition: 50/50 - 10 g Pt/Ir m ⁻² [375°C]	-1.19	-1.56	-2.09
BMM 14	Pt Ir composition: 30/70 - 10 g Pt/Ir m ⁻² [375°C]	-1.17	-1.36	-1.98
BMM 15	Pt Ir composition: 50/50 - 10 g Pt/Ir m ⁻² [375°C]	-0.26	-0.71	-1.05

Table 6.4: Effect of T on i_{red} for the Ce(IV) reduction reaction in $2 \times 10^{-1} \text{ mol dm}^{-3} \text{ Ce(IV)} | 6 \times 10^{-1} \text{ mol dm}^{-3} \text{ Ce(III)}$ and $6.9 \text{ mol dm}^{-3} \text{ CH}_3\text{SO}_3\text{H}$ for the Pt-Ir based electrodes; 20 mV s^{-1} ; No rotation.

For all the electrodes examined, the cathodic peak current densities (i_{red}) increased with temperature. Interestingly, from Table 6.4, the highest i_{red} values were found for the BMM11 electrode at 60°C followed by the BMM1, BMM3 and BMM13 substrates. The above electrodes were prepared at lower firing temperatures suggesting that at these temperatures there seems to be more available active sites to carry out the Ce(IV) reduction reaction. The data from these measurements are in good agreement with literature values regarding the effect of temperature [8] [23].

6.4.5 Pt substrates in $2 \times 10^{-1} \text{ mol dm}^{-3} \text{ Ce(IV)}$ and $6.9 \text{ mol dm}^{-3} \text{ CH}_3\text{SO}_3\text{H}$

The voltammetric behaviour of the SL1 (5 g Pt m^{-2}) at three different temperatures (25°C , 40°C and 60°C) is displayed in Fig.6.14 in a solution containing $2 \times 10^{-1} \text{ mol dm}^{-3} \text{ Ce(IV)}$ and $6.9 \text{ mol dm}^{-3} \text{ CH}_3\text{SO}_3\text{H}$. The scan rate employed was 20 mV s^{-1} . The sweep rate was reversed when the potential approached $+0.5 \text{ V vs Hg|Hg}_2\text{SO}_4 \text{ (sat.)}$.

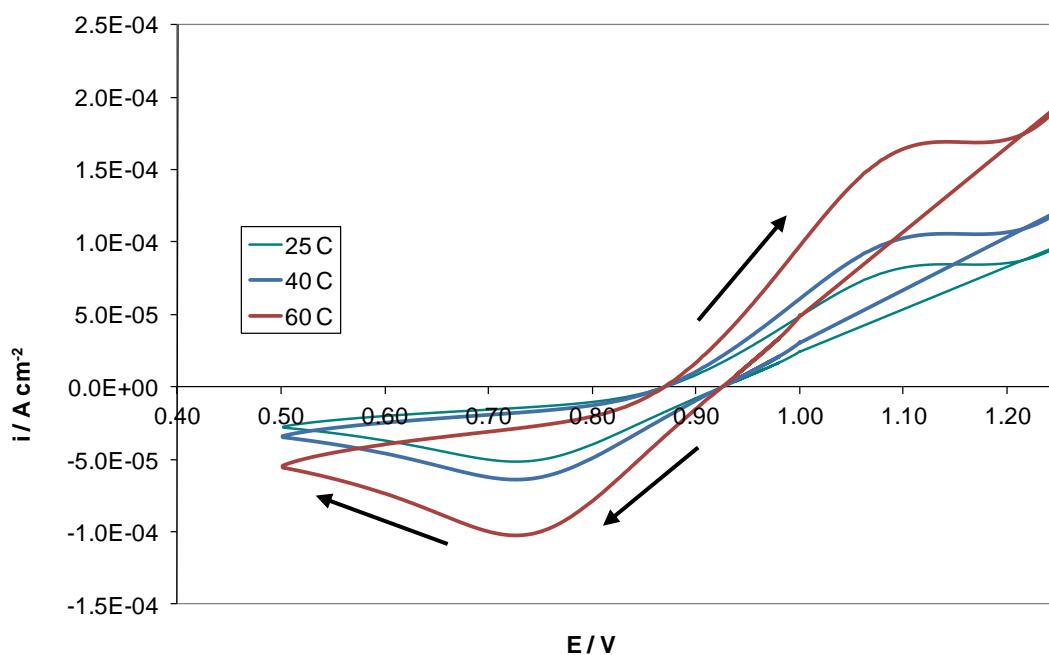


Fig.6.14: Effect of T on the Ce(IV) reduction reaction in a solution consisting of $2 \times 10^{-1} \text{ mol dm}^{-3} \text{ Ce(IV)}$ and $6.9 \text{ mol dm}^{-3} \text{ CH}_3\text{SO}_3\text{H}$ at 20 mV s^{-1} ; SL1 based electrode (120 cm^2); No rotation.

The effect of temperature on the cerium reduction reaction for all the Pt based substrates (SL) was similar to the one of the Pt-Ir electrodes (BMM). Thus, the current density obtained at 60°C for the Ce(IV) reduction ($-10 \times 10^{-4} \text{ A cm}^{-2}$) was larger by a factor of 2 to the one obtained at 25°C , *ca.* $-4.86 \times 10^{-5} \text{ A cm}^{-2}$. The same behaviour is noticed for the Ce(IV) oxidation reaction, where the highest current density is obtained at 60°C (*i.e.* $1.65 \times 10^{-4} \text{ A cm}^{-2}$). The onset potential for the reduction reaction did not shift with elevated temperature while for the oxidation reaction the shift was *ca.* 0.04 V . The peak separation of these reactions was *ca.* 0.39 V , larger than the ones of Table 6., which was under different electrolyte composition though. Hence, the behaviour of the voltammograms of Fig.6.14 suggest that the system is less reversible than the voltammogram of Fig.6.13 at all three temperatures investigated.

Nonetheless, Table 6. summarises the effect of temperature and current density for Ce(IV) reduction for the platinum based electrodes (SL). The results for the oxidation reaction showed the same trend as for the reduction reaction and hence were not included in the Table.

		25°C	40°C	60°C
Electrode	Description	$i_{red} / (10^{-4} \text{ A cm}^{-2})$	$i_{red} / (10^{-4} \text{ A cm}^{-2})$	$i_{red} / (10^{-4} \text{ A cm}^{-2})$
SL 1	5 g Pt m ⁻²	-0.48	-0.66	-1.00
SL 2	3 g Pt m ⁻²	-0.72	-1.12	-1.71
SL 3	(Etched) 5 g Pt m ⁻²	-0.18	-0.26	-0.32
SL 4	(Etched) 3 g Pt m ⁻²	-0.34	-0.51	-0.81
SL 5	(Sandblasted & etched) 3 g Pt m ⁻²	-0.22	-0.73	-1.02
SL 6	(Sandblasted & etched) 3 g Pt m ⁻²	-0.27	-0.46	-0.73
SL 7	(Sandblasted & etched) 3 g Pt m ⁻²	-0.17	-0.39	-0.65

Table 6.5: Effect of T on i_{red} for the Ce(IV) reduction reaction in $2 \times 10^{-1} \text{ mol dm}^{-3} \text{ Ce(IV)} | 6 \times 10^{-1} \text{ mol dm}^{-3} \text{ Ce(III)}$ and $6.9 \text{ mol dm}^{-3} \text{ CH}_3\text{SO}_3\text{H}$ for various Pt based electrodes; 20 mV s^{-1} ; No rotation.

As with the Pt-Ir substrates (Table 6.4), here also the effect of elevated temperatures was subtle as higher i_{red} were measured for the Ce(IV) reduction reaction. For instance, for the SL2 electrode, the current density at 60°C was 2.5 times larger than at 25°C. The highest current density was observed for the same electrode at 60°C *viz.* $-1.71 \times 10^{-4} \text{ A cm}^{-2}$, which is worth noting that has less amount of platinum coated (3 g Pt m⁻²) than the SL1 (5 g Pt m⁻²). This is surprising since the Pt electrode area was considerably larger (*i.e* by 50%) for the SL1 electrode. It could be that some deactivation process may have occurred on this electrode, reducing its surface conductivity and electrochemical activity. Another explanation could be that the distribution of the Pt on the surface of the SL1 electrode is less effective, leading to lower current densities.

6.5 Kinetics of the Ce(III)/Ce(IV) reaction onto different substrates

6.5.1 Introduction

The exchange current density (i_o) gives valuable information regarding the rates of electron transfer between the analyte and electrode. This depends critically on the nature of the electrode, its physical parameters such as surface roughness and on the electroactive species in the solution. Other important factors include the pH of the solution, the solvent and the temperature.

The kinetics of the Ce(III)/Ce(IV) reaction were investigated in a solution containing $2 \times 10^{-1} \text{ mol dm}^{-3}$ Ce(IV), $6 \times 10^{-1} \text{ mol dm}^{-3}$ Ce(III) and 6.9 mol dm^{-3} methanesulfonic acid at three different temperatures, *viz.* 25°C, 40°C and 60°C. Tafel extrapolation and polarisation resistance experiments were conducted at the three different temperatures while electrochemical impedance measurements were conducted only at room temperature *viz.* 25°C. The range of the substrates used in this study included the Pt-based electrodes, the Pt-Ir substrates, the Pt-Ti mesh and the platinum disk electrode (Table 6.1). The values of i_o are calculated with regards to the geometric surface area of the electrodes, *i.e.* the nominal surface area (1 cm^2), and then corrected for the effective surface area.

6.5.2 Polarisation resistance

The electrodes were scanned within 10 mV to 20 mV from the open circuit potential (E_{ocp}) and the current was measured using the 1286 Electrochemical Interface controlled by Corrware® software. The scan rate employed was 0.1667 mV s^{-1} . Vetter *et al.* [39] has shown that the charge transfer process is first order for the Ce(IV) reduction and Ce(III) oxidation reactions at low overpotentials ($\eta < 10 \text{ mV}$). Typical results from the polarisation resistance measurements obtained from the SL5 and BMM6 electrodes are shown in Fig.6.15 for 60°C and in Fig.6.16 for 40°C respectively. The Corrview® programme evaluated the E_{ocp} and i_o from each of the polarization curves. Table 6.6 summarises the results of the polarisation resistance technique for all the substrates used in this study.

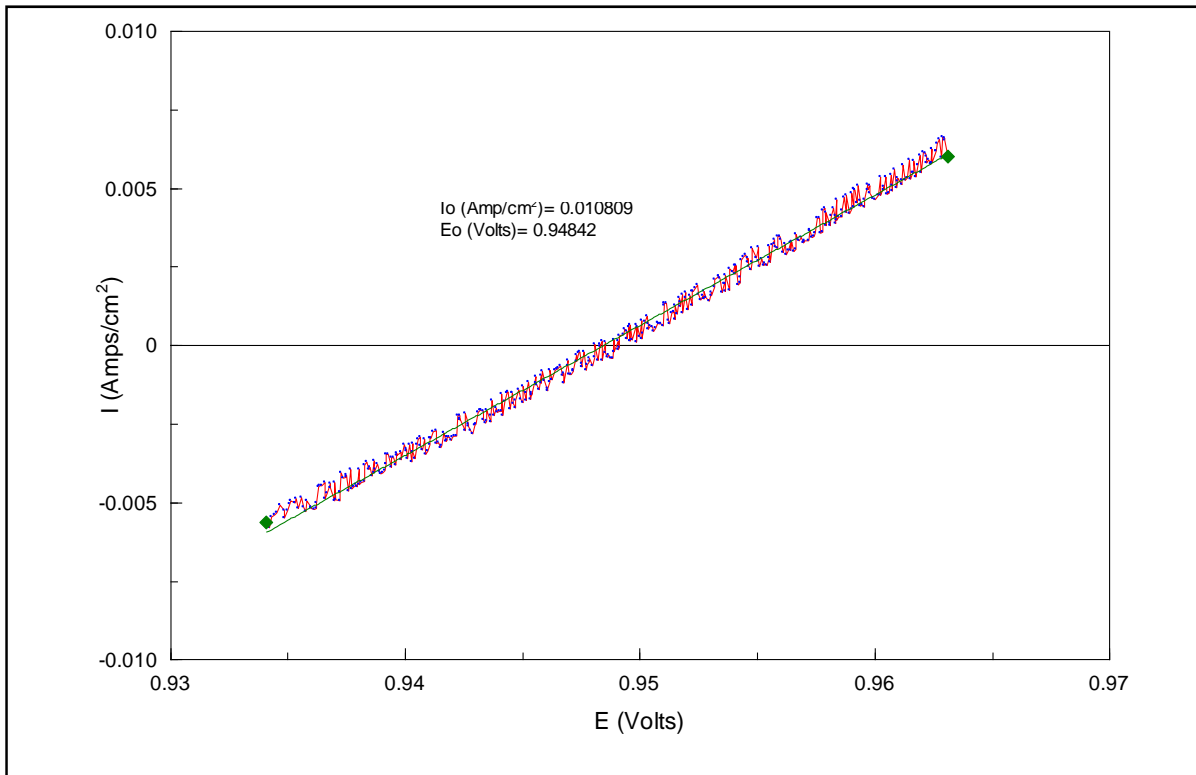


Fig.6.15: Polarisation resistance measurements in a solution containing $2 \times 10^{-1} \text{ mol dm}^{-3} \text{ Ce(IV)}$ and $6 \times 10^{-1} \text{ mol dm}^{-3} \text{ Ce(III)}$ and $6.9 \text{ mol dm}^{-3} \text{ CH}_3\text{SO}_3\text{H}$ at 60°C ; BMM6 (geometric surface area: 1 cm^2).

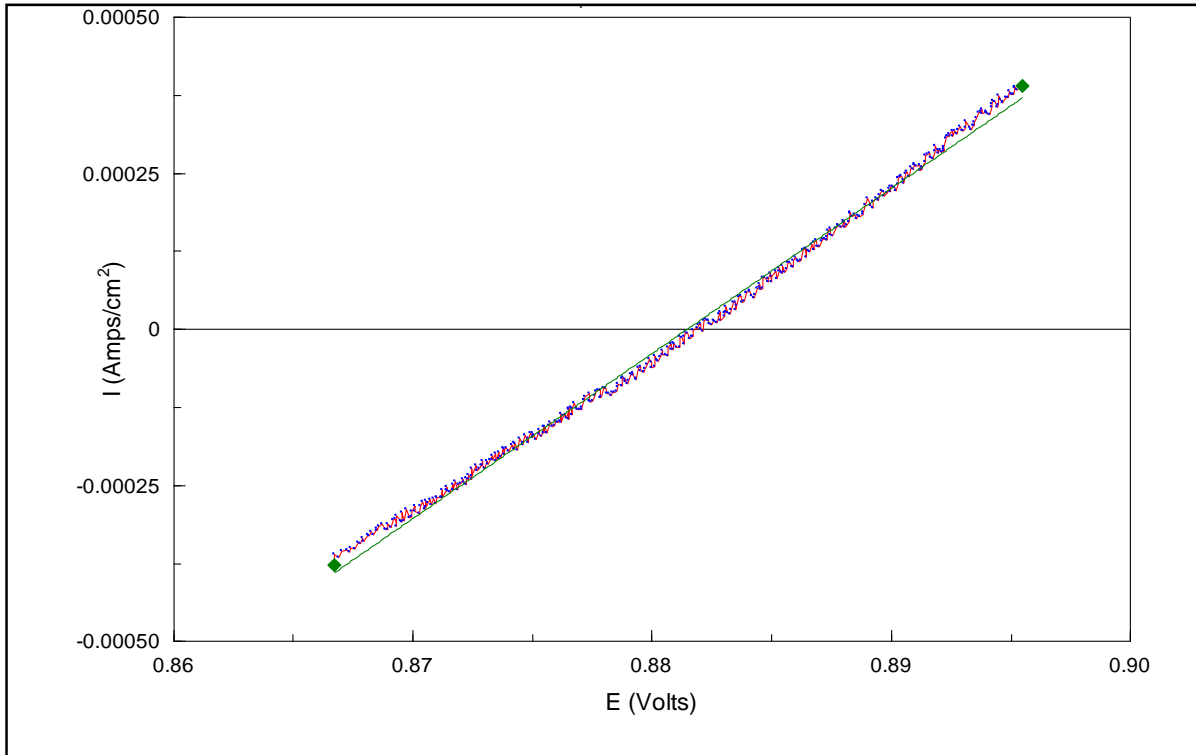


Fig.6.16: Polarisation resistance measurements in a solution containing $2 \times 10^{-1} \text{ mol dm}^{-3} \text{ Ce(IV)}$ and $6 \times 10^{-1} \text{ mol dm}^{-3} \text{ Ce(III)}$ and $6.9 \text{ mol dm}^{-3} \text{ CH}_3\text{SO}_3\text{H}$ at 40°C ; SL5 (geometric surface area: 1 cm^2).

		25°C	40°C	60°C
Electrodes	Description	$i_0 / (10^{-3} \text{ A cm}^{-2})$	$i_0 / (10^{-3} \text{ A cm}^{-2})$	$i_0 / (10^{-3} \text{ A cm}^{-2})$
BMM1	Pt Ir composition: 30/70 - 9.9 g Pt/Ir m ⁻² [375°C]	1.61	5.91	11.2
BMM2	Pt Ir composition: 50/50 - 9.25 g Pt/Ir m ⁻² [500°C]	1.32	1.41	2.52
BMM3	Pt Ir composition: 30/70 - 10 g Pt/Ir m ⁻² [375°C]	0.89	7.74	9.51
BMM4	Pt Ir composition: 50/50 - 10.2 g Pt/Ir m ⁻² [375°C]	0.82	2.71	9.2
BMM6	Pt Ir composition: 50/50 - 9.25 g Pt/Ir m ⁻² [500°C]	1.45	6.15	10.6
BMM11	Pt Ir composition: 30/70 - 10 g Pt/Ir m ⁻² [375°C]	1.41	2.31	4.72
BMM12	Pt Ir composition: 50/50 - 10 g Pt/Ir m ⁻² [375°C]	3.33	6.15	8.61
BMM13	Pt Ir composition: 30/70 - 10 g Pt/Ir m ⁻² [375°C]	1.40	2.84	5.21
BMM14	Pt Ir composition: 50/50 - 10 g Pt/Ir m ⁻² [375°C]	4.05	8.15	9.52
BMM15	Pt Ir composition: 30/70 - 9.9 g Pt/Ir m ⁻² [375°C]	3.81	4.71	10.6
SL1	5 g Pt m ⁻²	3.61	4.95	8.51
SL2	3 g Pt m ⁻²	0.91	3.28	3.33
SL3	(Etched) 5 g Pt m ⁻²	0.08	0.88	2.58
SL4	(Etched) 3 g Pt m ⁻²	0.05	1.32	1.75
SL5	(Sandblasted & etched) 3 g Pt m ⁻²	0.29	1.82	2.58
SL6	(Sandblasted & etched) 3 g Pt m ⁻²	0.36	0.85	2.66
SL7	(Sandblasted & etched) 3 g Pt m ⁻²	0.78	3.16	4.42
Pt-Ti mesh	10 g Pt m ⁻²	2.62	3.11	4.52
Pt Disk		0.64	3.36	5.32

Table 6.6: Effect of T on i_0 for the Ce(IV) reduction reaction in $2 \times 10^{-1} \text{ mol dm}^{-3} \text{ Ce(IV)} \mid 6 \times 10^{-1} \text{ mol dm}^{-3} \text{ Ce(III)}$ and $6.9 \text{ mol dm}^{-3} \text{ CH}_3\text{SO}_3\text{H}$ for various Pt and Pt-Ir electrodes; No rotation.

Regarding the Pt-Ti mesh, the i_o values increased with temperature but that increase was less dramatic than for some of the other samples such as SL3. The highest i_o achieved were for the BMM1, BMM4, BMM6, BMM15 and SL1 substrates, even higher than the platinum disk electrode, which is very encouraging. The above findings are in good agreement with the data of Matheswaran *et al.* [37] and Raju *et al.* [9] regarding the effect of temperature in the Ce(III) reduction reaction in the presence of methanesulfonic acid media. For all the range of substrates investigated, elevated temperatures (60°C) favoured the kinetics of the Ce(III)/Ce(IV) reaction as higher i_o values were recorded. The increase in i_o with temperature (from 25°C to 60°C) is by a factor of 10 for the BMM1, BMM3, BMM6 and SL5 electrodes and by a factor of 30 for the SL3 and SL4 electrodes over the temperature range studied. At 25°C, the electrochemical kinetics were considerably slower (approximately by a factor of 20 ($\sim 10^{-5}$ A cm⁻²)) for the platinum based substrates SL3 and SL4. For the majority of the other samples, i_o increased by a factor greater than 3 per 35°C. The values obtained in this study for the Ce(III)/Ce(IV) reduction reaction are in accordance with the i_o values found by Bonewitz *et al.* [40] and Maedaa *et al.* [41] in sulfuric, hydrochloric and nitric acid solutions for a gold and a boron-doped diamond electrode respectively ($i_o = \sim 10^{-4}$ A cm⁻²). The shift in the open circuit potential for the majority of samples was not significant, being nominally at +1.53 V \pm 0.05 V vs *S.H.E.* The slightly different values can be attributed to the effect of elevated temperatures and on the viscosity of the methanesulfonic acid as well as the cerium species [42].

6.5.3 Tafel extrapolation

In these experiments, the electrodes were polarised by ± 250 mV from the OCP potential at a scan rate of 2 mV s⁻¹. Examples of Tafel extrapolation (E_{ocp} versus $\log(i)$) are shown in Fig.6.17 and Fig.6. 18 for the SL1 and BMM4 electrodes at 25°C and 40°C correspondingly, assuming a geometric surface area of 1 cm². The cathodic scan represents the cerium reduction reaction while during the anodic scan the reverse reaction occurs, *i.e* cerium oxidation. The i_o values calculated in this study were based on the rising portion of the cathodic slope, *i.e* reduction of Ce(IV) as it has been shown in voltammetry that for the oxidation reaction a competing reaction takes place (*viz.* oxygen evolution reaction). For the majority of the substrates, the rising portion was between 150 mV and 250 mV from the OCP. This in turn resulted in higher than expected Tafel slope values (>120 mV per decade as shown in Fig.6.17 and Fig.6. 18) for both anodic and cathodic processes. The rising portion of the SL5, SL6 and BMM11 electrodes was between 120 mV and 200 mV per decade.

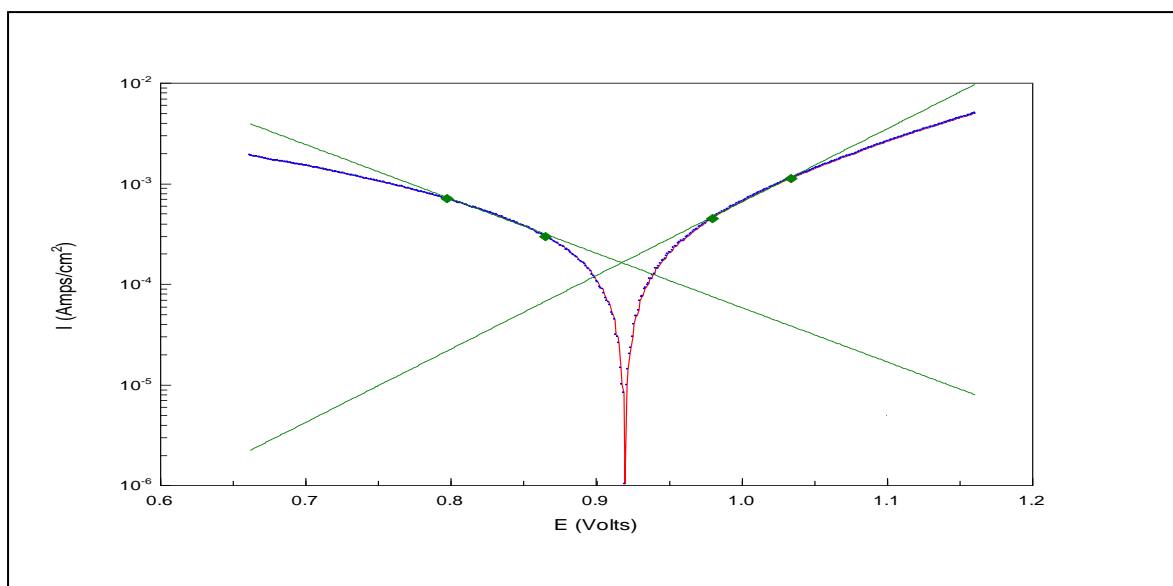


Fig.6.17: Tafel extrapolation measurements in a solution containing $2 \times 10^{-1} \text{ mol dm}^{-3} \text{ Ce(IV)}$ | $6 \times 10^{-1} \text{ mol dm}^{-3} \text{ Ce(III)}$ and $6.9 \text{ mol dm}^{-3} \text{ CH}_3\text{SO}_3\text{H}$ at 25°C ; SL1 substrate (1 cm^2).

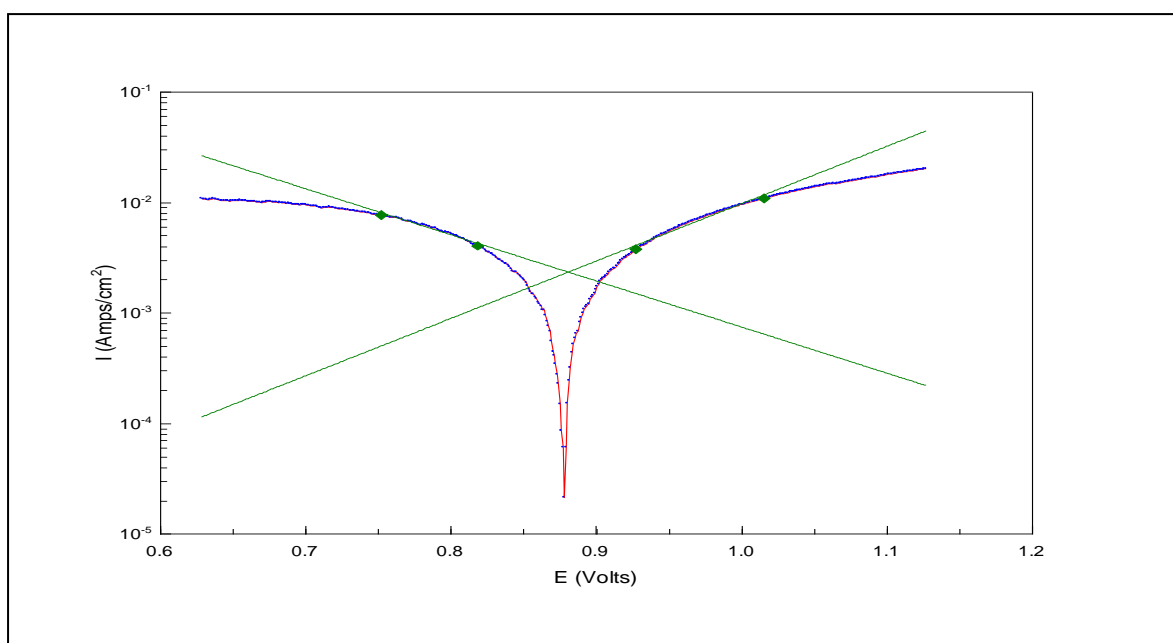


Fig.6. 18: Travel extrapolation measurements in a solution containing $2 \times 10^{-1} \text{ mol dm}^{-3} \text{ Coe (IV)}$ | $6 \times 10^{-1} \text{ mol dm}^{-3} \text{ Ce(III)}$ and $6.9 \text{ mol dm}^{-3} \text{ CH}_3\text{SO}_3\text{H}$ at 40°C ; BMM4 substrate (1 cm^2).

The Tafel slope values for the cerium reaction are considerably higher than the ones reported in literature. For instance, in nitric acid media the Tafel slope was *ca.* 85 mV per decade [43] while for the oxidation of cerium in $5 \times 10^{-1} \text{ mol dm}^{-3}$ total cerium and 1.6 mol dm^{-3} sulfuric acid the Tafel slope was *ca.* 36 mV per decade [36]. Greef *et al.* [42] found that the Tafel slope of a pure methanesulfonic acid solution was *ca.*117 mV per decade, in accordance to the one electron process Tafel slope. The i_o values obtained from the Tafel

extrapolation method at three different temperatures (25°C, 40°C and 60°C) are presented in Table 6. for the Pt/Ir, the Pt based electrodes and the Pt-Ti mesh. As with the polarisation resistance trials, the shift in the open circuit potential for the majority of samples was not significant, being nominally at +0.895 V \pm 0.02 V vs Hg|Hg₂SO₄|K₂SO₄ (sat.).

		25°C	40°C	60°C
Electrodes	Description	$i_0 / (10^{-3} \text{ A cm}^{-2})$	$i_0 / (10^{-3} \text{ A cm}^{-2})$	$i_0 / (10^{-3} \text{ A cm}^{-2})$
BMM1	Pt Ir composition: 30/70 - 9.9 g Pt/Ir m ⁻² [375°C]	6.25	7.28	8.43
BMM2	Pt Ir composition: 50/50 - 9.25 g Pt/Ir m ⁻² [500°C]	2.18	2.98	4.84
BMM3	Pt Ir composition: 30/70 - 10 g Pt/Ir m ⁻² [375°C]	1.01	7.68	9.27
BMM4	Pt Ir composition: 50/50 - 10.2 g Pt/Ir m ⁻² [375°C]	1.05	2.88	4.64
BMM6	Pt Ir composition: 50/50 - 9.25 g Pt/Ir m ⁻² [500°C]	1.85	5.15	11.2
BMM11	Pt Ir composition: 30/70 - 10 g Pt/Ir m ⁻² [375°C]	1.92	5.25	9.32
BMM12	Pt Ir composition: 50/50 - 10 g Pt/Ir m ⁻² [375°C]	4.58	6.81	8.62
BMM13	Pt Ir composition: 30/70 - 10 g Pt/Ir m ⁻² [375°C]	1.18	5.11	8.63
BMM14	Pt Ir composition: 50/50 - 10 g Pt/Ir m ⁻² [375°C]	1.96	7.95	9.85
BMM15	Pt Ir composition: 30/70 - 9.9 g Pt/Ir m ⁻² [375°C]	3.25	4.45	9.71
SL1	5 g Pt m ⁻²	3.41	8.70	11.1
SL2	3 g Pt m ⁻²	2.82	3.87	4.94
SL3	(Etched) 5 g Pt m ⁻²	0.06	1.71	6.14
SL4	(Etched) 3 g Pt m ⁻²	0.08	1.50	4.58
SL5	(Sandblasted & etched) 3 g Pt m ⁻²	0.51	2.21	7.90
SL6	(Sandblasted & etched) 3 g Pt m ⁻²	0.55	2.29	2.61
SL7	(Sandblasted & etched) 3 g Pt m ⁻²	0.10	5.37	6.73
Pt-Ti mesh	10 g Pt m ⁻²	5.54	8.12	10.4
Pt Disk		0.37	0.65	1.08

Table 6.7: Effect of T on i_0 for the Ce(IV) reduction reaction in $2 \times 10^{-1} \text{ mol dm}^{-3} \text{ Ce(IV)} | 6 \times 10^{-1} \text{ mol dm}^{-3} \text{ Ce(III)}$ and $6.9 \text{ mol dm}^{-3} \text{ CH}_3\text{SO}_3\text{H}$ for various Pt and Pt-Ir electrodes; No rotation; 2 mV s^{-1} .

The largest variations in i_o were obtained at 25°C. Typically the Pt only samples gave the highest i_o values in the range of $6 \times 10^{-3} \text{ A cm}^{-2}$ up to $3.41 \times 10^{-3} \text{ A cm}^{-2}$ for the SL4 and SL1 electrodes respectively. On repeating the same measurements at 60°C, the i_o values for these electrodes were only by a factor of 2 larger. The most noticeable increase in i_o as a function of temperature was found for the SL4 electrode. The values found for the Pt/Ir electrodes were generally much more modest, *i.e.* $1.85 \times 10^{-3} \text{ A cm}^{-2}$ at 25°C and $11.2 \times 10^{-3} \text{ A cm}^{-2}$ at 60°C. Chen *et al.* [7] reported that the presence of the iridium oxide leads to a more homogeneous dispersion of Pt particles (*i.e.* a more accessible surface area). It would appear that the etching of the Pt surface does not lead to active sites for the Ce(IV) reduction at room temperature but on increasing temperature to 60°C, more active surface sites become available.

High i_o values were recorded for the platinised titanium mesh at all temperatures. More precisely, at 25°C the highest i_o value was for the Pt-Ti mesh ($5.54 \times 10^{-2} \text{ A cm}^{-2}$) while at 40°C and 60°C where the cerium reduction reaction was proven to be electrochemically more favourable at the surface of the substrates, its i_o values were amongst the highest. The i_o values of the Pt disk electrode are very low compared to the rest of the electrodes. A possible explanation for these low values could be the formation of bubbles due to the hydrogen evolution reaction (it is the most likely parallel reaction to occur thermodynamically) on the Pt surface blocking the available electroactive surface area.

6.5.4 Electrochemical Impedance Spectroscopy

EIS measurements (Zplot[®] with Zview[™], Scribner Associates, Inc.) on the cerium reaction were conducted on the Pt disk electrode as well as the Pt and Pt-Ir based substrates at 25°C in a solution containing $2 \times 10^{-1} \text{ mol dm}^{-3}$ Ce(IV), $6 \times 10^{-1} \text{ mol dm}^{-3}$ Ce(III) in 6.9 mol dm^{-3} methanesulfonic acid. The potential at which these measurements were conducted, *i.e.* the open circuit potential, was determined from the voltammograms of the substrates. Then, more measurements were taken each time at 0.50 V increments towards the reduction reaction diffusion controlled peak.

In order to fit the data from the impedance measurements, the appropriate circuit was constructed with the aid of the Z-plot impedance software. It represents an electrode reaction with double layer capacitance (R2) and an uncompensated solution resistance (R1). R2 is always parallel to the Faradaic reaction impedance. The constant phase element (CPE-1) used in the circuit represents a distributed capacitance of the surface rather than the constant and fixed value of the double layer capacitance. It is defined by two values CPE1-T and CPE1-P (Table 6.). If CPE1-P equals to 1, then the CPE is identical to that of the capacitor. The reaction resistance has been resolved into the charge transfer resistance (R2) and the Warburg impedance (Fig.6.19). The latter is defined by W1-R, W1-T and W1-P. In the case where the data exhibit only the high frequency (45° slope) behaviour, W1-R and W1-P must be set as fixed (Table 6.).

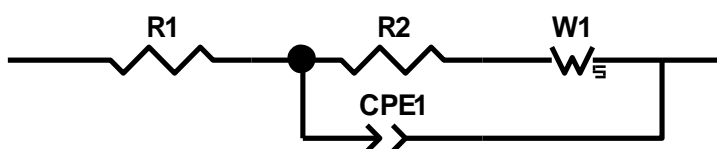


Fig.6.19: Circuit fit for the BMM3 electrode at 0.86 V (82 cm²).

Element	Freedom	Value	Error	Error %
R1	Free(+)	0.54791	0.0022656	0.4135
R2	Free(+)	1.747	0.010565	0.60475
W1-R	Fixed(X)	7.54	N/A	N/A
W1-T	Free(+)	69.77	1.2335	1.768
W1-P	Fixed(X)	0.425	N/A	N/A
CPE1-T	Fixed(X)	0.019	N/A	N/A
CPE1-P	Free(+)	0.73593	0.0015711	0.21348

Table 6.8: Impedance results of circuit fit for the BMM3 substrate at 0.86 V in $2 \times 10^{-1} \text{ mol dm}^{-3}$ Ce(IV) | $6 \times 10^{-1} \text{ mol dm}^{-3}$ Ce(III) and 6.9 mol dm^{-3} CH₃SO₃H.

As expected, the majority of the substrates of Table 6.1 are not diffusion controlled at the open circuit potential apart from SL7, SL4 and BMM3 and BMM4 electrodes. Fig.6.20 shows the equivalent circuit for a system where even close to the diffusion peak potential a large contribution from the charge transfer was still present. Hence, the Warburg impedance in this circuit is absent. The results from this circuit are presented in Table 6.10.

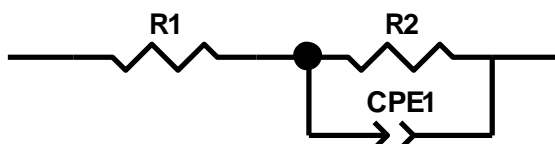


Fig.6.20 Circuit fit for a Pt based electrode at 0.70 V (SL7: 185 cm²).

Element	Freedom	Value	Error	Error %
R1	Free(+)	0.40099	0.0045262	1.1288
R2	Free(+)	239.3	2.175	0.9089
CPE1-T	Free(+)	0.00058592	5.1921E-06	0.88614
CPE1-P	Free(±)	0.78567	0.0012963	0.16499

Table 6.9: Impedance results of circuit fit for a SL7 electrode at 0.70 V in $2 \times 10^{-1} \text{ mol dm}^{-3} \text{ Ce(IV)} | 6 \times 10^{-1} \text{ mol dm}^{-3} \text{ Ce(III)}$ and $6.9 \text{ mol dm}^{-3} \text{ CH}_3\text{SO}_3\text{H}$.

The values of the solution resistance ($R1$) and double layer capacitance are in accordance with literature values [44] [45] in sulfuric acid media ($5 \times 10^{-1} \text{ mol dm}^{-3}$) on a platinum electrode (*viz.* $6 \times 10^{-1} \Omega$). The impedance modulus $|Z|$ and theta (θ) against frequency plots achieved at the halfwave potential for the BMM3 electrode are displayed in Fig.6.21 while Fig.6.22 shows the corresponding complex plane $|Z''|$ impedance plot. It is assumed that close to the reversible potential the relationship between current and potential is linear rather than logarithmic, which is true for a sinusoidal excitation voltage less than 5 mV amplitude on either side of the reversible potential. The frequency range (ω) was set between 10^{-1} Hz and 10^{-3} Hz . The depressed semicircle portion at the high frequency range represented the charge transfer process in parallel to the CPE suggesting that the electrode surface is rough, leading towards porous behaviour. The linear part in the low frequency range implied a diffusion limited process. The high frequency intercept gives the value of the uncompensated solution resistance ($R1$).

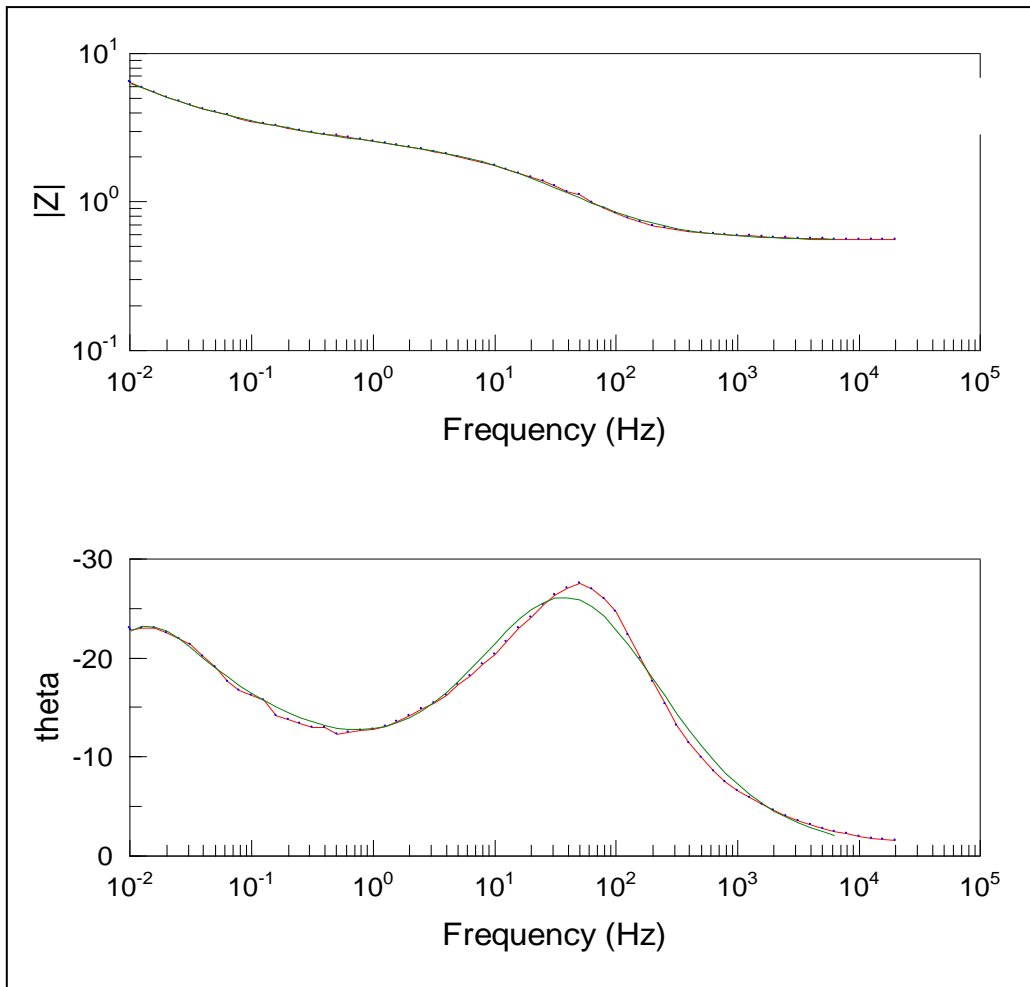


Fig.6.21: Impedance modulus and theta against frequency at 0.835 V in $2 \times 10^{-1} \text{ mol dm}^{-3} \text{ Ce(IV)} | 6 \times 10^{-1} \text{ mol dm}^{-3} \text{ Ce(III)}$ and $6.9 \text{ mol dm}^{-3} \text{ CH}_3\text{SO}_3\text{H}$; BMM3 substrate (82 cm^2).

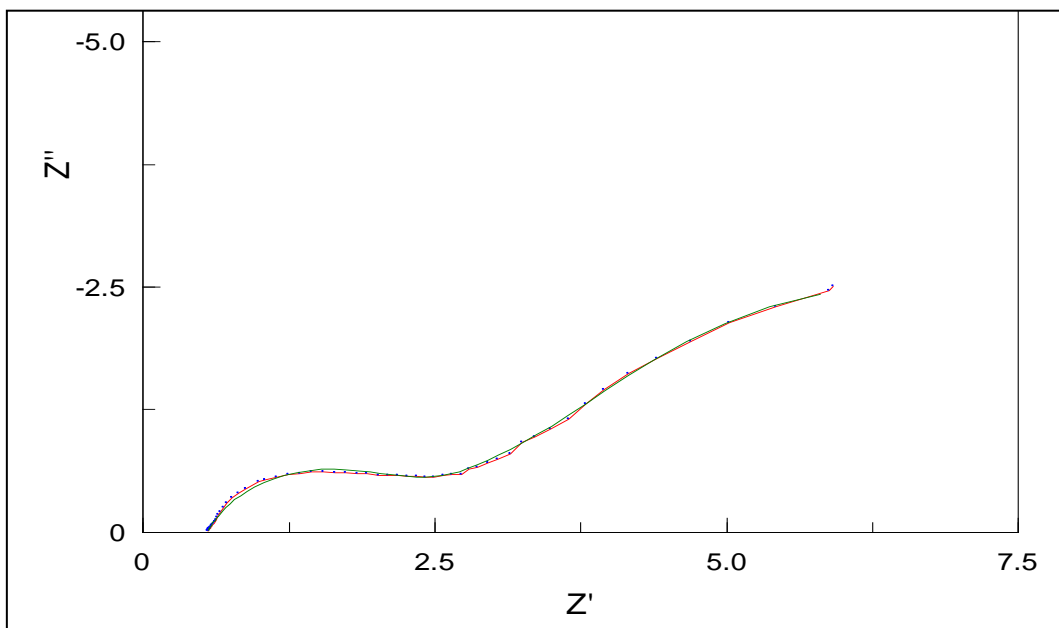


Fig.6.22: Complex plane impedance plot for the circuit of Fig.6.19 in $2 \times 10^{-1} \text{ mol dm}^{-3} \text{ Ce(IV)} | 6 \times 10^{-1} \text{ mol dm}^{-3} \text{ Ce(III)}$ and $6.9 \text{ mol dm}^{-3} \text{ CH}_3\text{SO}_3\text{H}$; BMM3 substrate (82 cm^2).

From the fitting of the experimental data in Fig.6.22, the charge transfer coefficient (R_{ct}) for a planar diffusion field was measured, leading to i_o from Eq.3.32 Chapter 3. The results for the Pt based (SL), the Pt-Ir based (BMM) electrodes and the Pt disk electrode are shown in Table 6.10 at 25°C. The i_o values obtained from the other two techniques (polarisation resistance, Tafel extrapolation) are also included in Table 6.10 allowing a direct comparison of the three techniques with regards to obtaining the kinetics of the cerium reduction reaction. The CPE1-P values of the platinum based substrates (SL) were between 0.88 ± 0.02 confirming the porosity and roughness of the surface of the substrates as expected since they have been sandblasted and etched. These values for the Pt-Ir based substrates were slightly lower, *ca.* 0.83 ± 0.03 .

	$i_o / (10^{-3} \text{ A cm}^{-2})$		
	Tafel extrapolation	Linear Polarisation	EIS
BMM 1	6.25	1.61	-*
BMM 2	2.18	1.32	0.82
BMM 3	1.01	0.89	0.91
BMM 4	1.05	0.82	1.60
BMM 6	1.85	1.45	0.63
BMM 11	1.92	1.41	0.97
BMM 12	4.58	3.33	1.46
BMM 13	1.18	1.40	1.53
BMM 14	1.96	4.05	-*
BMM 15	3.25	3.81	2.06
SL 1	3.41	3.61	3.37
SL 2	2.82	3.28	2.92
SL 3	0.06	0.08	0.21
SL 4	0.08	0.05	0.32
SL 5	0.5	0.29	0.65
SL 6	0.55	0.36	0.86
SL 7	0.10	0.78	0.11
Pt Disk	0.37	0.64	0.24

Table 6.10: Comparison of i_o from different techniques for the Ce(IV) reduction reaction in $2.0 \times 10^{-1} \text{ mol dm}^{-3} \text{ Ce(IV)} \mid 6 \times 10^{-1} \text{ mol dm}^{-3} \text{ Ce(III)}$ and $6.9 \text{ mol dm}^{-3} \text{ CH}_3\text{SO}_3\text{H}$ for various Pt and Pt-Ir based electrodes; T 25°C; No rotation.

*: Not measured

The majority of the EIS results were in good agreement with the data from the two other techniques, especially for the BMM3, BMM13 and SL1, SL2 and SL5 substrates. There are however some discrepancies such as in the case of the BMM6, BMM12 and SL3 and SL4 substrates where the i_o values obtained from impedance were lower by a factor of 3 than the values from Tafel extrapolation and polarisation resistance measurements. This difference can be attributed to changes on the surface activity of the substrates as they were in contact with highly acidic electrolytes. Part of the platinum and/or iridium coatings could deteriorate with prolonged use resulting in less active surface area available for the EIS measurements. Nevertheless, such a behaviour would be expected in media containing Cl^- ions [46] [47] but here, the complexing ability of methanesulfonic acid to Pt/Ir is not known and therefore the behaviour could not be predicted.

To summarise the results from Table 6.10, the highest current densities achieved at 25°C were for the SL1 and SL2 electrodes clearly highlighting the effect of platinum on the kinetics of the cerium reduction reaction (*i.e* fast kinetics in Pt as reported from the literature [8] [14]). Etching and sandblasting (SL substrates) did not seem to have an effect on the process as the values were considerably lower, in the case of the SL3 and SL4 electrodes by a factor of 10^2 . However the values of the etched and sandblasted electrodes increased along with temperature. The values of the Pt-Ir based substrates were between $1 \times 10^{-3} \text{ A cm}^{-2}$ and $3 \times 10^{-3} \text{ A cm}^{-2}$ with the exception of the BMM1 and BMM12 electrodes, which showed remarkably high i_o values from the Tafel extrapolation technique. Nothing seems to support the results of these two electrodes as both electrodes consisted of 70% iridium and 30% platinum and the rest of the data has shown that higher platinum compositions enhanced in a much greater extent the kinetics of the Ce(IV) reaction.

6.6 Galvanic cycles

6.6.1 Introduction

Charge-discharge trials (galvanic cycles) on the substrates listed in Table 6.1 were conducted on a jacketed three electrode cell in order to investigate the behavior of the electrodes when cycling in solutions containing various Ce(III) and Ce(IV) concentrations. For the Ce(IV) species, the concentration varied from $2 \times 10^{-1} \text{ mol dm}^{-3}$ to $4 \times 10^{-1} \text{ mol dm}^{-3}$ while for the Ce(III) species the concentration was between $6 \times 10^{-1} \text{ mol dm}^{-3}$ and $4 \times 10^{-1} \text{ mol dm}^{-3}$. As mentioned previously, thermodynamically during the cerium oxidation the oxygen evolution reaction occurs while at the Ce(IV) reduction the most likely parallel reaction to occur is the oxygen reduction reaction. However, the Ce(III) concentration will always be much lower than the reactant for oxygen evolution in acid medium, *i.e.* H_2O (55 mol dm^{-3}) and therefore it is more likely that the reaction becomes kinetically hindered. A 117 Nafion[®] membrane was used in the counter electrode (Pt gauze) to separate the working electrode from the main cell body. The use of the membrane was essential for preventing the back reaction (*i.e.* $\text{Ce}^{4+} + \text{e}^- \rightarrow \text{Ce}^{3+}$) occurring at the counter electrode.

Under the flow regimes used, *i.e.* 5 Hz to 30 Hz (*Re* from 62 to 375), the charge-discharge cycles for all the electrodes tested revealed coulombic efficiencies (η_C) of 100% for the solutions mentioned above at current densities ranging from 5 mA cm^{-2} to 30 mA cm^{-2} . However, there is no indication of the percentage of current that is used for the cerium reactions and the percentage for the competing reactions (*i.e.* mainly HER and OER). The software is built in a way that regardless of the actual coulombic efficiency of the Ce(III)/Ce(IV) reactions, the rest of the current will be carried from a parallel reaction so as to obtain η_C of 100%. Therefore, this study focused on the voltage efficiencies and how they interacted with parameters such as rotation rate, temperature, charge-discharge current densities and finally state of charge (SOC), *i.e.* the $[\text{Ce(IV)}]/[\text{Ce(III)}]$ ratio. The galvanic cycles conducted were based on the geometric area of the electrodes, *viz.* 1 cm^2 .

6.6.2 Effect of rotation rate

The effect of electrode rotation rate on the η_V can be gleaned from the data of Fig.6.23 for five charge-discharge cycles at $\pm 5 \text{ mA cm}^{-2}$ and 60°C . The galvanic cycles were conducted on a platinum based electrode that had been previously etched (SL4: 3 g Pt m^{-2}). The charging time was 1 minute for a solution containing $2 \times 10^{-1} \text{ mol dm}^{-3} \text{ Ce(IV)}$, $6 \times 10^{-1} \text{ mol dm}^{-3} \text{ Ce(III)}$ and 6.9 mol dm^{-3} methanesulfonic acid.

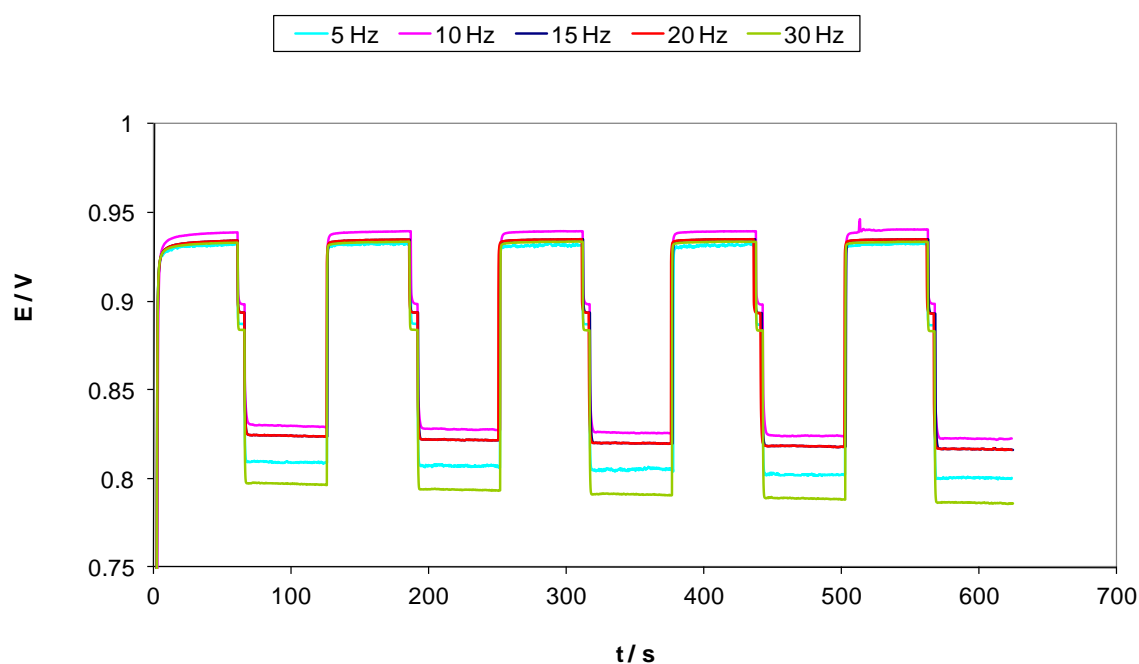


Fig.6.23: Effect of electrode rotation rate on the η_V for the SL4 (1 cm^2) substrate in $2 \times 10^{-1} \text{ mol dm}^{-3} \text{ Ce(IV)}$ / $6 \times 10^{-1} \text{ mol dm}^{-3} \text{ Ce(III)}$ and $6.9 \text{ mol dm}^{-3} \text{ CH}_3\text{SO}_3\text{H}$ solution at 60°C ; charge at 5 mA cm^{-2} for 1 minute / discharge at -5 mA cm^{-2} .

At the intermediate rotation rates of 10 Hz to 20 Hz, a constant potential of $0.825 \pm 0.02 \text{ V}$ was found during discharge (*i.e.* $\text{Ce}^{4+} + \text{e}^- \rightarrow \text{Ce}^{3+}$). This indicates that the reaction taking place to maintain the current demand is indeed the stated one. However, at 5 Hz and 30 Hz, the discharge potential was lower, at 0.81 V and 0.80 V respectively. For the lower flow rate, it could be the bubble formation on the surface of the substrate during the charge (due to the OER) was not completely removed and so the polarization (*i.e.* equilibrium potential) increased during discharge. At each rotation speed, the open circuit potential remained constant with respect to repetitive cycling *viz.* $0.89 \pm 0.02 \text{ V}$.

The effect of electrode rotation rate on the η_V for the cerium half cell reaction (charging time: 1 minute) is summarised in Table 6.11 for the various electrolytes containing different Ce(IV) and Ce(III) concentrations in $6.9 \text{ mol dm}^{-3} \text{ CH}_3\text{SO}_3\text{H}$ at 60°C . The charge-discharge current density applied was $\pm 5 \text{ mA cm}^{-2}$ and the materials examined were the Pt based (SL), the Pt-Ir based (BMM) and the Pt disk electrodes.

Rotation rate / Hz	5	10	20	30
<i>Re</i>	114	227	454	681
$2 \times 10^{-1} \text{ mol dm}^{-3} \text{ Ce(IV)} \mid 6 \times 10^{-1} \text{ mol dm}^{-3} \text{ Ce(III)}$ in $6.9 \text{ mol dm}^{-3} \text{ CH}_3\text{SO}_3\text{H}$				
SL1	82%	95%	90%	80%
SL2	85%	95%	91%	90%
SL4	86%	89%	89%	83%
SL7	42%	70%	68%	40%
BMM11	62%	94%	88%	42%
BMM12	54%	77%	72%	48%
BMM13	65%	79%	76%	60%
BMM14	85%	93%	89%	79%
Pt disk	88%	96%	94%	87%
$3 \times 10^{-1} \text{ mol dm}^{-3} \text{ Ce(IV)} \mid 5 \times 10^{-1} \text{ mol dm}^{-3} \text{ Ce(III)}$ in $6.9 \text{ mol dm}^{-3} \text{ CH}_3\text{SO}_3\text{H}$				
SL3	48%	78%	74%	65%
SL5	71%	94%	89%	45%
BMM 15	58%	93%	90%	69%
$4 \times 10^{-1} \text{ mol dm}^{-3} \text{ Ce(IV)} \mid 4 \times 10^{-1} \text{ mol dm}^{-3} \text{ Ce(III)}$ in $6.9 \text{ mol dm}^{-3} \text{ CH}_3\text{SO}_3\text{H}$				
SL2	90%	94%	91%	88%
SL3	68%	91%	84%	71%
SL7	87%	94%	92%	82%
BMM1	65%	90%	87%	57%
BMM2	92%	96%	95%	58%
BMM3	58%	90%	87%	54%
BMM6	91%	94%	91%	88%
BMM11	94%	96%	97%	87%

Table 6.11: Effect of electrode rotation rate on η_V for the Pt and Pt/Ir based electrodes in various [Ce(IV)] and [Ce(III)] in $6.9 \text{ mol dm}^{-3} \text{ CH}_3\text{SO}_3\text{H}$ solution at 60°C ; charge at 5 mA cm^{-2} for 1 minute / discharge at -5 mA cm^{-2} .

The similarity in the values at 10 Hz and 20 Hz indicate that mass transport was sufficient to satisfy the current demand at these rotation rates. The trend seen in Table 6.11 reflects the discussion carried out on the data of Fig.6.23 above. The data from Table 6.11 clearly indicate that the optimum rotation rate for most of the substrates was between 10 Hz and 20 Hz irrespective of the Ce(IV) and Ce(III) concentrations in 6.9 mol dm^{-3} total acid concentration. At low rotation rates (5 Hz) some substrates like the SL3, SL5 and the BMM1, BMM3 and BMM12 had 25% lower voltage efficiencies. During discharge, the potential dropped to 0.7 V, which is the potential where the oxygen reduction reaction occurs. Clearly, at this rotation rate the current is not sufficient to carry the Ce(IV) reaction leading to the next reaction in line, which is the reduction of oxygen.

It is worth noting that within the rotation rates *viz.* 10 Hz to 20 Hz, several substrates (SL1, SL2, SL4 and BMM11, BMM14) exhibited η_v values similar to those of the pure Pt disk electrode, for a solution containing $2 \times 10^{-1} \text{ mol dm}^{-3}$ Ce(IV), $6 \times 10^{-1} \text{ mol dm}^{-3}$ Ce(III) in 6.9 mol dm^{-3} methanesulfonic acid. This outcome is very encouraging suggesting that these substrates can potentially replace the use of platinum as a working electrode for the positive side of the zinc cerium flow cell.

6.6.3 Effect of temperature

The effect of temperature on η_V was investigated at two rotation rates *viz.* 10 Hz and 15 Hz onto the Pt and Pt-Ir substrates at 25°C and 60°C. The above rotation rates were selected because they are within the optimum rotation speed range established in the previous section. Table 6.12 sums up the effect of temperature on η_V for various electrolytes containing different Ce(IV) and Ce(III) concentrations in 6.9 mol dm⁻³ methanesulfonic acid, using a charge and discharge current density of ± 10 mA cm⁻².

Rotation Rate / Hz	10		15	
	25°C	60°C	25°C	60°C
2×10^{-1} mol dm⁻³ Ce(IV) 6×10^{-1} mol dm⁻³ Ce(III) in 6.9 mol dm⁻³ CH₃SO₃H				
SL1	57%	80%	77%	90%
SL2	73%	82%	72%	84%
SL4	36%	73%	34%	71%
SL7	63%	68%	67%	70%
BMM11	79%	83%	80%	81%
BMM12	77%	80%	79%	81%
BMM14	75%	85%	76%	88%
3×10^{-1} mol dm⁻³ Ce(IV) 5×10^{-1} mol dm⁻³ Ce(III) in 6.9 mol dm⁻³ CH₃SO₃H				
SL3	34%	68%	35%	82%
SL5	52%	65%	75%	83%
BMM15	49%	64%	55%	72%
4×10^{-1} mol dm⁻³ Ce(IV) 4×10^{-1} mol dm⁻³ Ce(III) in 6.9 mol dm⁻³ CH₃SO₃H				
SL2	70%	81%	77%	83%
SL3	53%	65%	55%	73%
SL4	55%	62%	50%	65%
SL7	66%	85%	43%	81%
BMM2	83%	75%	79%	88%
BMM6	85%	91%	84%	88%
BMM11	73%	83%	74%	80%
BMM15	36%	75%	41%	87%

Table 6.12: Effect of T on η_V for various Pt and Pt-Ir electrodes in various [Ce(IV)] and [Ce(III)] in 6.9 mol dm⁻³ CH₃SO₃H solution at 60°C; charge at 10 mA cm⁻² for 1 minute / discharge at -10 mA cm⁻² at 10 Hz and 15 Hz.

Table 6.12 showed an increase in η_V with increasing temperatures for all the substrates tested regardless of Ce(III) and Ce(IV) concentrations. This was due to the fact that elevated temperatures increased the kinetics of the Ce(III)/Ce(IV) reaction. The highest increase in η_V with temperature was recorded for the BMM15, SL3 and SL4 electrodes. The majority of the η_V values were between 80% and 90% at 60°C. Regarding the open circuit potential values, elevated temperatures increased the values to a small extent, *ca.* by 10-25 mV depending on the substrate. It is worth noting that the η_V values were lower than the ones of Table 6.11 as the current density in this case was twice as large as in Table 6.11 *viz.* $\pm 10 \text{ mA cm}^{-2}$ compared to $\pm 5 \text{ mA cm}^{-2}$. Higher current densities resulted in lower η_V values due to ohmic resistance losses. This was also found in the galvanic cycles conducted for the zinc half cell reaction (Chapter 5, Section 5.5.5).

The outcome of Table 6.12 is additional evidence to those reported from cyclic voltammetry, Tafel extrapolation and polarisation resistance that at elevated temperatures the Ce(III)/Ce(IV) reaction is favoured. Raju *et al.* [9] reported that the optimum temperature for the Ce(III)/Ce(IV) couple is 50°C resulting in higher current efficiencies in the generation of Ce(IV) ions in a solution containing $8 \times 10^{-1} \text{ mol dm}^{-3}$ Ce(III) and 5.4 mol dm^{-3} methanesulfonic acid.

6.6.4 Effect of charge and discharge current density

So far, only current densities of $\pm 5 \text{ mA cm}^{-2}$ and $\pm 10 \text{ mA cm}^{-2}$ were investigated with regards to the effect of temperature and of solution flow velocity. In the following experiments, the effect of higher charge and discharge current densities up to 25 mA cm^{-2} were investigated and the data are presented in Table 6.13 for the various electrode substrates (Table 6.1).

charge - discharge current density / mA cm^{-2}	± 5	± 10	± 20	± 25
$2 \times 10^{-1} \text{ mol dm}^{-3} \text{ Ce(IV)} \mid 6 \times 10^{-1} \text{ mol dm}^{-3} \text{ Ce(III)}$ in $6.9 \text{ mol dm}^{-3} \text{ CH}_3\text{SO}_3\text{H}$				
SL1	95%	80%	71%	62%
SL2	95%	82%	70%	54%
SL4	89%	73%	33%	<10%
SL7	67%	68%	41%	35%
BMM2	87%	76%	<10%	<10%
BMM11	77%	83%	31%	<10%
BMM12	79%	80%	<10%	<10%
BMM13	79%	73%	60%	46%
BMM14	93%	85%	70%	58%
Pt disk	88%	79%	45%	<10%
$3 \times 10^{-1} \text{ mol dm}^{-3} \text{ Ce(IV)} \mid 5 \times 10^{-1} \text{ mol dm}^{-3} \text{ Ce(III)}$ in $6.9 \text{ mol dm}^{-3} \text{ CH}_3\text{SO}_3\text{H}$				
SL3	78%	68%	45%	<20%
SL5	94%	65%	<20%	<20%
BMM15	93%	64%	48%	28%
$4 \times 10^{-1} \text{ mol dm}^{-3} \text{ Ce(IV)} \mid 4 \times 10^{-1} \text{ mol dm}^{-3} \text{ Ce(III)}$ in $6.9 \text{ mol dm}^{-3} \text{ CH}_3\text{SO}_3\text{H}$				
SL2	90%	81%	62%	55%
SL3	68%	65%	50%	35%
SL4	70%	62%	25%	<10%
SL7	87%	85%	66%	46%
BMM2	92%	75%	66%	48%
BMM6	91%	91%	78%	65%
BMM11	94%	83%	66%	42%
BMM15	78%	75%	37%	<10%

Table 6.13: Effect of charge and discharge current densities on η_V for various Pt and Pt-Ir electrodes in various $[\text{Ce(IV)}]$ and $[\text{Ce(III)}]$ in $6.9 \text{ mol dm}^{-3} \text{ CH}_3\text{SO}_3\text{H}$ solution at 60°C and 10 Hz ; charging time: 2 minutes.

As expected, the results from Table 6.13 showed that a decrease in η_V occurred with the application of higher charge and discharge current densities. At high charge current densities ($>25 \text{ mA cm}^{-2}$), the OER occurs on the electrode as seen from the potential during steady charge, some 300 mV more positive than the OCP (for the SL1 electrode Fig.6.24). A large part of this overpotential stems from the increased ohmic losses from the solution. The greatest loss of overpotential though occurs during discharge where the falling discharge potential signifies that insufficient Ce(IV) is present in the electrolyte to satisfy the current demand and a secondary reaction takes over to maintain this current. From this study, it would appear that the highest charge and discharge current densities that can be applied to this system are $\pm 20 \text{ mA cm}^{-2}$ with regards to the substrates listed in Table 6.1.

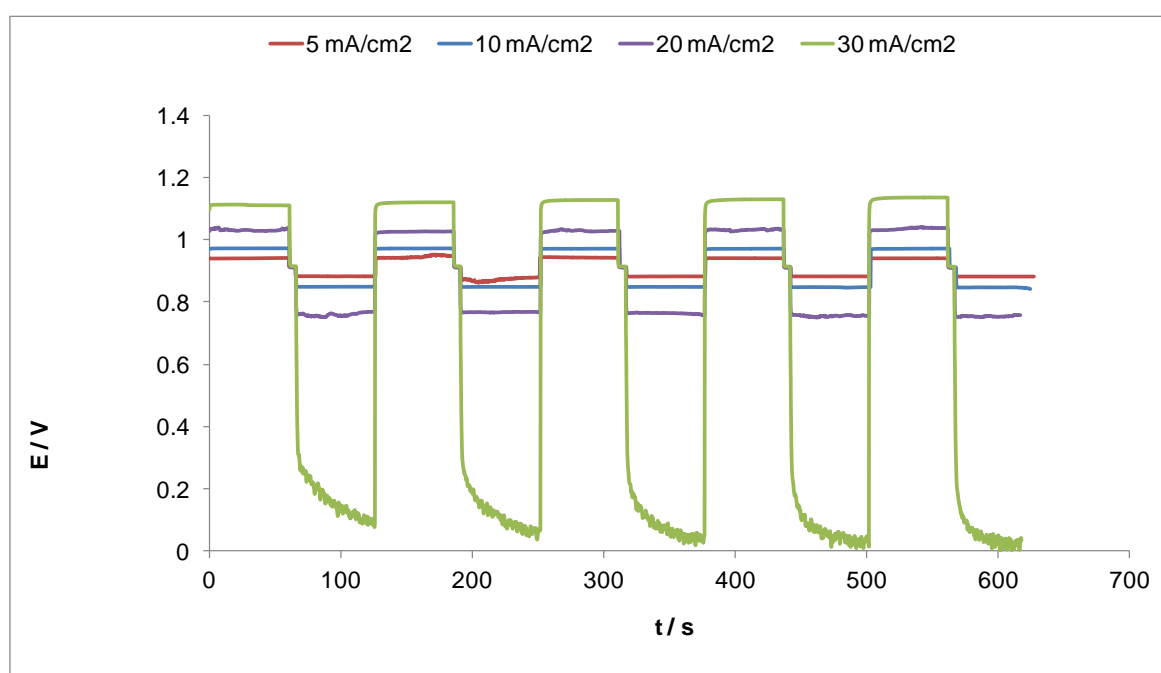


Fig.6.24: Effect of charge and discharge current density on η_V for the SL1 (1 cm^2) substrate in in $2 \times 10^{-1} \text{ mol dm}^{-3} \text{ Ce(IV)}$ / $6 \times 10^{-1} \text{ mol dm}^{-3} \text{ Ce(III)}$ and $6.9 \text{ mol dm}^{-3} \text{ CH}_3\text{SO}_3\text{H}$ solution at 60°C ; charge for 1 minute at 10 Hz.

6.6.5 Effect of prolonged cycling on the Pt and Pt-It substrates

The effect of prolonged cycling (at current densities between $\pm 5 \text{ mA cm}^{-2}$ and $\pm 20 \text{ mA cm}^{-2}$) on the Pt and Pt-Ir based materials was investigated by means of cyclic voltammetry. Fig 6.26 and Fig.6.27 show the Ce(III)/Ce(IV) reaction on the SL1 and BMM15 substrates in solutions containing Ce(IV) and Ce(II) in total 6.9 mol dm^{-3} methanesulfonic acid.

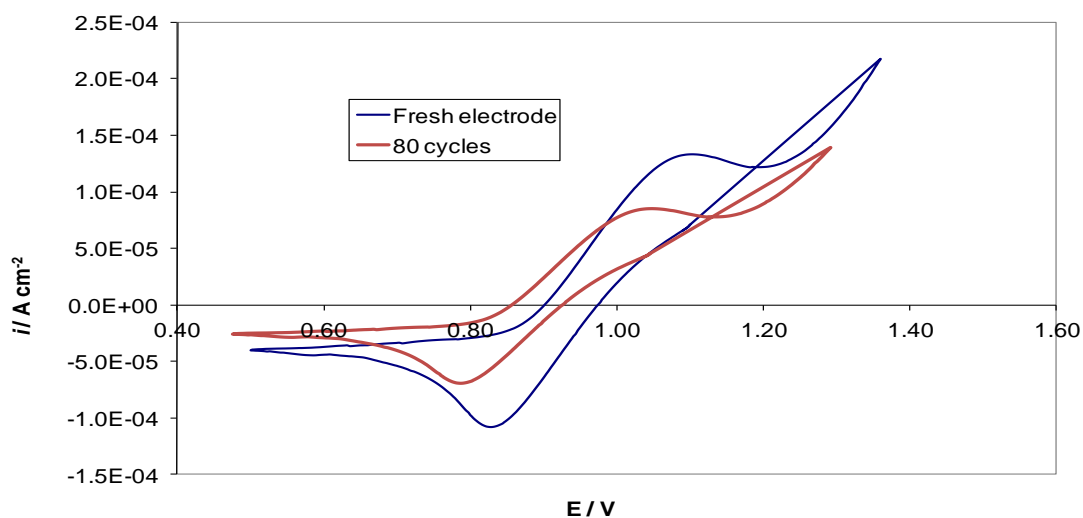


Fig.6.25: Cyclic voltammetry of the Ce(IV) reduction reaction onto the SL1 electrode in $2 \times 10^{-1} \text{ mol dm}^{-3}$ Ce(IV), $6 \times 10^{-1} \text{ mol dm}^{-3}$ Ce(III) and 6.9 mol dm^{-3} $\text{CH}_3\text{SO}_3\text{H}$ at 20 mV s^{-1} and 60°C .

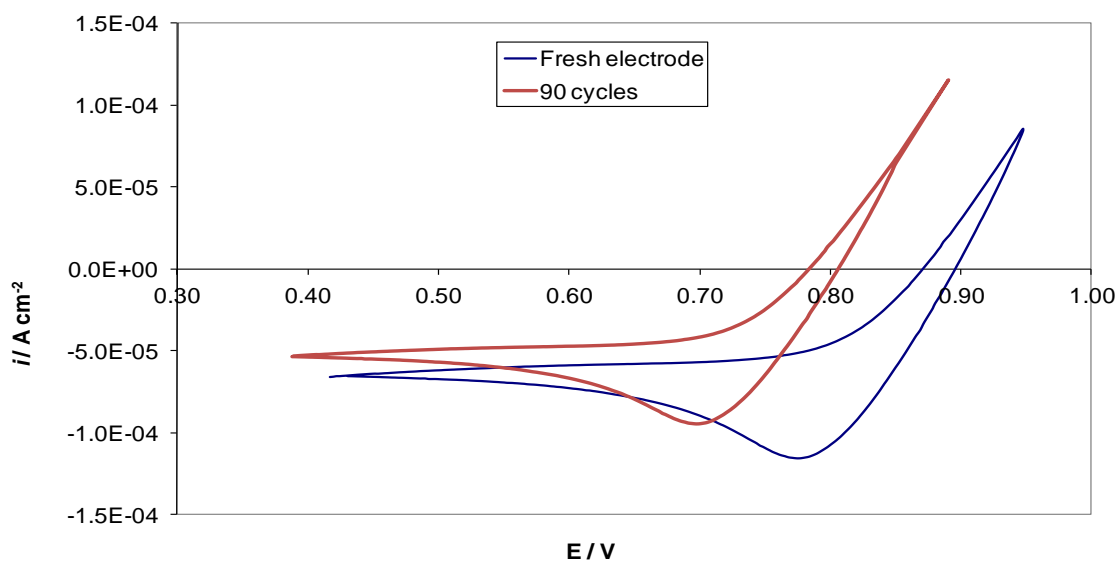


Fig.6.26: Cyclic voltammetry of the Ce(IV) reduction reaction onto the BMM15 electrode in $4 \times 10^{-1} \text{ mol dm}^{-3}$ Ce(IV), $4 \times 10^{-1} \text{ mol dm}^{-3}$ Ce(III) and 6.9 mol dm^{-3} $\text{CH}_3\text{SO}_3\text{H}$ at 20 mV s^{-1} and 25°C .

For the SL1 electrode, the peak potential for the cerium reduction shifted slightly to more negative values when compared with the fresh electrode from 0.815 V to 0.785 V vs Hg|Hg₂SO₄|K₂SO₄ (sat.). In addition, the peak current density decreased from -1×10^{-4} A cm⁻² (fresh electrode) to -7×10^{-5} A cm⁻² for the electrode under cycling. The same trend was observed from Fig.6.26 for a solution containing same amounts of Ce(III) and Ce(IV) (*i.e* 4×10^{-1} mol dm⁻³) and at room temperature. Therefore, it appears that the platinum (SL) and also the platinum-iridium (BMM) coatings activity deteriorated and could lead to less effective catalyst per unit surface area. This in turn resulted in the decrease of the current densities measured. The above trend prevailed for the majority of the materials listed in Table 6.1 after an average number of 80 to 100 cycles.

6.7 Conclusion

Cyclic voltammetry for various Ce(III)/Ce(IV) concentrations in 6.9 mol dm^{-3} methanesulfonic acid showed that elevated temperatures favoured the Ce(IV) reduction reaction onto various types of coated materials including platinum and iridium as well as on carbon composites. The highest cathodic peak current densities were recorded between 50°C and 60°C , with some dependence on the electrolyte compositions. The peak potentials shifted to more positive values with the increase of temperature suggesting that the reduction reaction became easier.

The oxidation of Ce(III) was very hard to delineate from the cyclic voltammograms because of the accompanying OER on the platinum based materials but notably, not on the platinised titanium mesh (Pt-Ti mesh). In the case of the carbon electrodes the OER was very evident while at the same time their choice as suitable materials for the cerium half cell was discarded due to the rapid deterioration of their surface in the presence of this highly acidic environment. The D values ($\sim 3.5 \times 10^{-7} \text{ cm}^2 \text{ s}^{-1}$) as well as the heterogeneous standard rate constant (k°) for the cerium reduction process ($\sim 2 \times 10^{-3} \text{ cm s}^{-1}$) increased as expected with temperature and cerium (IV) concentration. The exchange current density (i_o) showed a similar trend with temperature. It was also found that the substrates containing higher amounts of platinum demonstrated higher i_o values (*viz.* $\sim 10 \times 10^{-3} \text{ A cm}^{-2}$) at elevated temperatures (60°C). For the majority of the electrodes tested, there was a good agreement in the i_o values from the different techniques used (Tafel, polarisation resistance, EIS) at room temperature.

As far as the galvanic cycles are concerned, the majority of the substrates tested indicated the charge discharge current densities that could be applied were not greater than $\pm 25 \text{ mA cm}^{-2}$. Higher current densities ($> 20 \text{ mA cm}^{-2}$) led to the OER during charging and hydrogen evolution during discharge. The optimum rotation rate was found to be between 10 and 15 Hz (Re between 114 and 171) whereas the increase of temperature from 25°C to 60°C increased the voltage efficiency for all the substrates examined. The η_V values at 10 Hz and 60°C were greater than 85% for the majority of the materials examined. The majority (but not all) of the coatings examined lost some of their activity on prolonged cycling (80 to 100 cycles) which might be attributed to the loss of the catalyst from the surface.

-
- [1] J. Bard, L.R. Faulkner, *Electrochemical Methods - Fundamentals and Applications*, 2nd Edition, Wiley, (2001).
- [2] M.L. Hitchman, *Measurement of dissolved oxygen*, Wiley, New York, p197, (1978).
- [3] S.D. James, *J. Electrochem. Soc.*, **116**, 1681, (1969).
- [4] T. Biegler, D.A. Rand, R. Woods, *J. Electroanal. Chem.*, **29**, 269, (1971).
- [5] M.J. Weaver, S.G. Chang, L.W.H. Leung, X. Jiang, *J. Electroanal. Chem.*, **327**, 247, (1992).
- [6] R.W Lindström, K. Kortsdottir, G. Lindbergh, *J. Electrochem. Soc.*, **157**, 12, 1795-1801, (2010).
- [7] A. Chen, D.J. La Russa, B. Miller, *Langmuir.*, **20**, 9695-9702, (2004).
- [8] P.K. Leung, C. Ponce de León, C.T.J. Low, F.C. Walsh, *Electrochim. Acta.*, **56**, 5, 2415-2153, (2011).
- [9] T. Raju, C.A. Basha, *J. Ind. Eng. Chem. Res.*, **47**, 8947-8952, (2008).
- [10] E. Bishop, P. Cofré, *J. Analyst.*, **106**, 316-322, (1981).
- [11] D. Pletcher, E. Valdes, *Electrochim. Acta.*, **33**, 509-515, (1988).
- [12] P.K. Leung, C. Ponce-de-Leon, C.T.J. Low, F.C. Walsh, *Electrochim. Acta.*, **56**, 6536-6546, (2011).
- [13] J. Ludek, W. Yuezhou, M. Kumagai, *J. Rare Earths.*, **24**, 257-263, (2006).
- [14] A. Paulenova, S. Creager, J. Navratil, Y. Wei, *J. Power Sources.*, **109**, 431 (2002).
- [15] M. Spotnitz, R.P. Kreh, J.T. Lundquist, P.J. Press, *J. Appl. Electrochem.*, **20**, 209-215, (1990).
- [16] J.M. Nzikou, M. Aurousseau, F. Lopicque, *J. Appl. Electrochem.*, **25**, 967-972, (1995).
- [17] P. Kiekens, L. Steen, H. Donche, E. Temmerman, *Electrochim. Acta.*, **26**, 841, (1981).
- [18] P. Kohl, J.W. Schultze, *Ber. Bunsen Ges.*, **77**, 953, (1973).
- [19] P.R. Nadebaun, T.Z. Fahidy, *Electrochim. Acta.*, **17**, 9, 1659-1681, (1972).
- [20] G. Jerkiewitz, G. Vatankhah, J. Lessard, M.P. Soriaga, Y.S Park, *Electrochim. Acta.*, **49**, 1451-1459, (2004).
- [21] L. Qi, J. Li, 214th ECS meeting, Abstract 2905.
- [22] M. Matheswaran, S. Balaji, S.J. Chung, I.S. Moon, *Bull. Korean Chem. Soc.*, **28**, 1329-1334, (2007).
- [23] B. Fang, S. Iwasa, Y. Wei, T. Arai, M. Kumagai, *Electrochim. Acta.*, **47**, 3971-3976, (2002).
- [24] Z. Xie, D. Zhou, F Xiong, S. Zhang, K. Huang, *J. Rare Earths.*, **29**, 6, 567, (2011).

-
- [25] T. Vijayarathi, D. Velayutham, M. Noel, *J. Appl. Electrochem.*, **31**, 979, (2001).
- [26] L.A. Blatz, *J. Phys. Chem.*, **66**, 160-164, (1962).
- [27] T.J. Hardwick, E. Robertson, *Can. J. Chem.*, **29**, 828-837, (1951).
- [28] NORAM Engineering and construction Ltd. "Determination of physical properties for cerium and zinc electrolytes", October 2002.
- [29] D.B. Roitman, J.J. McAlister, F.L. Oaks, *J. Chem. Eng. Data.*, **39**, 56-60, (1994).
- [30] R. Clarke, B. Dougherty, S. Mohanta, S. Harrison, Abstract 520, Joint International Meeting: 206th Meeting of the Electrochemical Society/2004 Fall Meeting of the Electrochemical Society of Japan, Honolulu, Hawaii, October 3-8, (2004).
- [31] A. Abbaspour, M.A. Mehrgardi, *Talanta.*, **67**, 579-584, (2005).
- [32] J. Koutecky, V.G. Levich, *Zh. Fiz. Khim.*, **32**, 1565, (1956).
- [33] T.H. Randle, A.T. Kuhn, *J. Chem. Soc., Faraday Trans.*, **1**, 79, 1741-1756, (1983).
- [34] D.R. Lide, *CRC Handbook of Chemistry and Physics*, 75th Edition.
- [35] G.A. Sacchetto, P. Pastore, G. Favaro, M. Fiorani, *Anal. Chim. Acta.*, **258**, 99, (1992).
- [36] J. Been, C.W. Oloman, *J. Appl. Electrochem.*, **23**, 1301-1309, (1993).
- [37] M. Matheswaran, S. Balaji, S.J. Chung, I.S. Moon, *Chemosphere.*, **69**, 325-331, (2007).
- [38] Y. Wei, B. Fang, T. Arai, M. Kumagai, *J. Appl. Electrochem.*, **35**, 561-566, (2005).
- [39] K.J. Vetter, *Z. Phys. Chem. (Leipzig)*, **196**, 360, (1951).
- [40] R.A. Bonewitz, G.M. Schmid, *J. Electrochem. Soc.*, **11**, 117, 1367-1373, (1970).
- [41] Y. Maedaa, K. Satoa, R. Ramarajb, T.N. Raob, D.A. Trykb, A. Fujishima, *Electrochim. Acta.*, **44**, 3441-3449, (1999).
- [42] R.A.T. de Greef, L.J.J. Jansen, *J. Appl. Electrochem.*, **31**, 693-702, (2001).
- [43] T.S. Chen, K.J.C. Yeh, K.L. Huang, *J. Hazard. Mat.*, **152**, 922-928, (2008).
- [44] V. Horvat-Radosevic, K. Kvastek, M. Vukovic, D. Marijan, *J. Electroanal. Chem.*, **463**, 29-44, (1999).
- [45] M.E. van der Geest, N.J. Dangerfield, D.A. Harrington, *J. Electroanal. Chem.*, **420**, 89, (1997).
- [46] N. Priyantha, S. Malavipathirana, *J. Ntn. Sci. Count. Sri Lanka.*, **24**, 3, 237-246, (1996).
- [47] R.S. Patil, V.A. Juvekar, V.M. Naik, *Ind. Eng. Chem. Res.*, **50**, 23, 12946-12959, (2011).

Chapter 7

Zinc-Cerium flow cell

7.1 Introduction

Having investigated the zinc and cerium half cell reactions individually, the next step focused on the looking at the combined zinc cerium system. However, prior to the flow cell experiments, the system was investigated using the batch cell. For the batch cell, prolonged charge discharge cycles were conducted for electrolytes containing different zinc and cerium and methanesulfonic acid compositions. It should be noted that the batch cell employed here was not ideal for examining the zinc cerium system as it has some major drawbacks. It was not temperature controlled (limited to 25°C) and mass transport was an issue since the small stirrers immersed in the cell did not create well controlled forced convection. Also, the voltage efficiency was not taken into consideration in the analysis due to the deliberate large separation of the electrodes in the cell, which inevitably lead to high ohmic losses (. Nonetheless, it gave an indication of the current efficiency assuming adequate mass transport of the whole system with regards to the various electrolytes tested.

The flow battery experiments were carried out using a system obtained by Plurion Ltd. Two carbon composite materials were tested as the negative electrode in the cell, namely, the PVE (polyvinyl ester) and the PVDF (polyvinylidene difluoride) based electrodes. At the positive side, a platinised titanium mesh (10 g m⁻² Pt) was used instead. The investigations focused on the effect of various operating conditions such as charge and discharge current densities (10 mA cm⁻² to 35 mA cm⁻² and -2 mA cm⁻² to -10 mA cm⁻²), carbon composite materials, electrolyte compositions (different zinc and cerium concentrations), temperature (20°C to 60°C), flow velocity (5 cm s⁻¹ to 15 cm s⁻¹) and cycling on the energy efficiency of the cell. It has to be mentioned that in this system the limiting factor for discharge was the zinc negative electrode. As soon as all the zinc was removed from the electrode, the cell became fully discharged.

Finally, charge discharge trials were also conducted on an undivided cell, which has the advantage of the absence of a membrane and therefore leading to potentially high voltage efficiencies. On the other hand though, an undivided system could easily self-discharge at the open circuit potential *viz.* 2.44 V *vs* *S.H.E* because of the mixture of the reactive species of zinc and cerium. Again, several electrolytes were tested under the various operating conditions in order to find the optimum conditions (highest η_v) for operation.

7.2 Batch cell

7.2.1 Electrolytes

The various solution compositions used in this study are given in Table 7.1. Six different electrolyte compositions were investigated at various charging times ranging from 1 minute to 20 hours for two carbon composite materials namely the PVE and PVDF electrodes (used on the negative side of the cell). On the positive side, a platinised titanium mesh was used instead. The effect of charging time and cycling was monitored on the negative side of the cell while for the positive side the conversion of Ce(III) to Ce(IV) was a key aspect that was examined by titrating Ce(IV) against standardised ferrous ammonium sulfate.

Solution	1	2	3	4	5	6
	Negative electrolyte compositions / mol dm⁻³					
Ce (III)	-	-	0.25	0.25	0.4	-
Zn(II)	1.5	1.5	1.5	1.5	1.5	2
excess CH ₃ SO ₃ H	1.5	1.5	2.5	2.5	3	2.7
	Positive electrolyte compositions / mol dm⁻³					
Total Ce	0.8	0.8	0.8	0.4	0.8	0.7
Initial Ce(III)	0.8	0.8	0.8	0.4	0.34	0.11**
Ce (IV)	* 0.1	* 0.08	* 0.2	* 0.2	0.46	0.59**
Zn(II)	-	-	0.8	0.6	0.8	0.8
excess CH ₃ SO ₃ H	1.6	2.6	2.0	3.6	3.6	3.5

Table 7.1: List of positive and negative side electrolytes used for the zinc cerium batch cell.

* Initially not containing any Ce(IV) **Determined by ICP-MS

For *solutions 3, 4 and 5* the presence of Ce(III) and Zn(II) on both positive and negative sides should reduce the mass transfer losses from both anolyte and catholyte side of the system. Solutions *1 to 4* did not initially contain any Ce(IV). Thus, these were fresh solutions of Ce(III) carbonate in methanesulfonic acid. In this case, the state of charge was very low at the beginning of the trials. On the other hand, solutions *4 and 5* were *a priori* electrolyzed so they contained high Ce(IV) concentrations.

7.2.1 Solutions 1 and 2

Due to the low initial Ce(IV) concentration, $i_{discharge}$ was limited to values not greater than -5 mA cm^{-2} . The conversion of Ce(III) to Ce(IV) was poor under room temperature and poor mass transport conditions (*i.e.* no uniform mass transfer). Trials were conducted for this system with charging current densities ranging from 10 mA cm^{-2} to 20 mA cm^{-2} and charging times between 10 minutes and 4 hours at 25°C . The η_c values were very poor *viz.* 25% for both carbon composite electrodes. A typical example is given in Fig.7.1 for the PVDF electrode showing a cycle involving 30 minutes charging at 20 mA cm^{-2} (*i.e.* total charge passed = $0.2 \text{ A} \times 30 \text{ min} \times 60 \text{ sec} = 360 \text{ C}$) while the discharge current density was set to -4 mA cm^{-2} . During charge, the theoretical number of moles of Ce(III) converted was *c.a.* 2.23×10^{-3} moles (total charge passed / F) while during discharge the actual number of moles converted back was *c.a.* 1.24×10^{-3} moles (*i.e.* total charge = $3000 \text{ sec} \times 0.04 \text{ A} = 120 \text{ C}$) in 250 mL of solution.

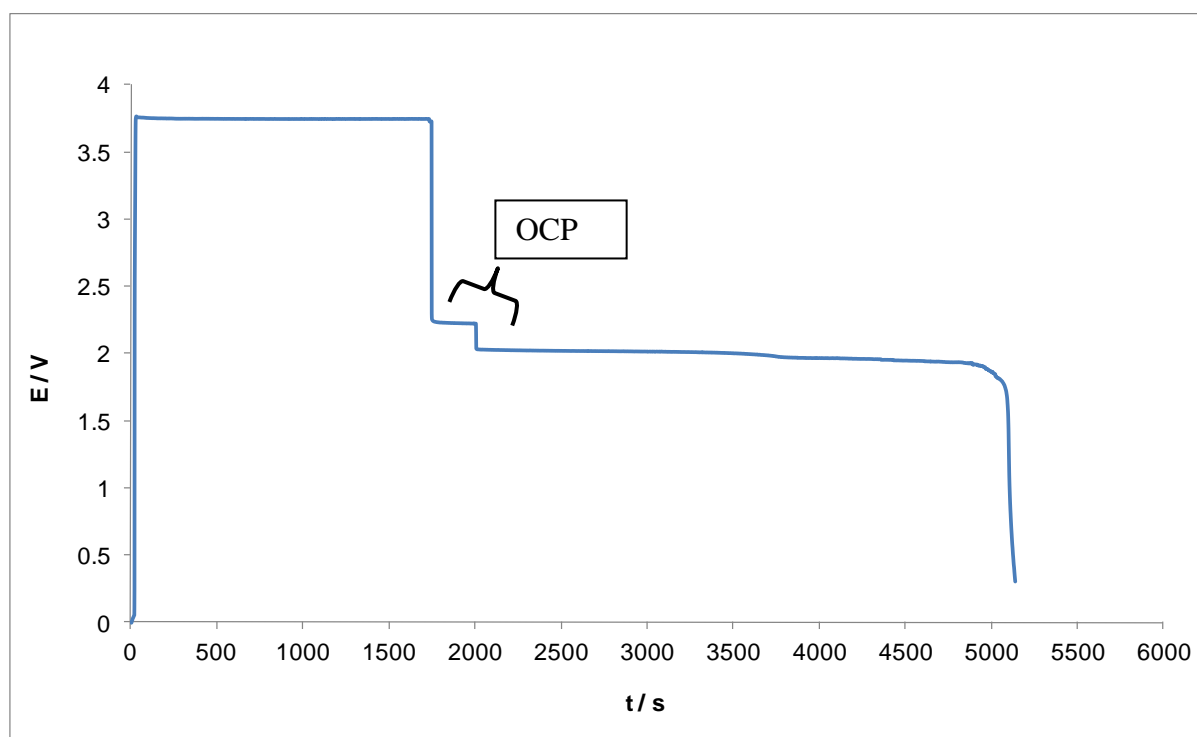


Fig.7.1: *Solution 1*; charge at 20 mA cm^{-2} for 1 hour / discharge at -4 mA cm^{-2} at 25°C ; PVDF electrode (6 cm^2).

The η_c calculated from Fig.7.1 was *ca.* 33%. A contribution to the poor η_c values could arise from the negative electrode reaction such as poor plating performance on the carbon composite surface. This could be due to either no adherence of the zinc to the carbon surface and/or the competing HER during the charging of the cell.

On increasing the concentration of the methanesulfonic acid by 1 mol dm^{-3} on the positive side (*Solution 2*) whilst keeping the negative side concentrations the same, the η_C values that were obtained from the galvanic cycles were much more encouraging. For the PVDF electrode η_C values of 65% were obtained after a charging time of 6 hours and η_C was equal to *ca.* 50% after 12 hours charging at a current density of 20 mA cm^{-2} and a discharge current density of -8 mA cm^{-2} . Furthermore, η_C increased to *c.a* 67% for a charge current density of 20 mA cm^{-2} for 3 hours and a discharge current density of 4 mA cm^{-2} .

7.2.2 Solution 3

Ce(III) was added to the negative side of the cell in order to investigate its effect on the coulombic efficiency. Having cerium on the negative side of the cell should prevent the diffusion of the Ce(III) ions species through the membrane, thus minimizing the IR_{membrane} losses. Charge and discharge current densities of $\pm 10 \text{ mA cm}^{-2}$ were used in the cell for a PVE carbon electrode on the negative side of the cell and a Pt-Ti mesh on the positive side.

Charge time / minutes	1		30		60		120		300	
$i_{\text{charge}} / i_{\text{discharge}}$ / $\pm 10 \text{ mA cm}^{-2}$	η_C	η_V	η_C	η_V	η_C	η_V	η_C	η_V	η_C	η_V
	72%	50%	64%	47%	65%	46%	61%	46%	60%	45%

Table 7.2: Effect of charging time on η_C and η_V on a PVE carbon electrode (6 cm^2) in *Solution 3* at 25°C .

The η_C values here increased to *ca.* 72% suggesting that the mass transfer losses are minimized in the anolyte. Thus more of the Ce(III) is retained on the anolyte side increasing the current efficiency during the charging period. There is a sharp fall in η_C going from 1 minute to 30 minutes charging and beyond this charging period the η_C values remain at *ca.* 60%. This would suggest that the nature of the zinc deposit stabilises somewhat beyond the 30 minute deposition time and becomes less likely to dislodge from the carbon substrate. It is worth noting that here η_V remained at the same levels ($\sim 47\%$) irrespective of the charging period. This would suggest that ohmic losses dominate the voltage losses in the cell.

7.2.3 Solution 4

Reducing the Ce(III) and the Zn(II) concentration on the positive side of the cell lead to a lowering in η_C . For this solution, the applied charge and discharge current densities were between $\pm 10 \text{ mA cm}^{-2}$ and $\pm 15 \text{ mA cm}^{-2}$ while the charging times ranged from 10 minutes to 2 hours. The η_C values obtained were between 45% and 50%. These values are lower by 10% to 20% when compared to the results obtained from *Solution 2*. Again, the low initial Ce(IV) concentration is the most obvious explanation for the poor η_C values. Furthermore, the increased excess methanesulfonic acid concentration could lead to competing reactions during the charge and discharge of the system, viz. OER during charge and HER during discharge since the oxygen reduction reaction current is very small, viz. $K_{sp} [\text{O}_2] = 8.24 \text{ mg L}^{-1}$ (K_{sp} : solubility product), at 25°C and 1 atm giving an $[\text{O}_2] = 2.5 \times 10^{-4} \text{ mol dm}^{-3}$ [1].

7.2.4 Solution 5

Fig.7.2 shows the charge-discharge cycles for the PVE electrode under the application of $\pm 20 \text{ mA cm}^{-2}$ for a charging time of 1 hour. The very high charge potential found here ($\sim 4.3 \text{ V}$) would indicate that some oxygen evolution was occurring (and/or HER) leading inevitably to low η_C values. It has to be noted though that the largest voltage loss will be due to ohmic losses.

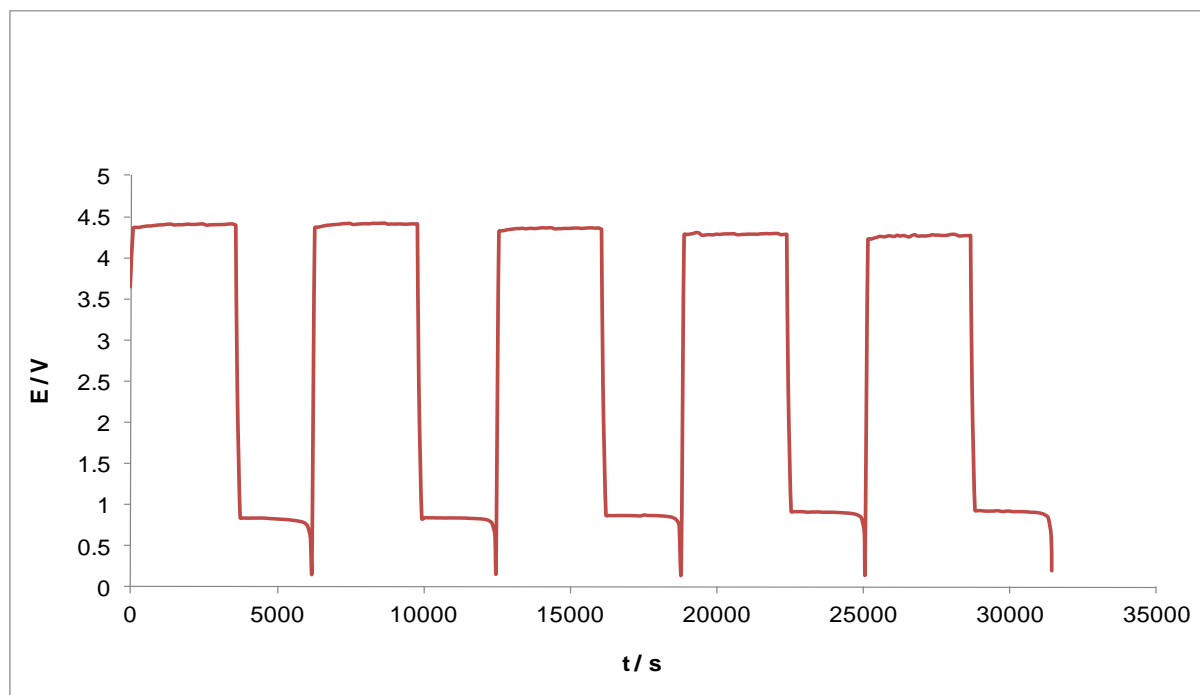


Fig.7.2: Charge discharge curves for a PVE (6 cm^2) electrode in *Solution 5* (250 mL); charge at 20 mA cm^{-2} for 1 hour / discharge at -20 mA cm^{-2} at 25°C.

The η_C and η_V values for the PVE electrode are presented in Table 7.3 for various charging times and charge-discharge current densities.

Charging time / hour	0.5		1		2		5		10		20	
$i_{\text{charge}} / i_{\text{discharge}} / \text{mA cm}^{-2}$	η_C	η_V	η_C	η_V	η_C	η_V	η_C	η_V	η_C	η_V	η_C	η_V
5 / -5	55%	69%	43%	67%	42%	70%	40%	75%	41%	76%	30%	74%
10 / -10	60%	41%	45%	47%	45%	48%	43%	49%	46%	44%	10%	37%
15 / -15	74%	28%	63%	34%	62%	39%	56%	34%	51%	27%	16%	24%
20 / -20	70%	13%	61%	24%	64%	22%	58%	20%	54%	15%	21%	20%

Table 7.3: Effect of charging time and charge and discharge current density on η_C and η_V on a PVE electrode in Solution 5 at 25°C.

The results from Table 7.3 show that η_C decreased with prolonged charging time, irrespective of charge and discharge current densities. However, for a given charging period (<20 hr), η_C increased with current density from 5 mA cm⁻² to 20 mA cm⁻². This is encouraging as it shows the process can be operated with 70% coulombic efficiency at 20 mA cm⁻². It also verifies the data from the zinc half cell reaction where higher η_C values were obtained at current densities greater than 20 mA cm⁻². Beyond 20 hours of charge, a significant decrease was noticed in the η_C values, which can be attributed to significant loss of electrolyte due to the parallel reactions occurring during charge, namely HER on the negative side and OER on the positive side of the cell. The η_V values decreased with increasing current density as expected due to ohmic losses. By comparison, for the PVDF electrode under the same conditions and electrolytes the η_C values were in the range of 77%.

7.2.5 Solution 6

In this solution, the electrolyte on the negative side of the cell contained 25% more zinc than the one of *Solution 5* viz. 2 mol dm^{-3} . Furthermore, on the positive side contained a solution with high Ce(IV) content was used, i.e. $5.9 \times 10^{-1} \text{ mol dm}^{-3}$ and $1.1 \times 10^{-1} \text{ Ce(III) mol dm}^{-3}$. The charge and discharge current densities applied were between $\pm 10 \text{ mA cm}^{-2}$ and $\pm 20 \text{ mA cm}^{-2}$. Five galvanic cycles were conducted at each of the charging times shown and the average value for the η_C and η_V values are displayed in Table 7.4 below.

Charge time / hour	1		2		5		10		20	
$i_{\text{charge}} / i_{\text{discharge}}$ / mA cm^{-2}	η_C	η_V	η_C	η_V	η_C	η_V	η_C	η_V	η_C	η_V
10 / -10	60%	40%	80%	44%	67%	42%	54%	41%	44%	39%
15 / -15	75%	22%	83%	28%	80%	26%	65%	23%	50%	23%
20 / -20	85%	11%	86%	15%	79%	11%	66%	13%	59%	13%

Table 7.4: Effect of charging time and charge and discharge current density on η_C and η_V on a PVE electrode in *Solution 6* at 25°C .

As expected, the η_C values increased with the application of higher current densities. The highest η_C values were ca. 86% for a charging time of 2 hours and a charge current density of 20 mA cm^{-2} . Longer charging times, i.e. 10 hours and 20 hours decreased the η_C by 30%. The trends observed here are very similar to the data in Table 7.3 but the key difference here is the increase in η_C with the zinc concentration (viz. less acid concentration to promote the HER process during charge).

7.2.6 Conclusions

The findings of the batch cell trials highlighted the importance of the methanesulfonic acid concentration on both anolyte and catholyte sides. The highest η_C values (80%) were obtained in the presence of high Ce(IV) and Zn(II) concentrations viz. $5.9 \times 10^{-1} \text{ mol dm}^{-3}$ and 2 mol dm^{-3} respectively upon the application of current densities of $\pm 20 \text{ mA cm}^{-2}$. The state of charge increased when high Ce(IV) concentrations are employed on the positive side of the batch cell, so enabling higher discharge current densities and therefore higher power output to be obtained. Increased current densities ($>20 \text{ mA cm}^{-2}$) resulted in higher η_C values for the same charging periods.

7.3 Zinc Cerium flow cell

7.3.1 Electrolytes

A number of different electrolytes was tested for the zinc cerium flow cell with relation to the coulombic (η_c) and voltage efficiencies (η_v). Other operating conditions that were examined involved temperature, carbon electrodes on the negative side and electrolyte flow rate. The different electrolytes employed in this study are presented in Table 7.5.

Electrolyte	1	2	3	4	5	6	7	8
	Negative electrolyte compositions / mol dm⁻³							
Ce (III)	0.25	-	-	0.25	0.25	-	0.25	-
Zn(II)	1.5	1.5	1.5	1.5	1.5	1.5	1.5	2
excess CH ₃ SO ₃ H	1.7	2.7	2.7	1.75	1.75	2.7	2.7	1.7
	Positive electrolyte compositions / mol dm⁻³							
Total Ce	0.8	0.8	0.8*	0.8	0.7	0.67***	0.67***	0.67***
Ce (III)	0.2	0.38	0.38	0.24	0.22			
Ce (IV)	0.6**	0.42**	0.42**	0.56**	0.45**	0.59**	0.59**	0.59**
Zn(II)	0.8	-	-	0.8	0.8	0.8	0.8	0.8
excess CH ₃ SO ₃ H	2	4.5	4.5	2.3	3.2	3.5	3.5	3.5

Table 7.5: List of positive and negative side electrolytes for the zinc cerium RFB.

*: From Sigma Aldrich

** : Maximum [Ce(IV)] during trials

***: Concentration determined by ICP-MS

Electrolytes containing both cerium (III) and zinc oxide, albeit at different concentration ratios were used on both sides of the flow cell (mixed electrolytes – *Electrolytes 4, 5 and 7*) whiel also electrolytes with only one species (either zinc or cerium) (*Electrolytes 2, 3, 6 and 8*). The purpose of these different compositions was to evaluate the impact of solution composition on the overall energy efficiency (η_e) of the system. The most promising compositions from the batch cell experiments (*i.e Solutions 6 and 7*) were initially employed in the flow cell. Thus, the effect of methanesulfonic acid and the concentration of Ce(III) ions on both sides of the cell was investigated through *Electrolytes 1 to 5*. All the solutions listed in Table 7.5 apart from *Electrolyte 3* used the Ce(III) carbonate supplied by Zibo Jiahua Advanced Material Resources Ltd. The cerium carbonate for *Electrolyte 3* was obtained from Sigma Aldrich [2].

7.3.1.1 Precipitation of cerium on the positive side of the zinc-cerium flow cell

Upon the running of the battery it was noticed that at the anolyte (*i.e* positive side of the cell) upon prolonged galvanic cycling, the cerium solution developed a yellow powder precipitate. This precipitate could be redissolved with de-ionised water but interestingly not with the stoichiometric H₂O:CH₃SO₃H ratio. Powder x-ray diffraction experiments were performed on the precipitate and the data presented in Fig.7.3 were compared with the XRD data of H. Baerninghausen and G.Schiller (1985) on cerianite-Ce₂O₃ and L. Thomassen on cerianite-CeO₂ (1923). From the data of Fig.7.3 it is clear that there is no correlation between the sample collected from the flow cell with either the literature data on CeO₂ or Ce₂O₃. The crystal structure of this sample is to be further investigated.

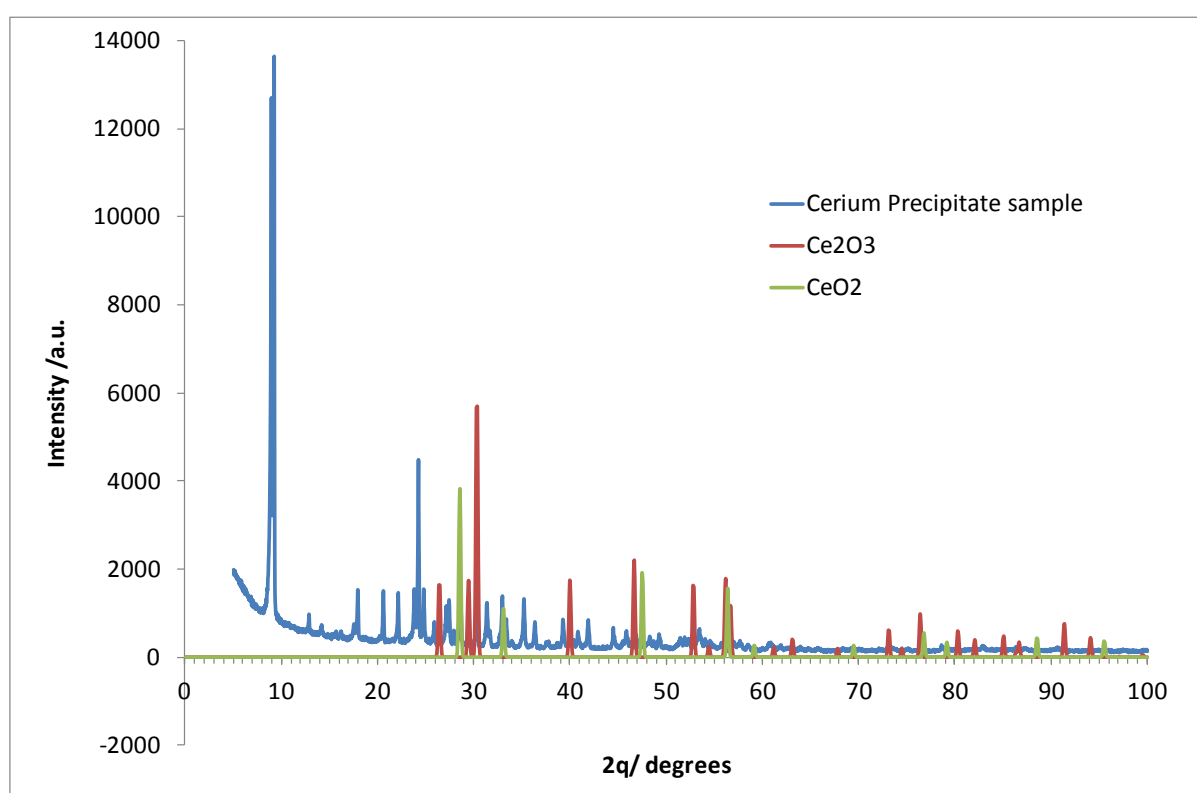


Fig.7.3: XRD on cerium precipitate collected from the zinc cerium flow cell.

Cerium precipitation has been reported by Raju *et al.* [3] [4] in solutions containing 1.4 mol dm⁻³ to 2 mol dm⁻³ Ce(III) and methanesulfonic acid concentrations in the range of 2 mol dm⁻³ to 4 mol dm⁻³ at 50°C. Also, Golden *et al.* [5] have reported that in a solution containing 1 × 10⁻¹ mol dm⁻³ cerium nitrate and at pH larger than 7. CeO₂ yellow precipitate forms at oxidizing voltages (*i.e* >1.0 V) as deduced from the Pourbaix diagram in Fig.7.4. However, in the present study, the pH of the solution is highly acidic, *i.e* 4.5 mol dm⁻³ excess methanesulfonic acid.

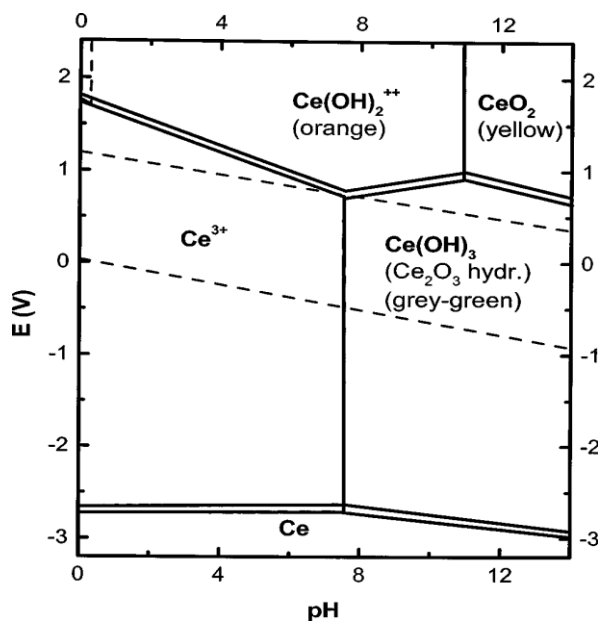


Fig.7.4: Pourbaix diagram on cerium species [6].

One possible explanation could be that the formation of the solid was due to the loss of water during the course of the flow cell experiments. In order to compensate for this water loss, distilled water was periodically added to keep the level constant. Nevertheless, adding water to the electrolyte compartment directly did not necessarily led to the solid redissolving. However, taking the solid out of the reservoir and isolating it, and then adding water led to the complete dissolution of the solid. This suggests that the methanesulfonate concentration plays a major role in the solubility of cerium. Indeed, the effect of the acid concentration on the Ce(IV)/Ce(III) species has been discussed by Raju *et al.* [4], Leung *et al.* [7] and Paulenova *et al.* [8]. Furthermore, Spotnitz *et al.* [9] reported that the solubility of Ce(III) decreases with increasing methanesulfonate acid concentration, limiting the reversibility of the Ce(III)/Ce(IV) couple. Also, the solubility of Ce(IV) was found to increase with increasing methanesulfonic acid concentration, unlike sulfuric acid solutions [10][11]. Another suggestion was that the purity of the cerium carbonate could have a bearing on this. Hence, cerium carbonate from a different supplier was used (Sigma Aldrich) and the behaviour of this anolyte was monitored with respect to the temperature. This investigation showed that the precipitation of the cerium complex still occurred after one week's trials (Table 7.6). Hence, it is clear that higher Ce(IV) concentrations on the positive side of the zinc cerium flow cell delayed the precipitation process. Finally, an optimum concentration of $8 \times 10^{-1} \text{ mol dm}^{-3}$ cerium (III) methanesulfonate was prepared in 4 mol dm^{-3} methanesulfonic acid as a compromise in order to maximize the solubility of both Ce(III) and Ce(IV) ions.

	Positive side of the zinc-cerium flow cell (+)							
Electrolyte	1	2	3	4	5	6	7	8
Cerium precipitated in days:	10	7	7	7	10	14	14	17

Table 7.6: Cerium precipitation on the positive side of the zinc cerium RFB

7.3.2 Electrolyte 1

The data from the charge discharge cycles conducted at 25°C for the PVDF and Pt-Ti mesh electrodes are summarised in Table 7.7. The charge and discharge current densities were *ca.* $\pm 12 \text{ mA cm}^{-2}$. At the end of the galvanic cycles *viz.* when the cerium carbonate precipitated the Ce(IV) concentration was *ca.* $6 \times 10^{-1} \text{ mol dm}^{-3}$.

Charging time / min	1		10		30		60	
$\frac{i_{\text{charge}}}{i_{\text{discharge}}}$ / mA cm^{-2}	η_C	η_V	η_C	η_V	η_C	η_V	η_C	η_V
$7.5 \text{ cm s}^{-1} - 5.9 \times 10^{-1} \text{ mol dm}^{-3} \text{ Ce(IV)}$								
12 / -12	85%	53%	57%	49%	38%	48%	33%	48%
$8.75 \text{ cm}^{-1} - 5.9 \times 10^{-1} \text{ mol dm}^{-3} \text{ Ce(IV)}$								
12 / -12	84%	55%	60%	50%	40%	50%	34%	49%

Table 7.7: Effect of f on η_C and η_V on a PVDF electrode in *Electrolyte 1* at 25°C.

The results gleaned from Table 7.7 showed that the η_C decreased significantly (40%) with increasing charging time (*i.e.* from a 1 minute to 1 an hour of charging). This same trend was observed from the study in the zinc half cell reaction (Chapter 5 Section 5.5.4). The η_V values were poor averaging 50% and suggesting that the reactions on both sides of the cell in *Electrolyte 1* at 25°C are slow and hence yielded low energy efficiencies. Nonetheless, the highest η_C and η_V values throughout the charge periods examined were at 8.75 cm s^{-1} . The η_C for this system was *ca.* 42% for the PVDF electrode. It can also be deduced from the table that under these charging/discharging conditions flow rate has little effect over the flow rate regime explored. The study conducted on a PVE based electrode under the same conditions but lower Ce(IV) concentration *i.e.* $4 \times 10^{-1} \text{ mol dm}^{-3}$ revealed lower η_C values *viz.* 35% for a 10 minute charge while η_V remained at *ca.* 50%. Table 7.8 shows the effect of flow velocity on the coulombic efficiency for this carbon electrode.

5 minute charge at $\pm 12 \text{ mA cm}^{-2}$ and 25°C - <i>Electrolyte 1</i>							
$f / \text{cm s}^{-1}$	5	6.25	7.5	8.75	10	11.25	12.5
Re	49	61	75	88	99	110	124
η_C	40%	47%	53%	60%	61%	59%	55%

Table 7.8: Effect of f on η_{CV} on a PVDF carbon substrate in *Electrolyte 1* at 25°C

From Table 7.8, it can be seen that the optimum flow velocity was between 8.75 cm s^{-1} and 9 cm s^{-1} . As confirmed from the zinc as well as cerium half cell studies, lower flow velocities (between 5 cm s^{-1} and 7.5 cm s^{-1}) give inadequate mass transport and bubble formation on the negative side. Higher flow rates can lead to shearing effects for the cerium reaction and zinc adhesion issues for the negative side of the cell.

7.3.3 Electrolytes 2 and 3

The results that came out from the galvanic cycle studies for the electrolytes containing one electroactive species only in each compartment were similar to the ones from the batch cell. The η_C and η_V values were very low, viz. 30% and 40% respectively, for a charge current density of 10 mA cm^{-2} and a discharge current density of -2 mA cm^{-2} at temperatures between 40°C and 60°C and a flow velocity of 8.25 cm s^{-1} . The carbon PVE composite electrode was used as the negative electrode here. The Ce(IV) concentration was measured to be $4.25 \times 10^{-1} \text{ mol dm}^{-3}$ at the end of the cycles. It is worth mentioning that at this discharge current density the cell voltage would hit the cut-off limit viz. 0.5 V with the application of discharge current densities greater than -2 mA cm^{-2} . This is surprising as the Ce(IV) concentration should have been able to support that discharge current density. To verify this, the characteristic curve of the flow battery under these conditions was measured using the same zinc source and negative electrode with the cerium carbonate provided by two suppliers. Fig.7.5 represents the solution containing the Ce(III) from Zibo Jiahua Advanced Material Resources Ltd. while Fig.7.6 from Sigma Aldrich [2].

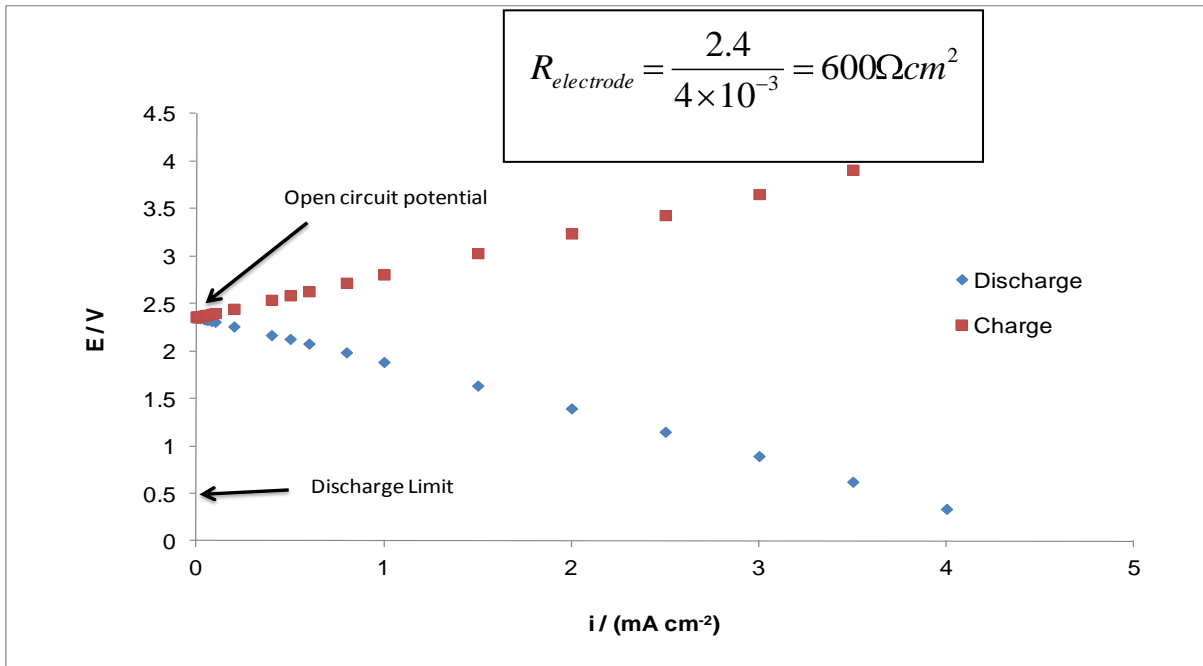


Fig.7.5: Characteristic curve of *Electrolyte 2*; PVE carbon / Pt-Ti mesh at 25°C and 8.25 cm s⁻¹ (*Re* = 82).

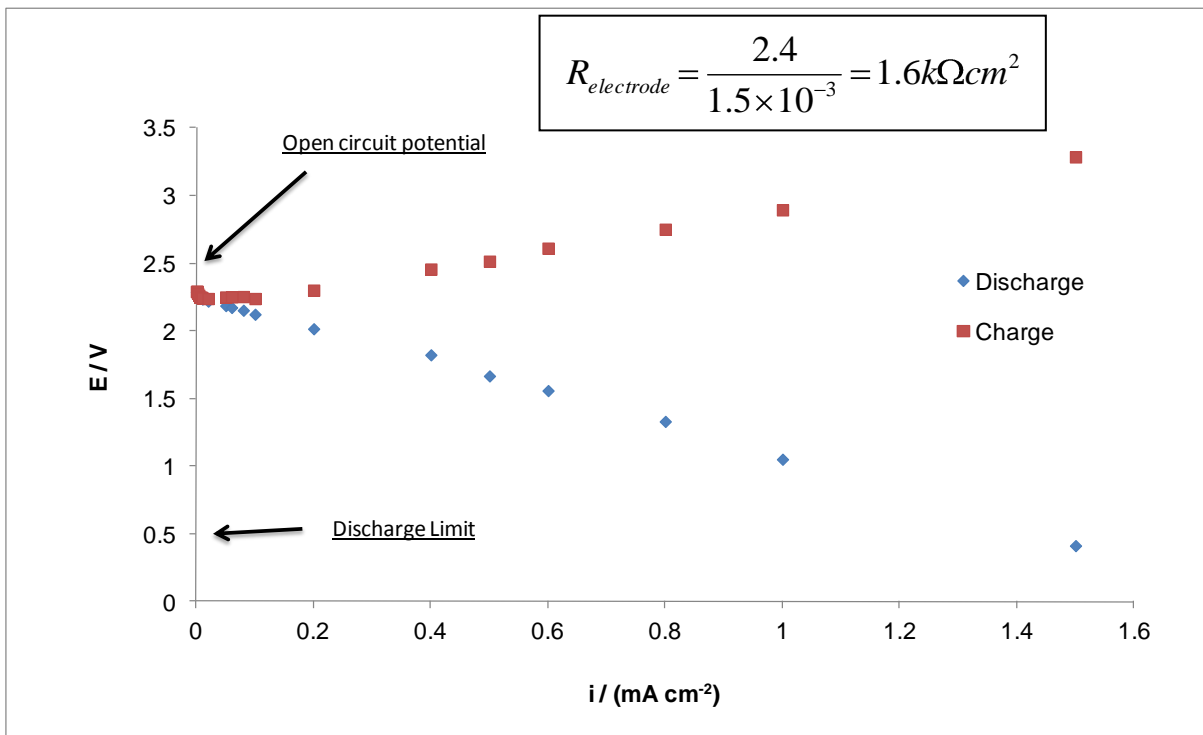


Fig.7.6: Characteristic curve of *Electrolyte 3*; PVE carbon / Pt-Ti mesh at 25°C and 8.25 cm s⁻¹ (*Re* = 82).

It can be seen from the data that although zinc is present on the surface ($E_{\text{OCP}} = 2.40\text{V}$) the resistance of the cell caused large voltage losses as current was passed. The area resistance of the cell can be calculated from the slope of the characteristic curve. From Fig.7.5, the area resistance of the electrode ($R_{\text{electrode}}$) calculated was $600 \Omega \text{ cm}^2$ while from Fig.7.6 it was significantly larger, *i.e.* $600 \Omega \text{ cm}^2$. From Fig.7.5 the discharge limit was equal to approximately -3.75 mA cm^{-2} while from Fig.7.6 it was equal to -1.5 mA cm^{-2} . The charge potentials increased as expected with the introduction of higher current densities recording values of 4.5 V at 4 mA cm^{-2} and 3.5 V at 1.5 mA cm^{-2} from Fig.7.5 and Fig.7.6 respectively.

7.3.4 Electrolyte 4

7.3.4.1 PVDF carbon electrode

The effect of charge current density on η_c was investigated in this section using a PVDF electrode (Fig.7.7). The charging time was set to 10 minutes at 25°C and 8.75 cm s^{-1} while the discharge current density was kept at *ca.* -12 mA cm^{-2} . It has to be noted that throughout the whole series of trials on the flow cell the highest discharge current density that could be introduced was -12 mA cm^{-2} due to the limitation of the potentiostat used for these trials. The Ce(IV) concentration during the trials was $5.6 \times 10^{-1} \text{ mol dm}^{-3}$.

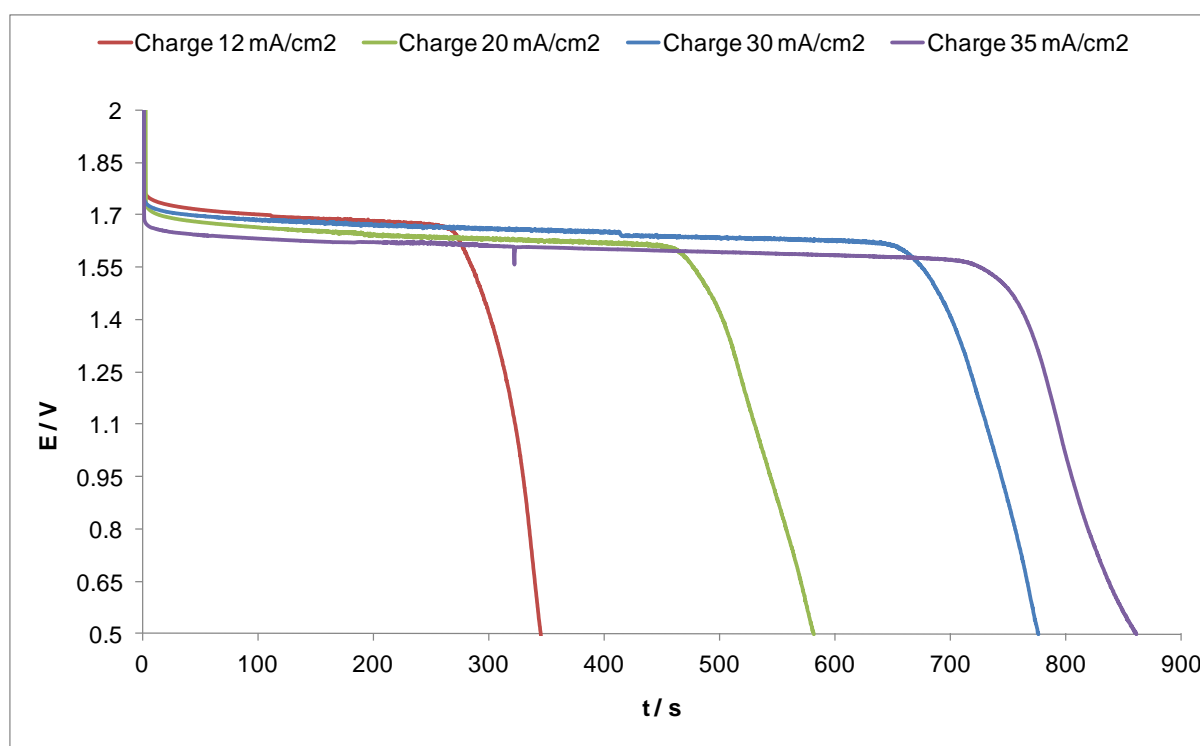


Fig.7.7: Effect of charge current density on *Electrolyte 4*; discharge current density curves at 25°C and 8.75 cm s^{-1} ($Re = 88$); PVDF electrode / Pt-Ti mesh.

As expected, the higher the charging current the longer it takes for the cell discharge (*i.e.* to reach the cut-off cell voltage (0.5 V)). When the charge and discharge current densities are the same, *i.e.* $\pm 12 \text{ mA cm}^{-2}$, the η_C was *ca.* 57% and the η_V 53% yielding an overall energy efficiency of 28%. The data from Fig.7.7 suggest that the increase in $i_{charging}$ caused a decrease in η_C from 49%, to 44% and 39% for the charging current densities of 20 mA cm^{-2} , 30 mA cm^{-2} and 35 mA cm^{-2} respectively. This could be attributed to the fact that higher current densities promoted the HER during the charging of the cell while also to the poor behaviour (low conversion, slow kinetics) of the cerium species at low temperatures as discussed in Chapter 6. Van Parys *et al.* [12] reported that the hydrogen bubble formation changes the flow distribution in the cell which in turn influences the mass transport of the electroactive species. Furthermore, the conductivity of the electrolyte is also affected by the presence of gas bubbles [13]. It is worth noting that gas bubbles are not immediately formed as they require a zone supersaturated with dissolved hydrogen gas and this becomes more prevalent at higher current densities [14].

7.3.4.2 PVE electrode

For the PVE electrode, galvanic cycles were conducted as a function of flow velocity at three temperatures *viz.* 40°C, 50°C and 60°C. The cycles involved the application of $\pm 10 \text{ mA cm}^{-2}$ for two charging periods, *i.e.* 30 minutes and 60 minutes. The Ce(IV) concentration was found to be between $2 \times 10^{-1} \text{ mol dm}^{-3}$ and $3 \times 10^{-1} \text{ mol dm}^{-3}$ throughout the charge-discharge cycles. Typical cycles obtained at 50°C are given in Fig.7.8 for a flow velocity of 7.5 cm s^{-1} and a charging time of 30 minutes. Five cycles were conducted at each trial and the average value was presented in Table 7.9 .

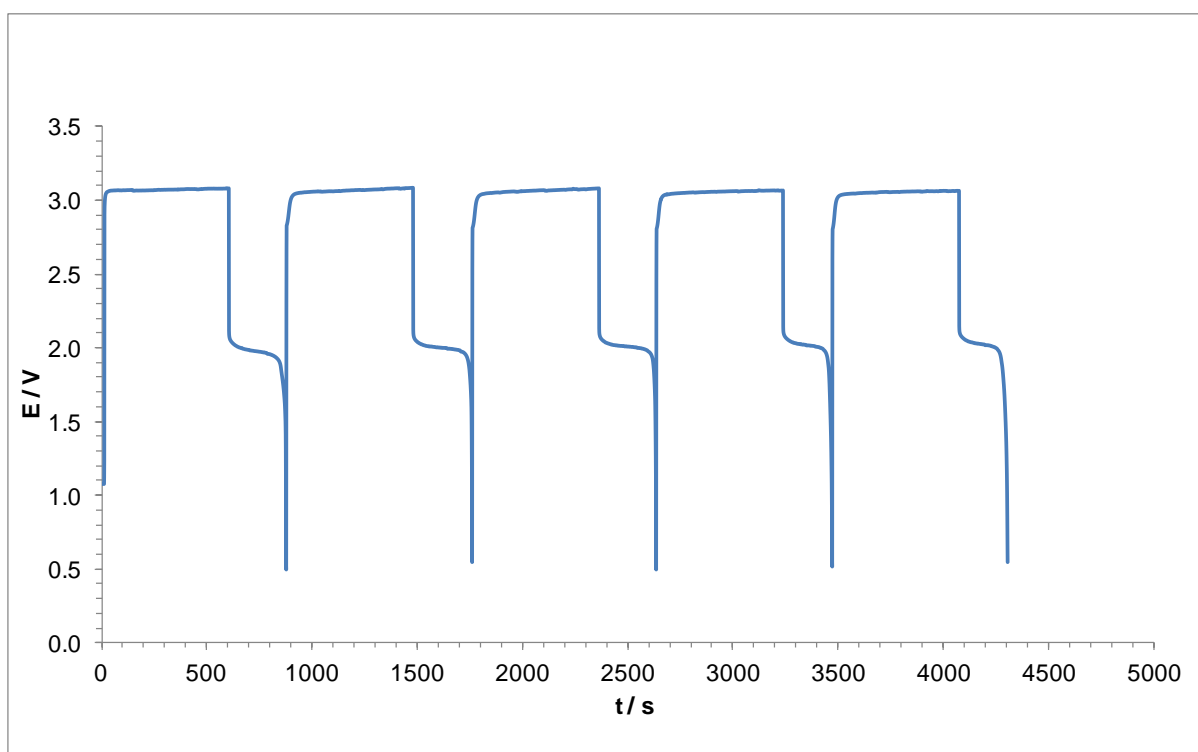


Fig.7.8: Charge discharge cycles for a PVE electrode in *Electrolyte 4* at 40°C and 7.5 cm s^{-1} , ($Re = 75$) charge/discharge at $\pm 10 \text{ mA cm}^{-2}$.

From the data of Fig.7.8 it can be seen that the η_C values are averaging at *c.a* 50%. When charging at 10 mA cm^{-2} the potential increased to 3.07 V, while during discharge the potential drops 460 mV to approximately 1.98 V relative to the open circuit potential of *ca.* 2.40 V. This drop is quite significant leading to η_V values of only 64%. It appears that the voltage drop could be minimized by increasing the Ce(IV) content on the positive side of the zinc cerium flow battery or by adjusting the operating temperature as indicated in the following table.

Charging time / min	30		60	
60°C				
$f / \text{cm s}^{-1}$	η_c	η_v	η_c	η_v
5.25	48%	61%	44%	60%
7	48%	60%	43%	60%
8.75	52%	60%	47%	61%
10.5	50%	59%	46%	59%
14	53%	60%	47%	59%
50°C				
	η_c	η_v	η_c	η_v
7	48%	65%	43%	63%
8.75	53%	69%	45%	68%
10.5	52%	66%	46%	65%
40°C				
	η_c	η_v	η_c	η_v
7	47%	58%	47%	56%
8.75	51%	59%	51%	59%
10.5	48%	58%	50%	56%

Table 7.9: Effect of f and T on η_c and η_v in Electrolyte 4, PVE carbon / Pt-Ti mesh.

From the data in Table 7.9, 50°C yielded the highest η_v values for the PVE electrode viz. 69% for all the flow velocities. The η_c the values did not show any particular trend with regards to temperature and flow velocity. However, there is some relation with regards to the charging time. The values averaged at 50% for a charging period of 30 minutes and decreased lower for prolonged charging times (1 hour) to 45%. This trend has already been reported and discussed in the zinc half cell studies. Overall, the highest η_ε was achieved at a temperature of 50°C and a flow velocity of 8.75 cm s⁻¹ viz. 38% for a 30 minute charge.

7.3.5 Electrolyte 5

In this case, the electrolyte composition at the negative side remained the same while at the positive side the initial cerium (III) carbonate concentration was increased by $2 \times 10^{-1} \text{ mol dm}^{-3}$. The excess methanesulfonic acid concentration also increased by $9 \times 10^{-1} \text{ mol dm}^{-3}$, to 3.2 mol dm^{-3} , which is well within the desirable region according to Clarke *et al.* [15]. The galvanic cycles conducted in this study, examined the effect of temperature, flow velocity and charge time on both η_V and η_C . The results are summarised in Table 7.10 for a PVE carbon electrode at charge-discharge current densities of $\pm 10 \text{ mA cm}^{-2}$.

T / °C	30		40		50		60	
	η_C	η_V	η_C	η_V	η_C	η_V	η_C	η_V
$f / \text{cm s}^{-1}$	5 minutes							
7.5	55%	54%	63%	65%	62%	63%	59%	63%
9	54%	56%	60%	66%	62%	64%	56%	63%
10.5	55%	56%	60%	67%	63%	64%	57%	64%
12	56%	57%	59%	66%	64%	64%	57%	63%
13.5	56%	57%	59%	67%	63%	64%	57%	63%
15	55%	53%	61%	65%	61%	61%	56%	62%
	10 minutes							
7.5	53%	62%	58%	70%	58%	64%	53%	62%
9	53%	61%	56%	68%	61%	63%	54%	63%
10.5	54%	61%	56%	68%	58%	63%	54%	62%
12	54%	62%	57%	67%	58%	64%	53%	63%
13.5	54%	61%	56%	71%	59%	66%	54%	62%
15	58%	61%	57%	68%	57%	67%	54%	62%
	30 minutes							
7.5	39%	61%	47%	63%	47%	64%	47%	60%
9	36%	60%	50%	67%	47%	63%	48%	61%
10.5	36%	61%	49%	64%	46%	63%	49%	62%
12	37%	60%	49%	68%	48%	64%	47%	61%
13.5	37%	60%	50%	65%	48%	65%	50%	60%
15	37%	60%	49%	65%	48%	65%	48%	60%
	60 minutes							
7.5	30%	59%	40%	64%	36%	63%	32%	62%
9	31%	59%	37%	68%	38%	64%	33%	65%
10.5	34%	60%	40%	69%	35%	65%	31%	65%
12	37%	60%	40%	67%	39%	64%	33%	63%
13.5	37%	60%	39%	65%	38%	65%	33%	62%
15	38%	60%	40%	64%	38%	65%	32%	61%

Table 7.10: Effect of f and T on η_c and η_v in *Electrolyte 5*, PVE carbon / Pt-Ti mesh.

From the data of Table 7.10 it can be seen that the highest η_V values of just below 70% were between 40°C and 50°C for the PVE carbon electrode throughout the range of flow velocities (7.5 cm s⁻¹ - 15 cm s⁻¹) and charging time examined (5 minutes - 1 hour). The η_V values recorded at 30°C and 60°C were lower than at 40°C and 50°C, *viz.* 60% and 63% respectively. There was no clear pattern regarding the impact of flow velocities on η_V . η_C was found however to be dependent on the cycling duration. The effect of temperature is however less clear but it is apparent that at 30°C the η_C values recorded were the lowest. Again, at that temperature there was no clear pattern between flow velocity and η_C values. It could well be that here, even the lowest flow velocity was sufficient to provide the positive electrode with the required reactions. The open circuit cell voltage value *viz.* 2.40 V was monitored periodically during the cycles and did not show any variation from the expected value. The low conversion efficiency found is more likely to be associated with the positive side even if it is the zinc which sets the voltage limit. The zinc negative electrode is the dominant factor; *i.e.* as soon as the zinc is stripped of the carbon surface the cell gets fully discharged.

Overall, the data for η_V were promising, as they reached values of 70% and demonstrated a stable performance. On the other hand though, the η_C values were rather poor and therefore there was no point in prolonging the charging time to periods greater than 1 hour. The low η_C can be attributed to the poor zinc deposition performance on the PVE electrode (poor adhesion, non uniform deposition). The PVDF based electrode yielded very similar results and behaviour, *i.e.* high η_V but low η_C values at longer charging times, indicating that the low η_C values are not due to the carbon materials used.

7.3.6 Electrolyte 6

In this study a solution containing high Ce(IV) content ($5.9 \times 10^{-1} \text{ mol dm}^{-3}$) was used as the positive electrolyte while at the negative side an electrolyte containing 1.5 mol dm^{-3} of Zn(II) and 2.7 mol dm^{-3} excess methanesulfonic acid was used. This solution had yielded high η_c values when used in the zinc half cell reaction (Section 5.5.6, Chapter 5). Since the optimum η_v values in *Electrolyte 5* were achieved at temperatures between 40°C and 50°C the same temperature range was used in this study. Galvanic cycles under these same conditions (charging time, charge and discharge current density) were conducted for a PVE electrode and the results are summarised in Table 7.11.

T / °C	45		55	
$f / \text{cm s}^{-1}$	η_c	η_v	η_c	η_v
5 minutes				
7.5	71%	62%	62%	64%
9	73%	63%	63%	64%
10.5	73%	62%	62%	65%
12	72%	63%	63%	64%
13.5	72%	63%	63%	65%
10 minutes				
7.5	71%	62%	62%	63%
9	69%	61%	60%	62%
10.5	69%	62%	61%	66%
12	68%	61%	60%	64%
13.5	69%	61%	61%	62%
30 minutes				
7.5	63%	59%	55%	64%
9	65%	60%	56%	63%
10.5	62%	60%	55%	65%
12	62%	61%	56%	64%
13.5	61%	59%	54%	62%
60 minutes				
7.5	58%	60%	52%	64%
9	59%	59%	51%	63%
10.5	56%	60%	52%	65%
12	56%	61%	52%	64%
13.5	57%	61%	50%	62%

Table 7.11: Effect of f and T on η_c and η_v in *Electrolyte 6*, PVE electrode / Pt-Ti mesh.

The η_V values from this study are marginally smaller when compared with the ones of Table 7.10 Fig.7.11. Higher temperatures yielded η_V values above 62%. As before, there was no specific pattern with regards to the flow velocity. It has to be mentioned that flow velocities higher than 13.5 cm s^{-1} were not included in this study as they caused rapid wear of the tubing of the peristaltic pump used for the flow cell. As far as the η_C values are concerned, there is a significant increase in these values, especially at longer cycling times, *i.e* 30 minutes and 1 hour when compared with the η_C of Table 7.10. The difference in η_C is greater by 25% for the case where the cell is charged for 1 hour. Furthermore, the η_C values at 45°C were generally higher than at 55°C . At short charging times (5 minutes) the values reached 72% and gave overall energy efficiencies (η_ϵ) of 47% at 45°C and 9 cm s^{-1} flow velocity. Similar behaviour was found for the PVDF electrode under the same conditions. The η_ϵ values were found to be 49% at 50°C and 10.5 cm s^{-1} flow velocity ($Re = 104$). An example of a charge discharge graph for the PVDF electrode is shown in Fig.7.9. On the whole, the η_ϵ values of this system are higher than the one of Section 7.3.5, mostly due to the improvement in the η_C values. This can be attributed to the higher Ce(IV) concentration on the acolyte, increasing the state of charge of the cell and minimizing the parallel reaction during discharge.

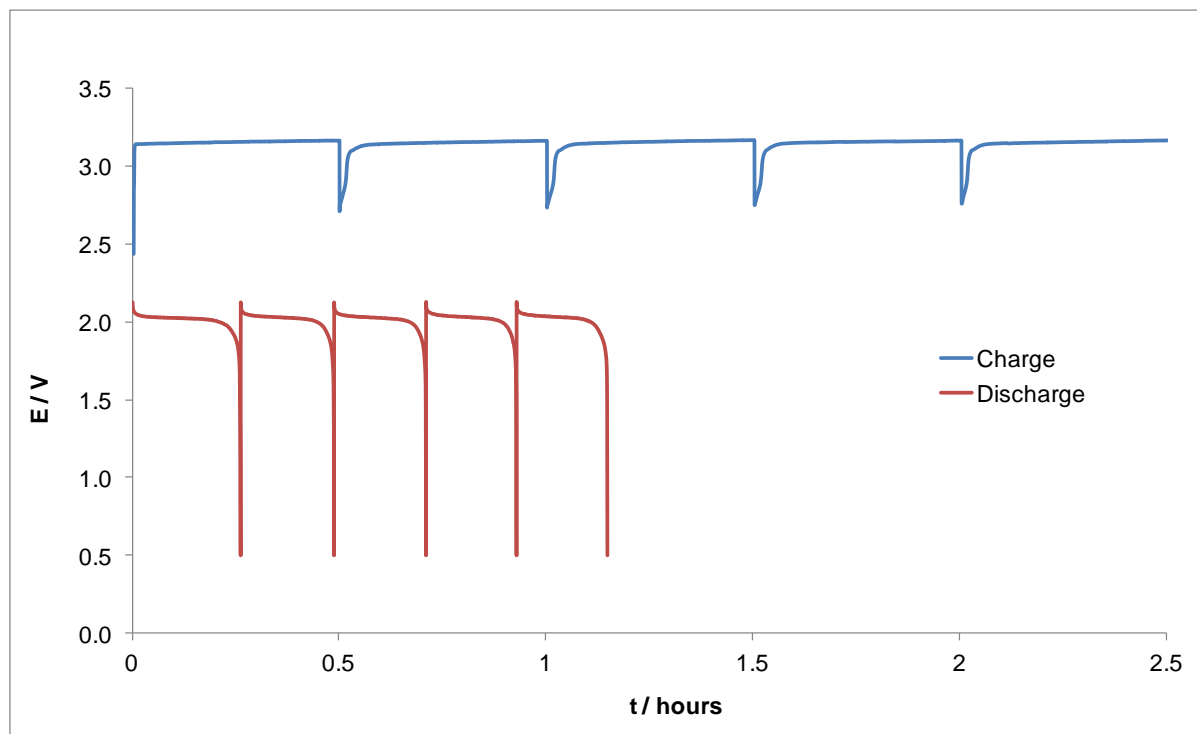


Fig.7.9: Charge discharge cycles for a PVDF electrode in *Electrolyte 6* at 55°C and 7.5 cm s^{-1} ; charge for 30 minutes at 10 mA cm^{-2} / discharge at same rate.

7.3.7 Electrolyte 7

In order to reduce the mass transfer losses on the catholyte, $2.5 \times 10^{-1} \text{ mol dm}^{-3}$ of Ce(III) was added to the negative side. The rationale here was that having Ce(III) at the negative side would prevent ions of Ce(III) from the positive side diffusing across the membrane. The Ce(III) should not be involved in any electrochemical reaction here as the Zn(0)/Zn(II) reaction would always be favoured, as long as zinc was present. The loss in η_C is therefore puzzling in this study. It could be attributed to the usage of the electrode (100 cycles) leading to the loss of active carbon surface sites. η_V increased slightly, *i.e.* 1-2% for prolonged charging times (30 minutes and 60 minutes) at 45°C while the η_C decreased to levels below 50% (Fig.7.10). This occurred for both carbon electrodes tested, namely the PVDF and PVE based composites.

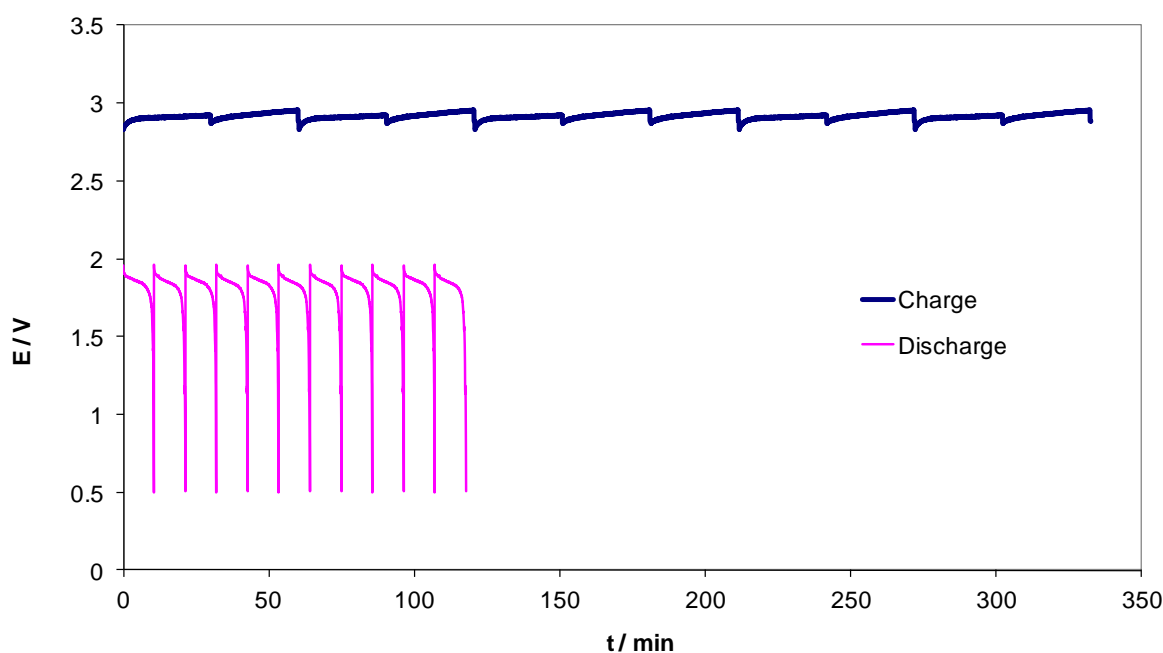


Fig.7.10: Charge discharge cycles for a PVE electrode in *Electrolyte 7* at 45°C and 10.5 cm s^{-1} ($Re = 104$); charge for 30 minutes at 10 mA cm^{-2} / discharge at same rate.

7.3.8 Electrolyte 8

Since the addition of Ce(III) on the negative side of the flow cell did not bring the expected results, further investigations were made on improving *Electrolyte 6*. More precisely, the zinc oxide concentration in the catholyte was increased by $5 \times 10^{-1} \text{ mol dm}^{-3}$ and as the acid concentration remained the same, the excess methanesulfonic acid concentration decreased to 1.7 mol dm^{-3} . According to Leung *et al.* [16] lower methanesulfonic acid concentrations would lead to higher η_C on the zinc negative electrode due to the suppression of the HER reaction (*i.e.* less protons). This fact was also confirmed in the zinc half cell studies *viz.* Chapter 5 Section 5.5.7.

The concentrations of the zinc and cerium ions at the positive side remained the same as in *Electrolyte 6*. The flow velocities as well as the charge and discharge current densities were the same as in the previous trials (Section 7.3.6) *viz.* 7.5 cm s^{-1} to 13.5 cm s^{-1} and $\pm 10 \text{ mA cm}^{-2}$ for a charging period up to 4 hours. An example of nine 1-hour charge discharge cycles at 45°C and $\pm 10 \text{ mA cm}^{-2}$ is shown in Fig.7.11 for the PVDF based electrode at a flow velocity of 10.5 cm s^{-1} .

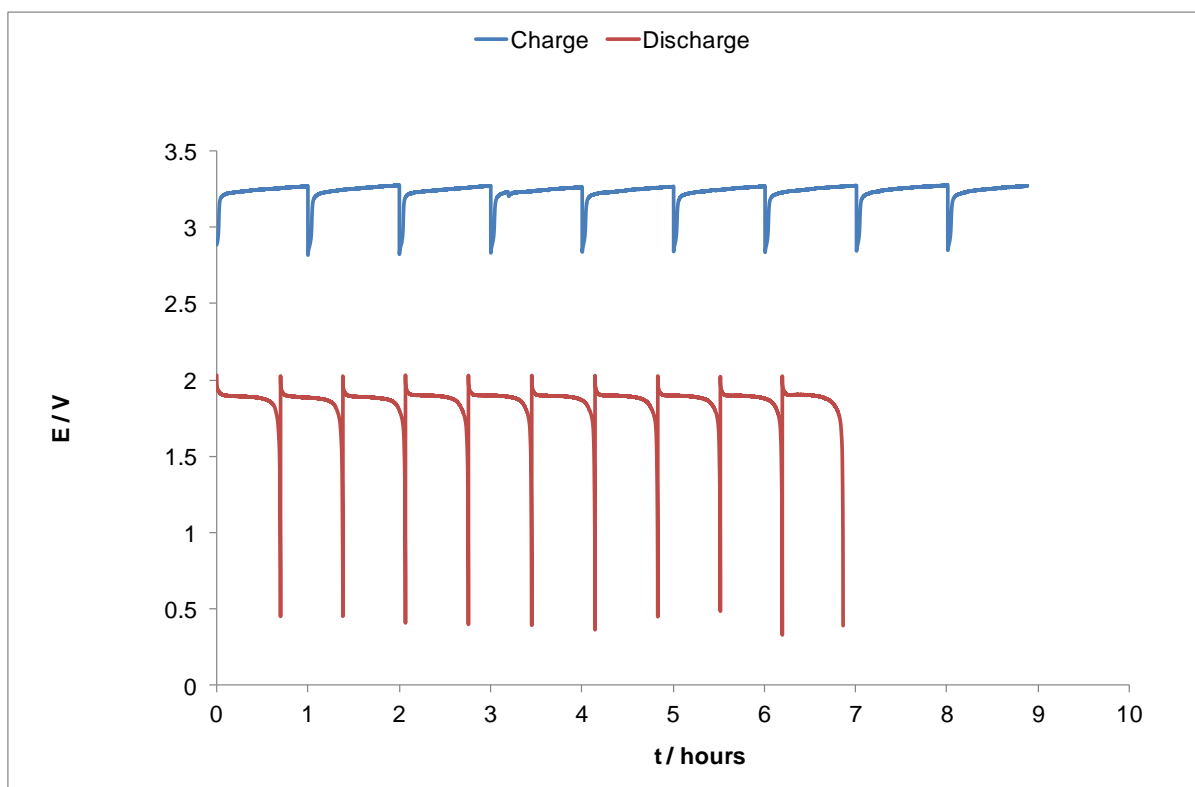


Fig.7.11: Charge discharge cycles for a PVDF electrode *Electrolyte 9* at 45°C , 1 hour charge and 10.5 cm s^{-1} ($Re = 104$); Pt-Ti mesh used on the positive side (10 g Pt m^{-2}).

From Fig.7.11 it can be seen that during charging the potential increased to 3.29 V, approximately 300 mV greater than the one of Fig.7.10. This increase on the cell charge potential can arise from the number of factors but the most likely explanation is that the solution is highly charged (*i.e* high state of charge) on the positive side and the current demand has to be satisfied with the oxygen evolution reaction.

T / °C	45		55	
$f / \text{cm s}^{-1}$	η_c	η_v	η_c	η_v
10 minutes				
7.5	85%	58%	66%	60%
9	83%	58%	68%	59%
10.5	82%	58%	67%	60%
12	83%	60%	68%	59%
13.5	82%	59%	66%	61%
30 minutes				
7.5	79%	58%	63%	60%
9	81%	59%	62%	60%
10.5	81%	59%	61%	60%
12	81%	60%	62%	59%
13.5	80%	59%	64%	58%
60 minutes				
7.5	78%	58%	61%	60%
9	79%	59%	61%	60%
10.5	80%	59%	60%	60%
12	78%	59%	61%	59%
13.5	79%	59%	60%	58%
120 minutes				
7.5	75%	60%	60%	60%
9	77%	61%	59%	60%
10.5	77%	61%	59%	61%
12	74%	61%	62%	59%
13.5	76%	59%	58%	58%
240 minutes				
7.5	73%	58%	55%	60%
9	71%	60%	56%	60%
10.5	73%	61%	55%	60%
12	71%	60%	56%	59%
13.5	72%	58%	57%	60%

Table 7.12: Effect of f and T on η_c and η_v in *Electrolyte 9*, PVDF electrode - Pt-Ti mesh, $\pm 10 \text{ mA cm}^{-2}$.

The data from Table 7.12 is very encouraging in that the η_C values obtained were close to 85% for a 10 minute charging period at 45°C, yielding η_ε values of *ca.* 51%. As observed in previous experiments (*Electrolytes 3 to 7*), the η_C values decreased with charge time; from 85% for 10 minutes to 73% for 4 hours at 45°C. This is a much smaller reduction in η_C compared to the data reported in Table 7.11 where a 25% decrease was found when the charging time increased from 5 minutes to 1 hour. The key difference here is clearly due to the change in the zinc concentration. These results suggest that loss of efficiency most likely occurs during charging where the HER accompanies the zinc deposition process. By increasing the zinc concentration the former is reduced and so η_C increases. Further comparison between the data of Table 7.11 and Table 7.12 shows that the η_C obtained for this electrolyte were larger by 15% to 25% throughout all the different charging periods. In addition, it can be clearly seen that 45°C is the most desirable temperature for the PVDF electrode as the η_C values are larger than the ones at 55°C. As far as the voltage efficiency is concerned, the values remained around 60%, irrespective of the charging time. A plausible explanation for the low voltage efficiencies could be simply the loss of contact resistance of the electrodes used in the cell, especially the carbon composite materials as the Pt-Ti mesh is heat pressed. For the PVE electrode the overall η_ε were also greatly improved. An example of 2 hour charge discharge cycles is shown in Fig.7.12 at 45°C, 10 mA cm⁻² and 9 cm s⁻¹.

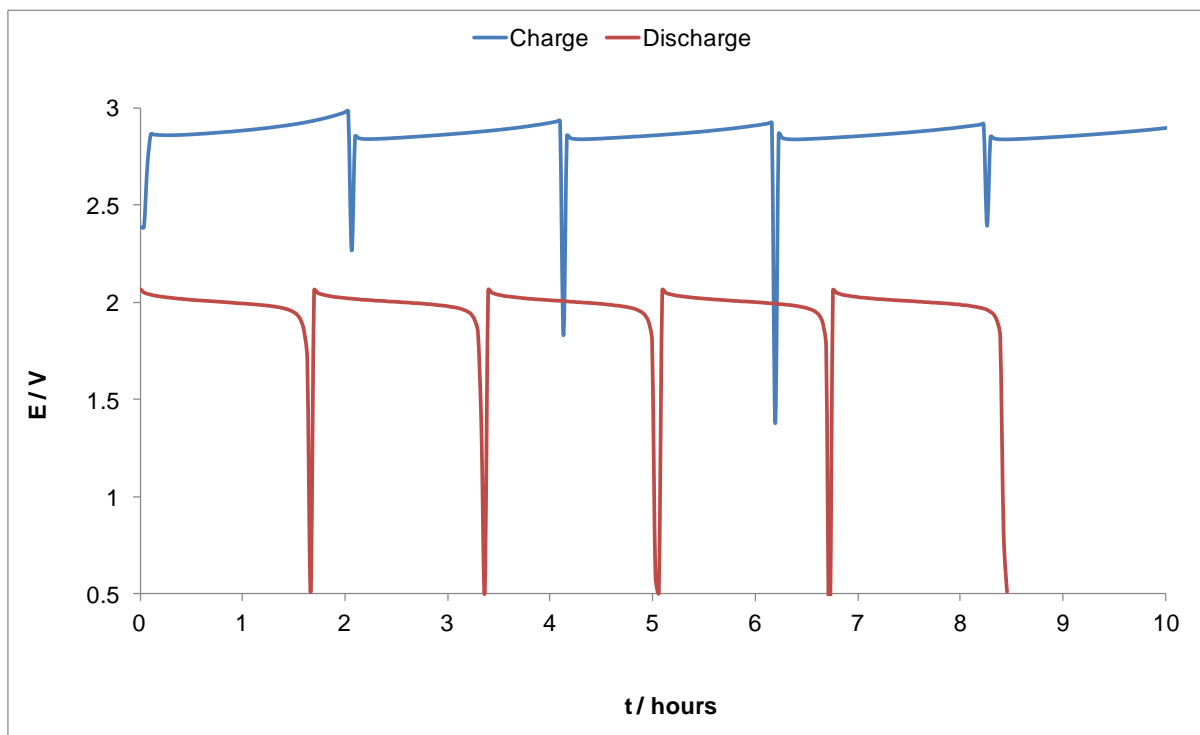


Fig.7.12: Charge discharge cycles for a PVE electrode *Electrolyte 9* at 45°C, 2 hr charge and 9 cm s⁻¹ ($Re = 91$).

The results summarised in Table 7.13, highlight the effect charging time and temperature at a flow velocity of 9 cm s^{-1} for the PVE electrode.

T / °C	35		45		55	
	η_c	η_v	η_c	η_v	η_c	η_v
Charge time / min	9 cm s^{-1}					
1	83%	60%	85%	66%	85%	65%
2	74%	63%	79%	66%	82%	66%
5	67%	62%	78%	65%	80%	65%
30	62%	64%	76%	65%	79%	65%
60	56%	62%	72%	63%	76%	64%
120	53%	61%	69%	64%	74%	65%
240	49%	64%	66%	65%	70%	64%

Table 7.13: Effect of charging time and T on η_c and η_v in *Electrolyte 8* at $\pm 10 \text{ mA cm}^{-2}$ and 9 cm s^{-1} ; PVE electrode.

For this electrode, the η_c values were higher at elevated temperatures, *viz.* 55°C yielding η_ε values of 51% for 1 minute charging. As previously observed, η_ε decreased with increasing charging time *i.e* to 43% for a 4 hour charge. However, the most profound decrease in the η_ε values was found at 35°C . The η_v values in this case were averaging at 65% irrespective of temperature. When compared to the data from the PVDF electrode (Table 7.12) the η_c are smaller by 5% to 15% at all the different charging times. However, the η_v values are larger by 5% to 7% when compared to the data of Table 7.12 but smaller by 4% to 5% to the data of Table 7.10. The data from Table 7.13 not only show an increase in η_c but also in η_v , suggesting that the carbon electrodes could be of importance to the increase of the overall η_ε of the zinc cerium battery. The effect of the different carbon composite materials on η_c and η_v for the zinc deposition reaction has already been discussed in Chapter 5 Section 5.5.3.

7.3.9 Conclusions

The highest η_C values in the flow cell *viz.* 90% were obtained from *Electrolyte 8* ($2 \text{ mol dm}^{-3} \text{ Zn(II)}$ in $1.7 \text{ mol dm}^{-3} \text{ CH}_3\text{SO}_3\text{H}$ on the negative side and on the positive side $5.9 \times 10^{-1} \text{ mol dm}^{-3} \text{ Ce(IV)}$ $8 \times 10^{-1} \text{ mol dm}^{-3} \text{ Ce(III)}$ in $3.5 \text{ mol dm}^{-3} \text{ CH}_3\text{SO}_3\text{H}$). In addition, this electrolyte showed the highest resilience to the cerium precipitation issue occurring in the anolyte *i.e.* 3 weeks. The η_ε values were *ca.* 55% for the PVE and PVDF carbon composite electrodes at current densities of $\pm 10 \text{ mA cm}^{-2}$. Leung *et al.* [17] reported η_C and η_ε values of 85% and 49% respectively under the application of $\pm 50 \text{ mA cm}^{-2}$ for a zinc cerium redox flow battery. The charging time was 15 minutes and the total number of cycles was 57. High energy efficiencies were also reported in the study of Xie *et al.* [18]. The η_ε was *ca.* 75% in a solution containing $5 \times 10^{-1} \text{ mol dm}^{-3} \text{ Ce(III)}$ in 2 mol dm^{-3} methanesulfonic acid on the positive electrode and $5 \times 10^{-1} \text{ mol dm}^{-3} \text{ ZnSO}_4$ of aqueous solution on the negative electrode. A constant current of 200 mA was applied for 10 cycles. The η_ε values are larger than the ones found in this study, however in this case the zinc-cerium flow cell demonstrated a robust and stable behaviour for a larger number of cycles that is 150.

The optimum operating temperature was found to be between 45°C and 55°C depending on the carbon electrode and electrolyte concentrations. η_C was found to be charging time dependant (due to HER and zinc adhesion issues), reducing from 90% at 2 minutes of charge to 72% for 4 hour trials. Higher zinc (1.5 mol dm^{-3} to 2 mol dm^{-3}) and Ce(IV) concentrations were found to enhance η_C (*i.e.* higher state of charge). However, while values of 90% were recorded for the η_C , the η_V did not exceed 70%. For the majority of the electrolytes tested (*Electrolytes 6 to 9*) the η_V values averaged between 60% and 65%, irrespective of temperature, flow velocity and charging time (high area resistance of cell, bad electrical contact of the carbon electrodes). The highest η_V values recorded, *viz.* 70% were for the *Electrolyte 5*. The PVE carbon electrode overall yielded higher η_V values than the PVDF based electrode.

7.4 Undivided cell

7.4.1 Electrolytes

Table 7.14 shows the different electrolytes used in the undivided cell trials.

Electrolyte	1	2	3	4	5	6
	Undivided zinc cerium cell / mol dm⁻³					
Ce (III)	0.25	0.4	0.4	0.25	0.5	0.8
Ce(IV)	0.22*	0.32*	0.25*	0.2*	0.23*	-
Zn(II)	1.5	1.5	1.5	2	2	1.5
excess CH ₃ SO ₃ H	3.25	2.8	3.5	2.25	3	2.5

Table 7.14: List of positive and negative side electrolytes for the zinc cerium undivided cell.

*: Maximum [Ce(IV)] during trials

The majority of the electrolytes contained less than 4×10^{-1} mol dm⁻³ of Ce(III). This is because of the data gleaned from the flow cell studies that indicated that cerium ions precipitated in concentrations higher than this. Nonetheless, the electrolytes containing high Ce(III) content (*i.e.* 5×10^{-1} mol dm⁻³ and 8×10^{-1} mol dm⁻³) precipitated during the charge discharge cycles as shown in Table 7.15. From the above electrolytes tested, only the first two (*Electrolyte 1* and *2*) showed good stability and did not precipitate. For the others, precipitation occurred within 1 week making it therefore impossible to conduct charge-discharge trials under these conditions.

Undivided zinc cerium cell						
Electrolyte	1	2	3	4	5	6
Cerium precipitation	✓	✓	✗	✗	✗	✗
Cerium precipitated in (days):	-	-	-	-	4	1
η_c	>35%	40%	<5%	<7%	-*	-*

Table 7.15: Days during which the undivided cell electrolyte precipitated with regards to the galvanic cycles. ✗: poses the problem. ✓: does not pose the problem.

*: Not estimated

7.4.2 Electrolyte 1

The galvanic cycles were conducted at three different temperatures *viz.* 25°C, 40°C and 60°C and the charge and discharge current densities varied between $\pm 20 \text{ mA cm}^{-2}$ and $\pm 25 \text{ mA cm}^{-2}$ for charging periods up to 2 hours. The results are summarised in Table 7.16.

T / °C	25		40		60	
	η_c	η_v	η_c	η_v	η_c	η_v
$i_{\text{charge}} / i_{\text{discharge}} / \text{mA cm}^{-2}$	10 minutes					
± 20	37%	73%	27%	74%	19%	77%
± 25	40%	70%	30%	70%	20%	70%
	30 minutes					
± 20	35%	68%	25%	73%	16%	75%
± 25	37%	66%	28%	68%	18%	71%
	60 minutes					
± 20	32%	64%	23%	72%	14%	73%
± 25	34%	61%	26%	67%	17%	71%
	120 minutes					
± 20	29%	62%	22%	70%	12%	70%
± 25	32%	58%	23%	64%	15%	70%

Table 7.16: Effect of charge-discharge current density and T on η_c and η_v in Electrolyte 1; PVE electrode / Pt-Ti mesh.

During the charge discharge cycles the maximum Ce(IV) concentration attained from titration measurements was found to be $2.2 \times 10^{-1} \text{ mol dm}^{-3}$ *i.e.* Ce(III)/Ce(IV) conversion of 88%. η_c were at *ca.* 40% for short charging times, *viz.* 10 minutes, yielding overall η_ε values equal to 30%. As expected, extended charging times decreased the η_c values. It is worth mentioning that higher η_c values were obtained at lower temperatures, *viz.* 25°C indicating better deposition efficiency at lower temperatures. Between 25°C and 60°C the difference in η_c was *ca.* 20%.

The absence of membrane increased the η_v values as expected due to lower ohmic and resistance losses. It is also worth noting that the η_c values decreased with increasing charging time indicating that the redox reaction between zinc and cerium increases with temperature (*viz.* $\text{Zn}^{2+} + 2\text{Ce}^{3+} \leftrightarrow \text{Zn} + 2\text{Ce}^{4+}$). An example of a charge discharge trial for the undivided system is given in Fig.7.13 under current densities of $\pm 20 \text{ mA cm}^{-2}$ at 40°C while the charge time was 30 minutes.

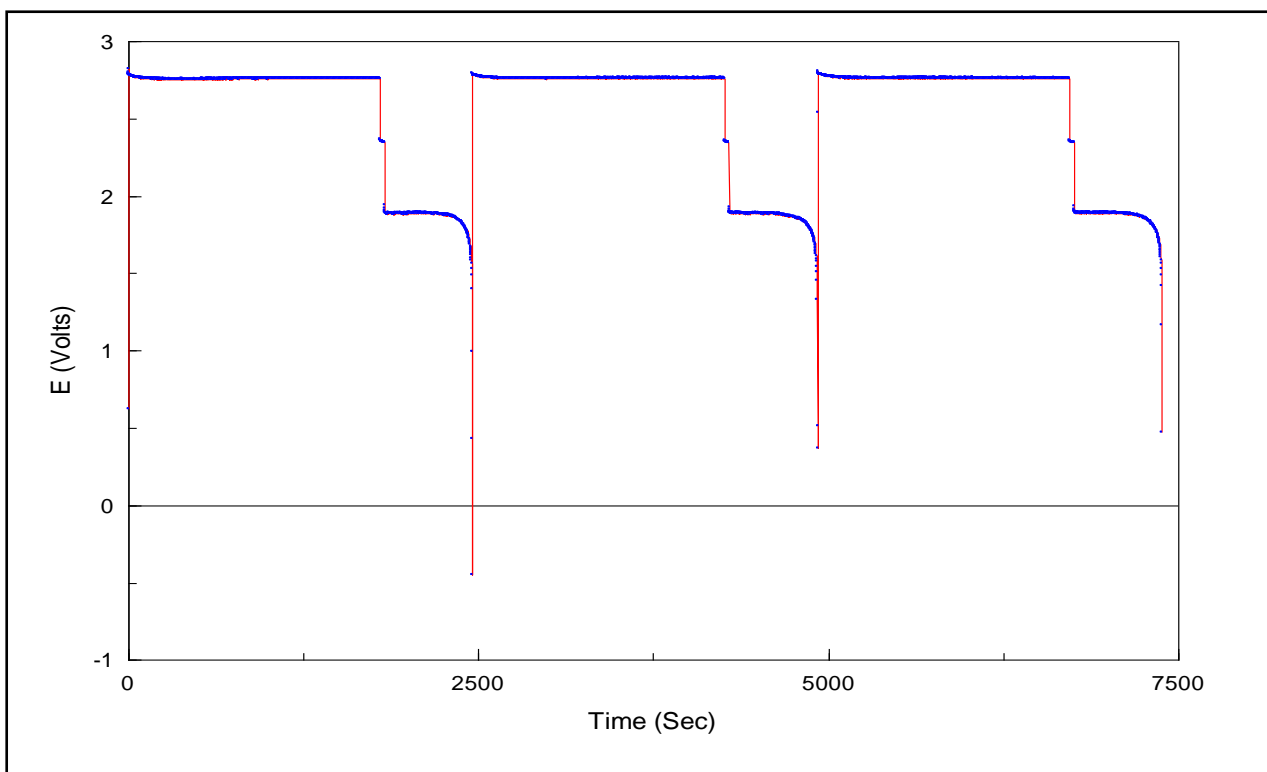


Fig.7.13: Charge discharge cycles in *Electrolyte 1*; PVE electrode / Pt-Ti mesh 30 minute charge at 40°C.

From Fig.7.13 under the application of 20 mA cm^{-2} the potential increased to 2.75 V compared to 3.29 V for the flow cell under 10 mA cm^{-2} (Fig.7.9). The difference in the charging potentials, *viz.* 540 mV can be attributed to the absence of the membrane. The potential during discharge for the undivided cell was at *ca.* 1.95 V, which is encouraging bearing in mind that the discharge current density was -20 mA cm^{-2} .

7.4.2 Electrolyte 2

This electrolyte contained a larger concentration of the cerium (III) ions ($8 \times 10^{-1} \text{ mol dm}^{-3}$) and therefore in theory an overall higher energy density assuming the open circuit potential under standard conditions (*i.e.* $2.2 \text{ V} \times 96485 \text{ A s} \times 3600 \text{ sec} = 59 \text{ W h L}^{-1}$). Table 7.17 summarises the results from the galvanic cycles obtained at various temperatures and charge discharge current densities. The highest Ce(IV) concentration achieved was *ca.* $3.2 \times 10^{-1} \text{ mol dm}^{-3}$ and was measured during the trials with the longest charging time, *i.e.* 4 hours.

T / °C	25		40		60	
	η_c	η_v	η_c	η_v	η_c	η_v
$i_{\text{charge}} / i_{\text{discharge}} / \text{mA cm}^{-2}$	30 minutes					
±20	22%	70%	24%	75%	14%	78%
±25	25%	66%	25%	73%	18%	74%
±30	26%	63%	28%	70%	16%	73%
±35	27%	58%	32%	66%	20%	68%
	1 hour					
±20	20%	68%	21%	74%	11%	81%
±25	29%	66%	24%	70%	13%	75%
±30	32%	61%	33%	58%	15%	71%
±35	32%	56%	29%	65%	24%	65%
	2 hours					
±20	22%	74%	18%	76%	8%	79%
±25	25%	63%	21%	65%	11%	69%
±30	30%	66%	25%	64%	13%	73%
±35	36%	55%	27%	67%	20%	68%
	4 hours					
±20	27%	68%	15%	74%	18%	78%
±25	29%	64%	19%	71%	15%	74%
±30	35%	55%	21%	68%	17%	72%
±35	34%	51%	22%	65%	20%	68%

Table 7.17: Effect of charge-discharge current density and T on η_c and η_v in *Electrolyte 2*, PVE electrode / Pt-Ti mesh.

Here, the current density range employed was larger than in the previous study *viz.* $\pm 35 \text{ mA cm}^{-2}$, which led to higher η_c values (*i.e.* 36% at 25°C and 2 hours charging). However, this increase was at the expense of the η_v . Elevated temperatures (60°C) favoured the η_v values, which increased to 81% for a 1 hour charge and a charge-discharge current densities of $\pm 20 \text{ mA cm}^{-2}$. The η_c decreased with the increase of temperature, a behaviour that has been observed using *Electrolyte 1* too. The optimum temperature for the η_c was between 25°C and 40°C. Higher temperatures showed very low efficiencies and this can be attributed to either the enhancement of the competing reactions of the cell or the slower kinetics of the zinc reaction at these electrodes at the higher temperature.

7.4.3 Summary of Electrolytes 3-6

Electrolyte 3 contained a higher concentration of methanesulfonic acid compared to *Electrolyte 2*. However, the η_C values in this system were significantly lower here. This was due to the HER process being enhanced in the presence of greater methanesulfonic acid concentrations as explained in Chapter 5 Section 5.1.5. The same behaviour was reported in the findings of Leung *et al.* in the same medium [19]. The results from *Electrolyte 4* were not encouraging as the increase of the zinc(II) concentration did not improve the η_C , *i.e.* $\eta_C < 30\%$ for 30 minute trials. On the contrary, the values were lower when compared to those of *Electrolyte 1* (*viz.* 40%). Finally, *Electrolytes 4* and *5* showed signs of cerium precipitation in a matter of days clearly suggesting that high cerium (III) carbonate concentrations cannot be used for the undivided zinc cerium cell.

7.4.5 Conclusions

The preliminary experiments that were carried out in an undivided cell containing various electrolytes resulted in η_C values of *ca.* 40% and η_C values in the range of 80%. Increasing the methanesulfonic acid concentration, led to Ce(III) precipitation and also to low η_C values due to Ce(III) oxidation reaction competing with the zinc deposition on the carbon surface. It has been reported that inhibitors such as indium oxide suppress the HER process in acidic media [20] and this could be employed here in future experiments. In addition, increasing the cerium (III) carbonate concentration also lead to the solution to precipitate. Elevated temperatures (*i.e.* 60°C) favoured the η_V values. As expected, prolonged charging times (from 30 minutes to 4 hours) decreased the η_C values and to a smaller extent the η_V values.

-
- [1] M.L. Hitchman, *Measurement of dissolved oxygen*, Wiley, New York, p197, (1978).
- [2] <http://www.sigmaaldrich.com/united-kingdom.html> accessed: Dec. 2011
- [3] T. Raju, C.A. Basha, *J. Portugaliae Electrochim. Acta.*, **23**, 367-378, (2005).
- [4] T. Raju, C.A. Basha, *Ind. Eng. Chem. Res.*, **47**, 8947-8952, (2008).
- [5] T.D. Goldenz, A.Q. Wang, *J. Electrochem. Soc.*, **150**, 9, 621-624, (2003).
- [6] M. Pourbaix, *Atlas of Electrochemical Equilibria in Aqueous Solutions*, NACE, Houston, Texas, (1974).
- [7] P.K. Leung, C. Ponce de León, C.T.J. Low, F.C. Walsh, *Electrochim. Acta.*, **56**, 5, 2415-2153, (2011).
- [8] A. Pavlenova, S. Creager, J. Navratil, Y. Wei, *J. Power Sources.*, **109**, 431, (2002).
- [9] M. Spotnitz, R.P. Kreh, J.T. Lundquist, P.J. Press, *J. Appl. Electrochem.*, **20**, 209-215, (1990).
- [10] J. Ludek, W. Yuezhou, M. Kumagai, *J. Rare Earths.*, **24**, 257-263, (2006).
- [11] H.L. Silcock, *Solubilities of Inorganic and Organic compounds*, Volume 3, Pergamon, New York, (1979).
- [12] H. Van Parys, G. Telias, V. Nedashkivskyi, B. Mollay, I. Vandendael, S. Van Damme, J. Deconinck, A. Hubin, *Electrochim. Acta.*, **55**, 20, 5709-5718, (2010).
- [13] H. Vogt, R.J. Balzer, *Electrochim. Acta.*, **50**, 2073, (2005).
- [14] P. Maciel, T. Nierhaus, S. Van Damme, H. Van Parys, J. Deconinck, A. Hubin *Electrochem. Comm.*, **11**, 875, (2009).
- [15] R.L. Clarke, B.J. Dougherty, S. Harrison, J.P. Millington, S. Mohanta, US 2006/0063065 A1, Battery with bifunctional electrolyte (2005).
- [16] P.K. Leung, C. Ponce de León, F.C. Walsh, *Electrochem. Communications.*, **13**, 770-773, (2011).
- [17] P.K. Leung, C. Ponce-de-Leon, A.A. Shah, F.C. Walsh, *J. Power Sources.*, **11**, 5174-5185, (2011).
- [18] Z. Xie, D. Zhou, F. Xiong, S. Zhang, K. Huang, *J. Rare Earths.*, **29**, 6, 567, (2011).
- [19] P.K. Leung, C. Ponce-de-Leon, C.T.J. Low, F.C. Walsh, *Electrochim. Acta.*, **56**, 6536-6546, (2011).
- [20] A.E. Saba, A.E. Elsherief, *Hydrometallurgy.*, **54**, 91, (2000).

Chapter 8

8.1. Conclusions

The ability to store and supply energy, in particular electrical energy, are important cornerstones for future stable and long term economic development, growth and security. Redox flow batteries have the potential of providing a realistic solution to medium and large scale electrical energy storage and so increase the flexibility of power systems and improve the response to a rising demand of energy. By enabling a fuller integration of the renewable energy generators, such as wind, photovoltaics and tidal, into the national grid or as stand alone 'island' systems, this projected increase in energy demand can be delivered with minimal damage to the environment.

This study was concerned with the evaluation of the hybrid zinc-cerium redox flow battery. The clear advantage that the zinc-cerium flow cell has over other flow battery systems such as the all-vanadium RFB is that the cell voltage is ~ 2.5 V (*c.f.* to 1.4 V for the latter) and hence greater power can be delivered from a single unit. During this project, the optimum operating parameters for the performance of the zinc-cerium hybrid redox flow battery (RFB) were examined. The half-cell reactions were studied under a variety of electrode substrates, temperature and electrolyte compositions.

The efficiency of the zinc-half cell reaction was examined at several carbon-based substrates and three of these (the PVE, HDPE-2 and PVDF composites) showed great potential in terms of coulombic and voltage efficiencies ($\eta_{\varepsilon} = 78\%$). The stability of the substrates following numerous zinc deposition-dissolution cycles were examined and although some deterioration of the electrode surface was found in most of the substrates examined, the PVE, HDPE and PVDF were not severely affected and good cycling performance could be maintained over 200 cycles. The zinc deposition/dissolution reaction was carried out in concentrated methanesulfonic acid solution and although the hydrogen evolution reaction is inhibited on the electrodeposited zinc substrate, at high current densities (*i.e.* >100 mA cm⁻²) the problem of HER became a serious issue. Nucleation studies indicated that a high density of nuclei (10^5 cm⁻²) was formed on these carbon substrates from these solutions which led to the formation of more uniform deposits and minimised dendritic growth. Evidence for this was obtained from optical microscopy and SEM analysis. Also, the diffusion coefficients from the methanesulfonate electrolyte increased with temperature from 4.6×10^{-6} cm² s⁻¹ to 1.38×10^{-5} cm² s⁻¹.

The study on the positive half-cell reaction was carried out using a range of Pt and Pt-Ir based coatings on a titanium base. The high positive potential (~ 1.4 V) of this reaction meant that carbon-based substrates were not suitable and would undergo oxidation over time. The kinetics of this reaction on the various substrates was examined through Tafel extrapolation, linear polarisation resistance and electrochemical impedance spectroscopy measurements. Good correspondence was found in the exchange current density values found using these techniques and with the literature. The substrates containing higher amounts of platinum demonstrated higher exchange current densities at the temperature range investigated (*viz.* $\sim 10 \times 10^{-3}$ A cm $^{-2}$ at 60°C). Higher temperatures were shown to favour the reaction but the solubility of the cerium species in the methanesulfonic acid was found to be dependent on both temperature and on the acid concentration/water content. In addition, the D values ($\sim 3.5 \times 10^{-7}$ cm 2 s $^{-1}$) increased with temperature and cerium (IV) concentration. As far as the galvanic cycles are concerned, higher current densities (>20 mA cm $^{-2}$) led to the oxygen evolution reaction during charging and to the HER during discharge.

The initial batch cell zinc-cerium system examined provided useful insight into the importance of mass transport, current density and solution composition on the coulombic efficiency of the reactions. This information was then applied to the full redox flow system and here, numerous cycling studies using a range of different operation conditions were undertaken in order to establish the key parameters for stable, efficient and long term performance of the hybrid zinc-cerium RFB. The temperature range between 45°C and 55°C was found to be best for operating the redox flow cell and the coulombic efficiency increased with zinc concentration with a $\eta_C \sim 95\%$ obtained at a 2 mol dm $^{-3}$ zinc concentration. The η_V did not exceed 70% but in the case of the undivided system (no membrane). The highest energy efficiency η_e achieved in this study was $\sim 55\%$, in good agreement with other studies on this system.

8.2. Future work

The results obtained during the early stage development of the Zn-Ce hybrid redox flow battery are very encouraging. However, further research is required on the various operating conditions such as establishing the state of charge (0-100%), current density (10 mA cm⁻² to 50 mA cm⁻²), electrolyte composition (zinc and cerium concentrations, *i.e* energy density) and cycling stability. Furthermore, the results from the positive half cell study indicated that there are other materials that exhibit similar behaviour to that of the Pt-Ti mesh, which is currently used at the positive side of the flow cell.

In addition, the next step should involve the scale up of the flow cell, which will in turn lead to the investigation and development of appropriate bipolar electrodes. The literature review on the carbon bipolar electrodes showed that they are widely used in the all-vanadium RFB. Therefore, for the negative side of the zinc cerium cell the characteristics of the carbon electrode should involve a high surface area and porosity (*i.e* carbon felt), resistance to acidic environment (prior treatment such as etching), durability, robustness and exhibition of fast kinetics for the Zn(0)/Zn(II) reaction (graphene oxide nanopellets). Nonetheless, both the PVE and PVDF electrodes do exhibit most of the desired features for the zinc deposition/dissolution reaction. Regarding the positive side of the zinc cerium cell, the Pt-Ti mesh reaction as platinum seems like the most reliable and suitable material to carry out the reaction on the positive side of the zinc-cerium cell (*i.e* fast kinetics, high conversion rates). However, since the negative side of the cell requires a carbon electrode, the bipolar electrode is more likely to be carbon based. Hence, the use of the Pt-Ti mesh on the positive side is rather difficult to achieve (*i.e* problems with the binding of the two materials (carbon and platinized titanium) are more likely to arise). Therefore, Pt and Ti coatings on the carbon substrate have to be investigated. The literature review on the surface titanium coatings showed that there are many ways on how to coat titanium, although not on a carbon surface. Methods that avoid the use of HF (to remove surface oxide of TiO₂) are preferred due to the environmental and health implication of HF. The same stands for the Pt coating where the use of platinum chloride to deposit platinum is preferred.